Technische Universität München
Fakultät für Maschinenwesen
Lehrstuhl für Flugsystemdynamik

Platform-autonomous Fault-tolerant Attitude/Heading Reference and Navigation Systems

Fedor Baklanov

Vollständiger Abdruck der von der Fakultät für Maschinenwesen der Technischen Universität München zur Erlangung des akademischen Grades eines Doktor-Ingenieurs (Dr.-Ing) genehmigten Dissertation.

Vorsitzende(r): Prof. Dr.-Ing. Manfred Hajek

Prüfer der Dissertation:

1. Prof. Dr.-Ing Florian Holzapfel
2. Prof. Dr.-Ing Alfred Kleusberg, Universität Stuttgart

Der Dissertation wurde am 10.11.2016 bei der Technischen Universität München eingereicht und durch die Fakultät für Maschinenwesen am 02.03.2017 angenommen.

Abstract

This thesis investigates possibility to improve reliability and performance of low-cost aeronautical integrated navigation systems by making use of robust autonomous measurements, namely of inertial measurement unit (IMU), air data system (ADS), and 3-axis magnetometer. The thesis begins with a systematic study of a problem of Air Data, Magnetometer, and INS integration, which includes derivation of high-fidelity measurement equations and analytical analysis of observability. Further, several alternative mechanizations of attitude and heading reference/back-up navigation system are proposed and compared by the means of simulation and flight tests. Then, applicability of existing redundancy concepts to the problem of integrated navigation is considered. It is argued that particular aspects of the problem make applying system level approaches problematic, and therefore homogeneous redundancy of the most crucial parts of the system, such as IMU and some of the aiding systems, is required. Two classical methods of fault detection and isolation, namely Parity Space method and Kalman filter innovation sequence monitoring are extended by exploiting Kolmogorov-Smirnov test for decision making. The central applied result of the research consists in proposing low size, weight, power, and cost (SWaP-C) design of a robust platform-autonomous fault-tolerant navigation system with the best in-IMU-class performance, which, in the events of failures, can gracefully degrade to attitude and heading reference system (AHRS). As a side effect of the observability analysis, a unified methodology of observability investigation in linear time-varying systems is developed, and a relation between observability matrix and observability Gramian is established. In the end it is demonstrated that suitable choice of filter mechanization can provide certain benefits for integrated navigation systems featuring low-cost inertial sensors.

Acknowledgements

At first, I would like to thank Prof. Florian Holzapfel for giving me a chance to become a doctoral candidate at the Technical University of Munich, Institute of Flight System Dynamics. Dr. Holzapfel, in fact, was the first professor, who responded to my application for a PhD position in Germany. I am very much grateful to him for accepting me to his institute and finding funding for me.

Next, I would like to express gratitude to Dr. Johann Dambeck, who supervised my research from the very beginning. Dr. Dambeck formulated a very interesting problem for me and helped me to understand better numerous aspects of applications. From him I learned to develop deeper understanding of research subjects, and his smart and sometimes unexpected questions, asked during our professional discussions, allowed to improve a lot quality of my results.

I must also thank Prof. Viktor Morozov for discussing various mathematical aspects of navigation with me, and Prof. Yuriy Bolotin for being a reviewer of the presentations that I gave on PhD seminars in Lomonosov Moscow State University.

Further, I would like to remember Russian-speaking group of young researchers, working in Garching, which met regularly for lunch, followed by drinking tea, cooked at first carefully by Anton Bogomolov, and later by Ivan Erofeev. Dear, Anton, Ivan, Ekaterina Fokina, Dmitriy Prisiazhniuk, Dmytro Meshcheriakov, Serhiy Mochalskyy, Anna Medvedeva, Kirill Nemkovski, Marina Haneft, Dmitriy Moseev, Didier Vicent, Valentin Igochine, Alexandra Kulik, Alexander Ivanov, Denis Kalupin, without you my life in Munich would not be so colorful.

I would also like to thank the State of Bavaria and the Bavarian Research Foundation for approving the scholarship for my research project. This beautiful land will always remain in my heart.

Lorenz Görcke and Yahao Cheng were my great officemates and I am very much grateful to them for always being friendly and ready to help.

And of course, I would not be able to complete my research without support from my parents and my future wife Tatsiana.

Munich, July 2016

Contents

List of Figures **13**

List of Tables **21**

Nomenclature **17**

1 Introduction **21**

2 Preliminaries **27**
2.1 Coordinate frames 27
2.1.1 Quasi-inertial coordinate frame (i-frame) 27
2.1.2 Earth-centered Earth-fixed coordinate frame (e-frame) 27
2.1.3 Body-fixed coordinate frame (b-frame) 28
2.1.4 Local-level North-indicating coordinate frame (n-frame) 28
2.2 Navigation equations 28
2.3 Error propagation equations 30
2.4 General measurement equations 31
2.5 Discretization of linear systems 32
2.6 Kalman filter 33
2.6.1 Discrete version 33
2.6.2 Continuous version 34
2.7 General structure of an integrated navigation system 34

3 Observability analysis **37**
3.1 Methodology for observability analysis 37
3.1.1 Basic facts and definitions 37
3.1.2 Analytical approach 40
3.1.3 Numerical approach 40
3.1.4 Numerical verification of analytical analysis 41
3.1.5 Trajectories of interest 42
3.2 Air data measurements 43
3.2.1 Air data measurement equations 43

3.2.2 Simplification of error propagation equations 46
3.2.3 Barometric altimeter measurement 47
3.2.4 True airspeed measurement 49
3.2.5 Combination of barometric altitude and TAS 51
3.2.6 Measurement of b-frame velocity w.r.t wind 52
3.2.7 Combination of barometric altitude and velocity w.r.t wind measurements 54
3.2.8 TAS combined with AOA 55
3.2.9 TAS combined with AOS 56
3.2.10 AOA combined with AOS 56
3.2.11 Unobservability of heading error 57
3.2.12 Discussion 59
3.3 The Earth's magnetic field measurements 59
3.3.1 Models of the Earth's magnetic field 59
3.3.2 Magnetometer measurement equations 65
3.3.3 Determination of magnetic heading 66
3.3.4 Simplification of error propagation equations 66
3.3.5 Simplification of magnetometer measurement model 67
3.3.6 Observable combinations 68
3.3.7 Discussion 69
3.4 Verification of observable combinations 71
3.5 Demonstration of observability properties by simulation 71
3.5.1 Aiding by ADS 71
3.5.2 Aiding by magnetometer 79
3.6 Conclusions 84

4 Alternative AHRS mechanizations 87
4.1 IMU + Magnetometer 87
4.2 IMU + Magnetometer + Barometric altimeter 89
4.3 IMU + Magnetometer + Barometric altimeter + Air Data System 90
4.4 Simulation and comparison of mechanizations 91
4.5 Real data processing 96
4.6 Conclusions 100

5 Fault-tolerance and reliability of AHR/navigation systems 103
5.1 Redundancy concepts 103
5.2 Sensor-level redundancy 103
5.2.1 Failure detection and isolation logic and related terminology 103
5.2.2 Parity space approach 104

5.2.2.1 Fault detection algorithm ... 105
5.2.2.2 Fault isolation algorithm ... 105
5.2.3 Optimal geometries ... 106
5.2.4 Kolmogorov-Smirnov test ... 107
5.2.5 Extension of parity space approach with Kolmogorov-Smirnov test ... 107
5.2.6 Simulation and comparison ... 109
5.2.7 Problems of low-cost applications ... 112
5.2.8 Modification of the methods for use in low-cost systems ... 113
5.2.8.1 Standard parity space method ... 113
5.2.8.2 KS modified parity space method ... 113
5.2.9 Monte Carlo simulation and discussion ... 115
5.2.10 Instantaneous vs. history-based failure detection ... 116
5.3 Model-based failure detection and integrity monitoring ... 117
5.3.1 Applicability of classical techniques ... 117
5.3.2 Innovation history monitoring using Kolmogorov-Smirnov test ... 118
5.3.3 Discussion ... 121
5.3.4 Simulation ... 121
5.4 Conclusions ... 125
5.5 Proposal for a minimum fault-tolerant design of AHRS ... 126
5.6 Never give-up concept of operation ... 127
5.7 Reliability analysis of the proposed design ... 129

6 Summary of results and conclusions ... 133

Appendix A. Proof of the Theorem 4. ... 137

Appendix B. Observability and Kalman filtering. ... 143
B.1 Solution of covariance equation in “zero noise” case ... 143
B.2 Kalman filter and Kalman canonical decomposition ... 145
B.3 Solution of covariance equation in “zero noise” case for decomposed LTI system ... 146
B.4 Example ... 149

Appendix C. Performance classes according to RTCA DO-334. ... 155

Appendix D. Simulation environment. ... 157
D.1 Trajectory generation ... 157
D.1.1 Trajectory for demonstration of observability properties ... 157
D.1.2 Trajectory for simulation of FDI methodologies ... 157

D.1.3 Highly dynamic (aerobatic) trajectory 159
D.2 IMU error model 161
D.3 Modeling of wind 161
D.4 Modeling of magnetic field disturbances 163
D.5 Modeling of errors of aiding sensors 163
D.6 Optimal filter 164
D.7 Initialization of covariance matrix 164
D.7.1 Initialization of the filter in Section 3.5.1 164
D.7.2 Initialization of the filter in Section 3.5.2 164
D.7.3 Initialization of the filter in Section 4.4 164
D.7.3.1 IMU+Magnetometer 164
D.7.3.2 IMU+Barometric altimeter+Magnetometer 165
D.7.3.3 IMU+Barometric altimeter+Magnetometer+Air Data 165
D.7.4 Initialization of the filter in Section 5.3.4 165
D.8 System noise matrix 166
D.8.1 System noise matrix of the filter in Section 3.5.1 166
D.8.2 System noise matrix of the filter in Section 3.5.2 166
D.8.3 System noise matrix of the filter in Section 4.4 166
D.8.3.1 IMU+Magnetometer 166
D.8.3.2 IMU+Barometric altimeter+Magnetometer 166
D.8.3.3 IMU+Barometric altimeter+Magnetometer+Air Data 167
D.9 Measurement noise matrices 167
D.10 Simple approach to reduce effect of wind gusts 167

Appendix E. Example of application of the verification approach. 169
E.1 Inertial measurement unit calibration as optimal estimation 169
E.2 Case of rotation around vertical axis 170
E.2.1 The first stage of calibration 170
E.2.2 The second stage of calibration 171
E.2.3 The third stage of calibration 172
E.2.4 Summary of the analysis 173
E.3 Case of rotating around horizontal axis 174
E.4 Numerical verification of observable combinations 175

Appendix F. Justification of linearized error propagation. 181

Appendix G. Derivation of equations for b-frame velocity vector. 185

Appendix H. Comparison of b- and n-frame mechanizations. 189

Appendix I. Optimal sensor geometries. 209
I.1 Three sensors 209
I.2 Four sensors 209
I.3 Five sensors 210
I.4 Six sensors 211
I.5 Seven sensors 212
I.6 Ten sensors 213

Bibliography 215

List of Figures

Fig. 1–Coordinate frames: e- and i-frames 27
Fig. 2–Coordinate frames: n-frame 28
Fig. 3–Structure of an integrated navigation system 35
Fig. 4–Dipole model of the Earth's magnetic field 60
Fig. 5–Comparison of models of the Earth's magnetic field. Dipole vs. EMM. 62
Fig. 6–Comparison of models of the Earth's magnetic field. WMM6 vs. EMM. 63
Fig. 7–Comparison of models of the Earth's magnetic field. WMM12 vs. EMM. 64
Fig. 8–Standard deviation of position 72
Fig. 9–Position error of the corrected total state 72
Fig. 10–Standard deviation of velocity 73
Fig. 11–Velocity error of the corrected total state 74
Fig. 12–Standard deviations of orientation errors 75
Fig. 13–Orientation errors of the corrected total state 75
Fig. 14–Standard deviations of accelerometer biases 76
Fig. 15–Estimates of accelerometer biases 77
Fig. 16–Standard deviations of the biases of gyroscopes 78
Fig. 17–Estimates of gyroscope biases 78
Fig. 18–Position error of the corrected total state 80
Fig. 19–Velocity error of the corrected total state 81
Fig. 20–Orientation error of the corrected total state 81
Fig. 21–Estimates of accelerometer biases 82
Fig. 22–Estimate of biases of the gyroscopes 82
Fig. 23–Estimates of biases of the magnetometer 83
Fig. 24–Estimate of the error of magnetic model 83
Fig. 25–Standard deviations of orientation errors. Tactical-grade IMU. 92
Fig. 26–Orientation errors of the corrected total state. Tactical-grade IMU. 92
Fig. 27–Standard deviations of orientation errors. Industrial-grade IMU. 93
Fig. 28–Orientation errors of the corrected total state. Industrial-grade IMU. 93
Fig. 29–Estimate of latitude. 94
Fig. 30–Estimate of longitude. 95
Fig. 31–Reference flight path and height. 97
Fig. 32–Air data measurements. 97

Fig. 33–B-frame measurement of the Earth's magnetic field. 98
Fig. 34–Orientation errors of the corrected total state. 99
Fig. 35–Standard deviations of roll, pitch, and heading. 99
Fig. 36–Position error. 100
Fig. 37–Fault detection and isolation logic 104
Fig. 38–Performance of standard parity space FDI 109
Fig. 39–Performance of modified parity space FDI 110
Fig. 40–Performance of standard parity space FDI 111
Fig. 41–Performance of modified parity space FDI 111
Fig. 42–Kalman filter innovation history monitoring. 119
Fig. 43–Altimeter and TAS innovations in normal mode 122
Fig. 44–AOA and AOS innovations in normal mode 123
Fig. 45–Altimeter and TAS innovations in failure mode 124
Fig. 46–AOA and AOS innovations in failure mode 124
Fig. 47–Minimum robust design of fault-tolerant AHRS 126
Fig. 48–Operation concept of the minimum design 128
Fig. 49 152
Fig. 50 153
Fig. 51 153
Fig. 52 154
Fig. 53 157
Fig. 54 158
Fig. 55 158
Fig. 56–Latitude ϕ, longitude λ, and height h profiles 159
Fig. 57–Orientation angles: roll φ, pitch ϑ, and yaw ψ 160
Fig. 58–Angle of attack and angle of sideslip 160
Fig. 59 162
Fig. 60 162
Fig. 61 163
Fig. 62–Test indicators 176
Fig. 63–Test indicators in case of mistake in combination $y_4^{2,hor}$ 177
Fig. 64–Test indicators in case of mistake in combination $y_2^{2,hor}$ 178
Fig. 65–Test indicators in simplified analysis 179
Fig. 66 180
Fig. 67–Kolmogorov's statistics. Case of tactical-grade IMU. 182
Fig. 68–Kolmogorov's statistics. Case of industrial-grade IMU 182
Fig. 69–Standard deviations of latitude, longitude, and height errors. Industrial-grade INS. Aerobatic trajectory. Purely inertial mode. 190

Fig. 70–Standard deviations of velocity errors in b- and n-frames, respectively. Industrial-grade INS. Aerobatic trajectory. Purely inertial mode. 190
Fig. 71–RSS of velocity vector standard deviations. Industrial-grade INS. Aerobatic trajectory. Purely inertial mode..... 191
Fig. 72–Standard deviations of orientation errors. Industrial-grade INS. Aerobatic trajectory. Purely inertial mode..... 191
Fig. 73–Standard deviations of latitude, longitude, and height errors. Industrial-grade INS. Aerobatic trajectory. Aiding by TAS, AOA, and AOS..... 193
Fig. 74–Standard deviations of latitude, longitude, and height errors. Industrial-grade INS. Aerobatic trajectory. Aiding by TAS, AOA, and AOS. Filter initialization according to relation (H.2). 193
Fig. 75–Standard deviations of velocity errors in b- and n-frames, respectively. Industrial-grade INS. Aerobatic trajectory. Aiding by TAS, AOA, and AOS. 194
Fig. 76–RSS of velocity vector standard deviations. Industrial-grade INS. Aerobatic trajectory. Aiding by TAS, AOA, and AOS. 194
Fig. 77–Standard deviations of errors of b-frame velocity vector. Industrial-grade INS. Aerobatic trajectory. Aiding by TAS, AOA, and AOS..... 195
Fig. 78–Standard deviations of errors of n-frame velocity vector. Industrial-grade INS. Aerobatic trajectory. Aiding by TAS, AOA, and AOS..... 195
Fig. 79–Standard deviations of orientation errors. Industrial-grade INS. Aerobatic trajectory. Aiding by TAS, AOA, and AOS. 196
Fig. 80–Standard deviations of latitude, longitude, and height errors. Tactical-grade INS. Aerobatic trajectory. Aiding by TAS, AOA, and AOS..... 196
Fig. 81–Standard deviations of velocity errors in b- and n-frames, respectively. Tactical-grade INS. Aerobatic trajectory. Aiding by TAS, AOA, and AOS. 197
Fig. 82–RSS of velocity vector standard deviations. Tactical-grade INS. Aerobatic trajectory. Aiding by TAS, AOA, and AOS. 197
Fig. 83–Standard deviations of errors of b-frame velocity vector. Tactical-grade INS. Aerobatic trajectory. Aiding by TAS, AOA, and AOS..... 198
Fig. 84–Standard deviations of errors of n-frame velocity vector. Tactical-grade INS. Aerobatic trajectory. Aiding by TAS, AOA, and AOS..... 198
Fig. 85–Standard deviations of orientation errors. Tactical-grade INS. Aerobatic trajectory. Aiding by TAS, AOA, and AOS. 199
Fig. 86–Standard deviations of latitude, longitude, and height errors. Industrial-grade INS. Aerobatic trajectory. Aiding by barometric altitude. 200
Fig. 87–Standard deviations of velocity errors in b- and n-frames, respectively. Industrial-grade INS. Aerobatic trajectory. Aiding by barometric altitude..... 201
Fig. 88–RSS of velocity vector standard deviations. Industrial-grade INS. Aerobatic trajectory. Aiding by barometric altitude..... 201

Fig. 89–Standard deviations of orientation errors. Industrial-grade INS. Aerobatic trajectory. Aiding by barometric altitude..... 202
Fig. 90–Standard deviations of latitude, longitude, and height errors. Tactical-grade INS. Aerobatic trajectory. Aiding by barometric altitude. 202
Fig. 91–Standard deviations of velocity errors in b- and n-frames, respectively. Tactical-grade INS. Aerobatic trajectory. Aiding by barometric altitude..... 203
Fig. 92–RSS of velocity vector standard deviations. Tactical-grade INS. Aerobatic trajectory. Aiding by barometric altitude..... 203
Fig. 93–Standard deviations of orientation errors. Tactical-grade INS. Aerobatic trajectory. Aiding by barometric altitude..... 204
Fig. 94–$\psi_{n\tilde{n}1}$ gains. 206
Fig. 95–$\psi_{n\tilde{n}2}$ gains. 206
Fig. 96–$\psi_{n\tilde{n}3}$ gains. 207

Nomenclature

Acronyms

AD-AHRS	Air data attitude and heading reference system
ADS	Air data system
AHR	Attitude and heading reference
AHRS	Attitude and heading reference system
AOA	Angle of attack
AOS	Angle of sideslip
CAS	Calibrated airspeed
CD	Correct detection
CDF	Cumulative distribution function
CI	Correct isolation
CR	Correct rejection
DCG	The United Kingdom's Defense Geographic Center
ECEF	Earth-centered Earth-fixed
EMM	Enhanced magnetic model
FA	False alarm
FAA	Federal Aviation Administration
FD	Fault detection
FDI	Fault detection and isolation
FI	False isolation
FOG	Fiber optic gyroscope
FP	Fault present
GNSS	Global navigation satellite system
GPS	Global positioning system
HP	High performance
IAGA	International Association of Geomagnetism and Aeronomy
IAS	Indicated airspeed
IERS	International Earth rotation and reference systems service
IGRF	International geomagnetic reference field
IMU	Inertial measurement unit
INS	Inertial navigation system
KF	Kalman filter
KS	Kolmogorov-Smirnov
LTI	Linear time invariant
MD	Missed detection
MEMS	Microelectromechanical system
MI	Missed isolation
NATO	North Atlantic Treaty Organization
NGA	The United States' National Geospatial-Intelligence Agency
OAT	Outside air temperature
RLG	Ring laser gyroscope
RMS	Root mean square
RSS	Root sum squared
RTCA	Radio Technical Commission for Aeronautics
TAS	True airspeed
UAV	Unmanned aerial vehicle
w.r.t.	With respect to
WGS	World geodetic system
WI	Wrong isolation
WMM	World magnetic model

Notation

Throughout this thesis the following notation rules are accepted.

Small regular letters x denote scalar values. Small boldface letters $\mathbf{x}$ denote vectors. Capital boldface letters $\mathbf{X}$ are used to denote matrices.

$\mathbf{z}$	True value
$\tilde{\mathbf{z}}$	Erroneous or estimated value of $\mathbf{z}$
$\delta\mathbf{z} = \mathbf{z} - \tilde{\mathbf{z}}$	Error vector
$\hat{\mathbf{z}}$	Estimate of $\mathbf{z}$
$\mathbf{I}$	Identity matrix
$\mathbf{z}_k$	Discrete-time variable at time t_k
$\sigma_{\cdot}$	Standard deviation of the quantity, defined in subscript
$\mathrm{E}[\cdot]$	Mathematical expectation of a random variable given in brackets
$\mathbf{x}_a$	Vector given in a-frame
$h.o.t.$	Higher order terms
$[\mathbf{a}\times]$	Skew-symmetric matrix operator, $[\mathbf{a}\times]\cdot\mathbf{b} = \mathbf{a}\times\mathbf{b}$

Symbols

i	Inertial coordinate frame
e	Earth-Centered Earth-fixed coordinate frame
n	Local level north-indicating coordinate frame
b	Body-fixed coordinate frame
t	Time
τ	Time
ϕ	WGS84 latitude
λ	WGS84 longitude
h	WGS84 height
$\mathbf{v}$	Velocity vector
φ	Roll angle
ϑ	Pitch angle
ψ	Heading angle
$\mathbf{R}_{ac}$	A matrix, defining rotation from c-frame to a-frame: $\mathbf{v}_a = \mathbf{R}_{ac}\mathbf{v}_c$.
$\boldsymbol{\omega}_{ie}$	Earth's rotation rate vector in e-frame
$\boldsymbol{\Omega}_{ie}$	Skew-symmetric matrix of vector $\boldsymbol{\omega}_{ie}$
$\boldsymbol{\omega}_{en}$	Transport rate vector in n-frame
$\boldsymbol{\Omega}_{en}$	Skew-symmetric matrix of vector $\boldsymbol{\omega}_{en}$
$\boldsymbol{\omega}_{ib}$	Rotation rate vector of b-frame relative to i-frame expressed in b-frame
$\boldsymbol{\Omega}_{ib}$	Skew-symmetric matrix of vector $\boldsymbol{\omega}_{ib}$
$\mathbf{f}_b$	Vector of specific force in b-frame
$\boldsymbol{\gamma}$	Gravity vector
g	Gravity constant
R	Mean radius of the Earth
$\delta\mathbf{f}_b$	Vector of instrumental errors of accelerometers
$\delta\boldsymbol{\omega}_{ib}$	Vector of instrumental errors of gyroscopes
$\boldsymbol{\Phi}(t_2, t_1)$	Transition matrix of linear dynamic system
α	Angle of attack, or false alarm rate
β	Angle of sideslip
$\mathbf{v}^W$	Wind speed
$\mathbf{a}^W$	Wind acceleration
u, v, w	B-frame projections of velocity vector
u^W, v^W, w^W	B-frame projections of wind speed
r	Curvature of a turn

$\mathbf{B}$	Magnetic field vector
j	Dipole moment
V	Potential of the Earth's magnetic field
$\mathbf{H}$	Measurement matrix
$\mathbf{P}$	Covariance matrix, or parity matrix
$\mathbf{Q}$	System noise covariance matrix
$\mathbf{\Gamma}$	Input matrix
$\mathbf{R}$	Measurement noise covariance matrix
$\hat{\mathbf{z}}_k^-$	A priori estimate of vector $\mathbf{z}$ at time t_k
$\hat{\mathbf{z}}_k^+$	A posteriori estimate of vector $\mathbf{z}$ at time t_k
$\mathbf{q}$	System noise vector
$\mathbf{y}$	Measurement vector
$\mathbf{r}$	Measurement noise vector
$\mathbf{s}$	Innovation, or residual
ν	Scalar white noise
$\mathbf{v}$	Vector white noise
$N(\mathbf{a},\mathbf{C})$	Multidimensional normal distribution with the mean $\mathbf{a}$ and covariance $\mathbf{C}$
$\mathbf{W}(t,t_0)$	Observability Gramian
$\mathbf{L}(t)$	Observability matrix
$D(t)$	Subspace observable at time t
D	Decision variable
D_n	Kolmogorov's statistics computed from a sample of a length n
K_α	Critical value of Kolmogorov's statistics for a given false alarm rate α
P	Probability, or a point
T	Threshold value
H	Hypothesis

List of Tables

Table 1–Observable combinations. Aiding using barometric altitude. 48
Table 2–Observable combinations. Aiding by TAS..... 51
Table 3–Observable combinations. Combined aiding using barometric altimeter and TAS. 52
Table 4–Observable combinations. Aiding by b-frame velocity w.r.t. wind measurement. 54
Table 5–Observable combinations. Combined aiding using altitude and b-frame velocity w.r.t. wind measurements. 55
Table 6–Observable combinations. Aiding by magnetometer. 70
Table 7–Position error after half an hour of operation. 95
Table 8–RMS, maximum, and average of roll, pitch, and heading errors..... 100
Table 9–Benefits and achievable performance of INS/ADS/Magnetometer integration. 101
Table 10..... 110
Table 11..... 112
Table 12–Probability of missed detection [%] rounded to 0.01 %, KS test/parity space..... 115
Table 13–Probability of correct isolation [%] rounded to 0.01 %, KS test/parity space..... 116
Table 14–Time to alert, [s]..... 117
Table 15..... 128
Table 16–Attitude performance requirements according to RTCA DO-334 155
Table 17–Heading performance requirements according to RTCA DO-334..... 155
Table 18. Parameters of the simulated sensor errors. 161

1 Introduction

The goal of the research being presented was to consider possibility to improve reliability and performance of low-cost aeronautical integrated navigation systems by making use of robust autonomous measurements, namely of air data system (ADS) and 3-axis magnetometer. ADS and magnetometer are specially highlighted throughout the study, because these systems are usually installed on board of almost any airplane.

As unmanned aerial vehicles (UAVs) are more and more widely used in civil life and economy, reliability issue becomes vitally important. In military applications occasional destruction and loss are, in general, accepted. Civil applications, in turn, are completely different from this perspective. Risk of endangering human lives or causing considerable destruction because of hard- or software failure cannot in this case be tolerated. Consequently, fault-tolerant and fail-safe performance of such systems is required to be ensured.

Modern UAVs are very often forced to make use of low-cost inertial sensors, because small size and tough payload limitations do not allow to install precise gyroscopes and accelerometers on board. Thus, the navigation solution, computed by onboard inertial navigation system, accumulates an error at a very high rate, and the INS needs to be permanently aided in order to provide reasonable accuracy throughout operation time. GNSS is currently the most popular source of INS aiding. The technology of INS/GNSS integration allows to obtain highly accurate position and orientation solutions even though accuracy of onboard inertial sensors can happen to be extremely low. However, GNSS radio signal is very weak and thus can, in principle, be remotely spoofed, jammed, or get considerably corrupted due to ionospheric scintillation. Consequently, such an integrated navigation system appears vulnerable and cannot provide high level of reliability. In contrast, onboard autonomous measurement systems, such as, for example, air data system and 3-axis magnetometer, appear much more robust, and therefore an intention to use them for improving performance and reliability in safety critical applications seems to be plain and natural. In fact, ADS and magnetometer have been used to aid INS since more than three decades, and classic books on integrated navigation very often mention the terms “air data” and “magnetic field”. However, a closer investigation of literature reveals that the book [1] states that ADS measurements present a poor source of information on speed relative to ground and thus can hardly be used for navigation. The book [2], in turn, contains a chapter dedicated to AHRS, but proposes only the simplest algorithm of INS/magnetometer integration, which is known to have a very limited performance [3] and, obviously, does not exploit the information on the Earth’s magnetic field optimally. At the moment several companies manufacture air data aided navigation systems, but nevertheless data fusion methodologies, implemented in these systems, are poorly

covered by publicly available literature. To the best author's knowledge, dedicated publications are [4] and [5]. Both of the works propose to compute roll and pitch angles of the vehicle under assumptions that

1. aircraft flies at relatively constant speed and angle of attack,
2. sideslip angle and lateral acceleration are small and can be neglected.

These assumptions restrict the scope of applicability of air data aiding to a straight flight in a very stable atmospheric conditions. Moreover, such an approach does not allow to use velocity w.r.t. wind information to improve position and velocity estimation.

There are, as well, works that consider integration of INS, ADS, and satellite navigation systems [6-8]. Though, the main purpose of such an integration is, apparently, wind field estimation and smoothing of air data measurements. Availability of information from satellite navigation system seems to be crucial, and the case of aiding INS solely by ADS is not considered in these works.

Apparently, publication [9], dated to 1972, presents one of the first attempts to aid INS by airspeed measurement.

The study of the available literature and the author's personal communication with several manufacturers led to making conclusion that a proper understanding of aiding INS using the measurements of air data system and the Earth's magnetic field was mostly missing inside the society of developers of navigation systems. That is why one part of this work was intended to study the problem systematically and answer the following questions:

- How are the ADS and magnetometer measurements related to navigation state vector, and what would be an appropriate model for integration with INS in conventional way?
- Which information on navigation error states do the measurements provide, i. e. which error states become observable in typical flight situations?
- How many error states shall be considered and estimated by navigation filter?
- Which applications can benefit from aiding by ADS and magnetometer?
- What will be achievable accuracy for tactical- and industrial-grade inertial sensors?

Another part of the research considered ensuring reliable availability of the most crucial navigation information, which in case of aeronautical applications is information on altitude and orientation. Actually, these parameters are the minimum information that enables a pilot or an autopilot to keep on flying, and therefore artificial horizon, altimeter, vertical speed indicator, and compass present essential part of onboard avionics. Thus, orientation determination and AHRS applications are emphasized throughout the study. Though, the problem is studied in a context of integrated navigation, and therefore most of the results are not related solely to AHRS but are, as well, applicable to navigation systems. The second part of the study was intended to answer the following questions:

- Which of the available onboard sensors and systems are most beneficial for accurate attitude determination?
- How shall the failures of IMU and aiding sensors be detected?

- Which of the sensors and systems shall be made redundant in order to ensure fault-tolerant performance of AHRS?
- How much will the accuracy of position and velocity determination degrade if system is aided by onboard autonomous measurement systems, i. e. with ADS and magnetometer, instead of GNSS?
- What is the minimum sensor suite to provide fault-tolerant performance of attitude and heading reference/navigation system, featuring low-cost inertial sensors?

This thesis starts with theoretical analysis of INS aiding using air data and magnetometer measurements. In the Chapter 3 measurement equations are derived, and analytical observability analysis is conducted. Further the analysis is demonstrated by the means of simulation and is discussed in the light of operational benefits. In the Chapter 4 the optimal designs are proposed, and their performance is compared by the means of simulations. Moreover, conclusions of theoretical investigation and results of simulation are confirmed by processing experimental data, collected in the test flight of the research airplane. In the Chapter 5 reliability of navigation systems is considered. At first, redundancy concept is discussed and the most suitable approaches are highlighted. Two classical fault detection and isolation (FDI) techniques are further extended and investigated. Finally, based on the conclusions of analytical investigation, a concept of fault tolerant attitude and heading reference/back-up navigation system is proposed.

So far certification rules and procedures for UAVs have not been developed by responsible organizations and are yet to come. However, these rules, no doubt, will impose high requirements on reliability of all the components of unmanned systems. Navigation system in this case is one of the most crucial systems and consequently requirements on its reliability shall be expected to be especially harsh. Therefore, the findings of this thesis shall become highly demanded in the nearest future.

2 Preliminaries

2.1 Coordinate frames

2.1.1 Quasi-inertial coordinate frame (i-frame)

Origin P_i of the quasi-inertial coordinate frame is located in the Earth's center of mass. The first axis $\mathbf{i}_1$ points towards the point of intersection at time t_0 of the zero meridian and equatorial plane. The third axis $\mathbf{i}_3$ points from the origin towards the IERS reference pole. The second axis $\mathbf{i}_2$ is the orthogonal completion of $\mathbf{i}_1$ and $\mathbf{i}_3$ to a right-handed axes system.

2.1.2 Earth-centered Earth-fixed coordinate frame (e-frame)

ECEF frame (e-frame) is a coordinate system with the origin P_e in the Earth's center of mass. The third axis $\mathbf{e}_3$ is pointing from the origin towards the IERS reference pole. The first axis points from the origin towards intersection of IERS reference meridian and the plane passing though origin and perpendicular to $\mathbf{e}_3$. The second axis $\mathbf{e}_2$ completes the right-handed system.

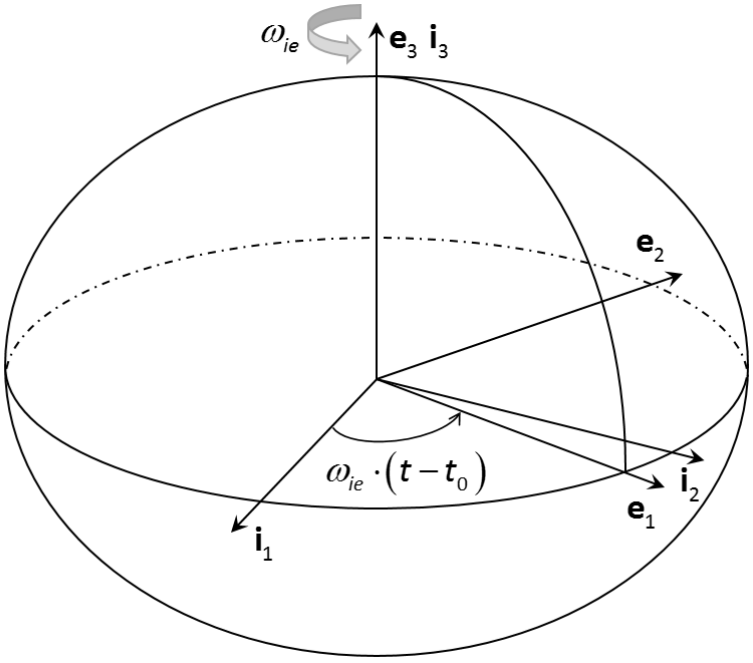

Fig. 1–Coordinate frames: e- and i-frames

2.1.3 Body-fixed coordinate frame (b-frame)

Origin P_b of the body-fixed coordinate frame (b-frame) is located in the arbitrarily chosen point of a vehicle. The first axis $\mathbf{b}_1$ points to front, the second axis $\mathbf{b}_2$ points right, and the third axis $\mathbf{b}_3$ completes the orthogonal right-handed system.

2.1.4 Local-level North-indicating coordinate frame (n-frame)

The third axis $\mathbf{n}_3$ is perpendicular to the local tangent plane to WGS84 Ellipsoid. The first axis $\mathbf{n}_1$ is parallel to the North direction in the local tangent plane to WGS84 Ellipsoid. The second axis $\mathbf{n}_2$ completes the right-handed system. Origin of the n-frame can be chose arbitrarily along the local vertical on the WGS84 Ellipsoid.

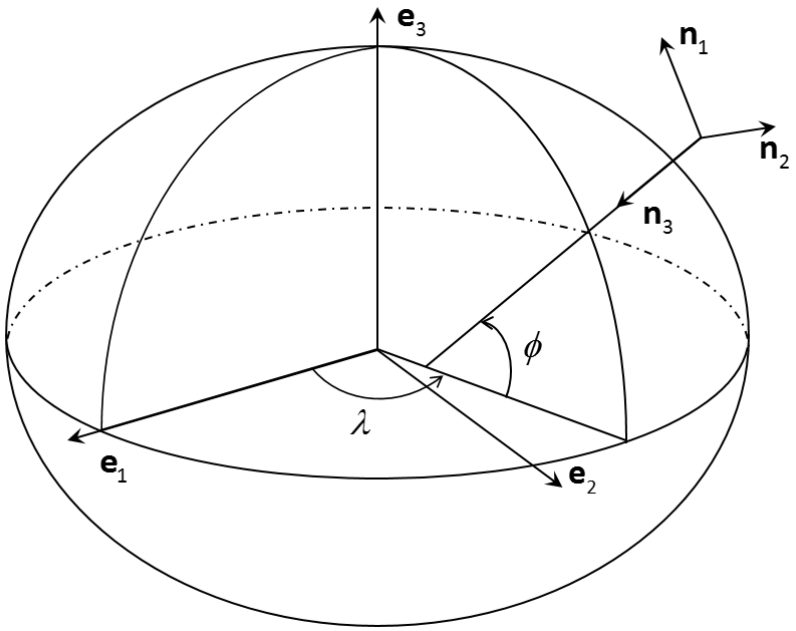

Fig. 2–Coordinate frames: n-frame

2.2 Navigation equations

The navigation equations are 1st order ordinary differential equations that describe the motion of a point mass in the neighborhood of the Earth. The navigation equations comprise a core of inertial navigation system. Given initial condition and measurements of vehicle's angular rate and specific force, acting on the vehicle, this equations are integrated numerically by onboard computer and therefore provide a pilot or flight control computer with the estimates of current position, velocity, and orientation with respect to the Earth. These equations can, for example, be written as follows

$$\begin{aligned}
&\dot{\boldsymbol{\lambda}} = \mathbf{D}^{-1}(\boldsymbol{\lambda}) \cdot \mathbf{v}_n, \\
&\dot{\mathbf{v}}_n = \mathbf{R}_{nb} \cdot \mathbf{f}_b + \boldsymbol{\gamma}_n(\boldsymbol{\lambda}) - \left(2\mathbf{R}_{en}^{\mathrm{T}}(\boldsymbol{\lambda}) \cdot \boldsymbol{\omega}_{ie} + \boldsymbol{\omega}_{en}(\boldsymbol{\lambda}, \mathbf{v}_n)\right) \times \mathbf{v}_n, \\
&\dot{\mathbf{R}}_{nb} = \mathbf{R}_{nb}\boldsymbol{\Omega}_{ib} - \boldsymbol{\Omega}_{in}\mathbf{R}_{nb}, \\
&\mathbf{D}(\boldsymbol{\lambda}) = diag\left(M(\phi) + h, \left(N(\phi) + h\right) \cdot \cos\phi, -1\right).
\end{aligned} \tag{2.1}$$

Here $\boldsymbol{\lambda}=\begin{pmatrix}\phi & \lambda & h\end{pmatrix}^{\mathrm{T}}$ is a vector, composed of geodetic latitude, longitude, and ellipsoidal height; $\mathbf{v}_n=\begin{pmatrix}v_{n1} & v_{n2} & v_{n3}\end{pmatrix}^{\mathrm{T}}$ is a vector of n-frame components of vehicle's velocity with respect to e-frame; $\mathbf{f}_b$ and $\boldsymbol{\gamma}_n$ denote specific force vector in b-frame and the Earth's gravity vector in n-frame, respectively. Rotation of some vector coordinates from b-frame to n-frame is given by matrix $\mathbf{R}_{nb}$ and from n-frame to e-frame by $\mathbf{R}_{en}$. $\boldsymbol{\omega}_{ie}$ denotes the Earth's rotation rate in e-frame, and $\boldsymbol{\omega}_{en}$ is rotation rate of n-frame relative to e-frame, commonly known as transport rate. $\boldsymbol{\Omega}_{ib}$ and $\boldsymbol{\Omega}_{in}$ are skew-symmetric matrices of generating vectors $\boldsymbol{\omega}_{ib}$ and $\boldsymbol{\omega}_{in}$, which are angular rates of b-frame and n-frame both relative to quasi-inertial i-frame, respectively. Derivation of equations (2.1) can be found in [1, 10, 11]. Note, that

$$\begin{aligned}&\mathbf{R}_{en}^{\mathrm{T}}(\phi,\lambda)\boldsymbol{\omega}_{ie}=\begin{pmatrix}\omega_{ie}\cos\phi & 0 & -\omega_{ie}\sin\phi\end{pmatrix}^{\mathrm{T}},\\&\boldsymbol{\omega}_{en}=\begin{pmatrix}v_{n2}/(N(\phi)+h) & -v_{n1}/(M(\phi)+h) & -v_{n2}/(N(\phi)+h)\cdot\tan\phi\end{pmatrix}^{\mathrm{T}},\\&\boldsymbol{\omega}_{in}=\mathbf{R}_{en}^{\mathrm{T}}(\phi,\lambda)\boldsymbol{\omega}_{ie}+\boldsymbol{\omega}_{en}.\end{aligned}\tag{2.2}$$

Herein $\omega_{ie}\approx 2\pi/24/3600$ is the modulus of the Earth's rotation rate. $N(\phi)$ and $M(\phi)$ are the Earth's normal and meridian curvature radii, whose explicit form is given by

$$N(\phi)=a/\sqrt{1-e^2\sin^2\phi},\ M(\phi)=a\left(1-e^2\right)/\left(1-e^2\sin^2\phi\right)^{3/2},\tag{2.3}$$

where a and e are the semi-major axis and the eccentricity of the WGS84 ellipsoid of revolution.

In general, vehicle's velocity vector can be expressed in e-, i-, b-, or some other coordinate frame, which allows to obtain different forms of navigation equations [12-14]. However, all the forms remain equivalent, because one is obtained from another simply by the means of a suitable coordinate transformation. In this thesis the form (2.1) is chosen, because n-frame representation of velocity vector suggests the simplest expressions of air data and magnetometer measurements.

It is well known that rotations from one coordinate system to another can be defined in terms of Euler angles and quaternions (see [1, 10] and references therein), which allows to reduce the number of rotational parameters from 9 to 3 and 4, respectively. Relation between rotation matrix and Euler angles is given by

$$\begin{aligned}\mathbf{R}_{nb}&=\begin{pmatrix}\cos\psi & -\sin\psi & 0\\ \sin\psi & \cos\psi & 0\\ 0 & 0 & 1\end{pmatrix}\begin{pmatrix}\cos\vartheta & 0 & \sin\vartheta\\ 0 & 1 & 0\\ -\sin\vartheta & 0 & \cos\vartheta\end{pmatrix}\begin{pmatrix}1 & 0 & 0\\ 0 & \cos\varphi & -\sin\varphi\\ 0 & \sin\varphi & \cos\varphi\end{pmatrix}=\\&=\begin{pmatrix}\cos\vartheta\cos\psi & \sin\varphi\sin\vartheta\cos\psi-\cos\varphi\sin\psi & \cos\varphi\sin\vartheta\cos\psi+\sin\varphi\sin\psi\\ \cos\vartheta\sin\psi & \sin\varphi\sin\vartheta\sin\psi+\cos\varphi\cos\psi & \cos\varphi\sin\vartheta\sin\psi-\sin\varphi\cos\psi\\ -\sin\vartheta & \sin\varphi\cos\vartheta & \cos\varphi\cos\vartheta\end{pmatrix}.\end{aligned}\tag{2.4}$$

Herein φ is the vehicle's roll (or bank) angle, ϑ is pitch angle, and ψ is heading angle.

Relation between arbitrary rotation matrix $\mathbf{R}$ and quaternion $\breve{\mathbf{q}}=(q_0,\mathbf{q})$, $\mathbf{q}=(q_1,q_2,q_3)^{\mathrm{T}}$, such that $q_0^2+q_1^2+q_2^2+q_3^2=1$, is given by

$$\mathbf{R}(q_0,q_1,q_2,q_3)=\begin{pmatrix} q_0^2+q_1^2-q_2^2-q_3^2 & 2(q_1q_2-q_0q_3) & 2(q_1q_3+q_0q_2) \\ 2(q_1q_2+q_0q_3) & q_0^2-q_1^2+q_2^2-q_3^2 & 2(q_2q_3-q_0q_1) \\ 2(q_1q_3-q_0q_2) & 2(q_2q_3+q_0q_1) & q_0^2-q_1^2-q_2^2+q_3^2 \end{pmatrix}. \tag{2.5}$$

Differential equations for Euler angles and quaternion $\breve{\mathbf{q}}_{nb}$, defining rotation from b- to n-frame, take the form

$$\begin{aligned} \dot{\varphi} &= \omega_{ib1}+\sin\varphi\tan\vartheta\cdot\omega_{ib2}+\cos\varphi\tan\vartheta\cdot\omega_{ib3}-\frac{\cos\psi}{\cos\vartheta}\cdot\omega_{in1}-\frac{\sin\psi}{\cos\vartheta}\cdot\omega_{in2}, \\ \dot{\vartheta} &= \cos\varphi\cdot\omega_{ib2}-\sin\varphi\cdot\omega_{ib3}+\sin\psi\cdot\omega_{in1}-\cos\psi\cdot\omega_{in2}, \\ \dot{\psi} &= \frac{\sin\varphi}{\cos\vartheta}\cdot\omega_{ib2}+\frac{\cos\varphi}{\cos\vartheta}\cdot\omega_{ib3}-\tan\vartheta\cos\psi\cdot\omega_{in1}-\tan\vartheta\sin\psi\cdot\omega_{in2}-\omega_{in2}, \end{aligned} \tag{2.6}$$

$$\dot{\breve{\mathbf{q}}}_{nb}=\frac{1}{2}\left(\breve{\mathbf{q}}_{nb}\cdot\breve{\boldsymbol{\omega}}_{ib}-\breve{\boldsymbol{\omega}}_{in}\cdot\breve{\mathbf{q}}_{nb}\right). \tag{2.7}$$

ω_{ibj} and ω_{inj}, $j=1,2,3$, denote projections of vectors $\boldsymbol{\omega}_{ib}$ and $\boldsymbol{\omega}_{in}$ to the axes of b- and n-frames, respectively. $\breve{\boldsymbol{\omega}}_{ib}=(0,\boldsymbol{\omega}_{ib})$, $\breve{\boldsymbol{\omega}}_{in}=(0,\boldsymbol{\omega}_{in})$. Product of two arbitrary quaternions $\breve{\mathbf{p}}=(p_0,\mathbf{p})$ and $\breve{\mathbf{q}}=(q_0,\mathbf{q})$ is defined as

$$\breve{\mathbf{p}}\cdot\breve{\mathbf{q}}=(p_0,\mathbf{p})\cdot(q_0,\mathbf{q})=(p_0q_0-\mathbf{p}^{\mathrm{T}}\mathbf{q},\ p_0\mathbf{q}+q_0\mathbf{p}+\mathbf{p}\times\mathbf{q}). \tag{2.8}$$

Equation (2.6) is nonlinear and is singular at $\vartheta=\pm\pi/2$. Equation (2.7), in turn, is linear and globally nonsingular. In modern navigation systems rotation matrix is usually parameterized by the means of quaternions, because it allows to avoid nonlinearities and singularities with a small number of parameters. In simulations, presented in this thesis, quaternion representation was employed, and therefore in filter implementation the third equation from (2.1) was replaced by equation (2.7).

2.3 Error propagation equations

Error propagation equations are the equations that describe dynamics of errors of the navigation state vector. Linearized error propagation equations, derived from (2.1), take the form [15]

$$\begin{aligned} \delta\dot{\boldsymbol{\lambda}} &= \left.\frac{\partial\left(\mathbf{D}^{-1}(\boldsymbol{\lambda})\cdot\mathbf{v}_n\right)}{\partial\boldsymbol{\lambda}^{\mathrm{T}}}\right|_{\tilde{\boldsymbol{\lambda}},\tilde{\mathbf{v}}_n}\cdot\delta\boldsymbol{\lambda}+\mathbf{D}^{-1}\left(\tilde{\boldsymbol{\lambda}}\right)\cdot\delta\mathbf{v}_n \\ \delta\dot{\mathbf{v}}_n &= \mathbf{A}_{21}\delta\boldsymbol{\lambda}+\mathbf{A}_{22}\delta\mathbf{v}_n-\left[\mathbf{R}_{\tilde{n}b}\tilde{\mathbf{f}}_b\times\right]\cdot\psi_{n\tilde{n}}+\mathbf{R}_{\tilde{n}b}\cdot\delta\mathbf{f}_b \\ \dot{\psi}_{n\tilde{n}} &= -\left.\frac{\partial\boldsymbol{\omega}_{in}(\boldsymbol{\lambda},\mathbf{v}_n)}{\partial\boldsymbol{\lambda}^{\mathrm{T}}}\right|_{\tilde{\boldsymbol{\lambda}},\tilde{\mathbf{v}}_n}\cdot\delta\boldsymbol{\lambda}-\left.\frac{\partial\boldsymbol{\omega}_{in}(\boldsymbol{\lambda},\mathbf{v}_n)}{\partial\mathbf{v}_n{}^{\mathrm{T}}}\right|_{\tilde{\boldsymbol{\lambda}},\tilde{\mathbf{v}}_n}\cdot\delta\mathbf{v}_n- \\ &\quad -\boldsymbol{\Omega}_{in}\left(\tilde{\boldsymbol{\lambda}},\tilde{\mathbf{v}}_n\right)\cdot\psi_{n\tilde{n}}+\mathbf{R}_{\tilde{n}b}\cdot\delta\boldsymbol{\omega}_{ib}. \end{aligned} \tag{2.9}$$

Therein $\delta\boldsymbol{\lambda}$, $\delta\mathbf{v}_n$ denote geodetic position and velocity errors; $\delta\mathbf{f}_b$ and $\delta\boldsymbol{\omega}_b$ are linear acceleration and angular rate sensor errors; $\psi_{n\tilde{n}}$ is orientation error vector. $\mathbf{A}_{21}$ and $\mathbf{A}_{22}$ are 3×3 matrices which are given by

$$\mathbf{A}_{21} = \frac{\partial \tilde{\boldsymbol{\gamma}}_n(\boldsymbol{\lambda})}{\partial \boldsymbol{\lambda}^{\mathrm{T}}}\bigg|_{\tilde{\boldsymbol{\lambda}}} - \frac{\partial\left(2\mathbf{R}_{ne}(\boldsymbol{\lambda})\boldsymbol{\Omega}_{ie}\mathbf{R}^{\mathrm{T}}{}_{ne}(\boldsymbol{\lambda}) + \boldsymbol{\Omega}_{en}\cdot\mathbf{v}_n\right)}{\partial \boldsymbol{\lambda}^{\mathrm{T}}}\bigg|_{\tilde{\boldsymbol{\lambda}},\tilde{\mathbf{v}}_n},$$
$$\mathbf{A}_{22} = -\frac{\partial\left(2\mathbf{R}_{ne}(\boldsymbol{\lambda})\boldsymbol{\Omega}_{ie}\mathbf{R}^{\mathrm{T}}{}_{ne}(\boldsymbol{\lambda}) + \boldsymbol{\Omega}_{en}\cdot\mathbf{v}_n\right)}{\partial \mathbf{v}_n{}^{\mathrm{T}}}\bigg|_{\tilde{\boldsymbol{\lambda}},\tilde{\mathbf{v}}_n}. \tag{2.10}$$

Symbol ~ over a vector or scalar denotes either measured or approximated value of a variable: $x = \tilde{x} + \delta x$. Throughout the work an error is defined as a difference between the true and the erroneous values. For an arbitrary three dimensional vector $\mathbf{a} = \begin{pmatrix} a_1 & a_2 & a_3 \end{pmatrix}^{\mathrm{T}}$

$$[\mathbf{a}\times] := \begin{pmatrix} 0 & -a_3 & a_2 \\ a_3 & 0 & -a_1 \\ -a_2 & a_1 & 0 \end{pmatrix}. \tag{2.11}$$

$\mathbf{R}_{\tilde{n}b}$ is an estimate of rotation matrix. It is related to the true rotation matrix as

$$\mathbf{R}_{\tilde{n}b} = \mathbf{R}_{\tilde{n}n}\mathbf{R}_{nb}. \tag{2.12}$$

Assuming orientation errors to be relatively small, orientation error vector $\psi_{n\tilde{n}} = \begin{pmatrix} \psi_{n\tilde{n}1} & \psi_{n\tilde{n}2} & \psi_{n\tilde{n}3} \end{pmatrix}^{\mathrm{T}}$ is introduced as follows

$$\mathbf{R}_{n\tilde{n}} = \mathbf{R}^{\mathrm{T}}_{\tilde{n}n} \approx \mathbf{I} + [\psi_{n\tilde{n}}\times]. \tag{2.13}$$

For evaluation of equations (2.9) the following approximation can be assumed

$$N(\phi) \approx R(\phi),\ M(\phi) \approx R(\phi). \tag{2.14}$$

Herein $R(\phi) = \sqrt{M(\phi)N(\phi)}$ is Gaussian mean curvature radius. Derivatives of $R(\phi)$ with respect to ϕ can be neglected, and therefore $R(\tilde{\phi})$ in (2.9) can be treated as constant.

2.4 General measurement equations

An expression of the form $\mathbf{y} = \mathbf{h}(\mathbf{z})$ that gives a relation between external aiding information $\mathbf{y}$ and navigation state vector $\mathbf{z}$ is called a measurement equation. For example, in case of a loosely coupled INS/GPS, respective position measurement equation takes the form

$$\mathbf{y}_{pos,GPS} = \begin{pmatrix} \phi & \lambda & h \end{pmatrix}^{\mathrm{T}}. \tag{2.15}$$

The actually measured value $\tilde{\mathbf{y}}$ is a superposition of the true value and an error. Thus, formally,

$$\tilde{\mathbf{y}} = \mathbf{y} - \delta\mathbf{y} = \mathbf{h}(\mathbf{z}) - \delta\mathbf{y}. \tag{2.16}$$

Equation of the form

$$\Delta\mathbf{y} = \frac{\partial \mathbf{h}(\mathbf{z})}{\partial \mathbf{z}^{\mathrm{T}}}\cdot\delta\mathbf{z} - \delta\mathbf{y} \approx \tilde{\mathbf{y}} - \mathbf{h}(\tilde{\mathbf{z}}) + h.o.t \tag{2.17}$$

is called linearized measurement equation. In general, measurement error $\delta\mathbf{y}$ is composed of both deterministic and stochastic parts. Deterministic parts of the measurement error are usually included into navigation error state vector and are estimated by the filter.

2.5 Discretization of linear systems

Consider linear stochastic system

$$\dot{\mathbf{z}} = \mathbf{A}(t)\mathbf{z} + \mathbf{\Gamma}(t)\mathbf{q}, \tag{2.18}$$

where $\mathbf{q}$ is zero-mean Gaussian white noise input, i. e.

$$\mathrm{E}\left[\mathbf{q}(t)\right] = \mathbf{0},\ \mathrm{E}\left[\mathbf{q}(t)\mathbf{q}^{\mathrm{T}}(\tau)\right] = \mathbf{Q}(t)\delta(t-\tau). \tag{2.19}$$

The continuous system (2.18) is equivalent to the discrete system

$$\mathbf{z}_{k+1} = \mathbf{\Phi}_{k+1,k}\mathbf{z}_k + \mathbf{q}_k^*. \tag{2.20}$$

Therein $\mathbf{\Phi}_{k+1,k} = \mathbf{\Phi}(t_{k+1}, t_k)$ is transition matrix of the system (2.18), which is defined as the unique solution of the system [16]

$$\frac{d\mathbf{\Phi}(t,t_0)}{dt} = \mathbf{A}(t)\mathbf{\Phi}(t,t_0),\ \mathbf{\Phi}(t_0,t_0) = \mathbf{I}, \tag{2.21}$$

where $\mathbf{I}$ is identity matrix. Note, that the solution of differential equation (2.18) with initial condition $\mathbf{z}(t_0) = \mathbf{z}_0$ is given by

$$\mathbf{z}(t) = \mathbf{\Phi}(t,t_0)\mathbf{z}_0 + \int_{t_0}^{t} \mathbf{\Phi}(t,\tau)\mathbf{\Gamma}(\tau)\mathbf{q}(\tau)d\tau. \tag{2.22}$$

In navigation applications the transition matrix is usually approximated as follows

$$\mathbf{\Phi}_{k+1,k} = \mathbf{I} + \mathbf{A}(t_k)(t_{k+1}-t_k) + \mathbf{A}^2(t_k)\frac{(t_{k+1}-t_k)^2}{2}. \tag{2.23}$$

Approximation (2.23) appears sufficient, because in navigation problems matrix $\mathbf{A}(t)$ changes slowly, and discretization step is relatively small [2].

The sequence $\mathbf{q}_k^*$ is given by

$$\mathbf{q}_k^* = \int_{t_k}^{t_{k+1}} \mathbf{\Phi}(t_{k+1},\tau)\mathbf{\Gamma}(\tau)\mathbf{q}(\tau)d\tau. \tag{2.24}$$

Since

$$\mathrm{E}\left[\mathbf{q}_k^*\right] = \mathrm{E}\left[\int_{t_k}^{t_{k+1}} \mathbf{\Phi}(t_{k+1},\tau)\mathbf{\Gamma}(\tau)\mathbf{q}(\tau)d\tau\right] = \int_{t_k}^{t_{k+1}} \mathbf{\Phi}(t_{k+1},\tau)\mathbf{\Gamma}(\tau)\mathrm{E}\left[\mathbf{q}(\tau)\right]d\tau = 0, \tag{2.25}$$

$$\begin{aligned}\mathrm{E}\left[\mathbf{q}_k^*\left(\mathbf{q}_l^*\right)^{\mathrm{T}}\right] &= \mathrm{E}\left[\int_{t_k}^{t_{k+1}} \mathbf{\Phi}(t_{k+1},\tau)\mathbf{\Gamma}(\tau)\mathbf{q}(\tau)d\tau \cdot \left(\int_{t_l}^{t_{l+1}} \mathbf{\Phi}(t_{l+1},s)\mathbf{\Gamma}(s)\mathbf{q}(s)ds\right)\right] = \\ &= \mathrm{E}\left[\int_{t_k}^{t_{k+1}}\int_{t_l}^{t_{l+1}} \mathbf{\Phi}(t_{k+1},\tau)\mathbf{\Gamma}(\tau)\mathbf{q}(\tau)\mathbf{q}^{\mathrm{T}}(s)\mathbf{\Gamma}^{\mathrm{T}}(s)\mathbf{\Phi}^{\mathrm{T}}(t_{l+1},s)d\tau ds\right] = \\ &= \int_{t_k}^{t_{k+1}}\int_{t_l}^{t_{l+1}} \mathbf{\Phi}(t_{k+1},\tau)\mathbf{\Gamma}(\tau)\mathrm{E}\left[\mathbf{q}(\tau)\mathbf{q}^{\mathrm{T}}(s)\right]\mathbf{\Gamma}^{\mathrm{T}}(s)\mathbf{\Phi}^{\mathrm{T}}(t_{l+1},s)d\tau ds = \end{aligned} \tag{2.26}$$

$$= \int_{t_k}^{t_{k+1}} \int_{t_l}^{t_{l+1}} \mathbf{\Phi}(t_{k+1},\tau)\mathbf{\Gamma}(\tau)\mathbf{Q}(\tau)\delta(\tau-s)\mathbf{\Gamma}^{\mathrm{T}}(s)\mathbf{\Phi}^{\mathrm{T}}(t_{l+1},s)d\tau ds =$$

$$= \begin{cases} 0, & k \neq l \\ \int_{t_k}^{t_{k+1}} \mathbf{\Phi}(t_{k+1},\tau)\mathbf{\Gamma}(\tau)\mathbf{Q}(\tau)\mathbf{\Gamma}^{\mathrm{T}}(\tau)\mathbf{\Phi}^{\mathrm{T}}(t_{k+1},\tau)d\tau, & k = l \end{cases},$$

the sequence $\mathbf{q}_k^*$ presents discrete zero-mean Gaussian white noise, whose covariance matrix is given by

$$\mathbf{Q}_k^* = \int_{t_k}^{t_{k+1}} \mathbf{\Phi}(t_{k+1},\tau)\mathbf{\Gamma}(\tau)\mathbf{Q}(\tau)\mathbf{\Gamma}^{\mathrm{T}}(\tau)\mathbf{\Phi}^{\mathrm{T}}(t_{k+1},\tau)d\tau. \tag{2.27}$$

A common approximation of the integral in (2.27) is [2]

$$\mathbf{Q}_k^* \approx \mathbf{\Gamma}(t_k)\mathbf{Q}(t_k)\mathbf{\Gamma}^{\mathrm{T}}(t_k)\cdot(t_{k+1}-t_k). \tag{2.28}$$

2.6 Kalman filter

2.6.1 Discrete version

In an integrated navigation system external information is used in order to estimate and correct errors of the navigation state vector. The errors are subject to stochastic linear dynamics of the form (2.18) and thus present a random process. It is known that conditional expectation $\mathrm{E}[X|Y]$ is the best estimate of the random variable X given the measurement $Y = f(X)$ in the sense that it minimizes mean squared error [17]. Kalman filter is a special case of an optimal estimator for linear processes with linear observations.

Consider discrete linear system

$$\begin{aligned} \mathbf{z}_{k+1} &= \mathbf{\Phi}_{k+1,k}\mathbf{z}_k + \mathbf{q}_k, \\ \mathbf{y}_k &= \mathbf{H}_k\mathbf{z}_k + \mathbf{r}_k, \end{aligned} \tag{2.29}$$

Assume that

$$\begin{aligned} &\mathbf{q}_k \sim N(\mathbf{0},\mathbf{Q}_k),\ \mathrm{E}\left[\mathbf{q}_k\mathbf{q}_l^{\mathrm{T}}\right] = \mathbf{0},\ k \neq l, \\ &\mathbf{r}_k \sim N(\mathbf{0},\mathbf{R}_k),\ \mathrm{E}\left[\mathbf{r}_k\mathbf{r}_l^{\mathrm{T}}\right] = \mathbf{0},\ k \neq l, \\ &\mathrm{E}\left[\mathbf{z}_k\mathbf{r}_l^{\mathrm{T}}\right] = \mathbf{0}, \\ &\mathrm{E}\left[\mathbf{z}_0\right] = \hat{\mathbf{z}}_0,\ \mathrm{E}\left[\left(\mathbf{z}_0 - \mathrm{E}\left[\mathbf{z}_0\right]\right)\left(\mathbf{z}_0 - \mathrm{E}\left[\mathbf{z}_0\right]\right)^{\mathrm{T}}\right] = \mathbf{P}_0. \end{aligned} \tag{2.30}$$

Then the conditional expectation of the vector $\mathbf{z}_k$ is normally distributed random variable with the mean $\tilde{\mathbf{z}}_k^+$ and covariance $\mathbf{P}_k^+$ subject to

$$
\begin{array}{ll}
\tilde{\mathbf{z}}_{k+1}^{-} = \boldsymbol{\Phi}_{k+1,k}\tilde{\mathbf{z}}_{k}^{-} & \text{Propagation of the mean} \\
\mathbf{P}_{k+1}^{-} = \boldsymbol{\Phi}_{k+1,k}\mathbf{P}_{k}^{-}\boldsymbol{\Phi}_{k+1,k}^{\mathsf{T}} + \mathbf{Q}_{k} & \text{Propagation of covariance matrix} \\
 & \\
\mathbf{K}_{k+1} = \mathbf{P}_{k+1}^{-}\mathbf{H}_{k+1}^{\mathsf{T}}\left(\mathbf{H}_{k+1}\mathbf{P}_{k+1}^{-}\mathbf{H}_{k+1}^{\mathsf{T}} + \mathbf{R}_{k+1}\right)^{-1} & \text{Computation of the gain matrix} \\
\tilde{\mathbf{z}}_{k+1}^{+} = \tilde{\mathbf{z}}_{k+1}^{-} + \mathbf{K}_{k+1}\left(\mathbf{y}_{k+1} - \mathbf{H}_{k+1}\tilde{\mathbf{z}}_{k+1}^{-}\right) & \text{Update of the mean} \\
\mathbf{P}_{k+1}^{+} = \left(\mathbf{I} - \mathbf{K}_{k+1}\mathbf{H}_{k+1}\right)\mathbf{P}_{k+1}^{-} & \text{Update of the covariance matrix}
\end{array}
\tag{2.31}
$$

Recursive formulas (2.31) are called the discrete Kalman filter.

2.6.2 Continuous version

Consider linear system

$$
\begin{aligned}
\dot{\mathbf{x}}(t) &= \mathbf{A}(t)\mathbf{x}(t) + \boldsymbol{\Gamma}(t)\mathbf{q}(t), \\
\mathbf{y}(t) &= \mathbf{H}(t)\mathbf{x}(t) + \mathbf{r}(t),
\end{aligned}
\tag{2.32}
$$

where $\mathbf{q}(t)$ and $\mathbf{r}(t)$ are Gaussian white noises, such that

$$
\begin{aligned}
&\mathrm{E}\left[\mathbf{q}(t)\right] = 0,\ \mathrm{E}\left[\mathbf{q}(t)\mathbf{q}^{\mathsf{T}}(\tau)\right] = \mathbf{Q}(t)\delta(t-\tau), \\
&\mathrm{E}\left[\mathbf{r}(t)\right] = 0,\ \mathrm{E}\left[\mathbf{r}(t)\mathbf{r}^{\mathsf{T}}(\tau)\right] = \mathbf{R}(t)\delta(t-\tau), \\
&\mathrm{E}\left[\mathbf{x}(t_0)\mathbf{r}^{\mathsf{T}}(t)\right] = 0,\ \mathrm{E}\left[\mathbf{x}(t_0)\mathbf{q}^{\mathsf{T}}(t)\right] = 0, \\
&\mathrm{E}\left[\mathbf{r}(t)\mathbf{q}^{\mathsf{T}}(\tau)\right] = 0.
\end{aligned}
\tag{2.33}
$$

Assume that $\mathbf{x}(t_0) \sim N(\tilde{\mathbf{x}}(t_0), \mathbf{P}(t_0))$. Then an optimal estimate of the state vector $\mathbf{x}(t)$ is given by

$$
\begin{aligned}
&\dot{\tilde{\mathbf{x}}}(t) = \mathbf{A}(t)\tilde{\mathbf{x}}(t) + \mathbf{K}(t)\left(\mathbf{y}(t) - \mathbf{H}(t)\tilde{\mathbf{x}}(t)\right), \\
&\mathbf{K}(t) = \mathbf{P}(t)\mathbf{H}^{\mathsf{T}}(t)\mathbf{R}^{-1}(t), \\
&\dot{\mathbf{P}}(t) = \mathbf{A}(t)\mathbf{P}(t) + \mathbf{P}(t)\mathbf{A}^{\mathsf{T}}(t) + \boldsymbol{\Gamma}(t)\mathbf{Q}(t)\boldsymbol{\Gamma}^{\mathsf{T}}(t) - \mathbf{P}(t)\mathbf{H}^{\mathsf{T}}(t)\mathbf{R}^{-1}(t)\mathbf{H}(t)\mathbf{P}(t), \\
&\tilde{\mathbf{x}}(t_0) = \mathrm{E}\left[\mathbf{x}(t_0)\right],\ \mathbf{P}(t_0) = \mathrm{E}\left[\left(\mathbf{x}(t_0) - \tilde{\mathbf{x}}(t_0)\right)\left(\mathbf{x}(t_0) - \tilde{\mathbf{x}}(t_0)\right)^{\mathsf{T}}\right].
\end{aligned}
\tag{2.34}
$$

Formulae (2.34) are called continuous Kalman filter, or Kalman-Bucy filter. In fact, (2.34) describes evolution of the mean and covariance of the conditional expectation $\mathrm{E}[x(t)\,|\,y(t)]$. The third equation in (2.34) is often called matrix Riccati equation.

2.7 General structure of an integrated navigation system

Modern integrated navigation systems consist usually of inertial measurement unit, external measurement systems, and onboard computer, which performs estimation of vehicle's navigation state, i. e. of position, velocity, and orientation. Conventionally, the estimation procedure is structured as follows.

Navigation equations are integrated numerically by the onboard computer given some initial condition $\tilde{\mathbf{x}}(t_0)$, measurements of specific force $\tilde{\mathbf{f}}_b$, acting on the vehicle, and vehicle's angular rate $\tilde{\boldsymbol{\omega}}_{ib}$. With

time the estimate of the navigation state accumulates error, which is due to instrumental errors of inertial sensors and an error of initial condition. That is why in parallel to numerical integration of navigation equations the onboard computer runs estimation of an error of navigation state, using information available from external measurement systems. The estimate of navigation state error can further be either fed back into inertial navigation algorithm, or used for correcting navigation information being provided to the user. Figure 3 presents the graphical illustration of the structure of an integrated navigation system.

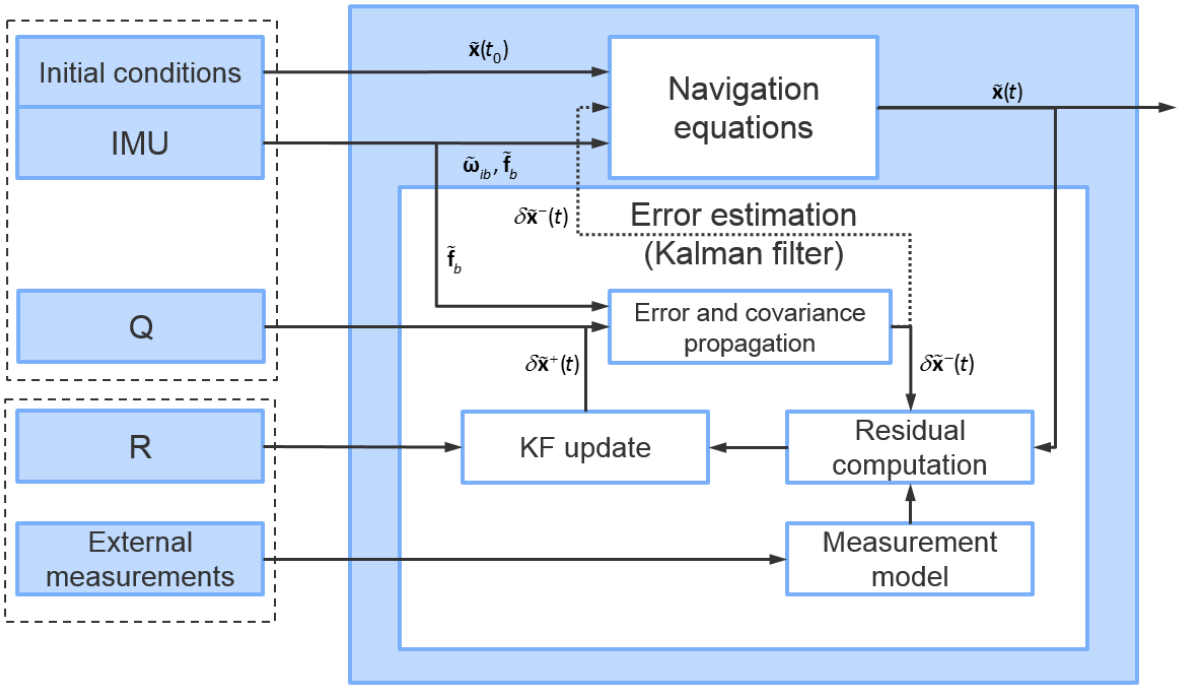

Fig. 3–Structure of an integrated navigation system

3 Observability analysis

Behavior of the Kalman filter is tightly related to the Kalman's concept of observability [18-20]. For example, if a linear time-varying system is completely observable, certain theorems guarantee that Kalman filter estimate has asymptotically stable error dynamics, and that matrix Riccati equation (2.34) has a unique steady-state solution, which is independent of initial condition [21]. However, in integrated navigation applications the system that describes dynamics of the navigation state error is usually incompletely observable. In this case there is no guarantee that aiding by the available measurement will allow to estimate and correct all the errors of the navigation solution. Moreover, Kalman canonical decomposition [18, 22] suggests that the filter itself is incapable of estimating unobservable linear combinations of navigation error states. For a user of navigation system it means that accuracy of some parts of the navigation information will degrade with time, and minimum performance requirements of the mission may become violated. This, in turn, may make successful mission accomplishment impossible or even endanger human lives. That is why fundamental behavior of navigation system must be thoroughly understood, analyzed, and documented at a stage of initial design. On the one hand, this knowledge can allow to guarantee high performance and safety, and on the other hand, to develop an optimal navigation solution for a particular application.

Observability analysis of linear dynamic system supposes determination of spaces of observable and unobservable linear combinations of the system's state vector. The fact, that some state vector component is observable does not imply, unfortunately, that it can be accurately estimated by the Kalman filter. Behavior of the filter appears to be governed by the matrix Riccati equation (2.34), whose solution depends, besides on observability properties, on initial condition, system noise covariance matrix $\mathbf{Q}(t)$ and measurement noise covariance matrix $\mathbf{R}(t)$. Thus, the information on observable and unobservable spaces, in general, helps to divide state vector components into two classes: those that may be estimated well enough by Kalman filter, and those that definitely cannot be. Knowing which states become observable at different situations, for example, at straight and leveled flight and during maneuvering, enables an engineer to predict behavior of the system, to ensure certain level of performance, to guarantee reliability, and to identify the most suitable system architecture based on details of an application.

3.1 Methodology for observability analysis

3.1.1 Basic facts and definitions

Consider a homogeneous linear dynamic system

$$\begin{aligned} \dot{\mathbf{x}} &= \mathbf{A}(t)\mathbf{x}, \\ \mathbf{y} &= \mathbf{H}(t)\mathbf{x}. \end{aligned} \tag{3.1}$$

Matrices $\mathbf{A}(t)$ and $\mathbf{H}(t)$ are assumed to be analytic functions of time, $\dim \mathbf{x} = n$, $\dim \mathbf{y} = m$.

Definition 1. *A costate is a vector in the dual space of* $\mathbb{R}^n$.

Definition 2. *Transition matrix of the system (3.1) is the unique solution of equation [16]*

$$\frac{d\mathbf{\Phi}(\tau,t)}{d\tau} = \mathbf{A}(\tau)\mathbf{\Phi}(\tau,t), \ \mathbf{\Phi}(t,t) = \mathbf{I}, \tag{3.2}$$

where $\mathbf{I}$ *is identity matrix.*

Definition 3. *A costate* $\boldsymbol{\zeta}^{\mathrm{T}}(t)$ *is said to be observable at time* t *if* $\exists t_0 < t$ *and a piecewise continuous function* $\mathbf{u}(t) \in \mathbb{R}^m$*, defined on time interval* $[t_0, t]$*, such that*

$$\boldsymbol{\zeta}(t) = \int_{t_0}^{t} \mathbf{\Phi}^{\mathrm{T}}(\tau,t)\mathbf{H}^{\mathrm{T}}(\tau)\mathbf{u}(\tau)d\tau \tag{3.3}$$

In other words, a costate is said to be observable, if its value can be computed by the means of a linear transformation of the output function $\mathbf{y}(t)$ given any current value of $\mathbf{x}(t)$.

Definition 3 was originally suggested by R. E. Kalman [18]. However, in Kalman's later works terminology was slightly changed [19, 20]. A word *observable* started to be referred to a costate, whose *initial* value could be evaluated given *future* measurements, and a costate, whose *current* value could be evaluated given measurements *from the past*, was referred to as *reconstructible* or, in some recent works [22], *determinable*. In this thesis the original terminology [18] will be followed, as is done in [23-25].

Linear dynamic system (3.1) is said to be *completely observable* at time t, if all the components of state vector $\mathbf{x}(t)$ can be evaluated by the means of a linear operation on system's output function given any current value of $\mathbf{x}(t)$, i. e. if $\exists t_0 < t$ and piecewise continuous functions $\mathbf{u}_i(t) \in \mathbb{R}^m$, defined on time interval $[t_0, t]$, such that

$$x_i(t) = \int_{t_0}^{t} \mathbf{u}_i^{\mathrm{T}}(\tau)\mathbf{y}(\tau)d\tau. \tag{3.4}$$

Definition 4.Observability Gramian [18, 22, 25] is a square matrix given by

$$\mathbf{W}(t,t_0) = \int_{t_0}^{t} \mathbf{\Phi}^{\mathrm{T}}(\tau,t)\mathbf{H}^{\mathrm{T}}(\tau)\mathbf{H}(\tau)\mathbf{\Phi}(\tau,t)d\tau, \tag{3.5}$$

where $\mathbf{\Phi}(\tau,t)$ *is transition matrix of dynamic system (3.1).*

It immediately follows from definition that observability Gramian is subject to the following linear dynamics

$$\dot{\mathbf{W}}(t,t_0) = -\mathbf{A}^{\mathrm{T}}(t)\mathbf{W}(t,t_0) - \mathbf{W}(t,t_0)\mathbf{A}(t) + \mathbf{H}^{\mathrm{T}}(t)\mathbf{H}(t),\ \mathbf{W}(t_0,t_0) = 0. \tag{3.6}$$

Equation (3.6) is commonly named Lyapunov's equation.

Denote $D(t)$ a set of observable costates at time t. Then, by definition,

$$D(t) = \bigcup_{t_0<t} \{ \int_{t_0}^{t} \mathbf{u}^{\mathrm{T}}(\tau)\mathbf{H}(\tau)\mathbf{\Phi}(\tau,t)d\tau : \mathbf{u}(t) \in C^{pc}([t_0,t]), \dim \mathbf{u} = m \}. \tag{3.7}$$

Assume that matrices $\mathbf{A}(t)$ and $\mathbf{H}(t)$ are $n-2$ and $n-1$ times continuously differentiable, respectively. Then the matrix

$$\mathbf{L}(t) = \begin{pmatrix} \mathbf{L}_0^{\mathrm{T}} & \dots & \mathbf{L}_{n-1}^{\mathrm{T}} \end{pmatrix}^{\mathrm{T}}, \tag{3.8}$$

where $\mathbf{L}_0 = \mathbf{H}(t)$, $\mathbf{L}_k = \dot{\mathbf{L}}_{k-1} + \mathbf{L}_{k-1}\mathbf{A}(t)$, $k = 1,\dots,n-1$, is called observability matrix. This so-called observability matrix $\mathbf{L}(t)$ relates the first $n-1$ derivatives of the output function $\mathbf{y}(t)$ and system's state vector $\mathbf{x}(t)$, i. e.

$$\begin{pmatrix} \mathbf{y}(t) \\ \mathbf{y}'(t) \\ \vdots \\ \mathbf{y}^{(n-1)}(t) \end{pmatrix} = \mathbf{L}(t)\mathbf{x}(t). \tag{3.9}$$

Theorem 1. Linear dynamic system is completely observable at time t iff $\exists t_0 < t$ such that $\operatorname{rank} \mathbf{W}(t,t_0) = \dim \mathbf{x}$.

Proof of the Theorem 1 can be found in [16, 19, 23, 24].

Alternatively, when system and measurement matrices are smooth enough, a sufficient condition, formulated in terms of observability matrix, can be used to check for complete observability of dynamic system.

Theorem 2. Suppose matrices $\mathbf{A}(t)$ and $\mathbf{H}(t)$ are $n-2$ and $n-1$ times continuously differentiable, respectively. Then a sufficient condition for the system (3.1) to be completely observable at time t is for $\operatorname{rank} \mathbf{L}(t_0) = n$, *for some $t_0 \le t$. Moreover, if the elements of $\mathbf{A}(t)$ and $\mathbf{H}(t)$ are analytic functions, then the latter condition is also necessary.*

Proof of the Theorem 2 can be found in [23, 26]. The next theorem describes the case, when dynamic system is not completely observable.

Theorem 3. Observable subspace $D(t)$ and unobservable subspace $D^{\perp}(t)$ can be determined by the means of observability Gramian as follows:

$$D(t) = \left(\bigcup_{t_0<t} \operatorname{Im} \mathbf{W}(t,t_0) \right)^{\mathrm{T}},\ D^{\perp}(t) = \bigcap_{t_0<t} \operatorname{Ker} \mathbf{W}(t,t_0). \tag{3.10}$$

Herein Im and Ker denote an image and a kernel of a linear operator, respectively. Proof of the Theorem 3 can be found in [22].

The next theorem relates observability matrix and observability Gramian in a special case and appears highly useful in practical applications.

Theorem 4. Suppose that rank of observability matrix $\mathbf{L}(\tau)$ *is constant on* $[t_*, t]$ *and equals to* r*, that there exists a set of* r *rows of* $\mathbf{L}(\tau)$ *which are linearly independent for* $\forall \tau \in [t_*, t]$*, and that ranks of observability matrices* $\mathbf{L}^1(\tau), \ldots, \mathbf{L}^m(\tau)$*, generated by rows of* $\mathbf{H}(\tau)$*, are constant on* $[t_*, t]$*. Then*

$$\bigcup_{t_* < t_0 < t} \mathrm{Im}\, \mathbf{W}(t, t_0) = \mathrm{Im}\, \mathbf{W}(t, t_1) = \mathrm{span}\{\mathbf{L}^{\mathrm{T}}(t)\},\ \forall t_1 \in [t_*, t). \tag{3.11}$$

The result states that on a suitable time interval $[t_*, t]$ observability matrix and observability Gramian can equivalently be used to determine observable and unobservable subspaces. Moreover, unlike in Theorem 3, it is not required to compute a union of observability Gramians' images (3.10). Either an image of just *one* observability Gramian, or the observability matrix appear to be sufficient. Proof of the Theorem 4 is given in Appendix A and presents theoretical achievement of the dissertation. Relation of observability and Kalman filtering, in turn, is illustrated in Appendix B. To the best author's knowledge some of the provided insights are new and therefore present important contribution as well.

3.1.2 Analytical approach

Due to physical reasons, in most applications system and measurement matrices are analytic, and observable space needs to be known for a particular set of trajectories. Hence, conditions of Theorem 4 appear to be satisfied, and techniques, presented below, can justifiably be used to conduct observability investigation.

When explicit forms of observable combinations need to be known, observability matrix shall be preferred for analysis. The following investigation procedure follows immediately from definition of observability matrix and Theorem 4.

1. Simplify initial dynamic system, if necessary
2. Compute observability matrix
3. Compute rank of observability matrix
4. Compute reduced row echelon form of observability matrix
5. Use reduced row echelon form to determine observable costates

Note that rows of observability matrix are observable costates, and, consequently, non-zero rows of reduced row echelon form of observability matrix define some basis in a space of observable costates.

3.1.3 Numerical approach

If observable costates do not need to be known explicitly, or if analytical analysis is problematic due to complexity of analytical computations, observability investigation can be conducted numerically by

the means of observability Gramian. The following procedure follows immediately from Theorems 3 and 4.

1. Compute observability Gramian for a set of end times $\{t_i\}_{i=1}^N$
2. Compute orthonormal basis for range of each observability Gramian $\mathbf{W}(t_i, t_0)$. In Matlab it can be done by function *orth()*. Transposed basis vectors will correspond to observable at time t_i costates.
3. Try to understand explicit dependency of observable costates on time

The third step may appear to be peculiar, and explicit dependency on time can remain unclear. Nevertheless the method will allow to understand, which components of the state vector $\mathbf{x}(t)$ appear in observable combinations, and how they are coupled with each other. These knowledge then may be used to get a deeper insight into Kalman filter performance, which is dependent on observability properties of dynamic system [21].

3.1.4 Numerical verification of analytical analysis

Analytical observability investigations very often imply long derivations and consequently a sudden mistake, such as a confused sign, a wrong coefficient, or a forgotten term, may be difficult to notice. Obviously, results must be verified, preferably by the means of some numerical method, which could easily be automated and thus could provide high level of reliability.

By *observable combination* will be meant a product of observable costate and system's state vector. Presenting observable combination instead of corresponding observable costate will help to shorten notation and to make results more illustrative.

Denote $\mathbf{s}(t) = \mathbf{S}(t)\mathbf{x}(t)$, $\dim \mathbf{s}(t) = m$, observable combinations that need to be verified. Based on the Theorem 4, the following algorithm can immediately be suggested for observable combination verification:

1. Take analytically computed basis of observable subspace
2. Compute $\mathbf{W}(t_i, t_0),\ i = 1, \ldots, p$ numerically using (3.6)
3. Compute orthonormal basis $\boldsymbol{\eta}_j(t_i),\ j = 1, \ldots, q$, of the right null space of $\mathbf{W}(t_i, t_0)$ at every time instance t_i
4. Compute test indicators

$$\chi_i = \max \operatorname{abs}\left(\begin{pmatrix} \mathbf{s}_1(t_i) / \|\mathbf{s}_1(t_i)\| \\ \vdots \\ \mathbf{s}_m(t_i) / \|\mathbf{s}_m(t_i)\| \end{pmatrix} \cdot \left(\boldsymbol{\eta}_1(t_i), \ldots, \boldsymbol{\eta}_i(t_i)\right) \right),\ i = 1, \ldots, p; \tag{3.12}$$

   Here $\mathbf{s}_i(t)$ denote corresponding rows of matrix $\mathbf{S}(t)$

5. Verify that all the χ_i are much less than 1, and that $m + q = \dim \mathbf{x}(t)$ at every time instance

If observable combinations were determined correctly, all the test indicators must be negligible. If some of the test indicators appear to be large, an error in analytical derivations shall be suspected. In

case test indicators are negligible, but $m+l \neq \dim \mathbf{x}(t)$, some observable combinations must be missing.

In fact, the algorithm proposed above verifies if analytically derived observable costates are orthogonal to numerically computed unobservable space.

3.1.5 Trajectories of interest

Three basic trajectories will be considered in observability analysis: unaccelerated straight and leveled flight, steady horizontal turn, and steady climb. These trajectories do not appear very specific and cover usual flight situations for most of the airplanes. Below the explicit parameterization of rotation matrix, specific force, and angular rate is presented. Transport and the Earth's rotation rates are neglected.

At straight and leveled unaccelerated flight

$$\begin{gathered}\mathbf{R}_{nb}=\begin{pmatrix}\cos\psi & -\sin\psi & 0\\ \sin\psi & \cos\psi & 0\\ 0 & 0 & 1\end{pmatrix},\ \mathbf{f}_n=\begin{pmatrix}0\\0\\-g\end{pmatrix},\ \boldsymbol{\omega}_{ib}=\begin{pmatrix}0\\0\\0\end{pmatrix},\\ v_{n1}=u\cos\psi,\ v_{n2}=u\sin\psi,\ v_{n3}=0,\ h=h_0.\end{gathered} \tag{3.13}$$

The steady climb is described by

$$\begin{gathered}\mathbf{R}_{nb}=\begin{pmatrix}\cos\vartheta\cos\psi & -\sin\psi & \sin\vartheta\cos\psi\\ \cos\vartheta\sin\psi & \cos\psi & \sin\vartheta\sin\psi\\ -\sin\vartheta & 0 & \cos\vartheta\end{pmatrix},\ \mathbf{f}_n=\begin{pmatrix}0\\0\\-g\end{pmatrix},\ \boldsymbol{\omega}_{ib}=\begin{pmatrix}0\\0\\0\end{pmatrix},\\ v_{n1}=u\cos\vartheta\cos\psi,\ v_{n2}=\cos\vartheta\sin\psi,\ v_{n3}=-u\sin\vartheta,\ h=h_0+\left(u\sin\vartheta\right)t.\end{gathered} \tag{3.14}$$

The steady turn is parameterized as follows

$$\begin{gathered}\mathbf{R}_{nb}=\begin{pmatrix}\cos\dfrac{ut}{r} & \sin\dfrac{ut}{r}\cos\varphi & -\sin\dfrac{ut}{r}\sin\varphi\\ -\sin\dfrac{ut}{r} & \cos\dfrac{ut}{r}\cos\varphi & -\cos\dfrac{ut}{r}\sin\varphi\\ 0 & \sin\varphi & \cos\varphi\end{pmatrix},\ \mathbf{f}_n=\begin{pmatrix}-\dfrac{u^2}{r}\sin\dfrac{ut}{r}\\ -\dfrac{u^2}{r}\cos\dfrac{ut}{r}\\ -g\end{pmatrix},\ \boldsymbol{\omega}_{ib}=\begin{pmatrix}0\\ \dfrac{u}{r}\sin\varphi\\ \dfrac{u}{r}\cos\varphi\end{pmatrix},\\ v_{n1}=u\cos\frac{ut}{r},\ v_{n2}=-u\sin\frac{ut}{r},\ v_{n3}=0,\ h=h_0.\end{gathered} \tag{3.15}$$

Here g is gravitational acceleration; φ is bank angle; ϑ is pitch angle; ψ is vehicle's heading; u is the first b-frame velocity component which is equal to absolute value of vehicle's velocity; r is radius of the turn.

3.2 Air data measurements

3.2.1 Air data measurement equations

Usual outputs of air data systems include barometric altitude, true air speed, angle of attack, and angle of sideslip [27-30].

Barometric altimeter gives a direct measurement of vehicle's altitude given normal atmospheric conditions

$$y_{baro} = h_{baro}. \tag{3.16}$$

The value measured by altimeter is superposed by an error, which is a sum of instrumental error and noise. Thus

$$\tilde{y}_{baro} = \tilde{h}_{baro} = h_{baro} - \delta h_{baro} = h_{baro} - b_{baro} - \nu_{baro}. \tag{3.17}$$

b_{baro} is altimeter instrumental error; $\nu_{\bullet}$ here and further denotes scalar zero-mean Gaussian white noise. True altitude of the vehicle is a sum of barometric altitude and normal atmosphere offset, which is due to a deviation of atmospheric conditions from normal

$$y_{baro} = h_{baro} = h - \delta h_{atm}. \tag{3.18}$$

Residual is formed as difference between measured barometric altitude and estimated vehicle's altitude. Thus, linearized observation equation takes the form

$$\begin{aligned} \Delta y_{baro} &= \tilde{y}_{baro} - \tilde{h} = h_{baro} - b_{baro} - \nu_{baro} - \tilde{h} = \\ &= h - \delta h_{atm} - b_{baro} - \nu_{baro} - \tilde{h} = \delta h - \delta h_{atm} - b_{baro} - \nu_{baro}. \end{aligned} \tag{3.19}$$

By definition, $h = \tilde{h} + \delta h$. $\delta h_{atm}(t)$ is normal atmosphere offset which is due to alternation of local atmospheric pressure. b_{baro} is modeled as a random constant, $\delta h_{atm}(t)$ is modeled as a random ramp

$$\dot{\delta b}_{baro} = 0, \quad \ddot{\delta h}_{atm} = 0. \tag{3.20}$$

The vertical channel of INS is known to be unstable [2, 10], which is why its permanent slaving becomes mandatory. This work is not intended to investigate baro-inertial vertical channel designs. The field by now appears to be very well covered by literature. Further reading can be found in [31-33].

Pitot-static systems measure both total and static pressure. The airspeed can be derived from the difference between total and static pressure. The indicated airspeed (IAS) is the one shown on the airspeed indicator cockpit instrument, which is calibrated to reflect standard atmosphere adiabatic compressible flow at sea level. IAS is converted to calibrated airspeed (CAS) by compensating for instrument, position and installation errors [12]. Under some conditions CAS is furthermore corrected for compression air in the pitot tube. CAS then is converted to true airspeed (TAS) by furthermore using Outside Air Temperature (OAT) and barometric altitude. True airspeed is a speed of an aircraft relative to surrounding air

$$y_{TAS} = \left\| \mathbf{v}_n - \mathbf{v}_n^W \right\|. \tag{3.21}$$

Measured TAS is superposed by an error, which is modeled as zero-mean Gaussian white noise:

$$\tilde{y}_{TAS} = y_{TAS} - \delta y_{TAS} = \left\| \mathbf{v}_n - \mathbf{v}_n^W \right\| - \nu_{TAS}. \tag{3.22}$$

Linearized TAS observation equation is given by

$$\begin{aligned} \Delta y_{TAS} = \tilde{y}_{TAS} - \left\| \tilde{\mathbf{v}}_n - \tilde{\mathbf{v}}_n^W \right\| = \left\| \mathbf{v}_n - \mathbf{v}_n^W \right\| - \left\| \tilde{\mathbf{v}}_n - \tilde{\mathbf{v}}_n^W \right\| - \nu_{TAS} \approx \\ \approx \frac{1}{\left\| \tilde{\mathbf{v}}_n - \tilde{\mathbf{v}}_n^W \right\|} \left(\tilde{\mathbf{v}}_n - \tilde{\mathbf{v}}_n^W \right)^{\mathrm{T}} \cdot \left(\delta \mathbf{v}_n - \delta \mathbf{v}_n^W \right) - \nu_{TAS}. \end{aligned} \tag{3.23}$$

Air Data System computes TAS from the difference between total and static pressure, which is, according to Bernoulli's principle [34], proportional to a square of velocity. Thus TAS measurement can also be modeled as a square of a speed of an aircraft relative to air

$$y_{TAS2} = \left\| \mathbf{v}_n - \mathbf{v}_n^W \right\|^2, \quad \tilde{y}_{TAS2} = y_{TAS2} - \delta y_{TAS2} = \left\| \mathbf{v}_n - \mathbf{v}_n^W \right\|^2 - \nu_{TAS2}. \tag{3.24}$$

This yields simpler linearized measurement equation in the form

$$\begin{aligned} \Delta y_{TAS2} = \tilde{y}_{TAS2} - \left\| \tilde{\mathbf{v}}_n - \tilde{\mathbf{v}}_n^W \right\|^2 = \left\| \mathbf{v}_n - \mathbf{v}_n^W \right\|^2 - \left\| \tilde{\mathbf{v}}_n - \tilde{\mathbf{v}}_n^W \right\|^2 - \nu_{TAS2} \approx \\ \approx 2 \left(\tilde{\mathbf{v}}_n - \tilde{\mathbf{v}}_n^W \right)^{\mathrm{T}} \cdot \left(\delta \mathbf{v}_n - \delta \mathbf{v}_n^W \right) - \nu_{TAS2}. \end{aligned} \tag{3.25}$$

Behavior of an atmosphere is highly volatile and can hardly be predicted. Thus, since no reliable deterministic model is available, speed of the wind will be modeled, dependent on situation, either as random constant, or as a random ramp, i. e.

$$\begin{aligned} &\dot{\mathbf{v}}_n^W = 0 \Leftrightarrow \mathbf{v}_n^W(t) = \mathbf{v}_n^W(t_0) = \mathbf{v}_n^{W,0}, \\ &\text{or} \\ &\dot{\mathbf{v}}_n^W = \mathbf{a}_n^W,\ \dot{\mathbf{a}}_n^W = 0 \Leftrightarrow \mathbf{v}_n^W(t) = \mathbf{v}_n^W(t_0) + \mathbf{a}_n^W(t_0) \cdot t = \mathbf{v}_n^{W,0} + \mathbf{a}_n^{W,0} \cdot t. \end{aligned} \tag{3.26}$$

Alternatively, Berman and Powell [35] suggest modeling velocity differences as a first order Gauss-Markov process. Aerodynamic vanes provide a direct measurement of aircraft's angle of attack and angle of sideslip [29]:

$$\begin{aligned} y_{AOA} &= \arctan \frac{w - w^W}{u - u^W}, \quad \tilde{y}_{AOA} = y_{AOA} - \delta y_{AOA} = \arctan \frac{w - w^W}{u - u^W} - \nu_{AOA}, \\ y_{AOS} &= \arctan \frac{v - v^W}{u - u^W}, \quad \tilde{y}_{AOS} = y_{AOS} - \delta y_{AOS} = \arctan \frac{v - v^W}{u - u^W} - \nu_{AOS}, \end{aligned} \tag{3.27}$$

where $\mathbf{v}_b = \mathbf{R}_{nb}^{\mathrm{T}} \mathbf{v}_n = \begin{pmatrix} u & v & w \end{pmatrix}^{\mathrm{T}}$ and $\mathbf{v}_b^W = \mathbf{R}_{nb}^{\mathrm{T}} \mathbf{v}_n^W = \begin{pmatrix} u^W & v^W & w^W \end{pmatrix}^{\mathrm{T}}$ denote total platform and wind velocity vectors expressed in b-frame, respectively. Flight control laws keep, dependent on aircraft, in general AOA in the range from -10 to +20 degrees and AOS about zero degrees. Hence, the following linearization holds for almost all duration of a flight.

$$
\begin{aligned}
&\Delta y_{AOA} = \tilde{y}_{AOA} - \arctan\frac{\tilde{w}-\tilde{w}^W}{\tilde{u}-\tilde{u}^W} = \arctan\frac{w-w^W}{u-u^W} - \arctan\frac{\tilde{w}-\tilde{w}^W}{\tilde{u}-\tilde{u}^W} - \nu_{AOA} \approx \\
&\approx \left.\frac{\partial\left(\frac{w-w^W}{u-u^W}\right)}{\partial\left(\mathbf{v}_b^{\mathsf{T}}, \left(\mathbf{v}_b^W\right)^{\mathsf{T}}\right)}\right|_{\tilde{\mathbf{v}}_b, \tilde{\mathbf{v}}_b^{\mathrm{w}}} \begin{pmatrix}\delta\mathbf{v}_b \\ \delta\mathbf{v}_b^{\mathrm{w}}\end{pmatrix} + h.o.t. - \nu_{AOA} \approx \\
&\approx \begin{pmatrix} -\frac{\tilde{w}-\tilde{w}^W}{\left(\tilde{u}-\tilde{u}^W\right)^2} & 0 & \frac{1}{\tilde{u}-\tilde{u}^W} & \frac{\tilde{w}-\tilde{w}^W}{\left(\tilde{u}-\tilde{u}^W\right)^2} & 0 & -\frac{1}{\tilde{u}-\tilde{u}^W} \end{pmatrix} \cdot \\
&\cdot \begin{pmatrix} \mathbf{R}_{\tilde{n}b}^{\mathsf{T}}\left(\delta\mathbf{v}_n + \left[\tilde{\mathbf{v}}_n \times\right]\cdot\psi_{n\tilde{n}}\right) \\ \mathbf{R}_{\tilde{n}b}^{\mathsf{T}}\left(\delta\mathbf{v}_n^{\mathrm{w}} + \left[\tilde{\mathbf{v}}_n^{\mathrm{w}} \times\right]\cdot\psi_{n\tilde{n}}\right) \end{pmatrix} - \nu_{AOA},
\end{aligned}
\tag{3.28}
$$

$$
\begin{aligned}
&\Delta y_{AOS} = \tilde{y}_{AOS} - \arctan\frac{\tilde{v}-\tilde{v}^W}{\tilde{u}-\tilde{u}^W} = \arctan\frac{v-v^W}{u-u^W} - \arctan\frac{\tilde{v}-\tilde{v}^W}{\tilde{u}-\tilde{u}^W} - \nu_{AOS} \approx \\
&\approx \left.\frac{\partial\left(\frac{v-v^W}{u-u^W}\right)}{\partial\left(\mathbf{v}_b^{\mathsf{T}}, \left(\mathbf{v}_b^W\right)^{\mathsf{T}}\right)}\right|_{\tilde{\mathbf{v}}_b, \tilde{\mathbf{v}}_b^{\mathrm{w}}} \cdot \begin{pmatrix}\delta\mathbf{v}_b \\ \delta\mathbf{v}_b^{\mathrm{w}}\end{pmatrix} + h.o.t. - \nu_{AOS} \approx \\
&\approx \begin{pmatrix} -\frac{\tilde{v}-\tilde{v}^W}{\left(\tilde{u}-\tilde{u}^W\right)^2} & \frac{1}{\tilde{u}-\tilde{u}^W} & 0 & \frac{\tilde{v}-\tilde{v}^W}{\left(\tilde{u}-\tilde{u}^W\right)^2} & -\frac{1}{\tilde{u}-\tilde{u}^W} & 0 \end{pmatrix} \cdot \\
&\cdot \begin{pmatrix} \mathbf{R}_{\tilde{n}b}^{\mathsf{T}}\left(\delta\mathbf{v}_n + \left[\tilde{\mathbf{v}}_n \times\right]\cdot\psi_{n\tilde{n}}\right) \\ \mathbf{R}_{\tilde{n}b}^{\mathsf{T}}\left(\delta\mathbf{v}_n^{\mathrm{w}} + \left[\tilde{\mathbf{v}}_n^{\mathrm{w}} \times\right]\cdot\psi_{n\tilde{n}}\right) \end{pmatrix} - \nu_{AOS}
\end{aligned}
$$

True values of TAS (ν_{TAS}), AOA (α), and AOS (β) allow to derive b-frame velocity with respect to wind as follows

$$
\mathbf{v}_b - \mathbf{v}_b^W = v_{TAS}\cdot\begin{pmatrix}\cos\alpha\cos\chi & \sin\chi & \sin\alpha\cos\chi\end{pmatrix}^{\mathsf{T}}, \tag{3.29}
$$

where $\tan\chi = \cos\alpha\tan\beta$. Thus, in case all the three measurements are available, one can consider b-frame velocity w.r.t. wind measurement

$$
\begin{aligned}
&\mathbf{y}_{\mathbf{vb},rel} = \mathbf{v}_b - \mathbf{v}_b^W = \mathbf{R}_{nb}^{\mathsf{T}}\left(\mathbf{v}_n - \mathbf{v}_n^W\right), \\
&\tilde{\mathbf{y}}_{\mathbf{vb},rel} = \mathbf{y}_{\mathbf{vb},rel} - \delta\mathbf{y}_{\mathbf{vb},rel} = \mathbf{R}_{nb}^{\mathsf{T}}\left(\mathbf{v}_n - \mathbf{v}_n^W\right) - \mathbf{v}_{\mathbf{vb}}.
\end{aligned}
\tag{3.30}
$$

Then a linearized measurement equation

$$
\begin{aligned}
&\Delta\mathbf{y}_{\mathbf{vb},rel} = \mathbf{R}_{\tilde{n}b}\tilde{\mathbf{y}}_{\mathbf{vb},rel} - \left(\tilde{\mathbf{v}}_n - \tilde{\mathbf{v}}_n^W\right) = \\
&= \mathbf{R}_{\tilde{n}b}\mathbf{R}_{nb}^{\mathsf{T}}\left(\mathbf{v}_n - \mathbf{v}_n^W\right) - \left(\tilde{\mathbf{v}}_n - \tilde{\mathbf{v}}_n^W\right) - \mathbf{R}_{\tilde{n}b}\mathbf{v}_{\mathbf{vb}} = \\
&= \mathbf{R}_{n\tilde{n}}^{\mathsf{T}}\left(\mathbf{v}_n - \mathbf{v}_n^W\right) - \left(\tilde{\mathbf{v}}_n - \tilde{\mathbf{v}}_n^W\right) - \mathbf{R}_{\tilde{n}b}\mathbf{v}_{\mathbf{vb}} \approx \\
&\approx \left(\mathbf{I} - [\psi_{n\tilde{n}}\times]\right)\left(\mathbf{v}_n - \mathbf{v}_n^W\right) - \left(\tilde{\mathbf{v}}_n - \tilde{\mathbf{v}}_n^W\right) - \mathbf{R}_{\tilde{n}b}\mathbf{v}_{\mathbf{vb}} \approx \\
&\approx \left(\delta\mathbf{v}_n - \delta\mathbf{v}_n^W\right) + \left[\left(\tilde{\mathbf{v}}_n - \tilde{\mathbf{v}}_n^W\right)\times\right]\psi_{n\tilde{n}} - \mathbf{R}_{\tilde{n}b}\mathbf{v}_{\mathbf{vb}}
\end{aligned}
\tag{3.31}
$$

can be used instead of (3.25) and (3.28). This is particularly helpful for analyzing system analytically, because measurement equation (3.31) appears to be much simpler than a combination of (3.25) and (3.28). However (3.25) and (3.28) shall be preferred for filter implementation, because original sensor noise does not experience a nonlinear transformation due to computation of b-frame velocity w.r.t. wind (3.29).

3.2.2 Simplification of error propagation equations

In order to preserve analytical computability, error propagation equations (2.9) are simplified under the following assumptions:

1. The Earth's gravity field can be assumed parallel,
2. The Earth's rotation rate is neglected,
3. Transport rate is neglected,
4. Inertial sensor errors are modelled as random constants,
5. Barometric altimeter instrumental error is modeled as random constant,
6. Normal atmosphere height error is modeled as random ramp,
7. Wind velocity errors are modeled as random constants if steady turn is considered and as random ramp otherwise, i. e.

$$\begin{aligned} &\delta\dot{\mathbf{v}}_n^W = \mathbf{0} \Leftrightarrow \delta\mathbf{v}_n^W = \delta\mathbf{v}_n^W(t_0), \\ &\text{or} \\ &\delta\dot{\mathbf{v}}_n^W = \delta\mathbf{a}_n^W,\ \delta\dot{\mathbf{a}}_n^W = \mathbf{0} \Leftrightarrow \delta\mathbf{v}_n^W = \delta\mathbf{v}_n^W(t_0) + \delta\mathbf{a}_n^W(t_0)\cdot t. \end{aligned} \tag{3.32}$$

Under the assumptions, listed above, the system of error propagation equations, extended by sensor error models, can be written in the form

$$\dot{\mathbf{x}} = \mathbf{F}(t)\mathbf{x} \tag{3.33}$$

where the state vector and simplified system matrix are

$$\mathbf{x} = \begin{pmatrix} \delta\boldsymbol{\lambda} \\ \delta\mathbf{v}_n \\ \psi_{n\tilde{n}} \\ \delta\mathbf{f}_b \\ \delta\boldsymbol{\omega}_b \\ b_{baro} \\ \delta h_{atm} \\ \delta\dot{h}_{atm} \\ \delta\mathbf{v}_n^W \\ \delta\mathbf{a}_n^W \end{pmatrix},\quad \mathbf{F}(t) = \begin{pmatrix} \mathbf{F}_{11} & \mathbf{F}_{12} & \mathbf{0}_{3\times3} & \mathbf{0}_{3\times3} & \mathbf{0}_{3\times3} & \mathbf{0}_{3\times1} & \mathbf{0}_{3\times1} & \mathbf{0}_{3\times1} & \mathbf{0}_{3\times3} & \mathbf{0}_{3\times3} \\ \mathbf{0}_{3\times3} & \mathbf{0}_{3\times3} & -[\mathbf{f}_n\times] & \mathbf{R}_{nb} & \mathbf{0}_{3\times3} & \mathbf{0}_{3\times1} & \mathbf{0}_{3\times1} & \mathbf{0}_{3\times1} & \mathbf{0}_{3\times3} & \mathbf{0}_{3\times3} \\ \mathbf{0}_{3\times3} & \mathbf{0}_{3\times3} & \mathbf{0}_{3\times3} & \mathbf{0}_{3\times3} & \mathbf{R}_{nb} & \mathbf{0}_{3\times1} & \mathbf{0}_{3\times1} & \mathbf{0}_{3\times1} & \mathbf{0}_{3\times3} & \mathbf{0}_{3\times3} \\ \mathbf{0}_{3\times3} & \mathbf{0}_{3\times3} & \mathbf{0}_{3\times3} & \mathbf{0}_{3\times3} & \mathbf{0}_{3\times3} & \mathbf{0}_{3\times1} & \mathbf{0}_{3\times1} & \mathbf{0}_{3\times1} & \mathbf{0}_{3\times3} & \mathbf{0}_{3\times3} \\ \mathbf{0}_{3\times3} & \mathbf{0}_{3\times3} & \mathbf{0}_{3\times3} & \mathbf{0}_{3\times3} & \mathbf{0}_{3\times3} & \mathbf{0}_{3\times1} & \mathbf{0}_{3\times1} & \mathbf{0}_{3\times1} & \mathbf{0}_{3\times3} & \mathbf{0}_{3\times3} \\ \mathbf{0}_{1\times3} & \mathbf{0}_{1\times3} & \mathbf{0}_{1\times3} & \mathbf{0}_{1\times3} & \mathbf{0}_{1\times3} & 0 & 0 & 0 & \mathbf{0}_{1\times3} & \mathbf{0}_{1\times3} \\ \mathbf{0}_{1\times3} & \mathbf{0}_{1\times3} & \mathbf{0}_{1\times3} & \mathbf{0}_{1\times3} & \mathbf{0}_{1\times3} & 0 & 0 & 1 & \mathbf{0}_{1\times3} & \mathbf{0}_{1\times3} \\ \mathbf{0}_{1\times3} & \mathbf{0}_{1\times3} & \mathbf{0}_{1\times3} & \mathbf{0}_{1\times3} & \mathbf{0}_{1\times3} & 0 & 0 & 0 & \mathbf{0}_{1\times3} & \mathbf{0}_{1\times3} \\ \mathbf{0}_{3\times3} & \mathbf{0}_{3\times3} & \mathbf{0}_{3\times3} & \mathbf{0}_{3\times3} & \mathbf{0}_{3\times3} & \mathbf{0}_{3\times1} & \mathbf{0}_{3\times1} & \mathbf{0}_{3\times1} & \mathbf{0}_{3\times3} & \mathbf{F}_{9,10} \\ \mathbf{0}_{3\times3} & \mathbf{0}_{3\times3} & \mathbf{0}_{3\times3} & \mathbf{0}_{3\times3} & \mathbf{0}_{3\times3} & \mathbf{0}_{3\times1} & \mathbf{0}_{3\times1} & \mathbf{0}_{3\times1} & \mathbf{0}_{3\times3} & \mathbf{0}_{3\times3} \end{pmatrix}. \tag{3.34}$$

$$\mathbf{F}_{11} = \begin{pmatrix} 0 & 0 & -\dfrac{v_{n1}}{\left(R(\phi)+h\right)^2} \\ \dfrac{v_{n2}\tan\phi}{\left(R(\phi)+h\right)\cos\phi} & 0 & -\dfrac{v_{n2}}{\left(R(\phi)+h\right)^2\cos\phi} \\ 0 & 0 & 0 \end{pmatrix},$$
$$\mathbf{F}_{12} = \begin{pmatrix} \dfrac{1}{\left(R(\phi)+h\right)} & 0 & 0 \\ 0 & \dfrac{1}{\left(R(\phi)+h\right)\cos\phi} & 0 \\ 0 & 0 & -1 \end{pmatrix}. \tag{3.35}$$

Here $\mathbf{F}_{9,10} = \mathbf{0}_{3\times3}$ in case wind is assumed a random constant, and $\mathbf{F}_{9,10} = \mathbf{I}_{3\times3}$ if wind is model as a random ramp. $R(\phi) = \sqrt{N(\phi)M(\phi)}$ is the Earth's geometric mean curvature radius.

In the following sections parts of observable linear combinations underlined with a single line will denote an impact of a strong steady wind velocity, and terms underlined by a double line will denote an impact of a large steady wind acceleration.

Steady climb will only be investigated for aiding using barometric altimeter.

3.2.3 Barometric altimeter measurement

Measurement matrix is given by

$$\mathbf{H}_{baro} = \frac{\partial \Delta y_{baro}}{\partial \mathbf{x}^{\mathrm{T}}} = \begin{pmatrix} 0 & 0 & 1 & \mathbf{0_{1\times12}} & -1 & -1 & \mathbf{0_{1\times7}} \end{pmatrix} \tag{3.36}$$

and does not depend on total navigation states and hence on trajectory. Observable combinations of error states are listed below.

At straight and leveled flight:

$$\delta h - b_{baro} - \delta h_{atm}, \quad \delta v_{n3} + \delta \dot{h}_{atm}, \quad \delta f_{b3}. \tag{3.37}$$

At steady climb:

$$\delta h - b_{baro} - \delta h_{atm}, \quad \delta v_{n3} + \delta \dot{h}_{atm}, \quad \sin\vartheta \cdot \delta f_{b1} - \cos\vartheta \cdot \delta f_{b3}. \tag{3.38}$$

At steady horizontal turn:

$$\begin{gathered} \delta h - b_{baro} - \delta h_{atm}, \quad \delta v_{n3} + \delta \dot{h}_{atm}, \\ \omega \cdot \psi_{n\hat{n}1} + \delta \omega_{n2}, \quad \omega \cdot \psi_{n\hat{n}2} - \delta \omega_{n1}, \\ \delta f_{n3} + u(\mathbf{R}_{nb}^{\mathrm{T}} \mathbf{e}_{n3} \times \mathbf{e}_{b1})^{\mathrm{T}} \cdot \delta \boldsymbol{\omega}_{ib}. \end{gathered} \tag{3.39}$$

Herein

$$\delta \mathbf{f}_n = \mathbf{R}_{nb} \delta \mathbf{f}_b = \begin{pmatrix} \delta f_{n1} & \delta f_{n2} & \delta f_{n3} \end{pmatrix}^{\mathrm{T}}, \tag{3.40}$$

$$\delta\boldsymbol{\omega}_{ib}^{n} = \mathbf{R}_{nb}\delta\boldsymbol{\omega}_{ib} = \begin{pmatrix}\delta\omega_{n1} & \delta\omega_{n2} & \delta\omega_{n3}\end{pmatrix}^{\mathrm{T}}. \tag{3.41}$$

$\mathbf{e}_{b1} = \begin{pmatrix}1 & 0 & 0\end{pmatrix}^{\mathrm{T}}$ denotes the first unit vector of b-frame and $\mathbf{R}_{nb}^{\mathrm{T}}\mathbf{e}_{n3} = \begin{pmatrix}0 & \sin\varphi & \cos\varphi\end{pmatrix}^{\mathrm{T}}$ denotes the third unit vector of n-frame rotated into b-frame. $\omega = u/r$, where r is a radius of the turn; ϑ and φ are vehicle's pitch and bank angles.

Combinations (3.37), (3.38) show, as expected, that at straight and leveled flight barometric altimeter allows to observe only combinations of error states related to vertical channel. During horizontal turn information on attitude and on one linear combination of sensor errors appears in the measurement. The higher the turn rate is, the more accurately attitude errors shall be estimated. At steady climb longitudal accelerometer error becomes observable in a combination with down accelerometer error. Thus, besides accelerometer errors, a trajectory, featuring a climb, horizontal flight, and a turn, shall also allow to improve significantly an estimate of the lateral gyroscope error.

Note that a more dynamical flight improves observability properties and should be expected to provide better performance.

Observable combinations (3.37), (3.38), (3.39) are summarized in Table 1. Rows of the table denote observable combinations, and columns denote components of the error state vector. Entries of the table indicate if error state appears in observable combination. "C" means that coefficient in front of the error state in the observable combination is constant. "M" indicates that coefficient depends explicitly on time, and "W" denotes coefficients that appear solely due to presence of strong wind. An empty cell means that the error state does not appear in observable combination.

Table 1–Observable combinations. Aiding using barometric altitude.

	$\delta\phi$	$\delta\lambda$	δh	δv_{n1}	δv_{n2}	δv_{n3}	$\psi_{n\hat{n}1}$	$\psi_{n\hat{n}2}$	$\psi_{n\hat{n}3}$	δf_{b1}	δf_{b2}	δf_{b3}	$\delta\omega_{b1}$	$\delta\omega_{b2}$	$\delta\omega_{b3}$	b_{baro}	δh_{atm}	$\delta\dot{h}_{atm}$	δv_{n1}^{W}	δv_{n2}^{W}	δv_{n3}^{W}	δa_{n1}^{W}	δa_{n2}^{W}	δa_{n3}^{W}
Straight and leveled			C			C						C				C	C	C						
Steady climb			C			C				C		C				C	C	C						
Steady horizontal turn			C			C	C	C			C C		M M M	M M M		C	C	C					n/a	

3.2.4 True airspeed measurement

Measurement matrix is given by

$$\mathbf{H}_{TAS2}=\frac{\partial \Delta y_{TAS2}}{\partial \mathbf{x}^{\mathrm{T}}}=\begin{pmatrix}\mathbf{0}_{1\times 3} & 2\left(\mathbf{v}_n-\mathbf{v}_n^W\right)^{\mathrm{T}} & \mathbf{0}_{1\times 12} & -2\left(\mathbf{v}_n-\mathbf{v}_n^W\right)^{\mathrm{T}} & \mathbf{0}_{1\times 3}\end{pmatrix}. \tag{3.42}$$

Observable combinations of error states are listed below.

At straight and leveled flight:

$$\begin{aligned}
&\left(\mathbf{v}_n-(\underline{\mathbf{v}_n^{W,0}}+\underline{\underline{\mathbf{a}_n^{W,0}}t)}\right)^{\mathrm{T}}\cdot\left(\delta\mathbf{v}_n-\delta\mathbf{v}_n^W\right),\\
&-\underline{\underline{\left(\mathbf{a}_n^{W,0}\right)^{\mathrm{T}}\cdot\left(\delta\mathbf{v}_n-\delta\mathbf{v}_n^W\right)}}-g\left(\mathbf{e}_{n3}\times\left(\mathbf{v}_n-(\underline{\mathbf{v}_n^{W,0}}+\underline{\underline{\mathbf{a}_n^{W,0}}t)}\right)\right)^{\mathrm{T}}\cdot\psi_{n\tilde{n}}+\\
&\quad+\left(\mathbf{v}_b-(\underline{\mathbf{v}_b^{W,0}}+\underline{\underline{\mathbf{a}_b^{W,0}}t)}\right)^{\mathrm{T}}\cdot\delta\mathbf{f}_b-\left(\mathbf{v}_n-(\underline{\mathbf{v}_n^{W,0}}+\underline{\underline{\mathbf{a}_n^{W,0}}t)}\right)^{\mathrm{T}}\cdot\delta\mathbf{a}_n^W,\\
&\underline{\underline{-2\left(\mathbf{a}_b^{W,0}\right)^{\mathrm{T}}\cdot\delta\mathbf{f}_b}}+\underline{\underline{2g\left(\mathbf{e}_{n3}\times\mathbf{a}_n^{W,0}\right)^{\mathrm{T}}\cdot\psi_{n\tilde{n}}}}-\\
&\quad-g\left(\mathbf{e}_{b3}\times\left(\mathbf{v}_b-(\underline{\mathbf{v}_b^{W,0}}+\underline{\underline{\mathbf{a}_b^{W,0}}t)}\right)\right)^{\mathrm{T}}\cdot\delta\boldsymbol{\omega}_{ib}+\underline{\underline{2\left(\mathbf{a}_n^{W,0}\right)^{\mathrm{T}}\cdot\delta\mathbf{a}_n^W}},\\
&\underline{\underline{g\left(\mathbf{e}_{b3}\times\mathbf{a}_b^{W,0}\right)^{\mathrm{T}}\cdot\delta\boldsymbol{\omega}_{ib}}}.
\end{aligned} \tag{3.43}$$

Herein $\mathbf{e}_{b3}=\begin{pmatrix}0 & 0 & 1\end{pmatrix}^{\mathrm{T}}$ denotes the third unit vector of b-frame, $\mathbf{a}_b^{W,0}=\mathbf{R}_{nb}^{\mathrm{T}}\mathbf{a}_n^{W,0}$, $\mathbf{v}_b=\mathbf{R}_{nb}^{\mathrm{T}}\mathbf{v}_n$, $\mathbf{v}_b^{W,0}=\mathbf{R}_{nb}^{\mathrm{T}}\mathbf{v}_n^{W,0}$.

At steady horizontal turn:

$$\begin{aligned}
&\left(\mathbf{v}_n-\mathbf{v}_n^W\right)^{\mathrm{T}}\cdot\left(\delta\mathbf{v}_n-\delta\mathbf{v}_n^W\right),\\
&\delta v_{n1}-\delta v_{n1}^W-\left(u\sin\omega t+\underline{v_{n2}^{W,0}}\right)\cdot\psi_{n\tilde{n}3}-\frac{r\left(u\sin\omega t+\underline{v_{n2}^{W,0}}\right)}{u^2}\cdot\delta f_{b1}-\\
&\quad\underline{-\frac{r\left(u\cos\omega t+v_{n1}^{W,0}\right)}{u^2\sin\varphi}\cdot\delta f_{b3}}+\frac{gr^2\left(u\sin\omega t+\underline{v_{n2}^{W,0}}\right)}{u^3}\cdot\delta\omega_{b1}-\\
&\quad\underline{-\left(\frac{gr^2\cos\omega t\cos\varphi}{u^2}+\frac{r\cos\omega t}{\sin\varphi}+\frac{gr^2v_{n1}^{W,0}\cos\varphi}{u^3}+\frac{rv_{n1}^{W,0}}{u\sin\varphi}+\frac{\underline{v_{n2}^{W,0}}v_{n3}^{W,0}\sin\varphi}{g}\right)\cdot\delta\omega_{b2}+}\\
&\quad\underline{+\left(\frac{gr^2\cos\omega t\sin\varphi}{u^2}+\frac{gr^2v_{n1}^{W,0}\sin\varphi}{u^3}-\frac{\underline{v_{n2}^{W,0}}v_{n3}^{W,0}\cos\varphi}{g}\right)\cdot\delta\omega_{b3}},
\end{aligned} \tag{3.44}$$

$$\delta v_{n2} - \delta v_{n2}^{W} - \left(u\cos\omega t - \underline{v_{n1}^{W,0}}\right)\cdot\psi_{n\tilde{n}3} - \frac{r\left(u\cos\omega t - \underline{v_{n1}^{W,0}}\right)}{u^2}\cdot\delta f_{b1} +$$
$$+\underline{\frac{r\left(u\sin\omega t - v_{n2}^{W,0}\right)}{u^2\sin\varphi}\cdot\delta f_{b3}} + \frac{gr^2\left(u\cos\omega t - \underline{v_{n1}^{W,0}}\right)}{u^3}\cdot\delta\omega_{b1} +$$
$$+\underline{\left(\frac{gr^2\sin\omega t\cos\varphi}{u^2} + \frac{r\sin\omega t}{\sin\varphi} - \frac{gr^2 v_{n2}^{W,0}\cos\varphi}{u^3} - \frac{rv_{n2}^{W,0}}{u\sin\varphi} + \frac{v_{n1}^{W,0}v_{n3}^{W,0}\sin\varphi}{g}\right)\cdot\delta\omega_{b2}} +$$
$$+\underline{\left(-\frac{gr^2\sin\omega t\sin\varphi}{u^2} + \frac{gr^2 v_{n2}^{W,0}\sin\varphi}{u^3} + \frac{v_{n1}^{W,0}v_{n3}^{W,0}\cos\varphi}{g}\right)\cdot\delta\omega_{b3}},$$

$$\omega\cdot\psi_{n\tilde{n}1} + \delta\omega_{n2} + \underline{\frac{v_{n1}^{W,0}\omega}{g}\cdot\delta\omega_{n3}},\ \omega\cdot\psi_{n\tilde{n}2} - \delta\omega_{n1} + \underline{\frac{v_{n2}^{W,0}\omega}{g}\cdot\delta\omega_{n3}},$$

If wind speed is zero $(\mathbf{R}_{nb}^{\mathrm{T}}\mathbf{e}_{n3}\times\mathbf{e}_{b1})^{\mathrm{T}}\cdot\delta\mathbf{f}_b - u\left(\mathbf{e}_{n3} + \frac{gr}{u^2}(\mathbf{R}_{nb}^{\mathrm{T}}\mathbf{e}_{n3}\times\mathbf{e}_{b1})\right)^{\mathrm{T}}\cdot\delta\boldsymbol{\omega}_{ib}$,

Otherwise $\underline{\delta f_{n3} + u(\mathbf{R}_{nb}^{\mathrm{T}}\mathbf{e}_{n3}\times\mathbf{e}_{b1})^{\mathrm{T}}\cdot\delta\boldsymbol{\omega}_{ib}}$.

(3.43), (3.44) allow to conclude that at straight and leveled flight TAS measurement allows to observe only some combinations of state, sensor errors, and wind effects. Aiding by the only TAS measurement shall not be efficient for slowly maneuvering platforms, especially in turbulent atmosphere. During a horizontal turn attitude errors become observable in a combination with sensor errors. The faster and the sharper the turn is, the more accurately attitude errors shall be estimated. Constant wind of reasonable strength (10-20 m/s) shall have a negligible effect on attitude error estimates, while frequent strong gusts shall deteriorate them. True airspeed shall be considered a poor source of information on velocity with respect to ground, since velocity and wind velocity errors always appear coupled in observable combinations. Vertical channel cannot be stabilized by the means of TAS measurement.

Results for wind and no wind situations appear slightly different, because setting some components of wind vector to zero leads to changes in a procedure of row reduction of the observability matrix.

Observable combinations (3.43), (3.44) are summarized in Table 2 for the case, when wind speed is nonzero.

Table 2–Observable combinations. Aiding by TAS.

	$\delta\phi$	$\delta\lambda$	δh	δv_{n1}	δv_{n2}	δv_{n3}	$\psi_{n\tilde{n}1}$	$\psi_{n\tilde{n}2}$	$\psi_{n\tilde{n}3}$	δf_{b1}	δf_{b2}	δf_{b3}	$\delta\omega_{b1}$	$\delta\omega_{b2}$	$\delta\omega_{b3}$	b_{baro}	δh_{atm}	$\delta\dot{h}_{atm}$	δv^W_{n1}	δv^W_{n2}	δv^W_{n3}	δa^W_{n1}	δa^W_{n2}	δa^W_{n3}
Straight and leveled				C	C	W													C	C	W			
				W	W	W	C	C		C	W	W							W	W	W	C	C	W
							W	W		W	W	W	W	C								W	W	W
													W	W										
Steady horizontal turn				C	C	W													C	C	W			
				C					M	M		W	M	M	M				C					
					C				M	M		W	M	M	M					C			n/a	
							C						M	M	M									
								C					M	M	M									
											W	W		W	W									

3.2.5 Combination of barometric altitude and TAS

Measurement matrix is given by

$$\mathbf{H}_{baro,TAS2} = \begin{pmatrix} \mathbf{H}_{baro} \\ \mathbf{H}_{TAS2} \end{pmatrix}. \tag{3.45}$$

At straight and leveled flight observable combinations are given by a union of (3.37) and (3.43).

At steady turn observable combinations are given by

$$\begin{aligned}
&\delta h - b_{baro} - \delta h_{atm}, \quad \delta v_{n3} + \delta\dot{h}_{atm}, \\
&\delta v_{n1} - \delta v^W_{n1} - \left(u\sin\omega t + \underline{v^{W,0}_{n2}}\right)\cdot\psi_{n\tilde{n}3} - \frac{r\left(u\sin\omega t + \underline{v^{W,0}_{n2}}\right)}{u^2}\cdot\delta f_{b1} + \\
&\quad + \frac{gr^2\left(u\sin\omega t + \underline{v^{W,0}_{n2}}\right)}{u^3}\cdot\delta\omega_{b1} + \underline{\frac{\left(u\cos\omega t + v^{W,0}_{n1}\right)v_{nw3}}{u^2 - (v^{W,0}_{n1})^2 - (v^{W,0}_{n2})^2}\cdot\delta\dot{h}_{atm}} + \\
&\quad + \underline{\frac{\left(u\cos\omega t + v^{W,0}_{n1}\right)v_{nw3}}{u^2 - (v^{W,0}_{n1})^2 - (v^{W,0}_{n2})^2}\cdot\delta v^W_{n3}}, \\
&\delta v_{n2} - \delta v^W_{n2} - \left(u\cos\omega t - \underline{v^{W,0}_{n1}}\right)\cdot\psi_{n\tilde{n}3} - \frac{r\left(u\cos\omega t - \underline{v^{W,0}_{n1}}\right)}{u^2}\cdot\delta f_{b1} + \\
&\quad + \frac{gr^2\left(u\cos\omega t - \underline{v^{W,0}_{n1}}\right)}{u^3}\cdot\delta\omega_{b1} - \underline{\frac{\left(u\sin\omega t - v^{W,0}_{n2}\right)v_{nw3}}{u^2 - (v^{W,0}_{n1})^2 - (v^{W,0}_{n2})^2}\cdot\delta\dot{h}_{atm}} + \\
&\quad + \underline{\frac{\left(-u\sin\omega t + v^{W,0}_{n2}\right)v_{nw3}}{u^2 - (v^{W,0}_{n1})^2 - (v^{W,0}_{n2})^2}\cdot\delta v^W_{n3}}, \\
&\omega\cdot\psi_{n\tilde{n}1} + \delta\omega_{n2}, \quad \omega\cdot\psi_{n\tilde{n}2} - \delta\omega_{n1}, \\
&\omega\cdot\delta f_{b2} - g\cos^2\varphi\cdot\delta\omega_{b2} - \left(\omega^2 r - g\cos\varphi\sin\varphi\right)\cdot\delta\omega_{b3} - \\
&\quad - \underline{\frac{\omega^3 r v^{W,0}_{n3}\cos\varphi}{(u^2 - (v^{W,0}_{n1})^2 - (v^{W,0}_{n2})^2)}\cdot\delta\dot{h}_{atm}} - \underline{\frac{\omega^3 r v^{W,0}_{n3}\cos\varphi}{(u^2 - (v^{W,0}_{n1})^2 - (v^{W,0}_{n2})^2)}\cdot\delta v^W_{n3}},
\end{aligned} \tag{3.46}$$

$$\omega \cdot \delta f_{b3} + \left(\omega^2 r + g\cos\varphi\sin\varphi\right)\cdot\delta\omega_{b2} - g\sin^2\varphi\cdot\delta\omega_{b3} + \\ + \underline{\frac{\omega^3 r v_{n3}^{W,0}\sin\varphi}{(u^2-(v_{n1}^{W,0})^2-(v_{n2}^{W,0})^2)}}\cdot\delta\dot{h}_{atm} + \underline{\frac{\omega^3 r v_{n3}^{W,0}\sin\varphi}{(u^2-(v_{n1}^{W,0})^2-(v_{n2}^{W,0})^2)}}\cdot\delta v_{n3}^{W},$$

$$\underline{\delta\omega_{n3}}.$$

Combining (3.37), (3.43), and (3.46) encourages to recommend combined aiding by barometric altimeter and TAS for highly dynamic platforms. Since aiding by TAS and altimeter allows to observe attitude errors separately from each other during maneuvering only, at straight and leveled flight combined aiding shall only allow to decrease attitude divergence rate and to stabilize vertical channel. Thus lack of maneuvering appears to mitigate efficiency of aiding and imposes higher requirements upon IMU accuracy.

Observable combinations (3.37), (3.43), (3.46) are summarized in Table 3.

Table 3–Observable combinations. Combined aiding using barometric altimeter and TAS.

	$\delta\phi$	$\delta\lambda$	δh	δv_{n1}	δv_{n2}	δv_{n3}	$\psi_{n\tilde{n}1}$	$\psi_{n\tilde{n}2}$	$\psi_{n\tilde{n}3}$	δf_{b1}	δf_{b2}	δf_{b3}	$\delta\omega_{b1}$	$\delta\omega_{b2}$	$\delta\omega_{b3}$	b_{baro}	δh_{atm}	$\delta\dot{h}_{atm}$	δv_{n1}^{W}	δv_{n2}^{W}	δv_{n3}^{W}	δa_{n1}^{W}	δa_{n2}^{W}	δa_{n3}^{W}
Straight and leveled			C													C	C							
						C												C						
												C												
				C	C	W													C	C	W			
				W	W	W	C	C		C	W	W							W	W	W	C	C	W
							W	W		W	W	W	W	C								W	W	W
													W	W										
Steady horizontal turn			C													C	C							
						C												C						
				C					M	M			M					W	C		W			
					C				M	M			M					W		C	W			
							C						M	M	M								n/a	
								C					M	M	M									
											C			C	C			W			W			
												C		C	C			W			W			
														W	W									

3.2.6 Measurement of b-frame velocity w.r.t wind

Measurement matrix is given by

$$\mathbf{H}_{\mathbf{vb},rel} = \frac{\partial\Delta\mathbf{y}_{\mathbf{vb},rel}}{\partial\mathbf{x}^{\mathrm{T}}} = \left(\mathbf{0}_{3\times3} \quad \mathbf{I}_{3\times3} \quad \left[\left(\mathbf{v}_n - \mathbf{v}_n^{W}\right)\times\right] \quad \mathbf{0}_{3\times9} \quad -\mathbf{I}_{3\times3} \quad \mathbf{0}_{3\times3}\right). \tag{3.47}$$

At straight and leveled flight observable are:

$$
\begin{aligned}
&\delta\mathbf{v}_n - \delta\mathbf{v}_n^W + \left(\mathbf{v}_n - (\underline{\mathbf{v}_n^{W,0}} + \underline{\underline{\mathbf{a}_n^{W,0}t}})\right)\times\psi_{n\tilde{n}},\\
&\left(\mathbf{g}_n - \underline{\underline{\mathbf{a}_n^{W,0}}}\right)\times\psi_{n\tilde{n}} + \delta\mathbf{f}_n - \delta\mathbf{a}_n^W +\\
&+\begin{pmatrix}
\dfrac{\begin{array}{c}\sin\psi\left(\underline{v_{n3}^{W,0}} + \underline{\underline{a_{n3}^{W,0}t}}\right)\cdot\delta\omega_{b1} + \cos\psi\left(\underline{v_{n3}^{W,0}} + \underline{\underline{a_{n3}^{W,0}t}}\right)\cdot\delta\omega_{b2} +\\ +\left(u\sin\psi - \underline{v_{n2}^{W,0}} - \underline{\underline{a_{n2}^{W,0}t}}\right)\cdot\delta\omega_{b3}\end{array}}{\begin{array}{c}-\cos\psi\left(\underline{v_{n3}^{W,0}} + \underline{\underline{a_{n3}^{W,0}t}}\right)\cdot\delta\omega_{b1} + \sin\psi\left(\underline{v_{n3}^{W,0}} + \underline{\underline{a_{n3}^{W,0}t}}\right)\cdot\delta\omega_{b2} +\\ +\left(-u\cos\psi + \underline{v_{n1}^{W,0}} + \underline{\underline{a_{n1}^{W,0}t}}\right)\cdot\delta\omega_{b3}\end{array}}\\
\dfrac{\begin{array}{c}\left(-(\underline{v_{n1}^{W}} + \underline{\underline{a_{n1}^{W,0}t}})\sin\psi + (\underline{v_{n2}^{W,0}} + \underline{\underline{a_{n2}^{W,0}t}})\cos\psi\right)\cdot\delta\omega_{b1} +\\ +\left(u - (\underline{v_{n1}^{W,0}} + \underline{\underline{a_{n1}^{W,0}t}})\cos\psi - (\underline{v_{n2}^{W,0}} + \underline{\underline{a_{n2}^{W,0}t}})\sin\psi\right)\cdot\delta\omega_{b2}\end{array}}{\left(g - \underline{\underline{2a_{n3}^{W,0}}}\right)\cdot\delta\omega_{n1} + \underline{\underline{2a_{b1}^{W,0}\cdot\delta\omega_{b3}}},\ \left(g - \underline{\underline{2a_{n3}^{W,0}}}\right)\cdot\delta\omega_{n2} + \underline{\underline{2a_{b2}^{W,0}\cdot\delta\omega_{b3}}}}
\end{pmatrix},
\end{aligned}
\tag{3.48}
$$

At steady turn observable are:

$$
\begin{aligned}
&\delta v_{n1} - \delta v_{n1}^W - \left(u\sin\omega t + \underline{v_{n2}^{W,0}}\right)\cdot\psi_{n\tilde{n}3},\\
&\delta v_{n2} - \delta v_{n2}^W - \left(u\cos\omega t - \underline{v_{n1}^{W,0}}\right)\cdot\psi_{n\tilde{n}3},\\
&\delta v_{n3} + r\cdot\delta\omega_{b1} - \delta v_{n3}^W,\\
&\omega\cdot\psi_{n\tilde{n}1} + \delta\omega_{n2},\quad \omega\cdot\psi_{n\tilde{n}2} - \delta\omega_{n1},\\
&\omega\cdot\delta f_{b1} - g\cdot\delta\omega_{b1},\\
&\omega\cdot\delta f_{b2} - g\cos^2\varphi\cdot\delta\omega_{b2} - \left(\omega^2 r - g\cos\varphi\sin\varphi\right)\cdot\delta\omega_{b3},\\
&\omega\cdot\delta f_{b3} + \left(\omega^2 r + g\cos\varphi\sin\varphi\right)\cdot\delta\omega_{b2} - g\sin^2\varphi\cdot\delta\omega_{b3},\\
&\underline{\delta\omega_{b1}},\quad \underline{(\mathbf{R}_{nb}^{\mathrm{T}}\mathbf{e}_{n3}\times\mathbf{e}_{b1})^{\mathrm{T}}\cdot\delta\boldsymbol{\omega}_{ib}}.
\end{aligned}
\tag{3.49}
$$

B-frame velocity w.r.t. wind appears to provide information on vehicle's attitude, down accelerometer, and longitudal and lateral gyroscope errors. This holds also when wind field is constant or slowly changing. However, rapidly changing wind field shall decrease efficiency of aiding dramatically. Maneuvering, in its turn, improves observability of attitude errors and allows to mitigate an impact of constant wind field.

Observable combinations (3.48), (3.49) are summarized in Table 4.

Table 4–Observable combinations. Aiding by b-frame velocity w.r.t. wind measurement.

	$\delta\phi$	$\delta\lambda$	δh	δv_{n1}	δv_{n2}	δv_{n3}	$\psi_{n\tilde{n}1}$	$\psi_{n\tilde{n}2}$	$\psi_{n\tilde{n}3}$	δf_{b1}	δf_{b2}	δf_{b3}	$\delta\omega_{b1}$	$\delta\omega_{b2}$	$\delta\omega_{b3}$	b_{baro}	δh_{atm}	$\delta\dot{h}_{atm}$	δv^W_{n1}	δv^W_{n2}	δv^W_{n3}	δa^W_{n1}	δa^W_{n2}	δa^W_{n3}
Straight and leveled				C				W	C										C					
					C		W		C											C				
						C	C	C													C			
							C		W	C	C		W	W	C							C		
								C	W	C	C		W	W	C								C	
							W	W				C	W	C										C
													C		W									
														C	W									
Steady horizontal turn				C					M										C					
					C				M											C				
						C							C								C			
							C						M	M	M									
								C					M	M	M									
										C			C										n/a	
											C			C	C									
												C		C	C									
													W											
														W	W									

3.2.7 Combination of barometric altitude and velocity w.r.t wind measurements

Measurement matrix is given by

$$\mathbf{H}_{baro,\mathbf{vb},rel} = \begin{pmatrix} \mathbf{H}_{baro} \\ \mathbf{H}_{\mathbf{vb},rel} \end{pmatrix}. \tag{3.50}$$

For this set of measurements observable at straight and leveled flight is a union of combinations (3.37) and (3.48).

Combinations, observable at steady turn, are given by

$$\begin{aligned}
&\delta h - b_{baro} - \delta h_{atm}, \quad \delta v_{n3} + \delta\dot{h}_{atm}, \\
&\delta v_{n1} - \delta v^W_{n1} - \left(u\sin\omega t + \underline{v^{W,0}_{n2}}\right)\cdot\psi_{n\tilde{n}3}, \\
&\delta v_{n2} - \delta v^W_{n2} - \left(u\cos\omega t - \underline{v^{W,0}_{n1}}\right)\cdot\psi_{n\tilde{n}3}, \\
&\omega\cdot\psi_{n\tilde{n}1} + \delta\omega_{n2}, \quad \omega\cdot\psi_{n\tilde{n}2} - \delta\omega_{n1}, \\
&\omega\cdot\delta f_{b1} - g\cdot\delta\omega_{b1}, \\
&\omega\cdot\delta f_{b2} - g\cos^2\varphi\cdot\delta\omega_{b2} - \left(\omega^2 r - g\cos\varphi\sin\varphi\right)\cdot\delta\omega_{b3}, \\
&\omega\cdot\delta f_{b3} + \left(\omega^2 r + g\cos\varphi\sin\varphi\right)\cdot\delta\omega_{b2} - g\sin^2\varphi\cdot\delta\omega_{b3}, \\
&\delta\omega_{b1} - \frac{1}{r}\cdot\delta\dot{h}_{atm} - \frac{1}{r}\cdot\delta v^W_{n3}, \quad \underline{\delta\omega_{b1}}, \quad \underline{\delta\omega_{b2}}, \quad \underline{\delta\omega_{b3}}.
\end{aligned} \tag{3.51}$$

Formulae (3.37), (3.48), and (3.51) show that altitude and b-frame velocity w.r.t. wind information form a powerful source of INS aiding. Such a combined aiding allows to estimate attitude and vertical channel errors both during cruise and dynamic flights. It shall also be noted that all the inertial sensor errors become observable if flight path features a turn in a constant wind field. However, in general this should not be expected to be fulfilled by a filter, because atmosphere is usually volatile and wind model, used by an estimator, remains too inaccurate.

Observable combinations (3.37), (3.48), (3.51) are summarized in Table 5.

Table 5–Observable combinations. Combined aiding using altitude and b-frame velocity w.r.t. wind measurements.

	$\delta\phi$	$\delta\lambda$	δh	δv_{n1}	δv_{n2}	δv_{n3}	$\psi_{n\hat{n}1}$	$\psi_{n\hat{n}2}$	$\psi_{n\hat{n}3}$	δf_{b1}	δf_{b2}	δf_{b3}	$\delta\omega_{b1}$	$\delta\omega_{b2}$	$\delta\omega_{b3}$	b_{baro}	δh_{atm}	$\delta\dot{h}_{atm}$	δv^W_{n1}	δv^W_{n2}	δv^W_{n3}	δa^W_{n1}	δa^W_{n2}	δa^W_{n3}
Straight and leveled			C													C	C							
						C												C						
												C												
				C				W	C										C					
					C		W		C											C				
						C	C	C													C			
							C		W	C	C		W	W	C							C		
								C	W	C	C		W	W	C								C	
							W	W				C	W	C										C
													C		W									
														C	W									
Steady horizontal turn			C													C	C							
						C												C						
				C					M										C					
					C				M											C				
							C						M	M	M									
								C					M	M	M									
										C			C										n/a	
											C			C	C									
												C		C	C									
													C					C			C			
													W											
														W										
															W									

3.2.8 TAS combined with AOA

Consider that velocity and acceleration of wind are approximately zero, i. e. $\mathbf{v}_n^W \approx \mathbf{0}$, $\mathbf{a}_n^W \approx \mathbf{0}$. Then the following linear combinations of error states are observable at straight and leveled flight situation.

$$
\begin{aligned}
&\cos\psi\cdot\left(\delta v_{n1}-\delta v_{n1}^{W}\right)+\sin\psi\cdot\left(\delta v_{n2}-\delta v_{n2}^{W}\right),\\
&\delta v_{n3}-\delta v_{n3}^{W}+\frac{u}{g}\cdot\delta f_{b1}-\frac{u\cos\psi}{g}\cdot\delta a_{n1}^{W}-\frac{u\sin\psi}{g}\cdot\delta a_{n2}^{W},\\
&\sin\psi\cdot\psi_{n\tilde{n}1}-\cos\psi\cdot\psi_{n\tilde{n}2}+\frac{1}{g}\cdot\delta f_{b1}-\frac{\cos\psi}{g}\cdot\delta a_{n1}^{W}-\frac{\sin\psi}{g}\cdot\delta a_{n2}^{W},\\
&\delta f_{b3}-\delta a_{n3}^{W},\ \delta\omega_{b2}.
\end{aligned}
\tag{3.52}
$$

From (3.52) it is seen that orientation errors appear in only one of the observable combinations, and that "roll" and "pitch" errors cannot be separated. Consequently, aiding by only TAS and AOA can hardly improve estimation of vehicle's orientation.

3.2.9 TAS combined with AOS

Under assumption that $\mathbf{v}_n^W\approx\mathbf{0}$, $\mathbf{a}_n^W\approx\mathbf{0}$, combination of TAS and AOS measurements make the following linear combinations observable at straight and leveled flight.

$$
\begin{aligned}
&\delta v_{n1}-\delta v_{n1}^{W}+u\sin\psi\cdot\psi_{n\tilde{n}3},\\
&\delta v_{n2}-\delta v_{n2}^{W}-u\cos\psi\cdot\psi_{n\tilde{n}3},\\
&\psi_{n\tilde{n}1}+\frac{\sin\psi}{g}\cdot\delta f_{b1}+\frac{\cos\psi}{g}\cdot\delta f_{b2}-\frac{u\cos\psi}{g}\cdot\delta\omega_{b3}-\frac{1}{g}\cdot\delta a_{n2}^{W},\\
&\psi_{n\tilde{n}2}-\frac{\cos\psi}{g}\cdot\delta f_{b1}+\frac{\sin\psi}{g}\cdot\delta f_{b2}-\frac{u\sin\psi}{g}\cdot\delta\omega_{b3}+\frac{1}{g}\cdot\delta a_{n1}^{W},\\
&\delta\omega_{b1},\ \delta\omega_{b2}.
\end{aligned}
\tag{3.53}
$$

(3.53) shows that aiding by TAS and AOS allows to observe attitude errors in a combination with sensor errors, but separately from each other. Moreover, biases of longitudal and lateral gyroscopes become observable. Therefore, this type of aiding appears highly promising for AHRS applications.

3.2.10 AOA combined with AOS

Assuming that $\mathbf{v}_n^W\approx\mathbf{0}$, $\mathbf{a}_n^W\approx\mathbf{0}$ yields the following observable combinations at straight and leveled flight in case the system is aided by AOA and AOS measurements.

$$
\begin{aligned}
&\sin\psi\cdot\left(\delta v_{n1}-\delta v_{n1}^{W}\right)-\cos\psi\cdot\left(\delta v_{n2}-\delta v_{n2}^{W}\right)+u\cdot\psi_{n\tilde{n}3},\\
&\cos\psi\cdot\left(\delta v_{n3}-\delta v_{n3}^{W}\right)+u\cdot\psi_{n\tilde{n}2}+\frac{u\sin\psi}{g}\cdot\delta f_{b2}-\frac{u^2\sin\psi}{g}\cdot\delta\omega_{b3}-\\
&\quad-\frac{u\cos\psi\sin\psi}{g}\cdot\delta a_{n2}^{W}+\frac{u\sin^2\psi}{g}\cdot\delta a_{n1}^{W},\\
&\cos\psi\cdot\psi_{n\tilde{n}1}+\sin\psi\cdot\psi_{n\tilde{n}2}+\frac{1}{g}\cdot\delta f_{b2}-\frac{u}{g}\cdot\delta\omega_{b3}+\frac{\sin\psi}{g}\cdot\delta a_{n1}^{W}-\frac{\cos\psi}{g}\cdot\delta a_{n2}^{W},\\
&\delta f_{b3}+u\cdot\delta\omega_{b2}-\delta a_{n3}^{W},\ \delta\omega_{b1}.
\end{aligned}
\tag{3.54}
$$

Orientation errors, namely $\psi_{n\tilde{n}1}$ and $\psi_{n\tilde{n}2}$ appear in two observable linear combinations. In general, this type of aiding can hardly be beneficial for estimation and correction of attitude errors, because in

the second observable combination from (3.54) $\psi_{n\tilde{n}2}$ is coupled with down velocity error, which is known to be unstable. However, if vertical channel of the system is aided, i. e. altitude measurement is additionally available, this coupling will disappear and attitude errors will become observable separately from each other, but in a combination with sensor errors. Therefore, combination of AOA and AOS measurements appears beneficial for attitude estimation and correction as long as additional altitude information is available.

3.2.11 Unobservability of heading error

In the previous sections it was shown that air data measurements allowed to observe the third component of orientation error only in combination with other orientation or velocity errors.
Then a natural question arises. Exists there a trajectory that makes heading error observable separately or in a combination with sensor errors? Intuition says that an answer to this question should be negative. Below we propose a mathematical proof of this guess.

Theorem 5. Heading error is completely unobservable in case INS is aided by information on projections of velocity vector onto the axes of body-fixed coordinate frame.

Proof: Consider vehicle's velocity vector in b-frame $\mathbf{v}_b = \mathbf{R}_{nb}^{\mathrm{T}}\mathbf{v}_n$. Then

$$\dot{\mathbf{v}}_b = \dot{\mathbf{R}}_{nb}^{\mathrm{T}}\mathbf{v}_n + \mathbf{R}_{nb}^{\mathrm{T}}\dot{\mathbf{v}}_n. \tag{3.55}$$

Substituting derivatives of rotation matrix and n-frame velocity with formulae (2.1) and with relation $\mathbf{v}_n = \mathbf{R}_{nb}\mathbf{v}_b$ yields a differential equation for $\mathbf{v}_b$ in the form

$$\dot{\mathbf{v}}_b = -\boldsymbol{\Omega}_{ib}\mathbf{v}_b + \mathbf{f}_b + \mathbf{R}_{nb}^{\mathrm{T}}\boldsymbol{\gamma}_n(\boldsymbol{\lambda}) - \mathbf{R}_{nb}^{\mathrm{T}}\left[\mathbf{R}_{en}^{\mathrm{T}}(\boldsymbol{\lambda})\boldsymbol{\omega}_{ie}\times\right]\mathbf{R}_{nb}\mathbf{v}_b. \tag{3.56}$$

Linearized velocity error propagation equation, derived from (3.56), can be written as

$$\delta\dot{\mathbf{v}}_b = \mathbf{A}_{21}\cdot\delta\boldsymbol{\lambda} - \left(\tilde{\boldsymbol{\Omega}}_{ib} + \mathbf{R}_{\tilde{n}b}^{\mathrm{T}}\left[\mathbf{R}_{en}^{\mathrm{T}}(\tilde{\boldsymbol{\lambda}})\boldsymbol{\omega}_{ie}\times\right]\mathbf{R}_{\tilde{n}b}\right)\cdot\delta\mathbf{v}_b + \mathbf{A}_{23}\cdot\psi_{n\tilde{n}} + \delta\mathbf{f}_b + [\tilde{\mathbf{v}}_b\times]\cdot\delta\boldsymbol{\omega}_{ib}, \tag{3.57}$$

where

$$\begin{aligned}
&\mathbf{A}_{21} = \mathbf{R}_{\tilde{n}b}^{\mathrm{T}}\left(\left.\frac{\partial\boldsymbol{\gamma}_n(\boldsymbol{\lambda})}{\partial\boldsymbol{\lambda}}\right|_{\tilde{\boldsymbol{\lambda}}} + [\mathbf{R}_{\tilde{n}b}\tilde{\mathbf{v}}_b\times]\cdot\left.\frac{\partial\mathbf{R}_{en}^{\mathrm{T}}(\boldsymbol{\lambda})\boldsymbol{\omega}_{ie}}{\partial\boldsymbol{\lambda}}\right|_{\tilde{\boldsymbol{\lambda}}}\right),\\
&\mathbf{A}_{23} = \mathbf{R}_{\tilde{n}b}^{\mathrm{T}}\left([\boldsymbol{\gamma}_n(\tilde{\boldsymbol{\lambda}})\times] + [\mathbf{R}_{en}^{\mathrm{T}}(\tilde{\boldsymbol{\lambda}})\boldsymbol{\omega}_{ie}\times]\cdot[\mathbf{R}_{\tilde{n}b}\tilde{\mathbf{v}}_b\times] - [(\mathbf{R}_{en}^{\mathrm{T}}(\tilde{\boldsymbol{\lambda}})\boldsymbol{\omega}_{ie}\times\mathbf{R}_{\tilde{n}b}\tilde{\mathbf{v}}_b)\times]\right),\\
&\delta\mathbf{v}_b = \mathbf{v}_b - \tilde{\mathbf{v}}_b.
\end{aligned} \tag{3.58}$$

Detailed derivation of (3.56) and (3.57) is presented in Appendix G. Under assumptions, introduced in Section 3.2.2, equations (3.56), (3.57) simplify to

$$\begin{aligned}
&\dot{\mathbf{v}}_b = -\boldsymbol{\Omega}_{ib}\mathbf{v}_b + \mathbf{R}_{nb}^{\mathrm{T}}\boldsymbol{\gamma}_n + \mathbf{f}_b,\\
&\delta\dot{\mathbf{v}}_b = -\tilde{\boldsymbol{\Omega}}_{ib}\delta\mathbf{v}_b + \mathbf{R}_{\tilde{n}b}^{\mathrm{T}}[\boldsymbol{\gamma}_n\times]\cdot\psi_{n\tilde{n}} + \delta\mathbf{f}_b + [\tilde{\mathbf{v}}_b\times]\cdot\delta\boldsymbol{\omega}_{ib}.
\end{aligned} \tag{3.59}$$

Note, that up to the first order terms

$$\delta\mathbf{v}_b = \mathbf{R}_{nb}^{\mathrm{T}}(\delta\mathbf{v}_n + [\mathbf{v}_n\times]\cdot\psi_{n\tilde{n}}). \tag{3.60}$$

Replacing in (3.33) differential equation for $\delta\mathbf{v}_n$ with the second equation from (3.59) and substituting $\delta\mathbf{v}_n$ in differential equations for position and orientation errors with (3.60) yields linear error propagation equations in the form

$$\dot{\mathbf{x}}_1 = \mathbf{F}_1(t)\mathbf{x}_1, \tag{3.61}$$

where

$$\mathbf{x}_1 = \begin{pmatrix} \delta\boldsymbol{\lambda} \\ \delta\mathbf{v}_b \\ \psi_{n\tilde{n}} \\ \delta\mathbf{f}_b \\ \delta\boldsymbol{\omega}_b \\ b_{baro} \\ \delta h_{atm} \\ \delta\dot{h}_{atm} \\ \delta\mathbf{v}_n^{\mathrm{W}} \\ \delta\mathbf{a}_n^{\mathrm{W}} \end{pmatrix}, \ \mathbf{F}_1(t) = \begin{pmatrix} \mathbf{F}_{11} & \mathbf{F}_{12}\mathbf{R}_{nb} & -\mathbf{F}_{12}[\mathbf{R}_{nb}\mathbf{v}_b\times] & \mathbf{0}_{3\times3} & \mathbf{0}_{3\times3} & \mathbf{0}_{3\times1} & \mathbf{0}_{3\times1} & \mathbf{0}_{3\times1} & \mathbf{0}_{3\times3} & \mathbf{0}_{3\times3} \\ \mathbf{0}_{3\times3} & -\boldsymbol{\Omega}_{ib} & \mathbf{R}_{nb}^{\mathrm{T}}[\boldsymbol{\gamma}_n\times] & \mathbf{I}_{3\times3} & [\mathbf{v}_b\times] & \mathbf{0}_{3\times1} & \mathbf{0}_{3\times1} & \mathbf{0}_{3\times1} & \mathbf{0}_{3\times3} & \mathbf{0}_{3\times3} \\ \mathbf{0}_{3\times3} & \mathbf{0}_{3\times3} & \mathbf{0}_{3\times3} & \mathbf{0}_{3\times3} & \mathbf{R}_{nb} & \mathbf{0}_{3\times1} & \mathbf{0}_{3\times1} & \mathbf{0}_{3\times1} & \mathbf{0}_{3\times3} & \mathbf{0}_{3\times3} \\ \mathbf{0}_{3\times3} & \mathbf{0}_{3\times3} & \mathbf{0}_{3\times3} & \mathbf{0}_{3\times3} & \mathbf{0}_{3\times3} & \mathbf{0}_{3\times1} & \mathbf{0}_{3\times1} & \mathbf{0}_{3\times1} & \mathbf{0}_{3\times3} & \mathbf{0}_{3\times3} \\ \mathbf{0}_{3\times3} & \mathbf{0}_{3\times3} & \mathbf{0}_{3\times3} & \mathbf{0}_{3\times3} & \mathbf{0}_{3\times3} & \mathbf{0}_{3\times1} & \mathbf{0}_{3\times1} & \mathbf{0}_{3\times1} & \mathbf{0}_{3\times3} & \mathbf{0}_{3\times3} \\ \mathbf{0}_{1\times3} & \mathbf{0}_{1\times3} & \mathbf{0}_{1\times3} & \mathbf{0}_{1\times3} & \mathbf{0}_{1\times3} & 0 & 0 & 0 & \mathbf{0}_{1\times3} & \mathbf{0}_{1\times3} \\ \mathbf{0}_{1\times3} & \mathbf{0}_{1\times3} & \mathbf{0}_{1\times3} & \mathbf{0}_{1\times3} & \mathbf{0}_{1\times3} & 0 & 0 & 1 & \mathbf{0}_{1\times3} & \mathbf{0}_{1\times3} \\ \mathbf{0}_{1\times3} & \mathbf{0}_{1\times3} & \mathbf{0}_{1\times3} & \mathbf{0}_{1\times3} & \mathbf{0}_{1\times3} & 0 & 0 & 0 & \mathbf{0}_{1\times3} & \mathbf{0}_{1\times3} \\ \mathbf{0}_{3\times3} & \mathbf{0}_{3\times3} & \mathbf{0}_{3\times3} & \mathbf{0}_{3\times3} & \mathbf{0}_{3\times3} & \mathbf{0}_{3\times1} & \mathbf{0}_{3\times1} & \mathbf{0}_{3\times1} & \mathbf{0}_{3\times3} & \mathbf{F}_{9,10} \\ \mathbf{0}_{3\times3} & \mathbf{0}_{3\times3} & \mathbf{0}_{3\times3} & \mathbf{0}_{3\times3} & \mathbf{0}_{3\times3} & \mathbf{0}_{3\times1} & \mathbf{0}_{3\times1} & \mathbf{0}_{3\times1} & \mathbf{0}_{3\times3} & \mathbf{0}_{3\times3} \end{pmatrix}. \tag{3.62}$$

Here $\mathbf{F}_{11}$, $\mathbf{F}_{12}$, and $\mathbf{F}_{9,10}$ are the same as in Section 3.2.2.

Then the measurement equation for b-frame velocity observation can be written as follows.

$$\Delta\mathbf{y}_{\mathbf{vb}} = \mathbf{v}_b - \tilde{\mathbf{v}}_b = \delta\mathbf{v}_b. \tag{3.63}$$

Measurement matrix takes the form

$$\mathbf{H}_{\mathbf{vb}} = \frac{\partial\Delta\mathbf{y}_{\mathbf{vb}}}{\partial\mathbf{x}^{\mathrm{T}}} = \begin{pmatrix} \mathbf{0}_{3\times3} & \mathbf{I}_{3\times3} & \mathbf{0}_{3\times3} & \mathbf{0}_{3\times3} & \mathbf{0}_{3\times3} & \mathbf{0}_{3\times9} \end{pmatrix}. \tag{3.64}$$

Computing observability matrix from system and measurement matrices given by (3.63), (3.64) yields

$$\mathbf{L}_{\mathbf{vb}}(t) = \begin{pmatrix} \mathbf{0}_{3\times3} & \mathbf{I}_{3\times3} & \mathbf{0}_{3\times3} & \mathbf{0}_{3\times3} & \mathbf{0}_{3\times3} & \mathbf{0}_{3\times9} \\ \mathbf{0}_{3\times3} & -\boldsymbol{\Omega}_{ib} & \mathbf{R}_{nb}^{\mathrm{T}}[\boldsymbol{\gamma}_n\times] & \mathbf{I}_{3\times3} & [\mathbf{v}_b\times] & \mathbf{0}_{3\times9} \\ \mathbf{0}_{3\times3} & -\boldsymbol{\Omega}_{ib}+\boldsymbol{\Omega}_{ib}^2 & -2\boldsymbol{\Omega}_{ib}\mathbf{R}_{nb}^{\mathrm{T}}[\boldsymbol{\gamma}_n\times] & -\boldsymbol{\Omega}_{ib} & [\dot{\mathbf{v}}_b\times]-\boldsymbol{\Omega}_{ib}[\mathbf{v}_b\times] & \mathbf{0}_{3\times9} \\ \mathbf{0}_{3\times3} & \mathbf{P}_1 & \mathbf{Q}_1\mathbf{R}_{nb}^{\mathrm{T}}[\boldsymbol{\gamma}_n\times] & \bullet & \bullet & \mathbf{0}_{3\times9} \\ \mathbf{0}_{3\times3} & \mathbf{P}_2 & \mathbf{Q}_2\mathbf{R}_{nb}^{\mathrm{T}}[\boldsymbol{\gamma}_n\times] & \bullet & \bullet & \mathbf{0}_{3\times9} \\ \vdots & \vdots & \vdots & \vdots & \vdots & \vdots \\ \mathbf{0}_{3\times3} & \mathbf{P}_{21} & \mathbf{Q}_{21}\mathbf{R}_{nb}^{\mathrm{T}}[\boldsymbol{\gamma}_n\times] & \bullet & \bullet & \mathbf{0}_{3\times9} \end{pmatrix}. \tag{3.65}$$

Here $\mathbf{P}_i$ and $\mathbf{Q}_i$, $i=1,\ldots,21$, are some polynomials of matrix $\boldsymbol{\Omega}_{ib}$ and its derivatives with respect to time. Symbol "$\bullet$" denotes some nonzero entries of matrix $\mathbf{L}_{\mathbf{v}_b}(t)$.

Note, that the third column of $[\boldsymbol{\gamma}_n\times]$ is zero-column. Consequently, all the elements in the 9th column of the matrix (3.65) are equal to zero, and thus $\psi_{n\tilde{n}3}$ does not appear in observable combinations, i. e. is completely unobservable independently of flight trajectory and dynamics. *End of Proof.*

In fact, appearance of $\psi_{n\tilde{n}3}$ in observable combinations, listed in Sections 3.2.4 and 3.2.6, is solely due to the choice of mechanization of error propagation equations and relation (3.60) between $\delta\mathbf{v}_n$ and $\delta\mathbf{v}_b$.

Complete navigation, error propagation, and air data measurements equations for the case, when velocity vector is expressed in b-frame, are presented in Appendix G. Performance of b- and n-frame mechanizations is studied and compared in Appendix H.

3.2.12 Discussion

Above it was shown that both TAS and barometric altitude were valuable sources of information on vehicle's attitude during maneuvering. Since at straight and leveled flight these measurements do not allow to observe attitude errors separately from each other, either high quality sensors or frequent maneuvering is required to achieve constant availability of attitude estimate of a reasonable accuracy.

Velocity w.r.t. wind, which can be computed from TAS, AOA, and AOS measurements, provides information on vehicle's attitude errors both at straight and leveled flight and during maneuvering. This shall allow to satisfy attitude performance requirements even with tactical-grade and high quality industrial-grade IMUs. However, an atmosphere shall not be highly volatile, and the wind is required to be slowly changing. Though, even a complete Air Data System presents a poor source of information on velocity with respect to ground, since velocity and wind velocity errors always appear coupled in observable combinations.

A complete set of air data measurements was shown to provide partially redundant information on attitude errors, i. e. that attitude errors remained observable separately from each other in any typical flight situation even if either TAS or AOA measurement became unavailable.

3.3 The Earth's magnetic field measurements

3.3.1 Models of the Earth's magnetic field

Magnetic field of the Earth can roughly be assumed originating from a tilted bar magnet with a dipole moment of $j = 7.95 \times 10^{22}\ \mathrm{A \cdot m^2}$ located near the center of the Earth [36]. Axis of the magnet is tilted at an angle of about 11 degrees in meridian plane passing through the eastern part of Canada. This model is, of course, very rough and thus is more suitable for gaining understanding of basic properties of magnetic field measurement, rather than for being used as a reference inside navigation algorithms.

Figure 4 illustrates the dipole model.

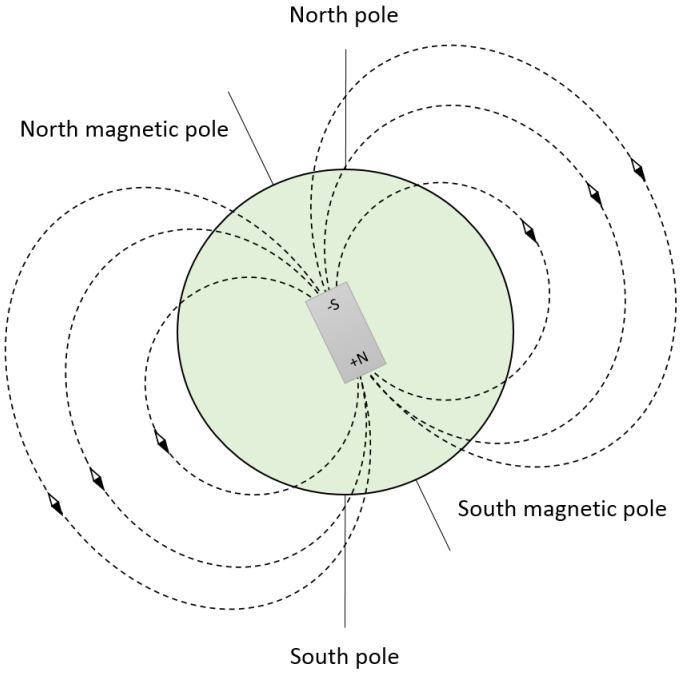

Fig. 4–Dipole model of the Earth's magnetic field

Modern empirical models, such as World Magnetic Model (WMM), Enhanced Magnetic Model (EMM), and International Geomagnetic Reference Field (IGRF), represent magnetic field of the Earth in terms of converging spherical harmonics series [37, 38]. Scalar potential of the field is expanded in the form

$$V = a\sum_{n=1}^{n_{max}}\left(\frac{a}{R}\right)^{n+1}\sum_{m=0}^{n}\left(g_n^m(t)\cos m\lambda + h_n^m(t)\sin m\lambda\right)P_n^m(\sin\phi'), \tag{3.66}$$

where a is geomagnetic reference radius; ϕ', λ, R are the spherical latitude, longitude, and radius in a spherical geocentric reference frame; $g_n^m(t)$ and $h_n^m(t)$ are Gauss coefficients of degree n and order m; $P_n^m(s)$ are associated Legendre polynomials [39], and n_{max} is the degree of expansion.

Given scalar potential (3.66), geocentric components of geomagnetic field in the northward, eastward, and radially inwards directions (X, Y, and Z) are computed by taking the gradient of V in spherical polar coordinates

$$X = \frac{1}{R}\frac{\partial V}{\partial \phi'},\quad Y = \frac{1}{R\cos\phi'}\frac{\partial V}{\partial \lambda},\quad Z = \frac{\partial V}{\partial R}. \tag{3.67}$$

WMM is a joint product of The United States' National Geospatial-Intelligence Agency (NGA) and The United Kingdom's Defense Geographic Centre (DGC). WMM uses spherical harmonics representation to degree and order 12 and resolves magnetic field at 3000 km wavelength. IGRF is produced as a part of voluntary research of scientific community of the International Association of Geomagnetism and Aeronomy (IAGA) and uses expansion to degree and order 13. Most of the users can choose between WMM and IGRF arbitrarily, because differences between them are within expected model inaccuracy. Though, WMM is a standard for Federal Aviation Administration (FAA),

the North Atlantic Treaty Organization (NATO), and some other institutions. WMM is valid for current epoch only, while IGRF offers retrospective compatibility as well. EMM is a further extension of WMM, which provides coefficients to degree and order 720 and resolves magnetic anomalies down to 56 km wavelength [40].

Figures 5–7 illustrates differences between magnetic models. Since EMM at the moment is the most accurate empirical model, it is used here as a reference. The plots at the top of the pages show the ratio of the strength of magnetic field vectors to the strength of EMM. The plots at the bottom show an angle between magnetic field vectors and the EMM vector ($\arccos((\mathbf{B}_n^{EMM})^T \cdot \mathbf{B}_n^X)$). "Dipole" stands for Dipole magnetic field model, "WMM6" denotes the WMM truncated after the sixth term in the series expansion, "WMM12" stands for complete World Magnetic Model. Figure 5 distinctly demonstrates that the dipole model is highly inaccurate and can hardly be used for navigation. WMM6, in turn, appears much more accurate and could already be considered in applications, where accuracy requirements are relaxed, but computational burden appears critical. The difference between the strengths of WMM12 and EMM is seen to be below 1%, and the angle from WMM12 vector to EMM vector hardly exceeds 0.5 degrees. Thus, the WMM12 shall be sufficient for most of navigation applications and can present a good tradeoff between computational complexity and model accuracy.

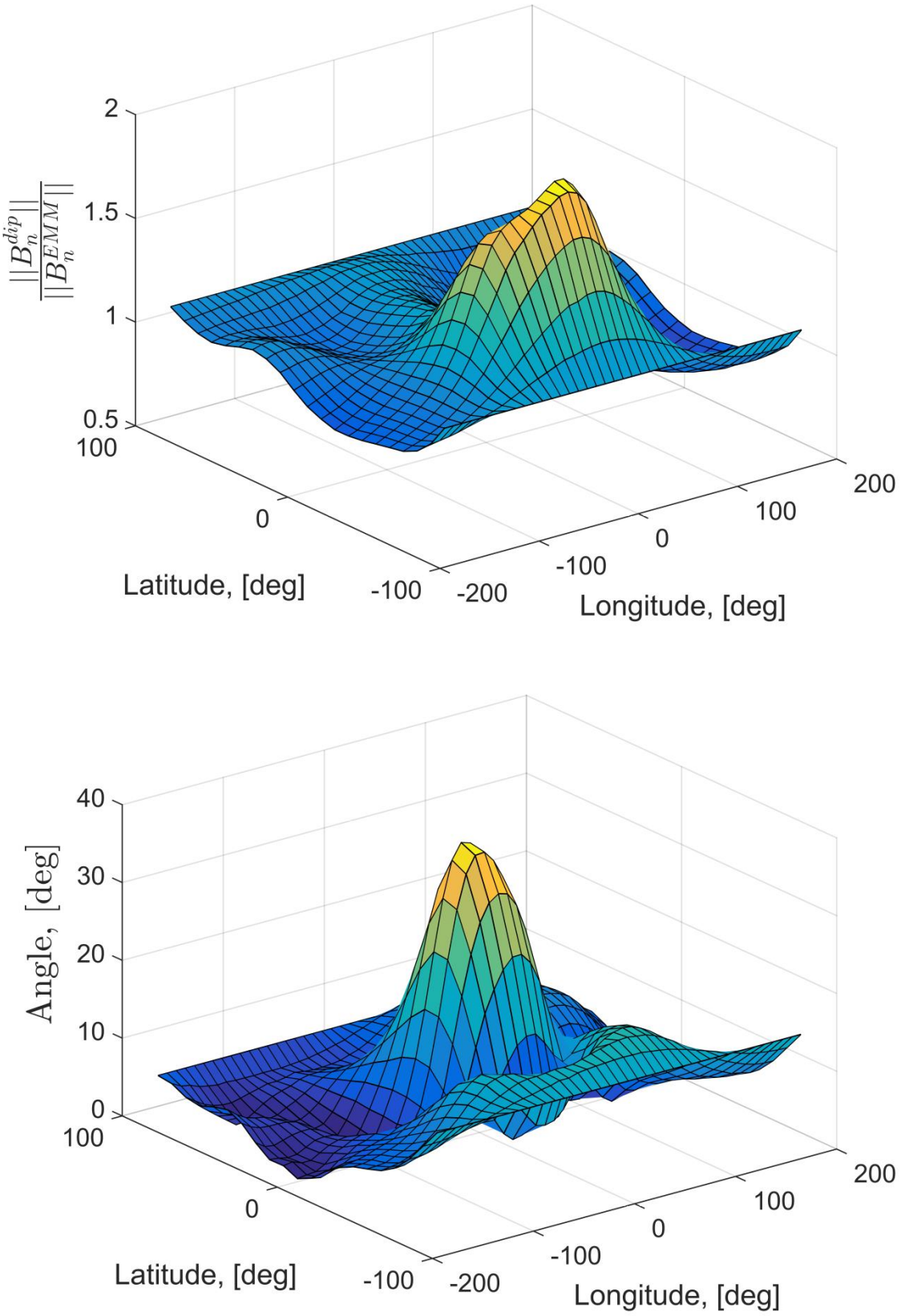

Fig. 5–Comparison of models of the Earth's magnetic field. Dipole vs. EMM.

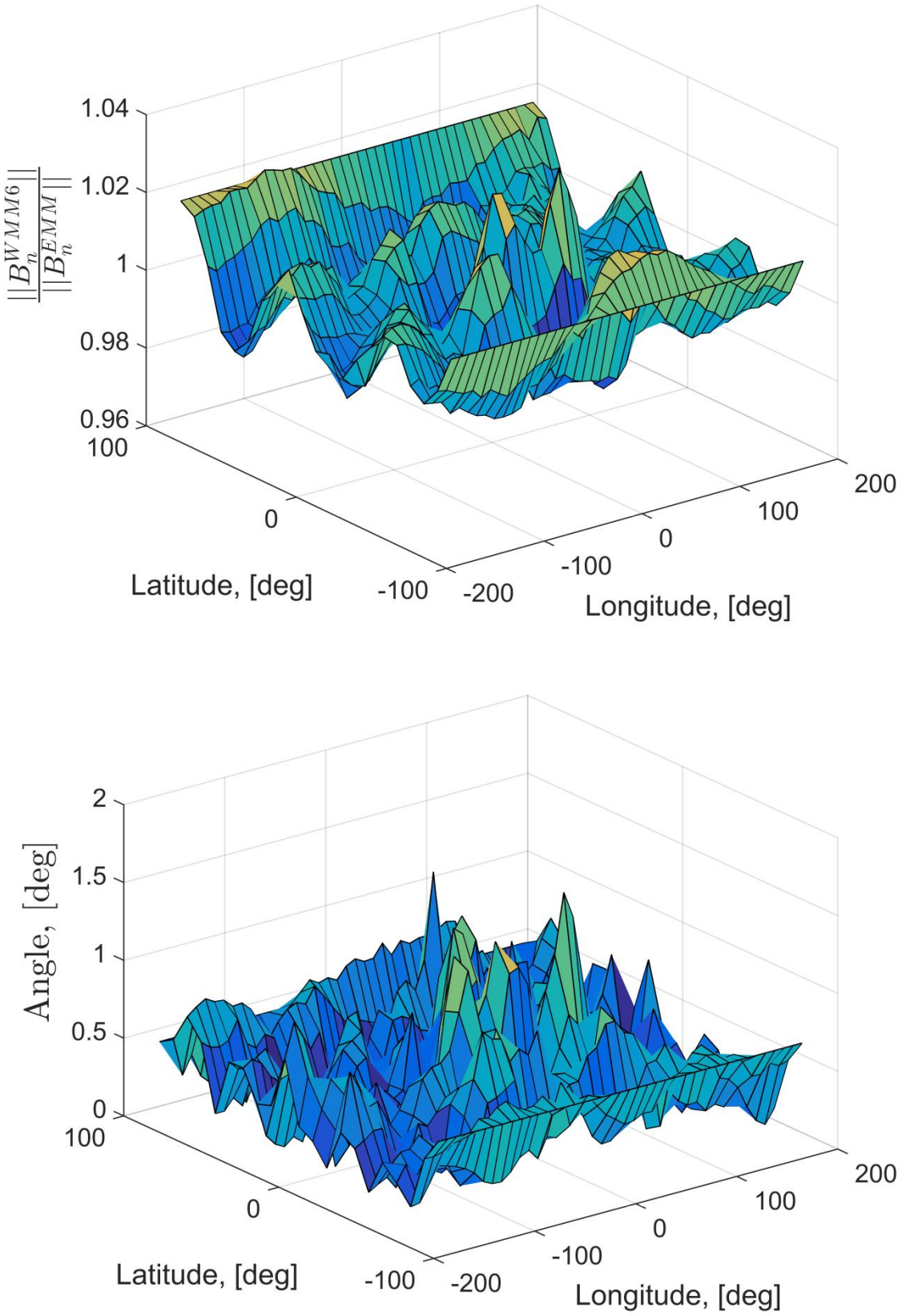

Fig. 6–Comparison of models of the Earth's magnetic field. WMM6 vs. EMM.

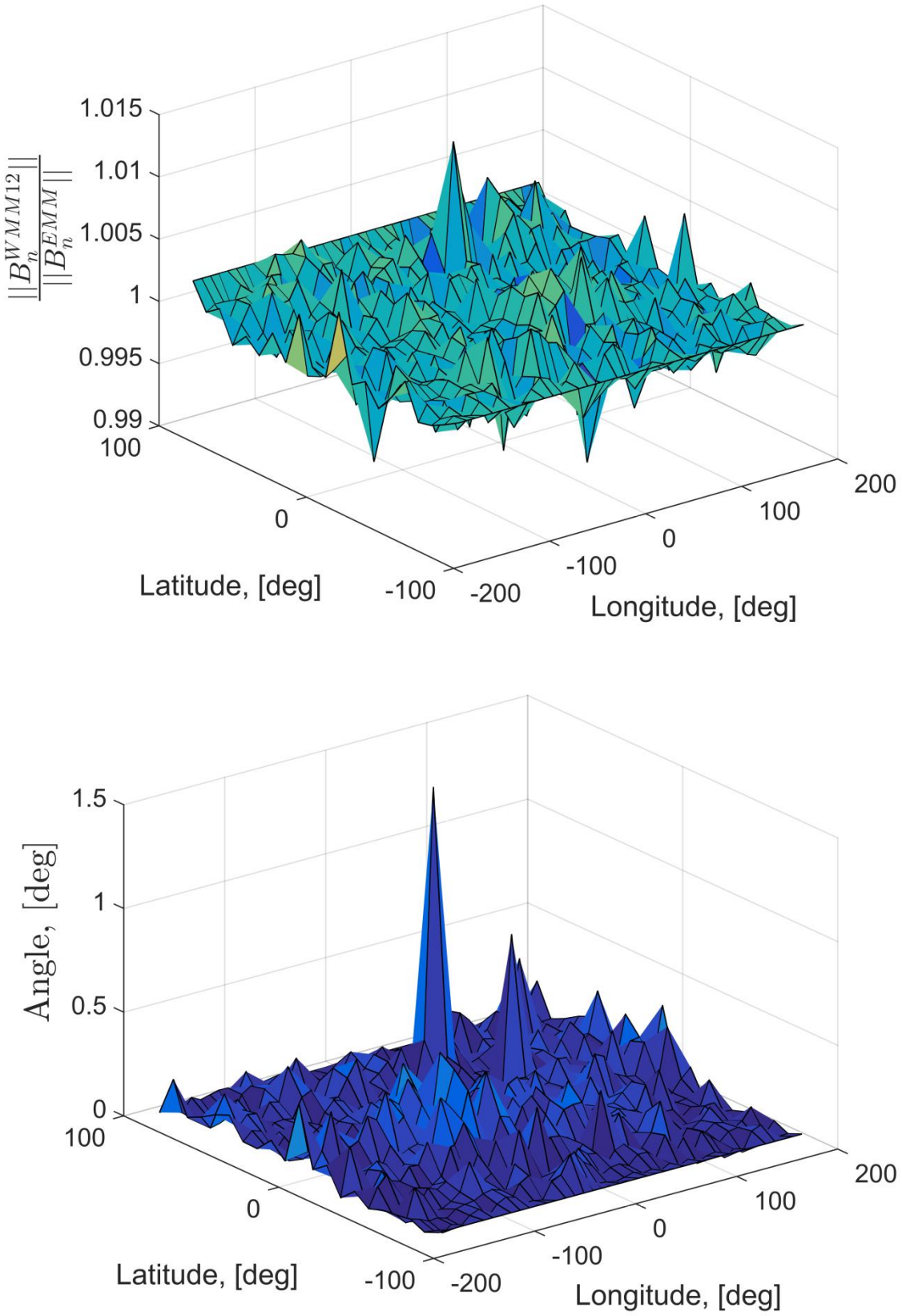

Fig. 7–Comparison of models of the Earth's magnetic field. WMM12 vs. EMM.

3.3.2 Magnetometer measurement equations

A three-axis magnetometer provides a measurement of the Earth's magnetic field expressed in b-frame. Measurement equation takes the form

$$\mathbf{y}_{\mathbf{B}} = \mathbf{B}_b. \tag{3.68}$$

Measured value is superposed by an error, which is assumed to be a sum of deterministic instrumental and stochastic errors. According to convention, accepted in this work, an error is defined as a difference between true and measured/estimated quantity. Thus

$$\tilde{\mathbf{y}}_B = \mathbf{y}_B - \delta\mathbf{y}_{\mathbf{B}} = \mathbf{B}_b - \delta\mathbf{B}_b - \mathbf{v}_{\mathbf{B}}. \tag{3.69}$$

Magnetometer instrumental error $\delta\mathbf{B}_b = \begin{pmatrix}\delta B_{b1} & \delta B_{b2} & \delta B_{b3}\end{pmatrix}^{\mathrm{T}}$ is modeled as a random constant, stochastic error $\mathbf{v}_{\mathbf{B}}$ is modeled as zero-mean Gaussian white noise. Residual is formed as

$$\Delta\mathbf{y}_{magn} = \mathbf{R}_{\tilde{n}b}\tilde{\mathbf{y}}_{\mathbf{B}} - \tilde{\mathbf{B}}_{n,mod}, \tag{3.70}$$

where $\tilde{\mathbf{B}}_{n,mod} = \mathbf{B}_{n,mod}(\tilde{\boldsymbol{\lambda}})$ is an estimate of the Earth's magnetic field, computed at the estimated position $\tilde{\boldsymbol{\lambda}}$ by the means of magnetic field model $\mathbf{B}_{n,mod}(\phi,\lambda,h)$. Consequently, linearized measurement equation takes the form

$$\begin{aligned}\Delta\mathbf{y}_{magn} = \left.\frac{\partial\mathbf{B}_{n,\mathrm{mod}}(\boldsymbol{\lambda})}{\partial\boldsymbol{\lambda}}\right|_{\boldsymbol{\lambda}=\tilde{\boldsymbol{\lambda}}}\cdot\delta\boldsymbol{\lambda} + [\tilde{\mathbf{B}}_{n,\mathrm{mod}}\times]\psi_{n\tilde{n}} - \\ -\mathbf{R}_{\tilde{n}b}\delta\mathbf{B}_b + \delta\mathbf{B}_{n,mod} - \mathbf{R}_{nb}\mathbf{v}_{\mathbf{B}}.\end{aligned} \tag{3.71}$$

Herein $\delta\mathbf{B}_{n,mod} = \begin{pmatrix}\delta B_{n1,\mathrm{mod}} & \delta B_{n2,\mathrm{mod}} & \delta B_{n3,\mathrm{mod}}\end{pmatrix}^{\mathrm{T}}$ is an error of the model of magnetic field. By definition, $\mathbf{B}_n(\boldsymbol{\lambda}) = \mathbf{B}_{n,mod}(\boldsymbol{\lambda}) + \delta\mathbf{B}_{n,mod}$. In general, $\delta\mathbf{B}_{n,mod}$ is position dependent, but since no deterministic model is available, we use a random constant model instead:

$$\delta\dot{\mathbf{B}}_{n,mod} = \mathbf{0}. \tag{3.72}$$

Equation (3.71) is derived as presented below.

$$\begin{aligned}\Delta\mathbf{y}_{magn} &= \mathbf{R}_{\tilde{n}b}\tilde{\mathbf{y}}_{\mathbf{B}} - \mathbf{B}_{n,\mathrm{mod}}(\tilde{\boldsymbol{\lambda}}) = \mathbf{R}_{\tilde{n}b}(\mathbf{B}_b - \delta\mathbf{B}_b - \mathbf{v}_{\mathbf{B}}) - \mathbf{B}_{n,\mathrm{mod}}(\tilde{\boldsymbol{\lambda}}) = \\ &= \mathbf{R}_{n\tilde{n}}^{\mathrm{T}}\mathbf{R}_{nb}(\mathbf{B}_b - \delta\mathbf{B}_b - \mathbf{v}_{\mathbf{B}}) - \mathbf{B}_{n,\mathrm{mod}}(\tilde{\boldsymbol{\lambda}}) = \mathbf{R}_{n\tilde{n}}^{\mathrm{T}}(\mathbf{B}_n - \mathbf{R}_{nb}\delta\mathbf{B}_b - \mathbf{R}_{nb}\mathbf{v}_{\mathbf{B}}) - \mathbf{B}_{n,\mathrm{mod}}(\tilde{\boldsymbol{\lambda}}) = \\ &= (\mathbf{I} - [\psi_{n\tilde{n}}\times])(\mathbf{B}_n - \mathbf{R}_{nb}\delta\mathbf{B}_b - \mathbf{R}_{nb}\mathbf{v}_{\mathbf{B}}) - \mathbf{B}_{n,\mathrm{mod}}(\tilde{\boldsymbol{\lambda}}) \approx \\ &\approx \mathbf{B}_n - \mathbf{R}_{nb}\delta\mathbf{B}_b + [\mathbf{B}_n\times]\psi_{n\tilde{n}} - \mathbf{B}_{n,\mathrm{mod}}(\tilde{\boldsymbol{\lambda}}) - \mathbf{R}_{nb}\mathbf{v}_{\mathbf{B}} \approx \\ &\approx \mathbf{B}_{n,\mathrm{mod}}(\boldsymbol{\lambda}) + \delta\mathbf{B}_{n,mod} + [\mathbf{B}_n\times]\psi_{n\tilde{n}} - \mathbf{R}_{nb}\delta\mathbf{B}_b - \mathbf{B}_{n,\mathrm{mod}}(\tilde{\boldsymbol{\lambda}}) - \mathbf{R}_{nb}\mathbf{v}_{\mathbf{B}} \approx \\ &\approx \left.\frac{\partial\mathbf{B}_{n,\mathrm{mod}}(\boldsymbol{\lambda})}{\partial\boldsymbol{\lambda}}\right|_{\boldsymbol{\lambda}=\tilde{\boldsymbol{\lambda}}} + [\mathbf{B}_n\times]\psi_{n\tilde{n}} - \mathbf{R}_{nb}\delta\mathbf{B}_b + \delta\mathbf{B}_{n,mod} - \mathbf{R}_{nb}\mathbf{v}_{\mathbf{B}} \approx \\ &\approx \left.\frac{\partial\mathbf{B}_{n,\mathrm{mod}}(\boldsymbol{\lambda})}{\partial\boldsymbol{\lambda}}\right|_{\boldsymbol{\lambda}=\tilde{\boldsymbol{\lambda}}}\cdot\delta\boldsymbol{\lambda} + [\tilde{\mathbf{B}}_{n,\mathrm{mod}}\times]\psi_{n\tilde{n}} - \mathbf{R}_{\tilde{n}b}\delta\mathbf{B}_b + \delta\mathbf{B}_{n,mod} - \mathbf{R}_{nb}\mathbf{v}_{\mathbf{B}}\end{aligned}$$

3.3.3 Determination of magnetic heading

If no information on position is available, magnetic field model cannot be used to compute a reference value of magnetic field vector, and, consequently, magnetic field vector cannot be used for true heading determination. Nevertheless, availability of a reference direction remains crucial for controlling airplane and therefore magnetic heading is widely used in aviation in case navigation system is unable to provide accurate enough estimate of true heading. Adjusting of heading estimate, computed by INS, to the value of an angle between horizontal component of vehicle's longitudal axis and horizontal component of magnetic field vector is called magnetic slaving. In the coordinate reference frame, whose first axis is aligned with horizontal component of magnetic field, third axis points down, and the second axis is chosen to complete a right-hand system (shorthand m-frame), magnetic field vector takes the form

$$\mathbf{B}_m = \begin{pmatrix} B_{m1} & 0 & B_{m3} \end{pmatrix}^{\mathrm{T}}. \tag{3.73}$$

The second component of $\mathbf{B}_m$, which is equal to zero, can be used to form residual

$$\begin{aligned} \Delta y_{magn,s} &= B_{m2} - \tilde{B}_{n2} = -\tilde{B}_{n2} \approx \\ &\approx -B_{m3} \cdot \psi_{n\tilde{n}1} + B_{m1} \cdot \psi_{n\tilde{n}3}. \end{aligned} \tag{3.74}$$

Estimates of B_{m1} and B_{m3} can be obtained as follows

$$\tilde{B}_{m1} = \sqrt{\tilde{B}_{n1}^2 + \tilde{B}_{n2}^2},\ \tilde{B}_{m3} = \tilde{B}_{n3}. \tag{3.75}$$

Herein $\tilde{\mathbf{B}}_n = \mathbf{R}_{\tilde{n}b}\tilde{\mathbf{B}}_b$. Measurement equation (3.74) can then be used at Kalman filter update step in order to slave heading.

3.3.4 Simplification of error propagation equations

In order to preserve analytical computability, error propagation equations (2.9) are simplified under the following assumptions:

1. The Earth's gravity field can be assumed parallel and constant,
2. The Earth's rotation rate is neglected,
3. Transport rate is neglected,
4. Inertial sensor errors, magnetometer instrumental errors, and errors of magnetic model are modelled as random constants.

Under the assumptions, listed above, the system of error propagation equations, extended by sensor error models, can be written in the form

$$\dot{\mathbf{x}} = \mathbf{F}(t)\mathbf{x}, \tag{3.76}$$

where the state vector and simplified system matrix are

$$\mathbf{x}=\begin{pmatrix}\delta\boldsymbol{\lambda}\\ \delta\mathbf{v}_n\\ \psi_{n\tilde{n}}\\ \delta\mathbf{f}_b\\ \delta\boldsymbol{\omega}_b\\ \delta\mathbf{B}_b\\ \delta\mathbf{B}_n^{\mathrm{mod}}\end{pmatrix},\quad \mathbf{F}(t)=\begin{pmatrix}\mathbf{F}_{11} & \mathbf{F}_{12} & \mathbf{0}_{3\times3} & \mathbf{0}_{3\times3} & \mathbf{0}_{3\times3} & \mathbf{0}_{3\times3} & \mathbf{0}_{3\times3}\\ \mathbf{0}_{3\times3} & \mathbf{0}_{3\times3} & -[\mathbf{f}_n\times] & \mathbf{R}_{nb} & \mathbf{0}_{3\times3} & \mathbf{0}_{3\times3} & \mathbf{0}_{3\times3}\\ \mathbf{0}_{3\times3} & \mathbf{0}_{3\times3} & \mathbf{0}_{3\times3} & \mathbf{0}_{3\times3} & \mathbf{R}_{nb} & \mathbf{0}_{3\times3} & \mathbf{0}_{3\times3}\\ \mathbf{0}_{3\times3} & \mathbf{0}_{3\times3} & \mathbf{0}_{3\times3} & \mathbf{0}_{3\times3} & \mathbf{0}_{3\times3} & \mathbf{0}_{3\times3} & \mathbf{0}_{3\times3}\\ \mathbf{0}_{3\times3} & \mathbf{0}_{3\times3} & \mathbf{0}_{3\times3} & \mathbf{0}_{3\times3} & \mathbf{0}_{3\times3} & \mathbf{0}_{3\times3} & \mathbf{0}_{3\times3}\\ \mathbf{0}_{3\times3} & \mathbf{0}_{3\times3} & \mathbf{0}_{3\times3} & \mathbf{0}_{3\times3} & \mathbf{0}_{3\times3} & \mathbf{0}_{3\times3} & \mathbf{0}_{3\times3}\\ \mathbf{0}_{3\times3} & \mathbf{0}_{3\times3} & \mathbf{0}_{3\times3} & \mathbf{0}_{3\times3} & \mathbf{0}_{3\times3} & \mathbf{0}_{3\times3} & \mathbf{0}_{3\times3}\end{pmatrix}. \tag{3.77}$$

$$\mathbf{F}_{11}=\begin{pmatrix}0 & 0 & -\dfrac{v_{n1}}{\left(R(\phi)+h\right)^2}\\ \dfrac{v_{n2}\tan\phi}{\left(R(\phi)+h\right)\cos\phi} & 0 & -\dfrac{v_{n2}}{\left(R(\phi)+h\right)^2\cos\phi}\\ 0 & 0 & 0\end{pmatrix},$$

$$\mathbf{F}_{12}=\begin{pmatrix}\dfrac{1}{\left(R(\phi)+h\right)} & 0 & 0\\ 0 & \dfrac{1}{\left(R(\phi)+h\right)\cos\phi} & 0\\ 0 & 0 & -1\end{pmatrix}. \tag{3.78}$$

Herein $R(\phi)=\sqrt{N(\phi)M(\phi)}$ is the Earth's geometric mean curvature radius.

3.3.5 Simplification of magnetometer measurement model

For the sake of analytical computability an untilted dipole model of the Earth's magnetic field is assumed in the analysis. According to the model magnetic field vector depends explicitly on latitude and height as

$$\mathbf{B}_{n,dip}(\boldsymbol{\lambda})=\begin{pmatrix}\dfrac{j\cos\phi}{(R+h)^3}\\ 0\\ \dfrac{2j\sin\phi}{(R+h)^3}\end{pmatrix}=\begin{pmatrix}B_{n1,dip}\\ 0\\ B_{n3,dip}\end{pmatrix}, \tag{3.79}$$

where j is a constant and R is the radius of the Earth. Corresponding potential takes the form $V=-j\sin\phi/(R+h)^2$. Jacobian matrix of $\mathbf{B}_{n,dip}(\boldsymbol{\lambda})$ is given by

$$\frac{\partial\mathbf{B}_{n,dip}(\boldsymbol{\lambda})}{\partial\boldsymbol{\lambda}^{\mathrm{T}}}=\begin{pmatrix}-\dfrac{j\sin\phi}{(R+h)^3} & 0 & -\dfrac{3j\cos\phi}{(R+h)^4}\\ 0 & 0 & 0\\ \dfrac{2j\cos\phi}{(R+h)^3} & 0 & -\dfrac{6j\sin\phi}{(R+h)^4}\end{pmatrix}. \tag{3.80}$$

Measurement matrix takes the form

$$\begin{aligned}\mathbf{H}_{\mathbf{B},dip} &= \frac{\partial \Delta \mathbf{y}_{magn}}{\partial \mathbf{x}^{\mathrm{T}}} = \\ &= \left(\frac{\partial \mathbf{B}_{n,dip}(\boldsymbol{\lambda})}{\partial \boldsymbol{\lambda}^{\mathrm{T}}} \quad \mathbf{0}_{3\times 3} \quad [\mathbf{B}_{n,dip}\times] \quad \mathbf{0}_{3\times 6} \quad -\mathbf{R}_{\tilde{n}b} \quad \mathbf{I}_{3\times 3} \right).\end{aligned} \tag{3.81}$$

3.3.6 Observable combinations

The following linear combinations of error states are observable at straight and leveled flight.

$$\begin{aligned}&\frac{j\sin\phi}{(h+R)^3}\cdot\delta\phi + \frac{3j\cos\phi}{(h+R)^4}\cdot\delta h + \frac{2j\sin\phi}{(h+R)^3}\cdot\psi_{n\tilde{n}2} + \cos\psi\cdot\delta B_{b1} - \sin\psi\cdot\delta B_{b2} - \delta B_{n1},\\ &\frac{2j\cos\phi}{(h+R)^3}\cdot\delta\phi - \frac{6j\sin\phi}{(h+R)^4}\cdot\delta h + \frac{j\cos\phi}{(h+R)^3}\cdot\psi_{n\tilde{n}2} - \delta B_{b3} + \delta B_{n3},\\ &\frac{ju\cos\psi\sin\phi}{(h+R)^5}\cdot\delta h - \frac{j\sin\phi}{(h+R)^4}\cdot\delta v_{n1} + \frac{3j\cos\phi}{(h+R)^4}\cdot\delta v_{n3} - \frac{2j\sin\phi}{(h+R)^3}\cdot\delta\omega_{n2},\\ &\sin\phi\cdot\psi_{n\tilde{n}1} - \frac{1}{2}\cos\phi\cdot\psi_{n\tilde{n}3} - \frac{(h+R)^3\sin\psi}{2j}\cdot\delta B_{b1} + \frac{(h+R)^3(1-\cos\psi)}{2j}\cdot\delta B_{n2},\\ &g\cdot\psi_{n\tilde{n}2} - \delta f_{n1},\ \ \delta f_{b3},\ \ \delta v_{n3},\\ &\sin\phi\cdot\delta\omega_{b1} - \frac{1}{2}\cos\psi\cos\phi\cdot\delta\omega_{b3},\ \sin\phi\cdot\delta\omega_{b2} + \frac{1}{2}\sin\psi\cos\phi\cdot\delta\omega_{b3}.\end{aligned} \tag{3.82}$$

Herein

$$\delta\mathbf{f}_n = \mathbf{R}_{nb}\delta\mathbf{f}_b = \left(\delta f_{n1} \quad \delta f_{n2} \quad \delta f_{n3}\right)^{\mathrm{T}}, \tag{3.83}$$

$$\delta\boldsymbol{\omega}_{ib}^{n} = \mathbf{R}_{nb}\delta\boldsymbol{\omega}_{ib} = \left(\delta\omega_{n1} \quad \delta\omega_{n2} \quad \delta\omega_{n3}\right)^{\mathrm{T}}. \tag{3.84}$$

Linear combinations of error states, listed below, become observable at steady turn.

$$\begin{aligned}&\cos\varphi\cdot\delta\phi - \frac{(h+R)^3\cos\phi}{2j}\cdot\delta B_{b3} - \frac{(h+R)^3\cos\varphi\sin\phi}{j}\cdot\delta B_{n1} + \frac{(h+R)^3\cos\varphi\cos\phi}{2j}\cdot\delta B_{n3},\\ &\cos\varphi\cdot\delta h + \frac{(h+R)^4\sin\phi}{6j}\cdot\delta B_{b3} - \frac{(h+R)^4\cos\varphi\cos\phi}{3j}\cdot\delta B_{n1} - \frac{(h+R)^4\cos\varphi\sin\phi}{6j}\cdot\delta B_{n3},\\ &\cos\varphi\cdot\delta v_{n1} + \frac{u(h+R)^3\sin\phi\cos\omega t}{6j}\cdot\delta B_{b3} - \frac{u(h+R)^3\cos\varphi\cos\phi\cos\omega t}{3j}\cdot\delta B_{n1} -\\ &-\frac{u(h+R)^3\cos\varphi\sin\phi\cos\omega t}{6j}\cdot\delta B_{n3},\end{aligned} \tag{3.85}$$

$$\delta v_{n3},\ \psi_{n\tilde{n}1},\ \psi_{n\tilde{n}2},\ \cos\phi\cdot\psi_{n\tilde{n}3}-\frac{(h+R)^3}{j}\cdot\delta B_{n2},$$

$$\cos\phi\cdot\delta f_{b1}+\frac{u^2(h+R)^3}{jr}\cdot\delta B_{n2},$$

$$\delta f_{b2}-\frac{u^2(h+R)^3\sin\phi}{6jr}\cdot\delta B_{b3}+\frac{u^2(h+R)^3\cos\varphi\cos\phi}{3jr}\cdot\delta B_{n1}+\frac{u^2(h+R)^3\cos\varphi\sin\phi}{6jr}\cdot\delta B_{n3},$$

$$\delta f_{b3}+\frac{u^2(h+R)^3\tan\varphi\sin\phi}{6jr}\cdot\delta B_{b3}-\frac{u^2(h+R)^3\sin\varphi\cos\phi}{3jr}\cdot\delta B_{n1}-\frac{u^2(h+R)^3\sin\varphi\sin\phi}{6jr}\cdot\delta B_{n3},$$

$$\delta\omega_{b1},\ \delta\omega_{b2},\ \delta\omega_{b3},\ \delta B_{b1},\ \cos\varphi\cdot\delta B_{b2}-\sin\varphi\cdot\delta B_{b3}.$$

g denotes gravitational acceleration; φ is bank angle; ψ is vehicle's heading; u is the first b-frame velocity component which is equal to absolute value of vehicle's velocity; r is radius of the turn and j is a dipole moment of the Earth's magnetic field. (3.82) shows that at straight and leveled flight magnetic field measurement allows to observe down velocity and down accelerometer errors. $\psi_{n\tilde{n}2}$ becomes observable in a combination with accelerometer errors. $\psi_{n\tilde{n}1}$ and $\psi_{n\tilde{n}3}$, in turn, appear coupled with each other, with longitudal magnetometer error, and with an error of the east component of magnetic field model. Thus, at straight and leveled flight aiding by magnetic field measurements cannot be considered sufficient for orientation determination. Additional aiding of attitude, by the means of leveling, for example, remains highly desirable. Moreover, in Polar Regions. i. e. where $\phi\approx\pm\pi/2$, coefficient in front of $\psi_{n\tilde{n}3}$ equals to zero, and thus heading error becomes completely unobservable.

At steady turn magnetic field measurement allows to observe down velocity error, attitude errors, gyroscope biases, two linear combinations of magnetometer biases, and several combinations of other error states. Heading error appears coupled with the error of the east component of magnetic field model. Consequently, high-fidelity magnetic field models shall be preferred for INS aiding, because otherwise estimate of heading may appear considerably biased. Similar to straight and leveled flight situation, heading error becomes completely unobservable at the North and the South magnetic poles.

Combinations (3.82) and (3.85) are summarized in Table 6. Rows of the table denote observable combinations, and columns denote components of the error state vector. Entries of the table indicate if error state appears in observable combination. Symbol "C" in a corresponding cell means that a coefficient in front of error state is constant, empty cell indicates that the error state is not present in the observable combination. Symbol "M" means that a coefficient in front of the error state depends explicitly on time.

3.3.7 Discussion

The analysis, presented above, shows that aiding by a sole magnetic field measurement can be efficient only if vehicle maneuvers frequently. Otherwise, in case intervals of cruise flight happen to be long, a one dimensional subspace of orientation error space remains unobservable, which causes orientation solution to degrade with time. This, in general, increases requirements to the accuracy of

inertial sensors. In order to avoid continuous degradation of orientation solution during cruise flight, additional orientation aiding shall be provided. This problem can be solved by either making use of air data, or by determining attitude by the means of accelerometers. The first approach shall be preferred since it appears highly robust to turbulence, disturbances, and maneuvering, while the second can appear in these cases problematic. The heading error always appears coupled with east component of magnetic model error. Consequently, usage of high-fidelity models of the Earth's magnetic field is of utmost importance, because otherwise a reference to the true heading can be determined only up to the level of uncertainty of magnetic model. Longitude error cannot be observed by the means of magnetic field and ADS measurements. Error of the east velocity component becomes observable solely due to ADS and always appears coupled with respective component of wind vector error. Magnetometer instrumental errors appear in several observable combinations both at cruise and dynamic flights. Provided that the vehicle maneuvers sufficiently, combined aiding by ADS and magnetometer shall allow to estimate them and to mitigate their effect on orientation solution.

Table 6–Observable combinations. Aiding by magnetometer.

	$\delta\phi$	$\delta\lambda$	δh	δv_{n1}	δv_{n2}	δv_{n3}	$\psi_{n\tilde{n}1}$	$\psi_{n\tilde{n}2}$	$\psi_{n\tilde{n}3}$	δf_{b1}	δf_{b2}	δf_{b3}	$\delta\omega_{b1}$	$\delta\omega_{b2}$	$\delta\omega_{b3}$	δB_{b1}	δB_{b2}	δB_{b3}	δB_{n1}^{dip}	δB_{n2}^{dip}	δB_{n3}^{dip}
Straight and leveled	C		C					C								C	C		C		
	C		C					C										C			C
			C	C										C							
						C															
							C		C							C				C	
								C		C											
												C									
													C		C						
														C	C						
Steady horizontal turn	C																	C	C		C
			C															C	C		C
				C														M	M		M
						C															
							C														
								C													
									C											C	
										C										C	
											C							C	C		C
												C						C	C		C
													C								
														C							
															C						
																C					
																	C	C			

3.4 Verification of observable combinations

The verification approach, suggested in the Section 3.1.4, was used to check correctness of analytical derivation of the observable combinations. System matrices (3.34) and (3.77) were used to compute the observability Gramian (3.6) and the test indicator (3.12). For all the observable combinations, presented in the Chapter 3, test indicator did not exceed 10^{-6}, which proves correctness of the results. Detailed example of the application of the verification approach can be found in Appendix E.

3.5 Demonstration of observability properties by simulation

In order to demonstrate how analytical analysis of observability is related to performance of the optimal navigation filter (Kalman filter), results of a simulation are demonstrated. For the sake of illustrativeness a class of tactical-grade inertial sensors was considered. Though, all the results are valid for lower-grade IMUs as well. Simulation environment, i. e. the reference trajectory, models of IMU errors and their magnitudes, models of wind, magnetic field disturbances, etc., are discussed in detail in Appendix D. Linearized error propagation is justified in Appendix F. Unlike in observability analysis, in the implementation of navigation filter wind velocity error was modeled as random walk process, and error of magnetic model was modeled as a first-order Gauss-Markov process, i. e.

$$\begin{aligned} \delta\dot{\mathbf{v}}_n^W &= \mathbf{v}_{\delta\mathbf{v}^W}, \\ \delta\dot{\mathbf{B}}_n^{WMM} &= -1/\tau_{\delta\mathbf{B}_n^{WMM}} \cdot \delta\mathbf{B}_n^{WMM} + \mathbf{v}_{\delta\mathbf{B}_n^{WMM}}. \end{aligned} \tag{3.86}$$

This was done for the sake of increasing statistical consistency of the filter and its robustness to *inaccurately modeled real-world effects*, such as wind and magnetic disturbances. Moreover, due to poor observability neither altimeter instrumental error, nor normal atmosphere offset were considered in the filter. The same assumption is made in all the simulations and experiments, presented throughout the thesis.

3.5.1 Aiding by ADS

Figures 8, 9 show standard deviation of position and the position error, respectively. Observation of velocity does not make position observable, which is why, aiding of INS by ADS can merely slow down the rate of gradual degradation of position accuracy. Vertical lines on the figures below mark the end of filter settling (approximately at 180 seconds), beginning of steady climb (approximately at 370 seconds), end of climb and beginning of steady turn (approximately at 800 seconds), end of steady turn (approximately at 830 seconds).

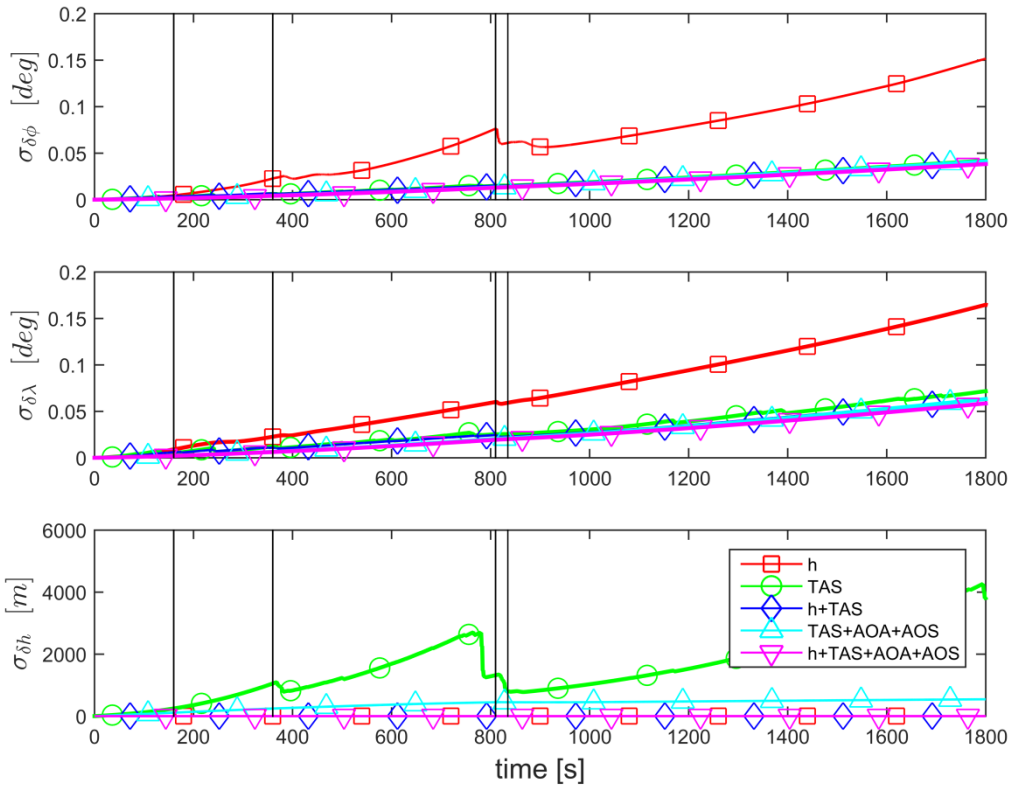

Fig. 8–Standard deviation of position

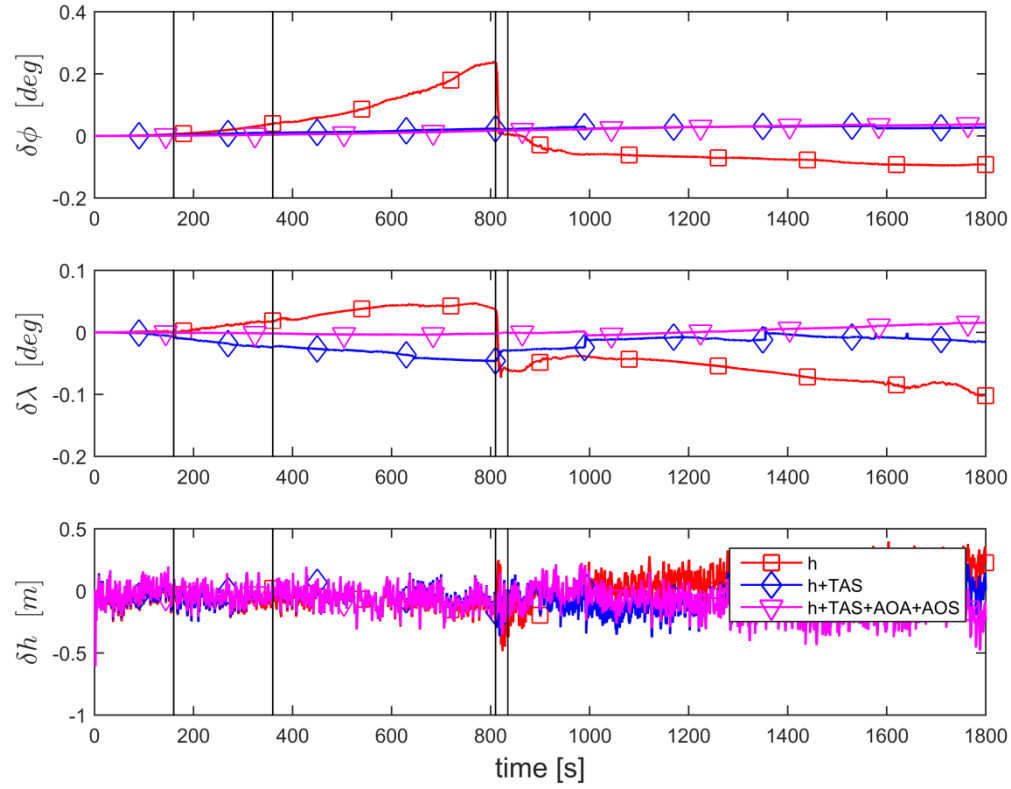

Fig. 9–Position error of the corrected total state

Figures 10, 11 show the standard deviation of velocity estimate and the velocity error, respectively. Despite instrumental errors of ADS are relatively small, variance of horizontal velocity remains large. This happens because ADS does not provide information on the speed relative to ground, but on the speed relative to the surrounding air mass. Therefore, velocity errors always appear in observable combinations coupled with errors of the wind speed, whose model is highly volatile and uncertain. Lack of an accurate model, in turn, does not allow to distinguish between the possible drift of the wind speed and the growth of the error of vehicle's velocity, which causes corresponding variances to remain large.

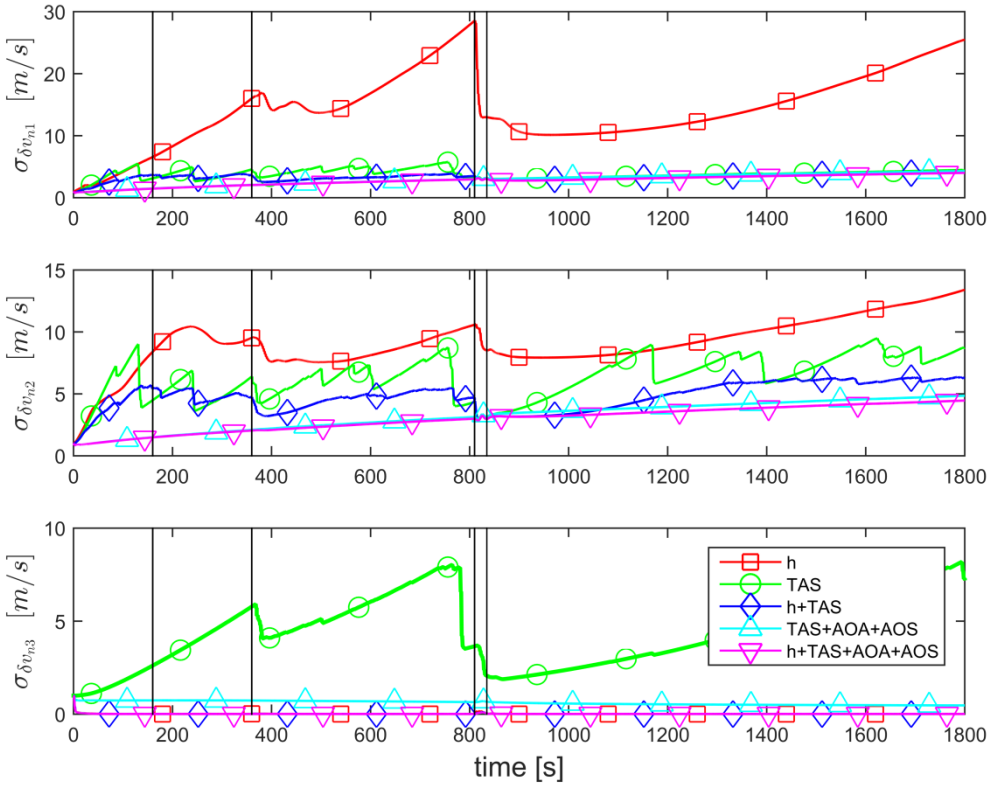

Fig. 10–Standard deviation of velocity

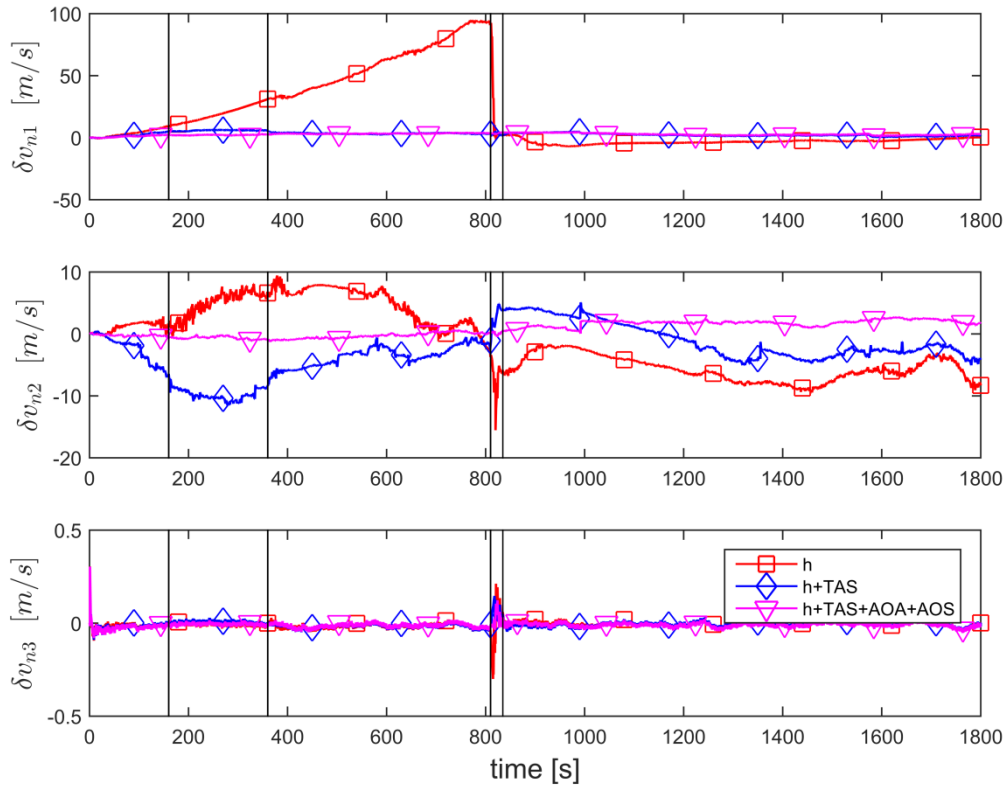

Fig. 11–Velocity error of the corrected total state

Figures 12, 13 show behavior of standard deviations of orientation errors and orientation errors of the corrected total state, respectively.

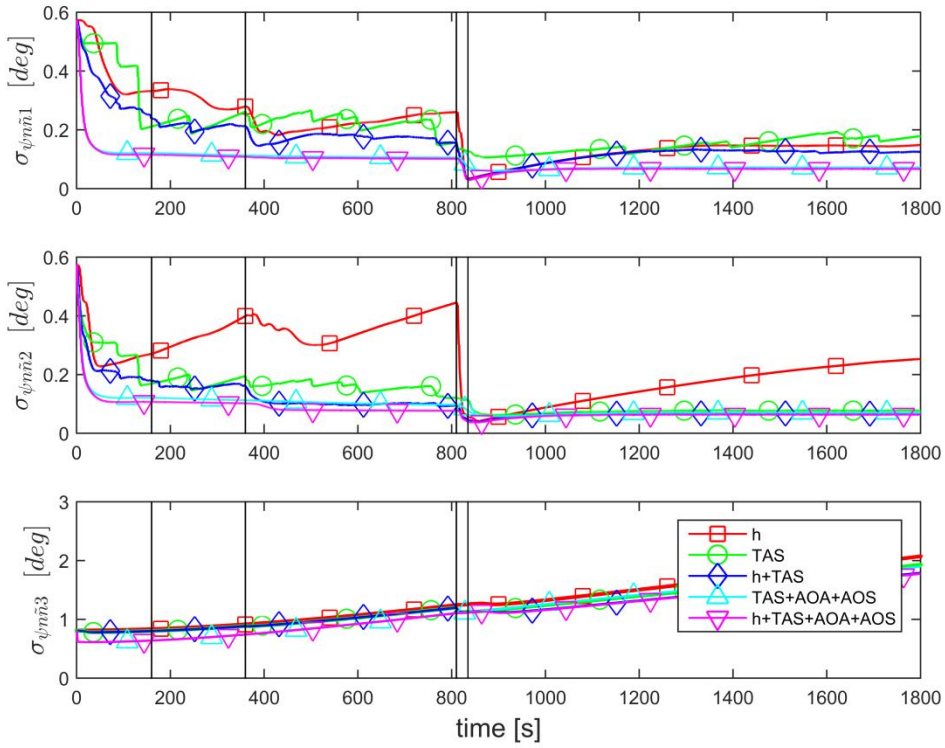

Fig. 12–Standard deviations of orientation errors

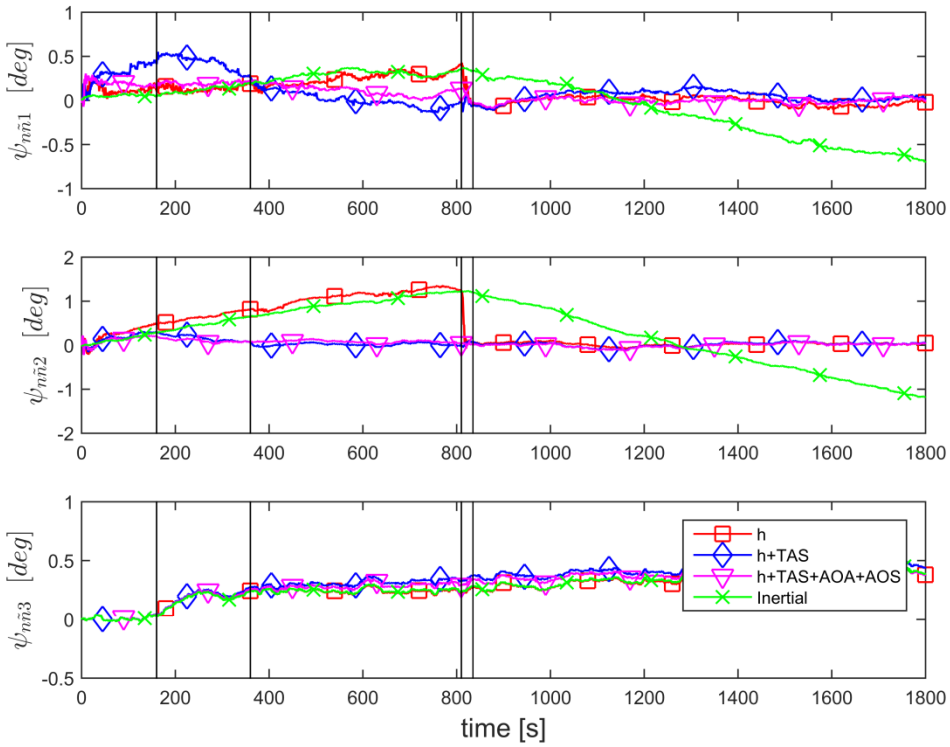

Fig. 13–Orientation errors of the corrected total state

Analytical observability analysis claims that information on attitude errors appears in barometric altitude measurement during turns. Accordingly, standard deviations of $\psi_{n\tilde{n}1}$ and $\psi_{n\tilde{n}2}$ are seen to drop steeply during the turn and grow monotonically at straight and leveled flight. The same holds also for TAS measurement. B-frame velocity w.r.t. wind was shown to make attitude errors observable in a combination with inertial sensor errors both at steady turn and at straight and leveled flight. In accordance with that standard deviations of $\psi_{n\tilde{n}1}$ and $\psi_{n\tilde{n}2}$ are seen to decrease throughout the flight whenever AOA, AOS, and TAS measurements are available simultaneously. None of considered measurements allows to observe heading error separately and thus $\sigma_{\psi_{n\tilde{n}3}}$ grows monotonically in all the cases.

Absolute values of attitude errors remain below 1.5 degrees for baro-aided INS and below 0.3 degrees for air data aided. It is seen that aiding of INS by ADS provides improved long-term performance compared to pure inertial mode.

Figures 14, 15 show standard deviations of accelerometer biases and their estimates, respectively.

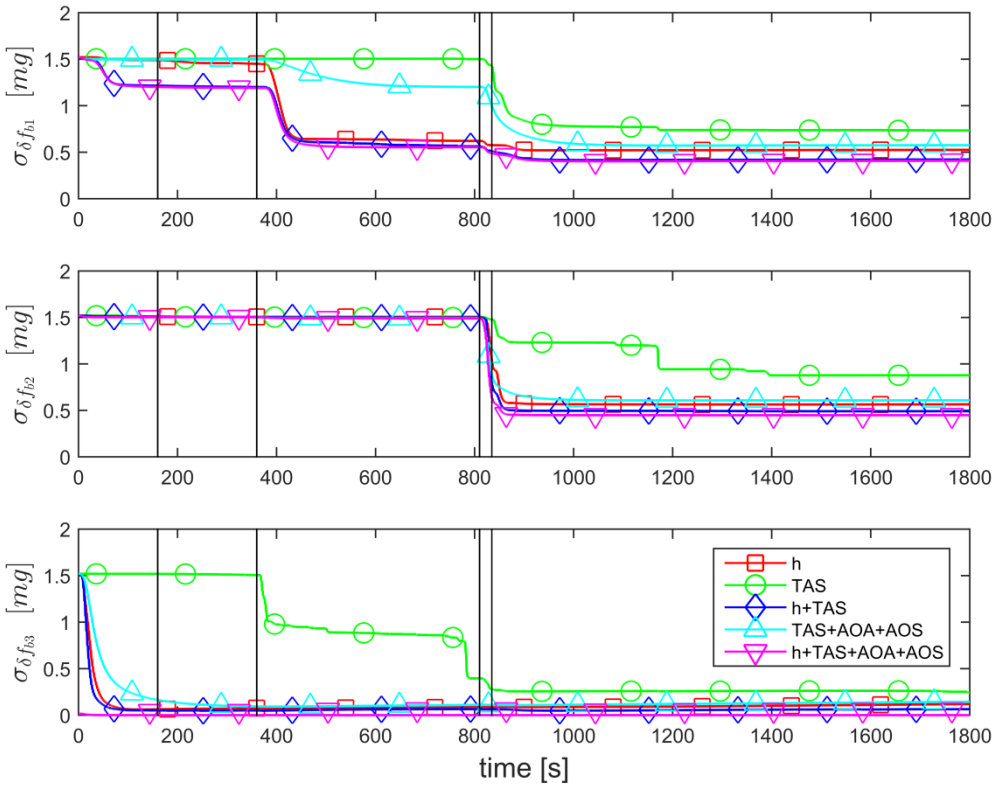

Fig. 14–Standard deviations of accelerometer biases

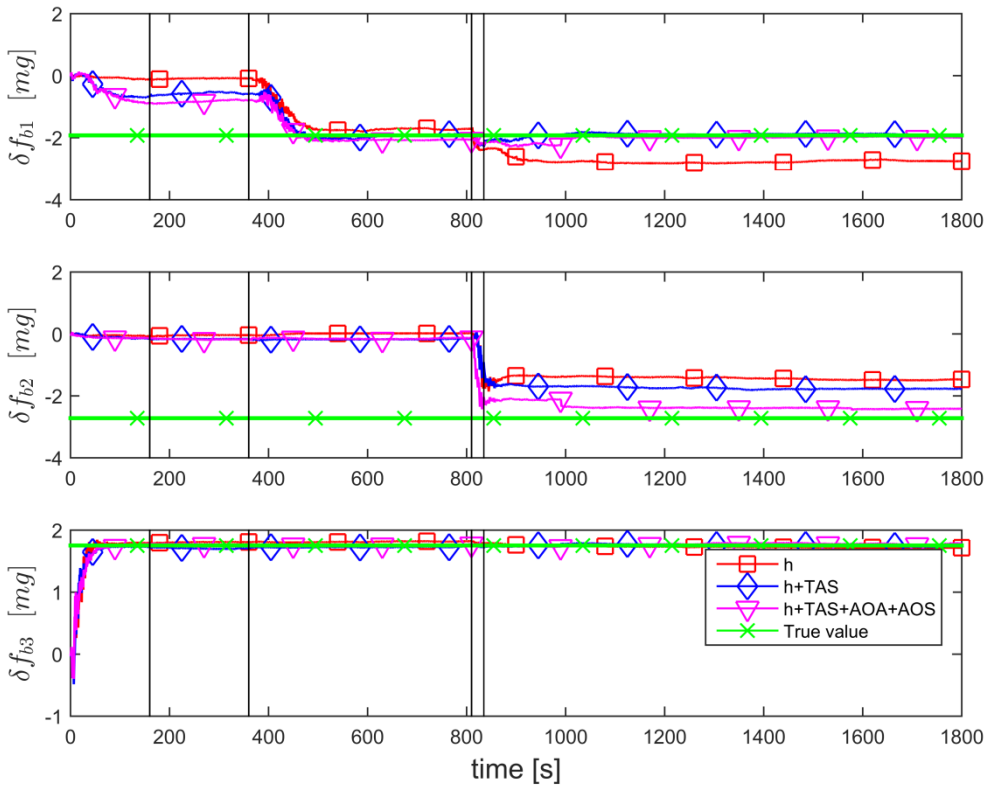

Fig. 15–Estimates of accelerometer biases

Down accelerometer error is observable at straight and leveled flight if system is aided by either barometric altimeter or by a complete ADS, i.e. by TAS, AOA, and AOS. Accordingly, Figure 14 shows down accelerometer error standard deviation decreasing monotonically whenever these measurements are present. Longitudal accelerometer error becomes observable in a combination with down accelerometer error at steady climb. Corresponding standard deviation is seen to drop when vehicle starts climbing after flying straight and leveled. Lateral accelerometer error appears in observable combinations (3.39), (3.46), (3.49), and (3.51). Consequently, Figure 14 shows its standard deviation dropping after a turn in all the aided cases except for TAS only.

Figures 16, 17 show standard deviations of gyroscope biases and their estimates, respectively.

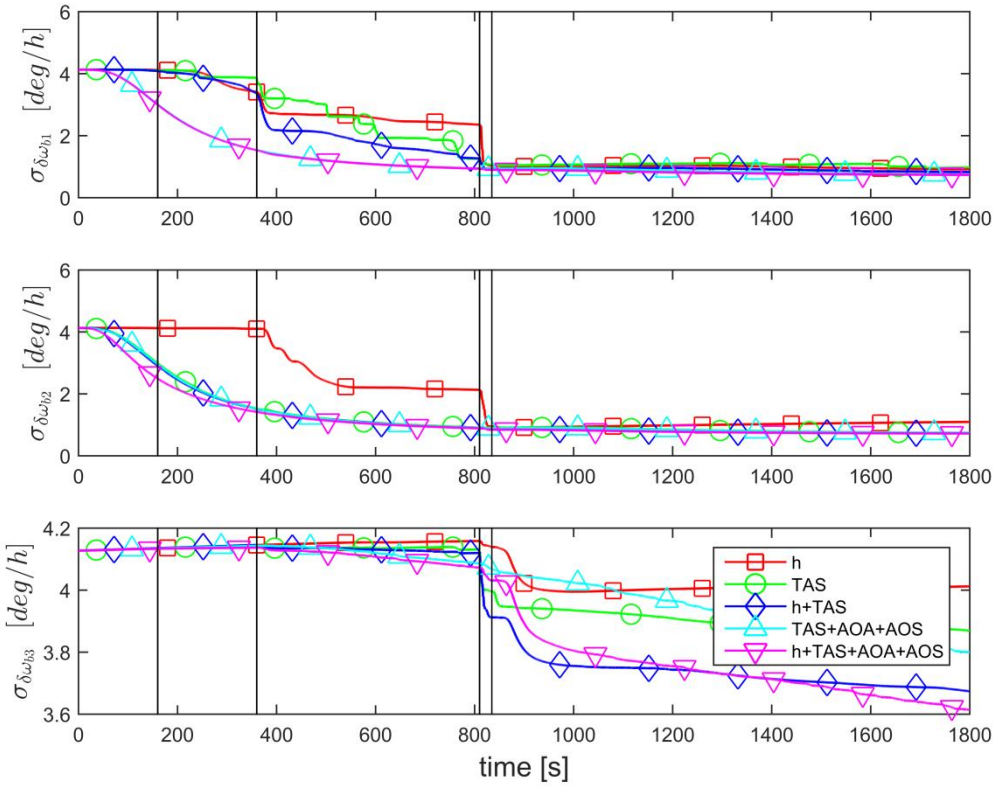

Fig. 16–Standard deviations of the biases of gyroscopes

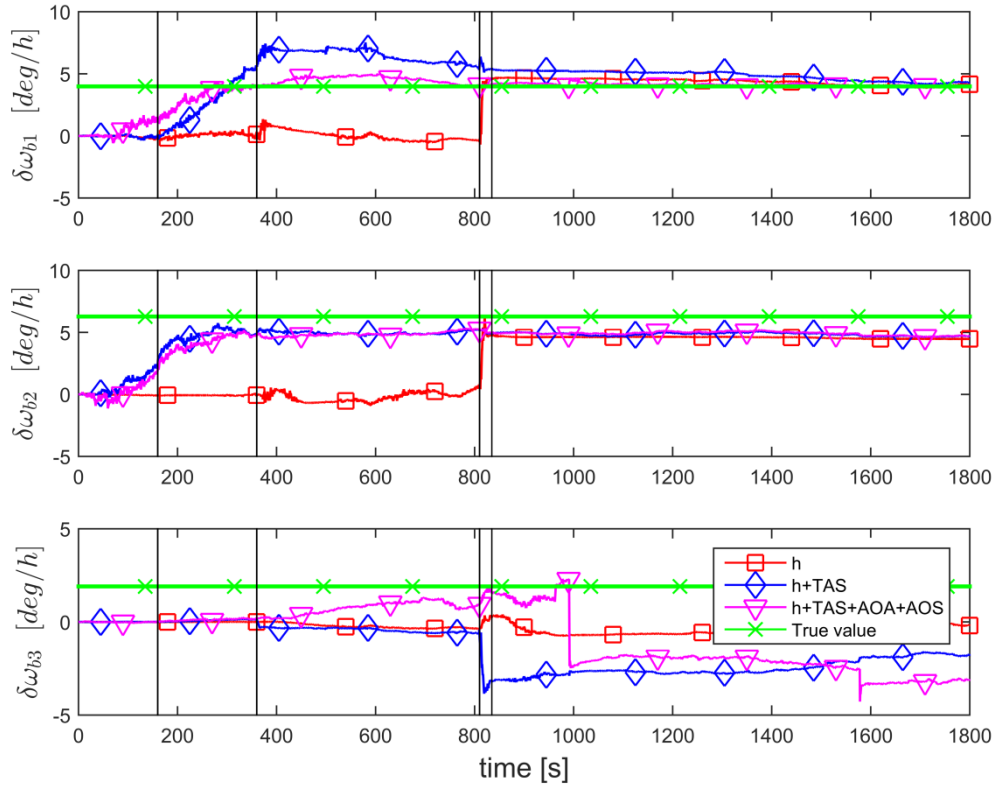

Fig. 17–Estimates of gyroscope biases

Lateral gyroscope error becomes observable due to TAS measurement. Accordingly, on the Figure 16 the corresponding standard deviation is seen to decrease monotonically throughout the flight in all the aided modes except for altimeter-only. Down gyroscope error appears observable in a linear combination with other inertial sensor errors at steady turn. However, the coefficient in front of it is small compared to coefficients in front of other sensor errors in the combinations. Thus, $\delta\omega_{b3}$ has a small "weight" in observable combinations, i. e. is weakly observable, and its standard deviation remains just slightly influenced in considered aiding modes. Longitudal gyroscope error becomes observable if all the three ADS measurements are available. In this case $\sigma_{\delta\omega_{b1}}$ is seen to decrease monotonically throughout the flight.

Estimates of inertial sensor errors are statistically consistent and converge to their true values provided that vehicle performs the discussed maneuvers.

3.5.2 Aiding by magnetometer

Figures 18–24 show the results of a simulation of an INS aided by magnetic field measurement. Estimates of the position, velocity, and orientation errors were fed back to the strapdown navigation solution. Thus, Figures 18–20 show the final errors of the navigation solution, i. e. errors of the corrected total state. Figures 21–24, in turn, show the estimates of corresponding errors.

Overall, aiding by solely the measurement of the Earth's magnetic field does not appear highly beneficial. However, the rate of divergence of position standard deviation is seen to be smaller than in unaided mode. Moreover, standard deviation of the height error $\sigma_{\delta h}$ and the height error δh itself experience stabilization. Such a behavior can be explained by observability of down accelerometer error δf_{b3}, down velocity error δv_{n3}, and several other linear combinations of error states, in which height error is present (see equations (3.82), (3.85)).

Orientation errors $\psi_{n\tilde{n}1}$ and $\psi_{n\tilde{n}3}$ remain coupled at straight and leveled flight and appear independently observable during steady turn. Accordingly, their variances are seen to grow before the vehicle turns and to decay after the maneuver has been accomplished. At straight and leveled flight "pitch" error $\psi_{n\tilde{n}2}$ is observable in a combination with accelerometer errors. This causes its variance to converge to a steady state value, which can further be improved if vehicle maneuvers.

Biases of lateral and longitudal accelerometers, δf_{b1} and δf_{b2}, become observable during steady turn in a combination with magnetometer instrumental errors and errors of the magnetic model (see (3.82), (3.85)). Since uncertainty of the magnetic model errors remains large, such a coupling shall not allow to improve the knowledge of δf_{b1} and δf_{b2}. Accordingly, their variances are seen to remain almost constant. Down accelerometer error δf_{b3} is observable both at straight and leveled flight and during maneuvering. That is why the estimate of δf_{b3} is seen to converge to its true value.

Biases of gyroscopes become observable independently of other error states during a steady turn (see (3.85)), and two more linear combinations of them are observable at straight and leveled flight (see (3.82)). Consequently, occasional changes in vehicle's dynamics are supposed to allow to estimate them, which is, indeed, fulfilled by the filter (see Figure 22).

Bias of the longitudal magnetometer δB_{b1} is observable independently during a turn, but the biases of the two remaining magnetometers, δB_{b2} and δB_{b3} remain coupled (see (3.85)). Consequently, high dynamics and several turns with a different bank angle φ are required to calibrate them. Accordingly, on the Figure 23, corresponding estimates and variances remain constant during straight and leveled flight and drop during the turn.

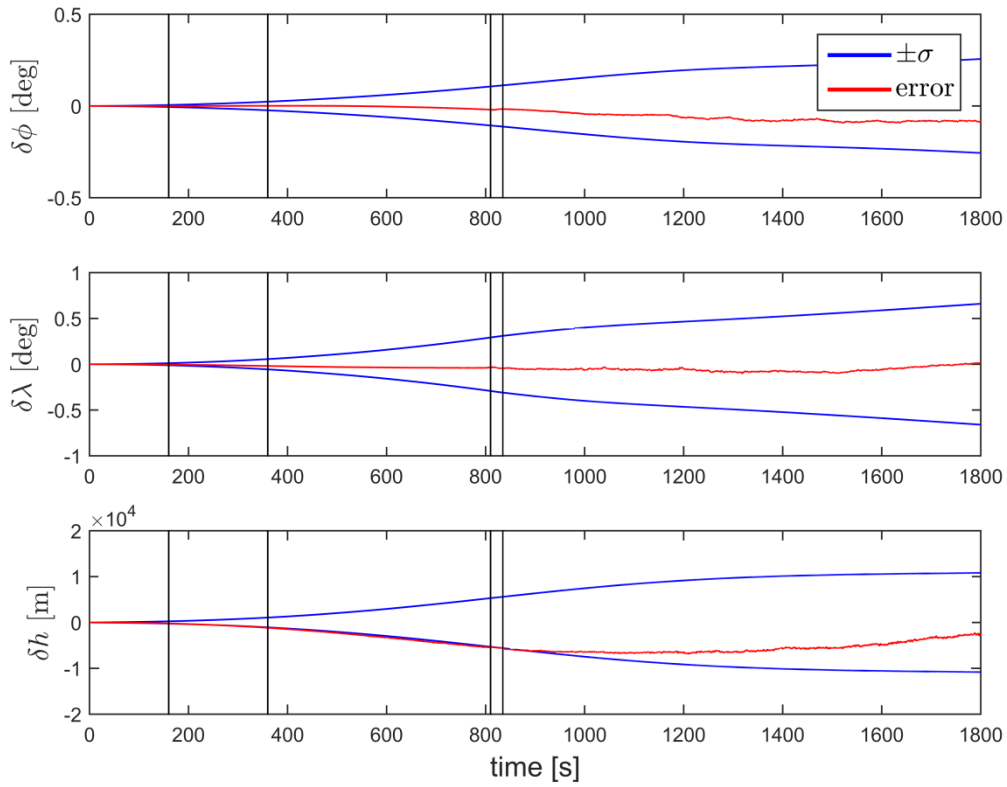

Fig. 18–Position error of the corrected total state

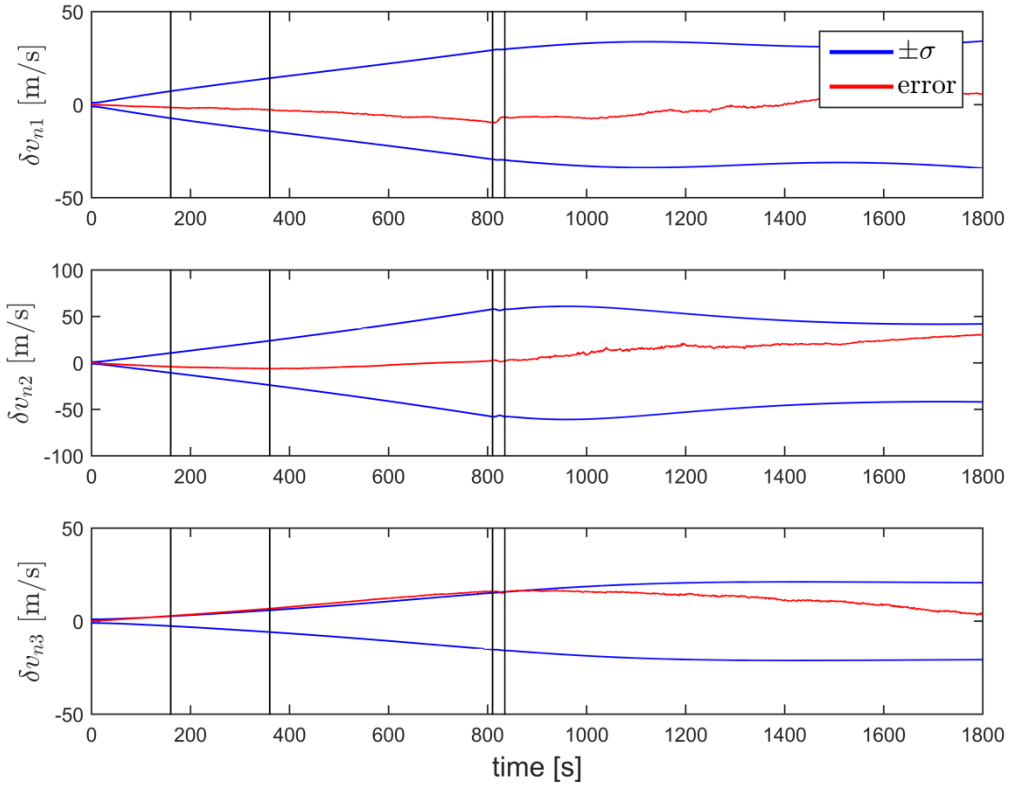

Fig. 19–Velocity error of the corrected total state

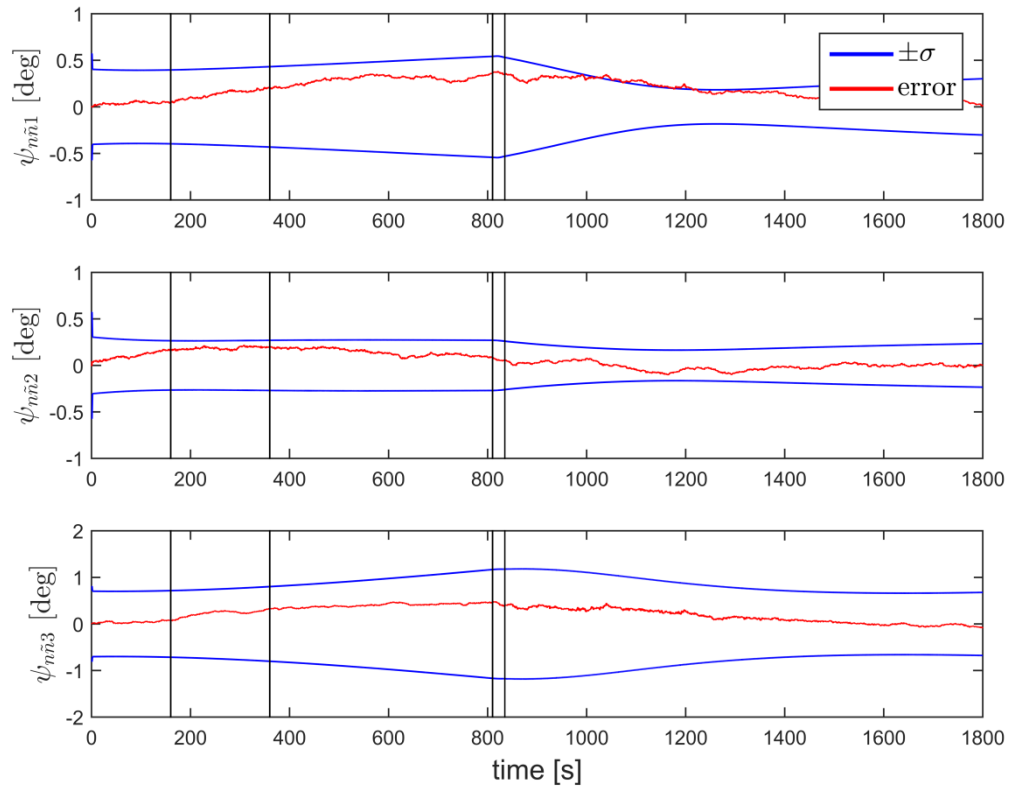

Fig. 20–Orientation error of the corrected total state

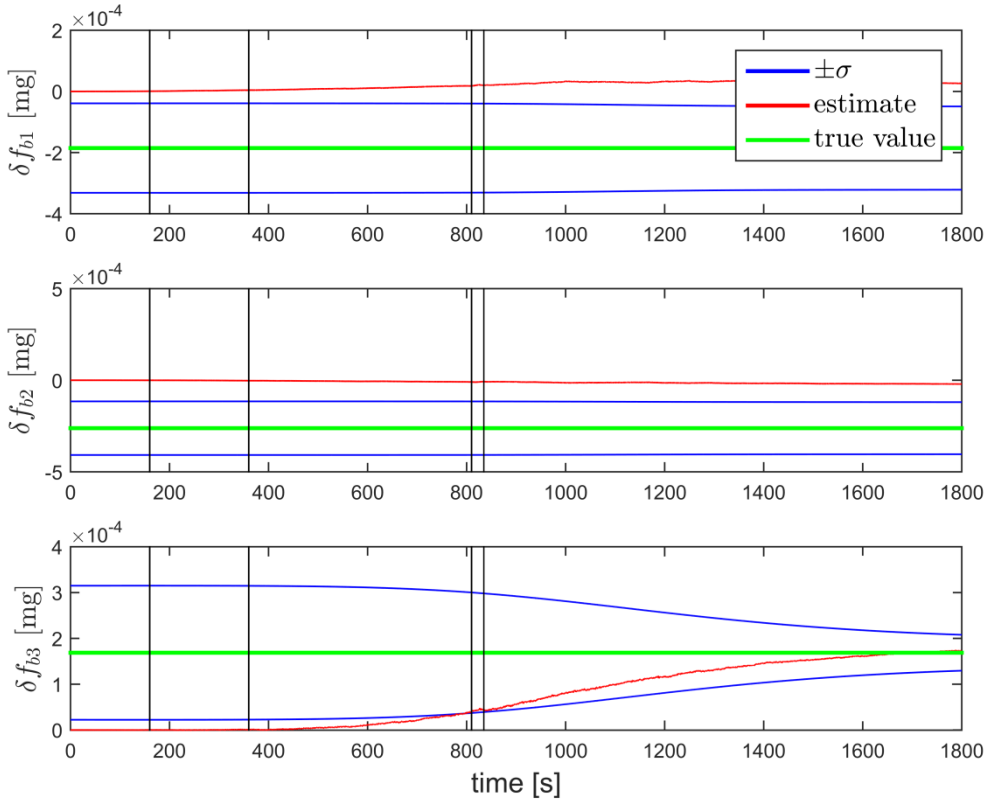

Fig. 21–Estimates of accelerometer biases

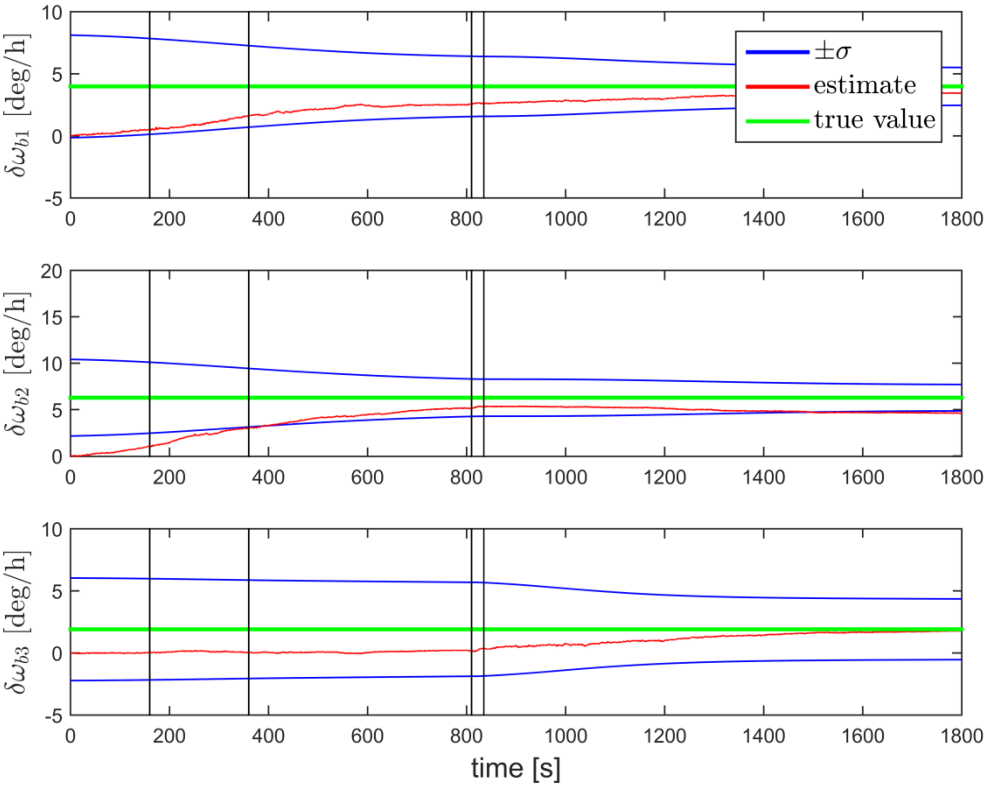

Fig. 22–Estimate of biases of the gyroscopes

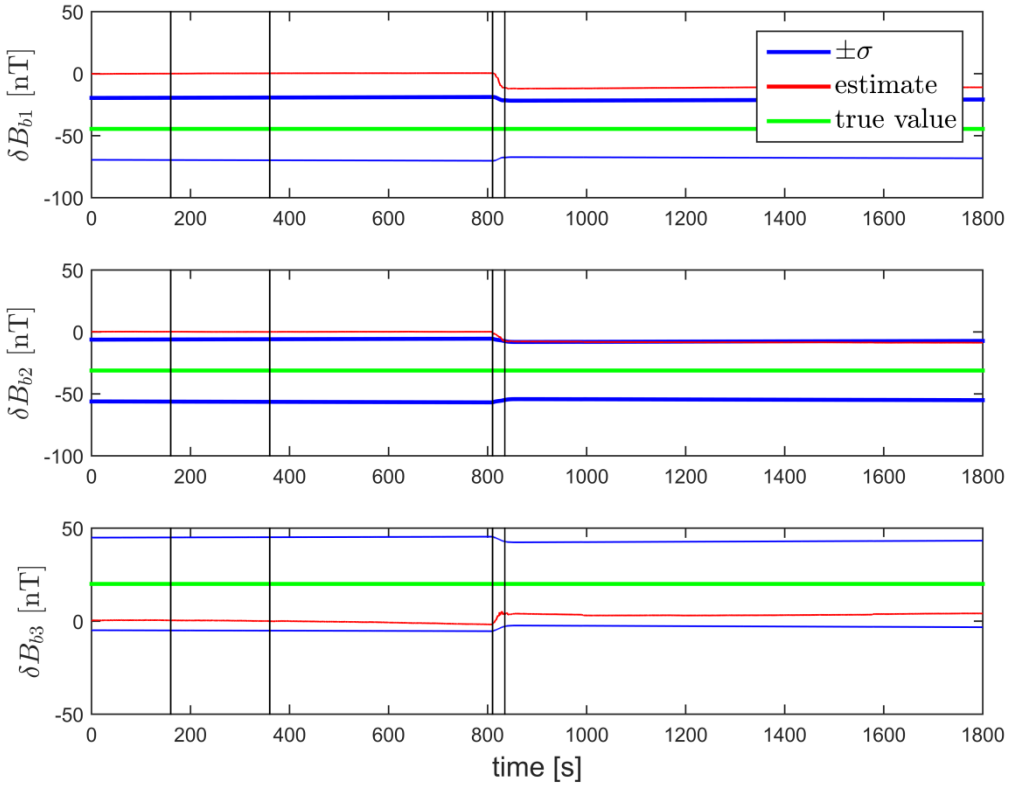

Fig. 23–Estimates of biases of the magnetometer

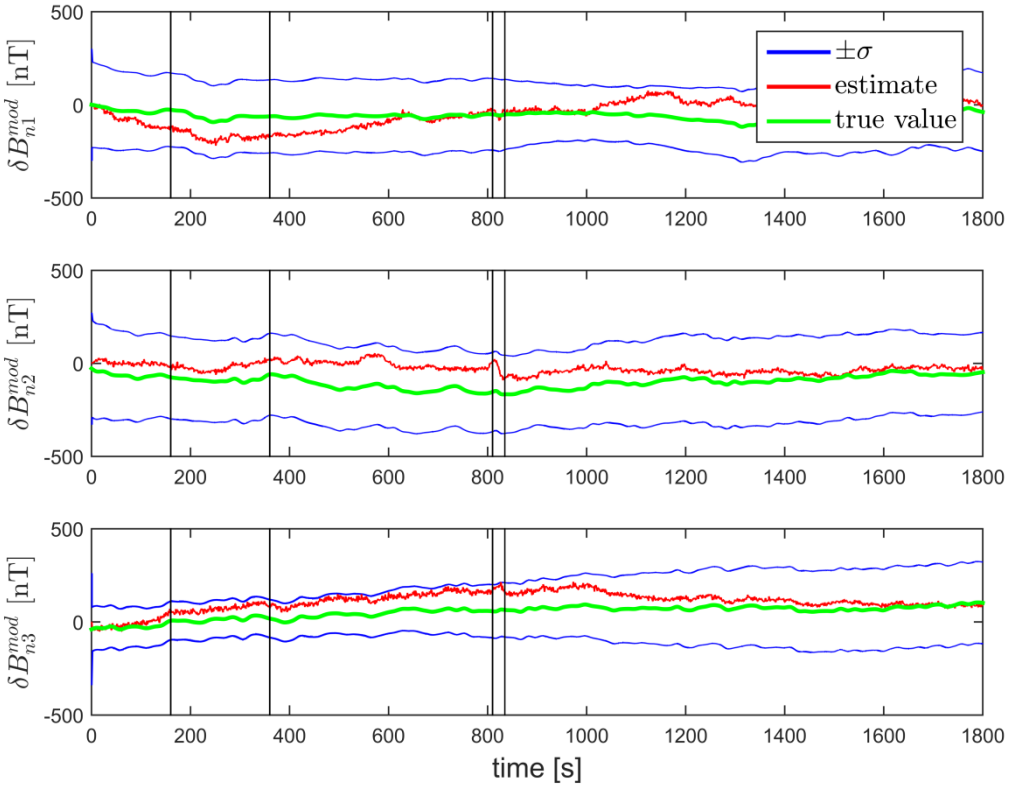

Fig. 24–Estimate of the error of magnetic model

3.6 Conclusions

Simulation results and observability analysis, presented above, suggest that considered aiding sources are highly beneficial for correction of INS. Besides INS and sensor errors, related to vertical channel, barometric altimeter allows to estimate attitude errors and accelerometer biases if platform performs maneuvers (see Table 1). The maneuvers that are required to estimate these errors do not appear to be specific and are always performed by an arbitrary aircraft, e. g. during take-off. Moreover, if INS is aided both by barometric altitude and airspeed, maneuvering, in addition, allows to estimate longitudal and lateral gyroscope biases (see Table 3). This improves propagation of attitude error during the following cruise flight and reduces significantly error growth rate. Aiding of INS by barometric altitude and a complete set of ADS measurements, namely by TAS, AOA, and AOS, allows, in turn, to observe and estimate attitude errors and lateral and longitudal gyroscope errors both at cruise and dynamic flights (see Table 5). This fact appears to be very promising because it states a continuous maneuver-independent availability of attitude aiding. This allows to relax significantly sensor accuracy requirements in AHRS applications without loss of performance.

Originally, AD-AHRS used fixed-gain filtering loops, tuned for cruise flight situation, and, consequently, its performance cannot be optimal at dynamic flight. In contrast, if vehicle maneuvers, optimal gain filtering was shown to improve its performance, which cannot be guaranteed otherwise.

The analytical analysis and simulation results, presented above, encourage to legitimate the following fields of application for air data aided INS:

1. A back-up autonomous navigation system in case of GNSS signal loss or spoofing,
2. Primary attitude and heading reference system.

In case air-data system is meant to be used as primary AHRS, two designs can be reasonable dependent on the platform type. Frequently maneuvering platforms, like, for example, short-range general aviation aircrafts and gliders, or platforms that can afford to perform maneuvers in order to increase navigational performance, like, for example, unmanned aerial vehicles, may feature only a pitot-static system and aid the INS by height and TAS measurements only. Platforms, whose usual flight path features long intervals of cruise flight, shall in turn, feature a complete ADS in order to preserve high performance and robustness.

Nevertheless, integration of INS and ADS does not solve the problem of orientation determination completely, because the third component of orientation error, $\psi_{n\tilde{n}3}$, which corresponds to the error of heading at straight and leveled flight situation, does not appear sufficiently observable. In general this problem can be solved either by making use of more accurate inertial sensors and operating unaided, or by integrating a magnetometer into the system. The conducted analysis of the magnetometer measurement showed that besides information on heading, it could provide information on other navigation error states and even on the errors of magnetic model. In fact, dimension of a subspace observed due to magnetometer appears larger, than dimension of a subspace observed in case of aiding by the measurement of b-frame velocity w.r.t. wind. Such good observability properties show the need

to model magnetic measurements properly and to consider errors of both magnetic model and magnetometer itself in the navigation filter. This shall allow to considerably mitigate an impact of magnetic disturbances on the navigation solution and to improve estimates of attitude errors, heading error, biases of the gyroscopes, and magnetometer instrumental errors.

When INS is aided both by ADS and magnetometer, most or the navigation error states appear observable. Unobservable, or insufficiently observable, remain only the latitude error $\delta\lambda$, error of the east velocity component δv_{n2}, some linear combinations of wind velocity errors $\delta\mathbf{v}_n^W$, and the error of the east component of magnetic model δB_{n2}^{mod}.

The revealed observability properties of an INS integrated with ADS and magnetometer demonstrate that such a design is highly promising in the applications that require high levels of performance and robustness. Though, in order to exploit all the available information, hidden in the measurements, the integrated navigation system needs to run an optimal filter of increased dimensionality, i. e. the filter that is augmented with wind errors, errors of the magnetic model, and magnetometer instrumental errors. This, for sure, leads to an increase of computational burden.

Achievable performance of ADS/Magnetometer aided INS is further discussed in Chapter 4.

4 Alternative AHRS mechanizations

There exists a wide range of applications, which cannot operate without information on orientation of some object or vehicle. The most well-known examples are civil and military aviation [41-44], quadrocopters and other UAVs [45-49], missiles, robotics [50], analysis of human motion [51-53]. All these applications differ strongly from each other and thus experience diverse size, payload, and cost limitations. For example, commercial airline and military aircrafts, whose cost amounts to tens of millions of dollars, can easily make use of high-quality inertial navigation systems, featuring highly accurate ring laser gyroscopes and quartz accelerometers [54]. Such navigation systems can provide the user with up to several hundredth of a degree accurate orientation, and better than 1 nautical mile per hour position drift rate. Though, cost of such a system can reach 100 thousand dollars, and thus it is, obviously, not an option for a general aviation aircraft, whose total price usually varies from 200 thousands to one million. RLG-based INS is, as well, not an option for most of the drones and especially quadrocopters, because its size, weight, and power (SWaP) do not allow it to be installed on board. Moreover, all the applications have different performance requirements and certification rules. For example, orientation accuracy requirements in quadrocopter and human motion analysis applications are much lower than in civil aviation. Therefore, system designers face from the beginning a problem of choosing a suitable AHRS/navigation solution, capable of satisfying very particular application requirements and guaranteeing safe and efficient operation of the system. The current chapter will consider and compare several architectures of an AHRS/back-up navigation system, which can be reasonable dependent on application. GNSS aided INS is not considered in the work, because on the one hand the field appears by now very well studied [55, 56], and on the other hand GNSS information does not present a robust platform-autonomous measurement, which puts it out of the scope of this study. However, such an option shall also be kept in mind.

4.1 IMU + Magnetometer

Classical books on integrated navigation [1, 2] suggest AHRS algorithms, whose core idea consists in using accelerometers for attitude determination and correction at the moments when vehicle's motion can approximately be considered unaccelerated. Provided that attitude estimate is accurate enough, a measurement from three-axis magnetometer can then be used to compute magnetic heading and to slave heading estimate computed by INS. This approach is very well known and its modifications are widely used in various low-cost applications [57-59]. Such a design appears very attractive, as it does not require complicated data fusion. However, accuracy of both attitude and heading estimates degrades dramatically if vehicle moves dynamically during a relatively long period of time [3].

Below we recapitulate the described approach and highlight possible improvements that follow immediately from observability analysis presented above. 1st order ordinary differential equation for rotation matrix (or equaivalent equation for quaternion)

$$\dot{\mathbf{R}}_{\tilde{n}b} = \mathbf{R}_{\tilde{n}b}\tilde{\boldsymbol{\Omega}}_{ib} - \underline{\tilde{\boldsymbol{\Omega}}^{n}_{ie}\mathbf{R}_{\tilde{n}b}} \tag{4.1}$$

is integrated given measurement of angular rates. The Earth's rotation rate can optionally be compensated for provided that initial position is at least approximately known and that the mission is carried out within a short distance from starting point. Note, that consideration of the Earth's rotation rate can be optional in case aiding is almost continuously available, however, neglecting it in unaided mode causes a systematic orientation error growth rate of up to 15 degrees per hour. Thus, compensation of the Earth's rotation rate appears highly desirable for high-quality industrial-grade and higher class inertial systems. From here on underlined terms denote parts of equations that can optionally be considered if an initial estimate of position is available and the system is intended to be operated within a short range from initial location.

Error state propagation equations are given by

$$\begin{aligned} &\dot{\psi}_{n\tilde{n}} = \underline{-\tilde{\boldsymbol{\Omega}}^{n}_{ie}\left(\tilde{\boldsymbol{\lambda}}\right)\cdot\psi_{n\tilde{n}}} + \mathbf{R}_{\tilde{n}b}\cdot\delta\boldsymbol{\omega}_{ib}, \\ &\delta\dot{\mathbf{f}}_{b} = \mathbf{0},\ \delta\dot{\boldsymbol{\omega}}_{ib} = \mathbf{0}. \end{aligned} \tag{4.2}$$

Consideration of the Earth's rotation in orientation error propagation is not important in case of industrial-grade systems, because contribution of sensor errors appears dominating. In case of tactical-grade systems contribution of the Earth's rotation becomes considerable, and in case of navigation-grade systems, crucial.

Provided that vehicle is not accelerating, accelerometers can be used to aid orientation. Assuming in (2.9) $\dot{\mathbf{v}}_{n} = 0$ and neglecting a cross product yields

$$\mathbf{R}_{nb}\mathbf{f}_{b} + \boldsymbol{\gamma}_{n} \approx 0 \Leftrightarrow \mathbf{R}_{nb}\mathbf{f}_{b} \approx -\boldsymbol{\gamma}_{n}. \tag{4.3}$$

Consequently, residual can be formed as

$$\Delta\mathbf{y}_{g} = (-\boldsymbol{\gamma}_{n}) - \mathbf{R}_{\tilde{n}b}\tilde{\mathbf{f}}_{b} \tag{4.4}$$

and thus linearized measurement equation takes the form

$$\begin{aligned} \Delta\mathbf{y}_{g} &= (-\boldsymbol{\gamma}_{n}) - \mathbf{R}_{\tilde{n}b}\tilde{\mathbf{f}}_{b} = -\boldsymbol{\gamma}_{n} - \mathbf{R}_{\tilde{n}b}\left(\mathbf{f}_{b} - \delta\mathbf{f}_{b}\right) = \\ &= -\boldsymbol{\gamma}_{n} - \mathbf{R}_{\tilde{n}b}\left(-\boldsymbol{\gamma}_{b} - \delta\mathbf{f}_{b}\right) \approx \\ &\approx -\boldsymbol{\gamma}_{n} + \left(\mathbf{I} - [\psi_{n\tilde{n}}\times]\right)\mathbf{R}_{nb}\boldsymbol{\gamma}_{b} + \mathbf{R}_{\tilde{n}b}\delta\mathbf{f}_{b} = \\ &= -\boldsymbol{\gamma}_{n} + \left(\mathbf{I} - [\psi_{n\tilde{n}}\times]\right)\boldsymbol{\gamma}_{n} + \mathbf{R}_{\tilde{n}b}\delta\mathbf{f}_{b} = \\ &= [\boldsymbol{\gamma}_{n}\times]\cdot\psi_{n\tilde{n}} + \mathbf{R}_{\tilde{n}b}\delta\mathbf{f}_{b}. \end{aligned} \tag{4.5}$$

Herein $\boldsymbol{\gamma}_{n} = \boldsymbol{\gamma}_{n}(\boldsymbol{\lambda}) = \begin{pmatrix} 0 & 0 & \gamma_{n3} \end{pmatrix}^{\mathrm{T}}$.

[2] suggests the following conditions to check for validity of (4.3):

1. $\left|\left\|\tilde{\mathbf{f}}_b\right\| - \gamma_{n3}\right| < T_1$,
2. $\left\|\tilde{\boldsymbol{\omega}}_{ib}\right\| < T_2$,
3. $lowpass(\left|\left\|\tilde{\mathbf{f}}_b\right\| - \gamma_{n3}\right|) < T_3$.

Threshold values T_1, T_2, and T_3 shall be chosen dependent on specification of the inertial measurement unit being used.

Provided that information on initial position is available and that only local missions are considered, magnetic field vector can be used for aiding. Neglecting instrumental errors of the magnetometer, measurement equation (3.71) simplifies to

$$\Delta\mathbf{y}_{magn} = [\tilde{\mathbf{B}}_n^{WMM}\times]\cdot\psi_{n\tilde{n}} + \delta\mathbf{B}_n^{WMM} - \mathbf{R}_{nb}\mathbf{v}_{\mathbf{B}}. \tag{4.6}$$

In case estimate of initial position is unavailable or the system needs to be operated far away from the point of start, magnetic slaving and measurement equation (3.74) shall be used instead. Note that using magnetic field vector along with high-fidelity magnetic model for aiding of AHRS improves orientation accuracy and makes the system less vulnerable to dynamic maneuvering.

4.2 IMU + Magnetometer + Barometric altimeter

In the previous chapter it was demonstrated that aiding by barometric altitude allowed to improve considerably orientation accuracy if vehicle performed steady turns. Therefore usage of information on altitude for AHRS correction can appear highly beneficial in various applications. Total state navigation equations (4.1) in this case need to be completed by equations of vertical channel, which yields

$$\begin{aligned}
&\dot{\tilde{h}} = -\tilde{v}_{n3},\\
&\dot{\tilde{v}}_{n3} = R_{\tilde{n}b}^{31}\cdot\tilde{f}_{b1} + R_{\tilde{n}b}^{32}\cdot\tilde{f}_{b2} + R_{\tilde{n}b}^{33}\cdot\tilde{f}_{b3} + \tilde{\gamma}_{n3},\\
&\dot{\mathbf{R}}_{\tilde{n}b} = \mathbf{R}_{\tilde{n}b}\tilde{\boldsymbol{\Omega}}_{ib} - \underline{\tilde{\boldsymbol{\Omega}}_{ie}^{n}\mathbf{R}_{\tilde{n}b}}.
\end{aligned} \tag{4.7}$$

Then error state propagation equations take the form

$$\begin{aligned}
&\delta\dot{h} = -\delta v_{n3},\\
&\delta\dot{v}_{n3} = \tilde{f}_{\tilde{n}2}\cdot\psi_{n\tilde{n}1} - \tilde{f}_{\tilde{n}1}\cdot\psi_{n\tilde{n}2} + R_{\tilde{n}b}^{31}\cdot\delta f_{b1} + R_{\tilde{n}b}^{32}\cdot\delta f_{b2} + R_{\tilde{n}b}^{33}\cdot\delta f_{b3},\\
&\dot{\psi}_{n\tilde{n}} = \underline{-\tilde{\boldsymbol{\Omega}}_{ie}^{n}\left(\tilde{\boldsymbol{\lambda}}\right)\cdot\psi_{n\tilde{n}}} + \mathbf{R}_{\tilde{n}b}\cdot\delta\boldsymbol{\omega}_{ib},\\
&\delta\dot{\mathbf{f}}_b = \mathbf{0},\ \delta\dot{\boldsymbol{\omega}}_{ib} = \mathbf{0}.
\end{aligned} \tag{4.8}$$

As aiding by barometric altitude allows to estimate attitude errors during maneuvering only, accelerometers still need to be used to correct attitude errors during cruise flight. Though, if an application is highly dynamic or inertial sensors are accurate enough to maintain AHRS performance between maneuvers, corrections of this type may be omitted. When AHRS is aided by barometric altitude and at the same time accelerometers are used to correct attitude, n-frame vector of small

acceleration $\delta\mathbf{a}_n$ needs to be considered as an error state in order to preserve all the benefits that aiding by altitude suggests. Consideration of $\delta\mathbf{a}_{\tilde{n}}$ transforms measurement equation (4.5) to the form

$$\Delta\mathbf{y}_g = [\boldsymbol{\gamma}_n\times]\cdot\psi_{n\tilde{n}} + \mathbf{R}_{\tilde{n}b}\delta\mathbf{f}_b + \delta\mathbf{a}_{\tilde{n}}. \tag{4.9}$$

$\delta\mathbf{a}_n$ can be modeled as a first order Gauss-Markov process, namely

$$\delta\dot{\mathbf{a}}_{\tilde{n}} = -1/\tau_{\delta a}\delta\mathbf{a}_{\tilde{n}} + \mathbf{v}_{\delta a}. \tag{4.10}$$

Magnetometer measurement equation (3.71), in turn, is simplified to

$$\Delta\mathbf{y}_{magn} = \underline{\left.\frac{\partial\mathbf{B}_n^{WMM}(\boldsymbol{\lambda})}{\partial h}\right|_{\boldsymbol{\lambda}=\tilde{\boldsymbol{\lambda}}}\cdot\delta h} + [\tilde{\mathbf{B}}_n^{WMM}\times]\cdot\psi_{n\tilde{n}} - \mathbf{R}_{\tilde{n}b}\delta\mathbf{B}_b + \delta\mathbf{B}_n^{WMM} - \mathbf{R}_{\tilde{n}b}\mathbf{v}_{\mathbf{B}}. \tag{4.11}$$

Note that if no information on position is available, magnetic slaving and measurement equation (3.74) shall be used instead of (4.11). Barometric altimeter measurement equation is given by (3.19). Normal atmosphere offset and altimeter instrumental errors shall not be considered in navigation filter, since they appear coupled with height error in observable combination unless other altitude references are available.

4.3 IMU + Magnetometer + Barometric altimeter + Air Data System

Total state navigation equations are given by

$$\begin{aligned}
&\dot{\tilde{\phi}} = \underline{\frac{\tilde{v}_{n1}}{M(\tilde{\phi})+\tilde{h}}},\\
&\dot{\tilde{\lambda}} = \underline{\frac{\tilde{v}_{n2}}{\left(N(\tilde{\phi})+\tilde{h}\right)\cdot\cos\tilde{\phi}}},\\
&\dot{\tilde{h}} = -\tilde{v}_{n3},\\
&\dot{\tilde{\mathbf{v}}}_n = \mathbf{R}_{\tilde{n}b}\cdot\tilde{\mathbf{f}}_b + \boldsymbol{\gamma}_n(\tilde{\boldsymbol{\lambda}}) - \underline{\left(2\mathbf{R}_{en}^{\mathrm{T}}(\tilde{\boldsymbol{\lambda}})\cdot\boldsymbol{\omega}_{ie} + \boldsymbol{\omega}_{en}(\tilde{\boldsymbol{\lambda}},\tilde{\mathbf{v}}_n)\right)\times\tilde{\mathbf{v}}_n},\\
&\dot{\mathbf{R}}_{\tilde{n}b} = \mathbf{R}_{\tilde{n}b}\tilde{\boldsymbol{\Omega}}_{ib} - \underline{\tilde{\boldsymbol{\Omega}}_{in}\mathbf{R}_{\tilde{n}b}}.
\end{aligned} \tag{4.12}$$

Error state propagation equations take the form

$$
\begin{aligned}
&\delta\dot{\phi} = -\frac{\tilde{v}_{n1}}{\left(R(\tilde{\phi})+\tilde{h}\right)^2}\cdot\delta h + \frac{1}{\left(R(\tilde{\phi})+\tilde{h}\right)}\cdot\delta v_{n1},\\
&\delta\dot{\lambda} = \frac{\tilde{v}_{n2}\tan\tilde{\phi}}{\left(R(\tilde{\phi})+\tilde{h}\right)\cos\tilde{\phi}}\cdot\delta\phi - \frac{\tilde{v}_{n2}}{\left(R(\tilde{\phi})+\tilde{h}\right)^2\cos\tilde{\phi}}\cdot\delta h + \frac{1}{\left(R(\tilde{\phi})+\tilde{h}\right)\cos\tilde{\phi}}\cdot\delta v_{n2},\\
&\delta\dot{h} = -\delta v_{n3},\\
&\delta\dot{\mathbf{v}}_n = \mathbf{A}_{21}\delta\boldsymbol{\lambda} + \mathbf{A}_{22}\delta\mathbf{v}_n - \left[\mathbf{R}_{\tilde{n}b}\tilde{\mathbf{f}}_b\times\right]\cdot\psi_{n\tilde{n}} + \mathbf{R}_{\tilde{n}b}\cdot\delta\mathbf{f}_b,\\
&\dot{\psi}_{n\tilde{n}} = -\left.\frac{\partial\boldsymbol{\omega}_{in}\left(\boldsymbol{\lambda},\mathbf{v}_n\right)}{\partial\boldsymbol{\lambda}^{\mathrm{T}}}\right|_{\tilde{\boldsymbol{\lambda}},\tilde{\mathbf{v}}_n}\cdot\delta\boldsymbol{\lambda} - \left.\frac{\partial\boldsymbol{\omega}_{in}\left(\boldsymbol{\lambda},\mathbf{v}_n\right)}{\partial\mathbf{v}_n{}^{\mathrm{T}}}\right|_{\tilde{\boldsymbol{\lambda}},\tilde{\mathbf{v}}_n}\cdot\delta\mathbf{v}_n -\\
&\qquad -\boldsymbol{\Omega}_{in}\left(\tilde{\boldsymbol{\lambda}},\tilde{\mathbf{v}}_n\right)\cdot\psi_{n\tilde{n}} + \mathbf{R}_{\tilde{n}b}\cdot\delta\boldsymbol{\omega}_{ib},\\
&\delta\dot{\mathbf{f}}_b = \mathbf{0},\ \delta\dot{\boldsymbol{\omega}}_{ib} = \mathbf{0}.
\end{aligned}
\tag{4.13}
$$

Air data measurement equations are given by formulae (3.19), (3.23), (3.28), magnetometer measurement equation is given by (4.11). However, if no information on position is available, magnetic slaving and measurement equation (3.74) shall be used instead of (4.11). Note, that normal atmosphere offset and altimeter instrumental error shall not be considered in navigation filter in case barometric altimeter is the only source of altitude reference.

4.4 Simulation and comparison of mechanizations

Figures 25, 27 show standard deviations of orientation errors, and Figures 26, 28 show orientation error of corrected total state in case of tactical- and industrial-grade inertial sensors, respectively. Vertical lines on the figures below mark the end of filter settling (approximately at 180 seconds), beginning of steady climb (approximately at 370 seconds), end of climb and beginning of steady turn (approximately at 800 seconds), end of steady turn (approximately at 830 seconds). The simulated trajectory is presented in Appendix D.1.1, modeling of sensor errors and initialization of navigation filters is discussed in Appendices D.2–D.9. The list below introduces the meaning of the legend.

1. “IMU+Slave” denotes the mechanization, presented in the Section 4.1, magnetic slaving is used, initial position is assumed to be unknown;
2. “IMU+M” denotes the mechanization, presented in the Section 4.1, measurement of magnetic field is used, initial position is assumed to be known;
3. “IMU+B+M” denotes the mechanization, presented in the Section 4.2, measurement of magnetic field is used, initial position is assumed to be known;
4. “IMU+B+AD+M” denotes the mechanization, presented in the Section 4.3, measurement of magnetic field is used, initial position is assumed to be known;
5. “inertial” denotes purely inertial mode;
6. “Magn declin” denotes the magnitude of local magnetic declination.

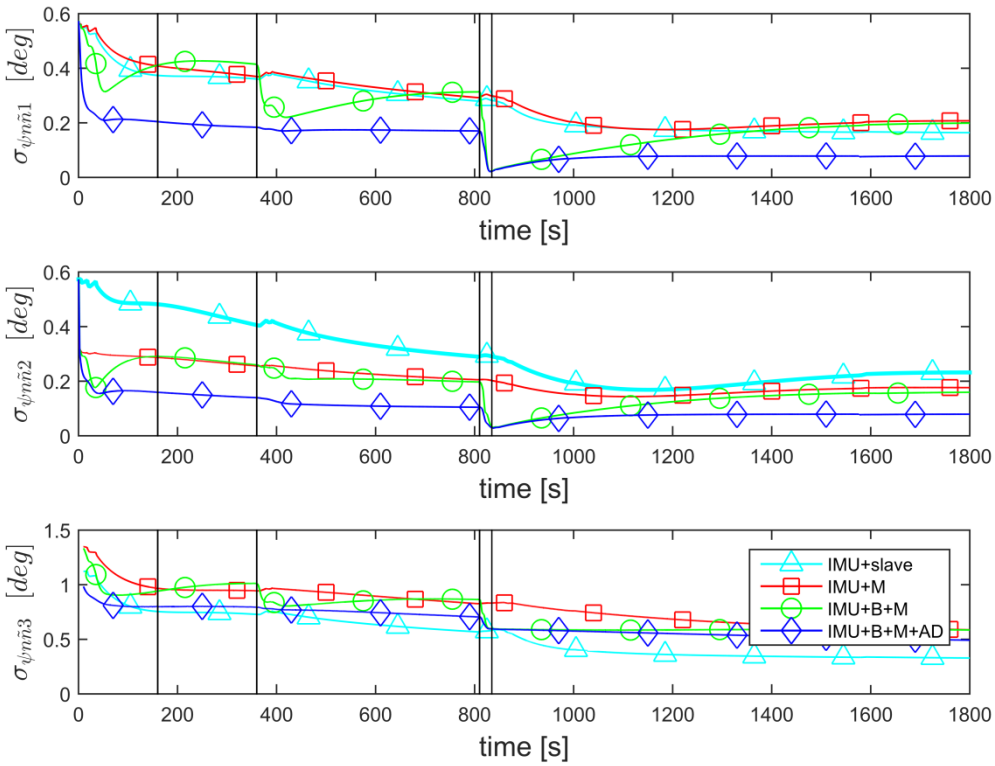

Fig. 25–Standard deviations of orientation errors. Tactical-grade IMU.

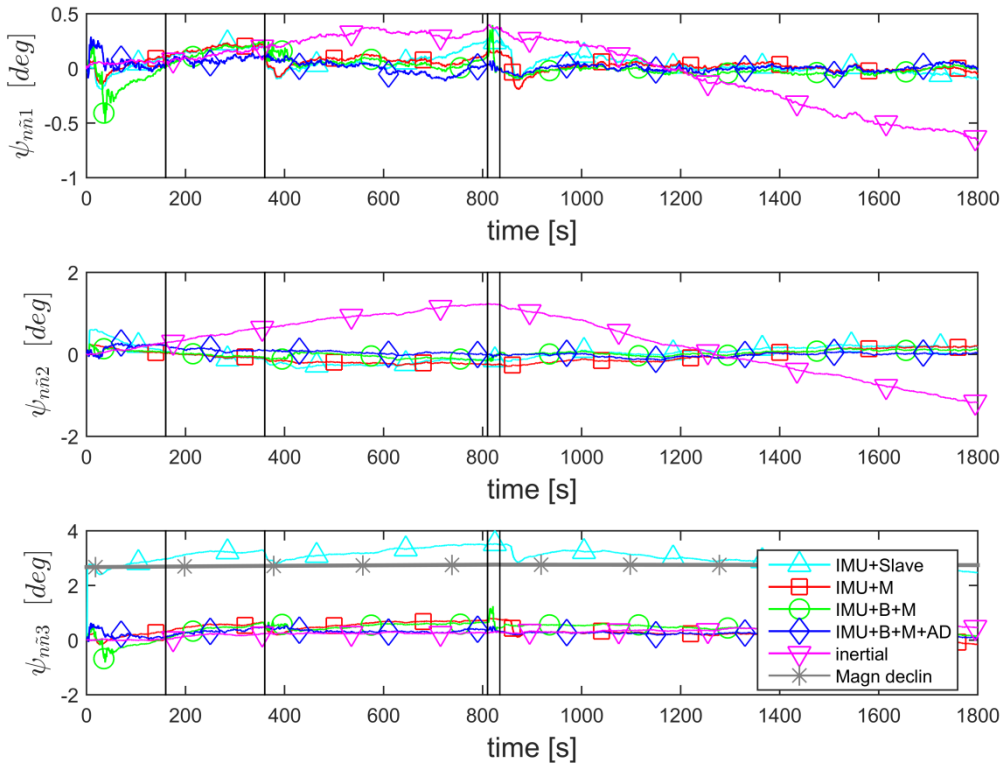

Fig. 26–Orientation errors of the corrected total state. Tactical-grade IMU.

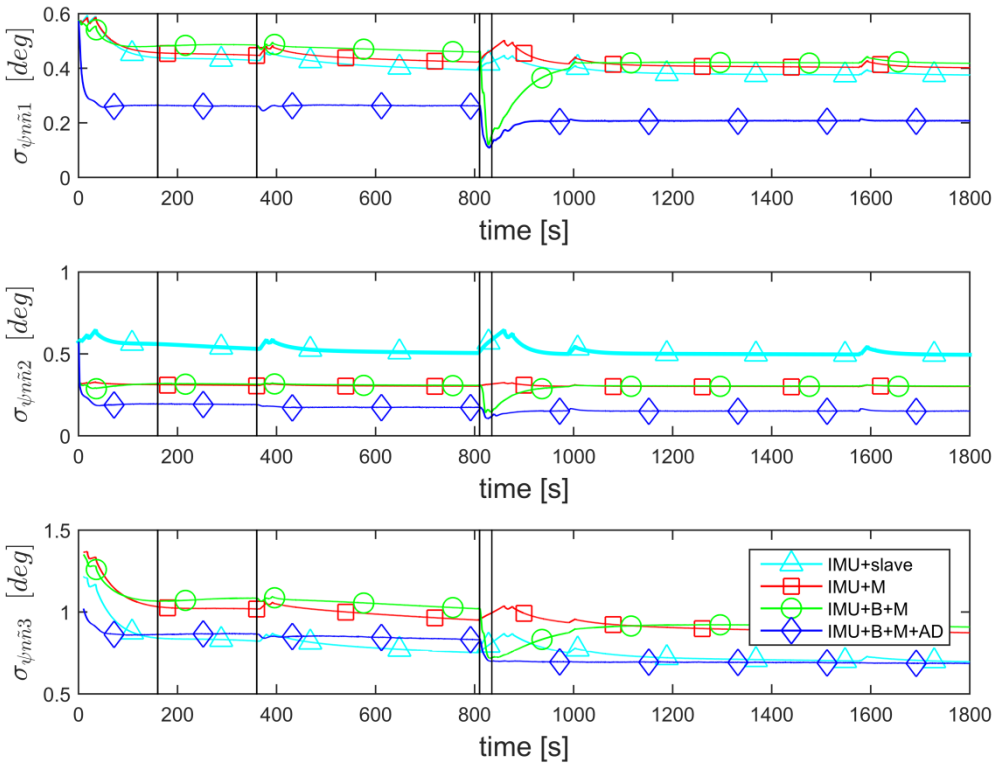

Fig. 27–Standard deviations of orientation errors. Industrial-grade IMU.

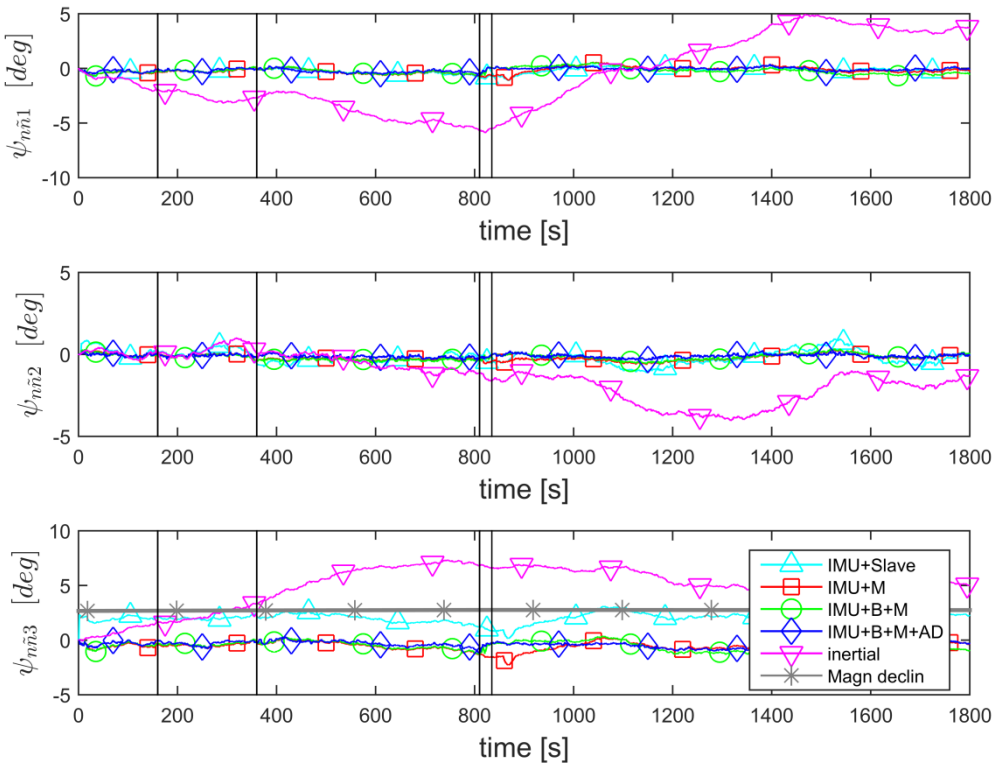

Fig. 28–Orientation errors of the corrected total state. Industrial-grade IMU.

It is seen that usage of high-fidelity model of magnetic field measurement (3.71) instead of magnetic slaving (3.74) allows to improve accuracy of attitude, which is due to better observability of $\psi_{n\tilde{n}2}$. Furthermore, such an approach enables to obtain a reference to the true heading, rather than to the magnetic. Though, if position states are not estimated by navigation filter, the approach appears to be restricted to local and short-range applications.

Aiding of INS/AHRS by barometric altitude improves significantly accuracy of attitude during maneuvering, and, accordingly, variances of $\psi_{n\tilde{n}1}$ and $\psi_{n\tilde{n}2}$ are seen to decrease steeply at presence of aiding by barometric altimeter when vehicle performs the steady turn. Further aiding by TAS, AOA, and AOS enables to achieve higher attitude performance at cruise flight as well. Behavior of estimates of inertial sensors' errors agrees mostly with results of observability analysis presented in Chapter 3, and thus their plots are omitted here. However, usage of magnetic field measurement improves observability of gyroscope errors, and, consequently, standard deviation of $\delta\omega_{b3}$ appears to converge, rather than to remain unaffected, which happens if system is aided solely by air data.

Orientation errors of corrected total state, presented on Figures 26, 28, are statistically consistent and do not exceed $\pm 2\sigma$ threshold.

Figures 29, 30 show estimates of latitude and longitude, respectively, in case of aiding both by a complete air data system and magnetic field.

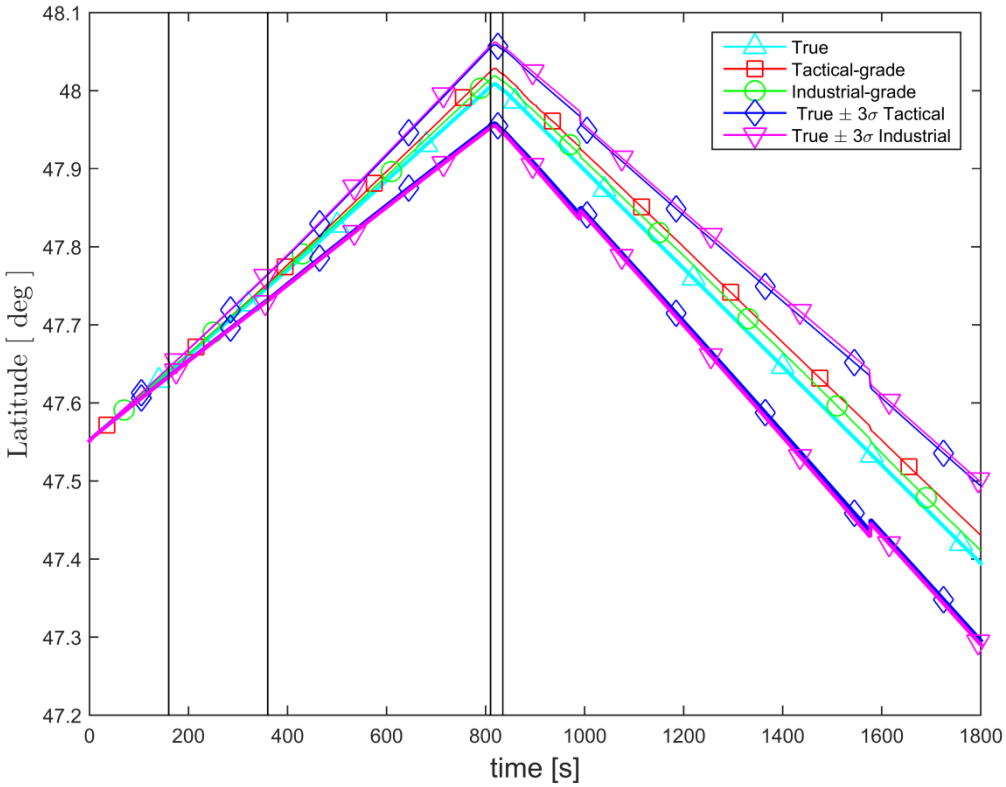

Fig. 29–Estimate of latitude.

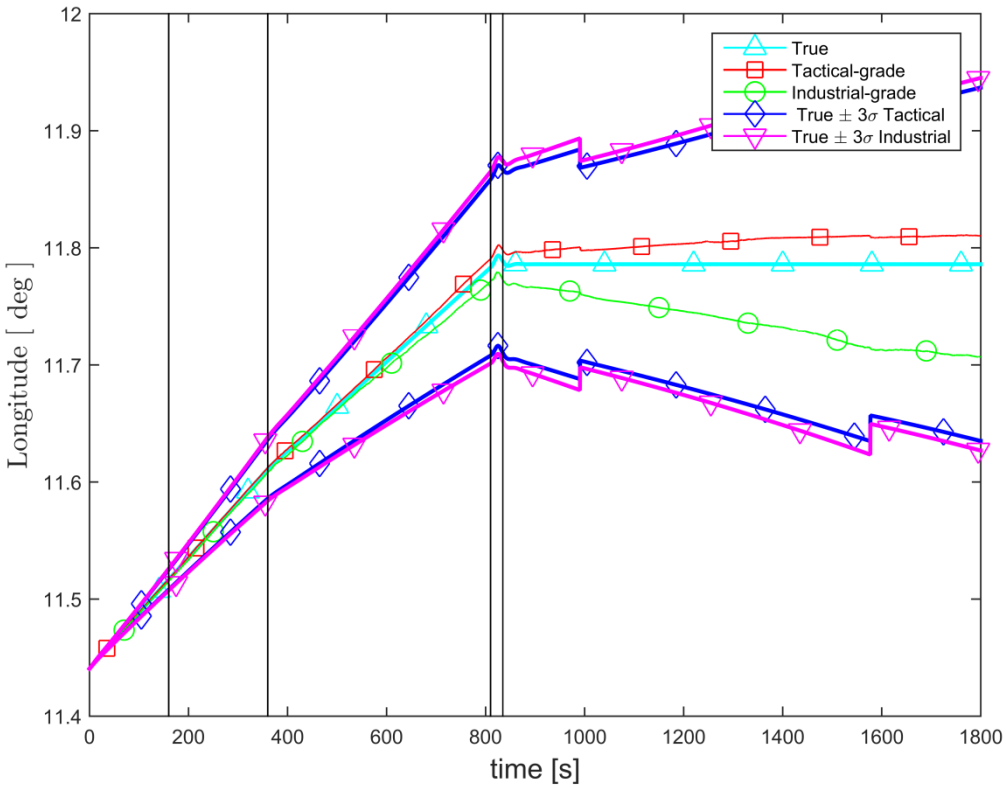

Fig. 30–Estimate of longitude.

Position error after half an hour of operation along with reference values are given in Table 7.

Table 7–Position error after half an hour of operation.

	Tactical-grade	**Industrial-grade**
Combined aiding by air data and magnetic field	4.3 km	6.2 km
Air data aided	4.3 km	12.4 km
Baro-aided	148.3 km	594 km

The result demonstrates that aiding of INS by ADS and magnetometer allows to improve significantly accuracy of position determination, despite presence of wind and disturbances of magnetic model. Moreover, accuracy of the navigation solution, provided by such a system, approaches the accuracy of the solution, provided by navigation-grade systems (one nautical mile per hour position drift). This fact is remarkable, because it appears possible to achieve just 10 times less accurate result in spite of using 100 to 1000 times less accurate inertial sensors.

4.5 Real data processing

Diamond DA42, four seat, twin-engine, propeller driven aircraft of the TUM Institute of Flight System Dynamics served as an experimental platform. The aircraft was equipped with iMAR RQH1003 INS, Novatel OEM628 GNSS receiver, Honeywell HMR2300 three-axis digital magnetometer, and Simtec PSS-8 air data system. RQH1003 is a navigation-grade INS that provides highly accurate measurements of specific force and aircraft's angular rate [60]. Neither tactical-, nor industrial-grade inertial units were additionally available on board, and therefore the errors, specific to low-cost inertial sensors, needed to be modeled. Navigation solution, computed by RHQ1003 in GNSS aided mode was used as a reference. Flight path and height profile are shown on Figure 31.

Figure 32 shows the ADS measurements. Output of the magnetometer is given on Figure 33. Parameters of simulated errors of inertial sensors correspond to the specification of Analog Devices ADIS16362 and are listed in the Table 18.

For the sake of minimizing hard-iron effects, the magnetometer was installed in the right wing of the aircraft, roughly 40 cm from the end. INS, in turn, was installed inside of the fuselage. During maneuvering the wing was discovered to oscillate significantly relatively to the fuselage, and thus a very pessimistic assumptions of dynamics of magnetic model error $\delta\mathbf{B}_n^{WMM}$ had to be made in order to keep the filter statistically consistent and stable. In the first order Gauss-Markov model

$$\delta\dot{\mathbf{B}}_n^{WMM} = -1/\tau_{\delta\mathbf{B}_n} \cdot \delta\mathbf{B}_n^{WMM} + \mathbf{v}_{\delta\mathbf{B}_n} \tag{4.14}$$

parameters $\tau_{\delta\mathbf{B}_n}$ and $\sigma^2_{\delta\mathbf{B}_n}$ were set to 10 $[\mathrm{s}]$ and 200000 $[\mathrm{nT}^2 \cdot \mathrm{Hz}^2]$, respectively, instead of 100 $[\mathrm{s}]$ and 1800 $[\mathrm{nT}^2 \cdot \mathrm{Hz}^2]$ used in simulations. Moreover, larger value of altimeter noise standard deviation had to be assumed. Instead of 1 $[\mathrm{m}]$ it was set to 5 $[\mathrm{m}]$.

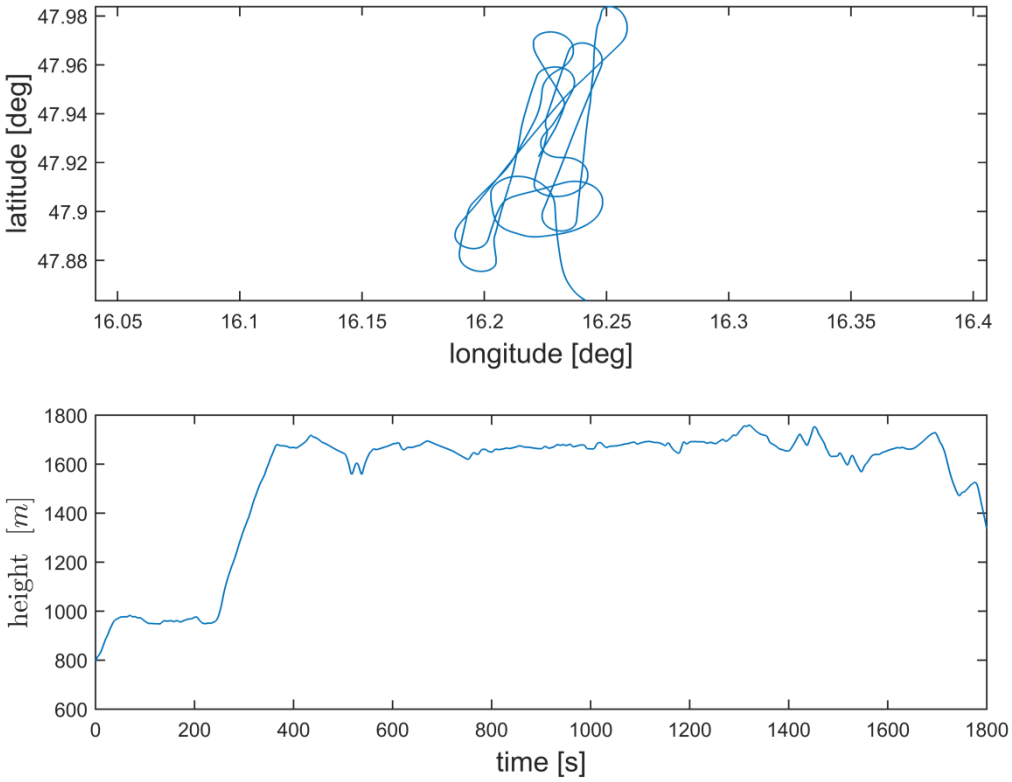

Fig. 31–Reference flight path and height.

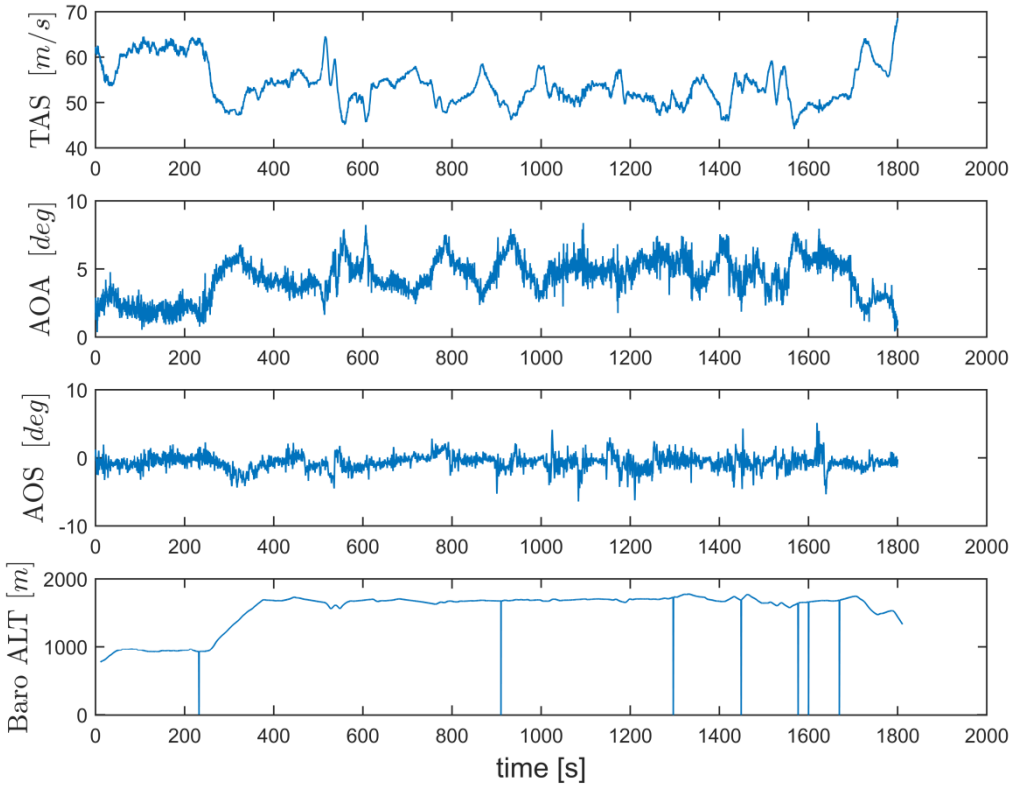

Fig. 32–Air data measurements.

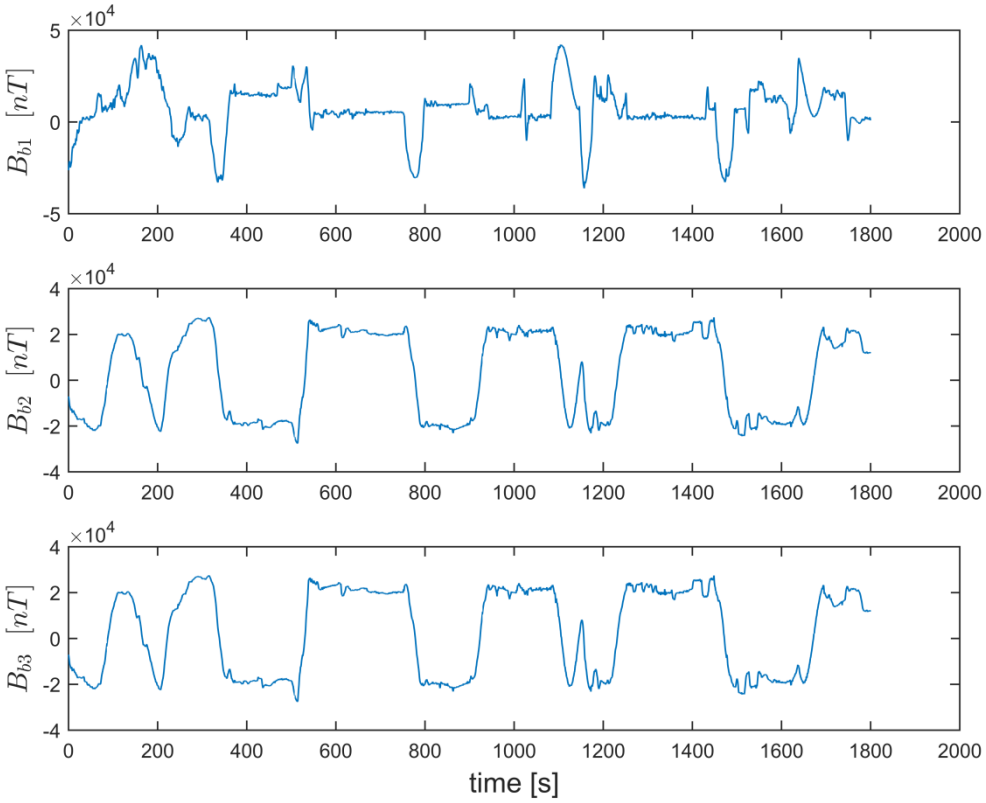

Fig. 33–B-frame measurement of the Earth's magnetic field.

Figure 34 presents errors of orientation in different modes of INS aiding, and Figure 35 shows corresponding standard deviations. On the legends "B" stands for barometric altitude aiding, "WMM" for aiding by the Earth's magnetic field, "G" for aiding by the Earth's gravity vector at the moments when aircraft does not accelerate, "AD" for combined aiding using TAS, AOA, and AOS, and "slave" stands for magnetic slaving. Root mean square, mean, and maximum absolute values of roll, pitch, and heading errors are given in Table 8. Figure 36 presents the position error, i.e. a distance from computed aircraft's position to its reference value. Experimental results are seen to confirm the conclusions of the simulation study, presented above, and demonstrates that usage of air data and magnetic field aiding allows to improve considerably accuracy of both orientation and navigation solutions and to fulfill higher operational performance requirements with lower-cost inertial sensors.

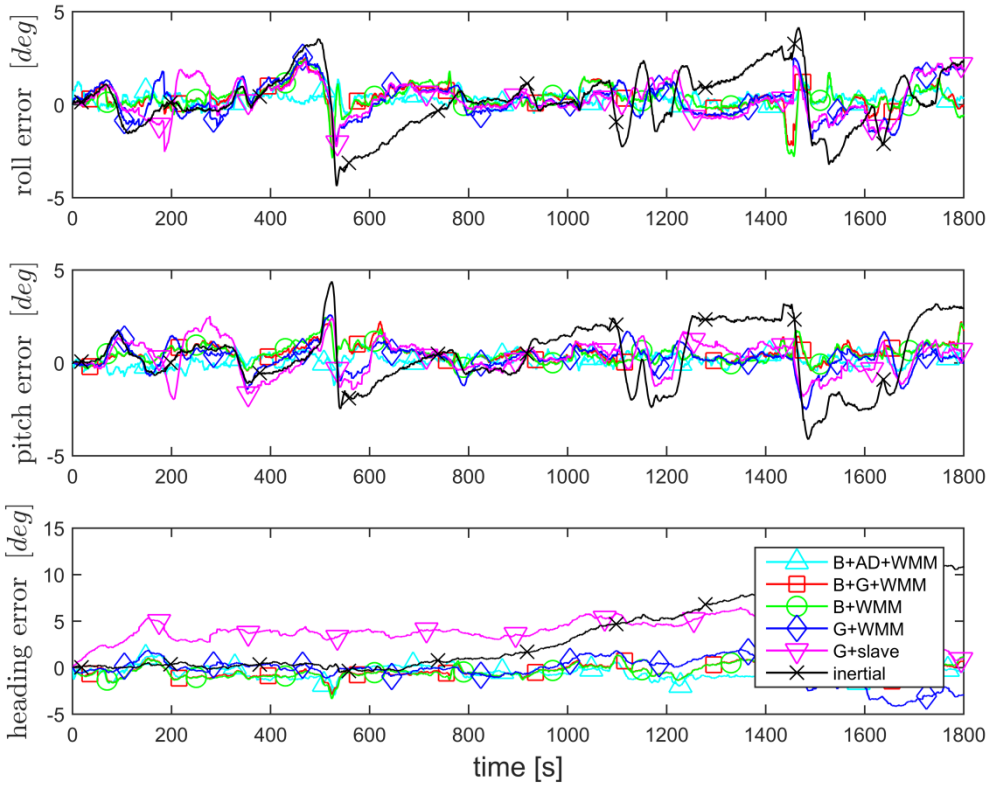

Fig. 34–Orientation errors of the corrected total state.

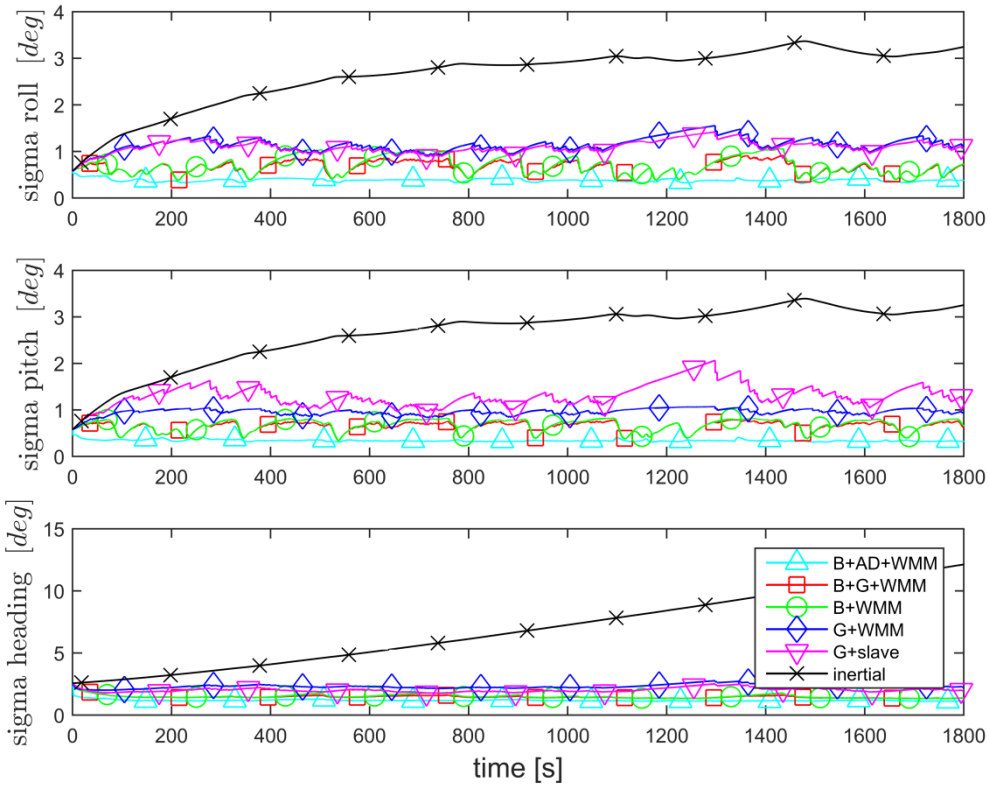

Fig. 35–Standard deviations of roll, pitch, and heading.

Table 8–RMS, maximum, and average of roll, pitch, and heading errors.

Error, deg	**Inertial**	**G+Slave**	**G+WMM**	**B+WMM**	**B+G+WMM**	**B+AD+WMM**
RMS	1.55; 1.67; 5.17	0.95; 0.92; 3.84	0.97; 0.73; 1.39	0.76; 0.68; 0.92	0.71; 0.68; 0.82	0.46; 0.38; 0.89
Max	4.37; 4.39; 11.03	2.54; 2.52; 6.50	2.80; 2.61; 4.17	2.89; 2.46; 3.98	2.64; 2.25; 2.88	1.43; 1.24; 3.00
Mean	0.18; 0.31; 3.57	0.29; 0.28; 3.52	0.28; 0.26; -0.20	0.37; 0.50; -0.27	0.37; 0.51; -0.30	0.32; 0.16; -0.61

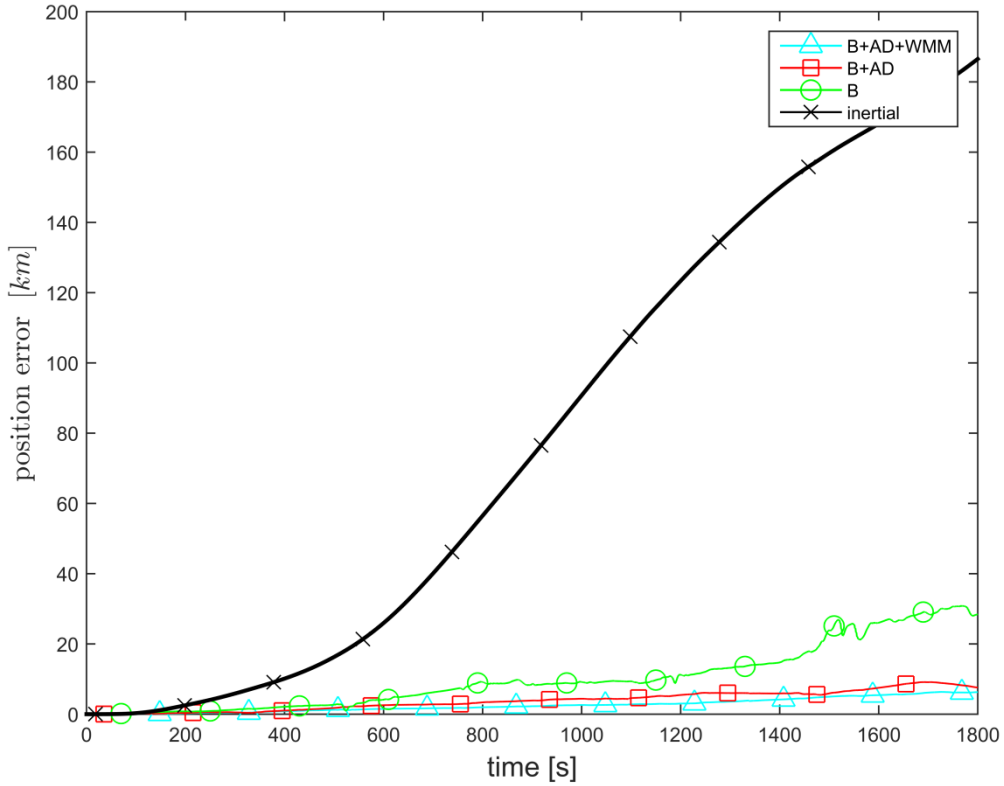

Fig. 36–Position error.

4.6 Conclusions

Simulation results and experiment, presented above, demonstrate that accurate modeling of air data and magnetic field measurements along with usage of optimal filtering allowed to satisfy higher accuracy requirements [61] with lower-class inertial sensors even if GNSS signal was unavailable throughout operation time. The main advantage of aiding of INS/AHRS by air data consists in the opportunity to compensate attitude errors both at cruise and dynamic flights. Moreover, unlike in traditional approaches [1, 2], attitude accuracy improves during maneuvering, rather than degrades. In case a highly dynamic platform is considered, a sole barometric altimeter is sufficient for attitude error compensation, and thus a complete ADS may even appear excessive for some applications. Usage of magnetic field measurement updates instead of magnetic slaving suggests, in turn, further improvement of attitude performance and allows to compensate heading error. However, this approach requires availability of an estimate of vehicle's position, because otherwise magnetic field vector

cannot be modeled. Consequently, position must either be estimated by the navigation filter, or its initially known value shall be used throughout operation time for magnetic model computation. The former requires more computational power, while the latter restricts the system to short-range applications. Evaluation of position estimates suggests that a tactical-grade INS, integrated with a magnetometer and ADS, could even provide navigation performance for relatively long period of time. This encourages to recommend to use it as a back-up navigation system during GNSS outages. Moreover, usage of GNSS would allow to calibrate INS, magnetometer, and magnetic model errors better, and thus the back-up navigation performance could be improved even more.

Table 9 summarizes advantages and expectable performance of alternative mechanizations of the system. Rows of the table represent the system being sequentially extended by additional measurement devices, while columns represent IMU accuracy and alternative ways of using magnetometer information. Cells of the table contain achievable attitude and heading performance classes defined by [61]. Description of these classes is recapitulated in Appendix C.

Table 9–Benefits and achievable performance of INS/ADS/Magnetometer integration.

IMU	**Magnetic slaving**		**Magnetic field vector aiding**	
	Tactical-grade	Industrial-grade	Tactical-grade	Industrial-grade
+ 3-axis magnetometer standalone longtime orientation determination	A3,H3	A4,H3	A2,H2	A3,H2
+ Barometric altimeter improved attitude accuracy during maneuvering	A3,H3	A4,H3	A2,H2	A3,H2
+ TAS, AOA, AOS attitude correction both at cruise and dynamic flights, back-up navigation	A1,H2	A2,H2	A1,H2	A2,H2

Results of analytical investigation, simulation, and flight test show that GNSS signal availability is not crucial in AHRS application even if low-cost inertial sensors are used. Aiding by GNSS can easily be replaced by aiding using ADS and magnetometer without any loss of AHRS performance. Moreover, integrated INS/ADS/Magnetometer system can be used as a back-up source of position information for a relatively long period of time. Consequently, performance and reliability of low-cost GNSS aided systems can considerably be improved by making use of magnetometer and air data system that are usually present on board of a conventional aircraft.

5 Fault-tolerance and reliability of AHR/navigation systems

5.1 Redundancy concepts

By now there exist several approaches to ensuring availability of reliable navigation information. A good survey can be found in the dedicated PhD thesis [62].

The first possible solution consists in installing several independent navigation systems on board. By comparing their navigation solutions one could make a decision if a problem exists. Capability simply to detect a failure or malfunction requires installation of minimum of two identical systems, and capability to isolate the failed system, i. e. to identify which of the systems does not operate properly, requires minimum of three. A disadvantage of duplicating the system is a very high cost and considerable increase of weight, which is usually critical in small-size applications.

Another approach consists in installing a redundant number of inertial sensors inside of a single navigation system. For example, measuring of angular rate and specific force requires installation of minimum three accelerometers and three gyroscopes. Installation of the fourth non collinear sensor is known to allow to detect failures, and installation of the fifth to isolate the faulty one. This approach appears very powerful and has already been implemented in a product, for example, by Honeywell [63].

The third possible way to detect problems of navigation system is to make use of external information, such as vehicle's dynamic and kinematic models, or measurements of aiding sensors. This approach is called analytical redundancy. It supposes monitoring of the system in whole and is tightly related to observability concept.

The first approach can by now be considered archaic, and that is why it will not be considered further. The second and the third, in turn, will be addressed below.

5.2 Sensor-level redundancy

5.2.1 Failure detection and isolation logic and related terminology

Figure 37 recapitulates introduction of the work [64] and illustrates the logic of failure detection and isolation. To detect failure means to alarm the user in case failure occurs, and to isolate error means to determine, which of the sensors is faulty. Decision making leads to one of the following outcomes: normal operation, correct rejection, false isolation, missed detection, missed isolation, wrong isolation, and correct isolation. The most unfavorable outcomes that can make system operation dangerous are

missed detection, missed isolation, and wrong isolation. Therefore, probabilities of this events shall be minimized. All the other outcomes do not, in general, present any danger and thus do not appear critical.

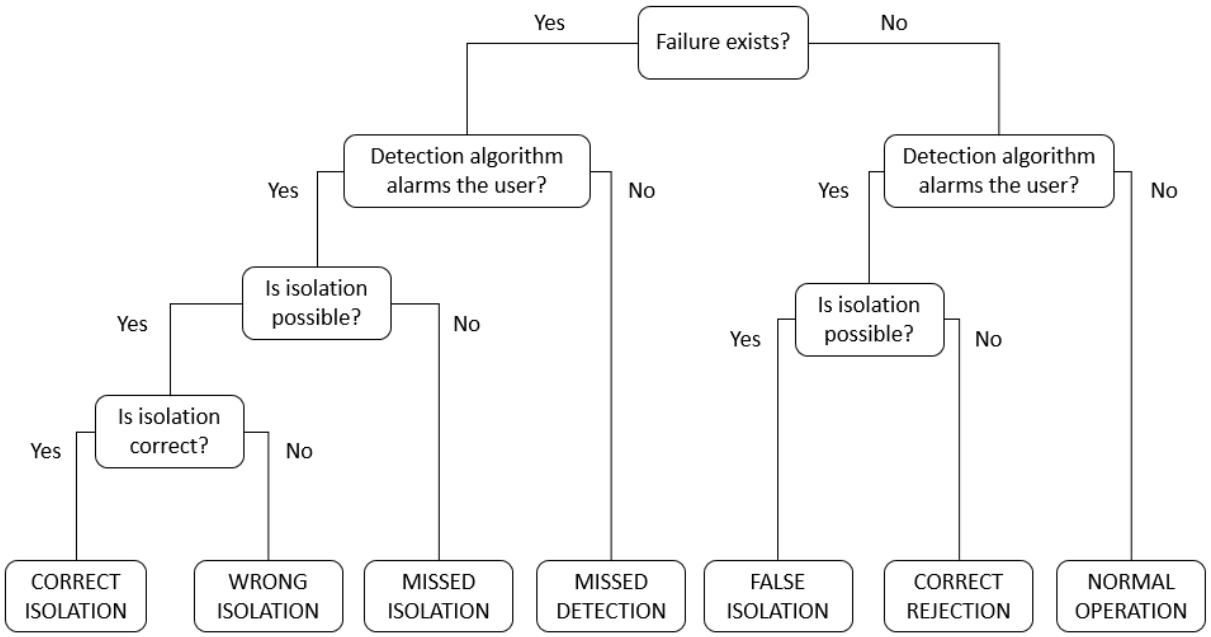

Fig. 37–Fault detection and isolation logic

5.2.2 Parity space approach

Consider that a sensor system measures m projections of a vector quantity $\mathbf{x}$ of dimension n, and that $m > n$. Moreover, consider that measurement error presents zero-mean Gaussian white noise with variance σ_r^2. Then the output $\mathbf{z}$ is related to the vector $\mathbf{x}$ as follows

$$\mathbf{z} = \mathbf{H} \cdot \mathbf{x} + \mathbf{r}, \tag{5.1}$$

where $\mathbf{H}$ is a constant $m \times n$ matrix of rank n, and $\mathbf{r} \sim N\left(\mathbf{0}, \sigma_r^2 \cdot \mathbf{I}\right)$ is the error of the measurement. The problem of obtaining an estimate of vector $\mathbf{x}$ with the minimum variance from (5.1) is known as a least squares problem [65]. The solution is given by

$$\hat{\mathbf{x}} = \left(\mathbf{H}^{\mathrm{T}}\mathbf{H}\right)^{-1}\mathbf{H}^{\mathrm{T}} \cdot \mathbf{z}\,. \tag{5.2}$$

Moreover,

$$\mathrm{E}\left[\left(\mathbf{x} - \hat{\mathbf{x}}\right)\left(\mathbf{x} - \hat{\mathbf{x}}\right)^{\mathrm{T}}\right] = \sigma_r^2\left(\mathbf{H}^{\mathrm{T}}\mathbf{H}\right)^{-1}. \tag{5.3}$$

The matrix $\mathbf{H}$ is $m \times n$ and $\operatorname{rank}\mathbf{H} = n$. Consequently, $\dim \operatorname{Ker}\mathbf{H}^{\mathrm{T}} = m - n$ and there exists an orthonormal system of $m - n$ vectors $\mathbf{p}_i$, such that $\mathbf{H}^{\mathrm{T}} \cdot \mathbf{p}_i = \mathbf{0}$, $i = 1, \ldots, m - n$. Thus, the matrix

$$\mathbf{P} = \left(\mathbf{p}_1 \quad \ldots \quad \mathbf{p}_{m-n}\right)^{\mathrm{T}} \tag{5.4}$$

has the following properties

$$\mathbf{P} \cdot \mathbf{H} = \mathbf{0}, \quad \mathbf{P} \cdot \mathbf{P}^{\mathrm{T}} = \mathbf{I}_{(m-n)\times(m-n)}. \tag{5.5}$$

Existence of the matrix $\mathbf{P}$ with properties (5.5) led to development of the so-called parity space approach to fault detection and isolation [64, 66], which was later adapted to the case of cross-correlated measurement noise [67]. The approach consists in the following.

Consider parity vector

$$\mathbf{p} = \mathbf{P}\mathbf{z}. \tag{5.6}$$

Then, if measurement is not corrupted by an error,

$$\mathbf{p} = \mathbf{P}\cdot\left(\mathbf{H}\mathbf{x}+\mathbf{r}\right) = \mathbf{P}\mathbf{H}\cdot\mathbf{x}+\mathbf{P}\cdot\mathbf{r} = \mathbf{P}\cdot\mathbf{r}. \tag{5.7}$$

Therefore,

$$\begin{aligned} &\mathrm{E}\left[\mathbf{p}\right] = \mathrm{E}\left[\mathbf{P}\cdot\mathbf{r}\right] = \mathbf{P}\cdot\mathrm{E}\left[\mathbf{r}\right] = \mathbf{0}, \\ &\mathrm{E}\left[\mathbf{p}\mathbf{p}^{\mathrm{T}}\right] = \mathrm{E}\left[\mathbf{P}\mathbf{r}\mathbf{r}^{\mathrm{T}}\mathbf{P}^{\mathrm{T}}\right] = \mathbf{P}\cdot\mathrm{E}\left[\mathbf{r}\mathbf{r}^{\mathrm{T}}\right]\cdot\mathbf{P}^{\mathrm{T}} = \sigma_r^2\mathbf{I}_{(m-n)\times(m-n)}, \end{aligned} \tag{5.8}$$

and the random variable $D = 1/\sigma_r^2\cdot\mathbf{p}^{\mathrm{T}}\mathbf{p}$ is χ^2 distributed with $m-n$ degrees of freedom. In case of a failure, i. e. if

$$\mathbf{z} = \mathbf{H}\mathbf{x}+\mathbf{r}+\mathbf{b}, \tag{5.9}$$

expectation of the parity vector appears to be nonzero,

$$\mathrm{E}\left[\mathbf{p}\right] = \mathrm{E}\left[\mathbf{P}\cdot\mathbf{r}+\mathbf{P}\cdot\mathbf{b}\right] = \mathbf{P}\cdot\mathrm{E}\left[\mathbf{b}\right], \tag{5.10}$$

and the distribution of D becomes noncentral. Thus, deciding if an error is present in the measurement can be reduced to testing the hypothesis [68] that D is chi-squared distributed, which leads to the following procedure.

In the problem of detecting failures of IMU n usually equals to 3, and $m \geq 4$. It is known that the minimum of 4 sensors is required to detect failures, and the minimum of 5 to isolate one faulty sensor.

5.2.2.1 Fault detection algorithm

0. Declare acceptable false alarm probability α
1. At each moment of time compute $D = 1/\sigma_r^2\cdot\mathbf{p}^{\mathrm{T}}\mathbf{p}$
2. Declare that fault occured if $D > T_\alpha$, where $\mathbf{P}\left(D > T_\alpha\right) = \alpha$

(5.11)

The value T_α, corresponding to specified false-alarm probability α, can be found in statistical tables of chi-square distribution. False alarm means that the user is warned, when the system, in fact, performs normally.

5.2.2.2 Fault isolation algorithm

Consider the residual

$$\mathbf{f} = \mathbf{z}-\mathbf{H}\cdot\hat{\mathbf{x}}. \tag{5.12}$$

(5.12) can further be rearranged to the form

$$\mathbf{f} = \mathbf{S} \cdot \mathbf{z}, \tag{5.13}$$

where

$$\mathbf{S} = \mathbf{I}_{m \times m} - \mathbf{H}\left(\mathbf{H}^{\mathrm{T}}\mathbf{H}\right)^{-1}\mathbf{H}^{\mathrm{T}}. \tag{5.14}$$

Then

$$\mathrm{E}\left[\mathbf{f}\right] = \mathbf{0},\ \mathrm{E}\left[\mathbf{f}\mathbf{f}^{\mathrm{T}}\right] = \sigma_r^2 \mathbf{S}. \tag{5.15}$$

In case FD algorithm declares presence of failure, the following consideration can be applied to identify the source of the problem.

1. Compute $\mathbf{f} = \mathbf{S} \cdot \mathbf{z}$ if fault was detected
2. Compute f_i^2 / S_{ii} for $i = 1, \ldots, m$
3. Declare the i^{th} sensor faulty if it maximizes f_i / S_{ii},
   i. e. $i_{fault} = \arg\max_i \left(f_i^2 / S_{ii} \right)$

(5.16)

In [66] it is shown that i_{fault}, given by (5.16), maximizes the probability $P(\mathbf{p} \mid b_i)$ under assumption that only one sensor at a time can be faulty, i. e. that

$$\mathbf{b} = \begin{pmatrix} 0 & \ldots & 0 & b_i & 0 & \ldots & 0 \end{pmatrix}^{\mathrm{T}}. \tag{5.17}$$

5.2.3 Optimal geometries

Besides for increasing reliability, many works [67, 69-74] considered usage of redundant number of sensors for accuracy improvement. In most of the works sensor geometry $\mathbf{H}$ is said to be optimal if

$$\mathbf{H} = \arg\min_{\mathbf{H}} \operatorname{trace}\left(\mathbf{H}^{\mathrm{T}}\mathbf{H}\right)^{-1}. \tag{5.18}$$

Since covariance matrix of the estimate, given by (5.2), takes the form (5.3), such a choice will allow to minimize the variances of components of $\hat{\mathbf{x}}$. In general, there can be more than one optimal geometry for a given number of sensors. Moreover, the number can even happen to be infinite. The following theorem states necessary and sufficient condition of optimality of sensor configuration in the sense (5.18).

Theorem 6. Sensor geometry minimizes the trace of $\left(\mathbf{H}^{\mathrm{T}}\mathbf{H}\right)^{-1}$ *iff* $\mathbf{H}^{\mathrm{T}}\mathbf{H} = \frac{n}{m}\mathbf{I}$.

Proof of this fact can be found in [72]. It is, as well, possible to show that minimization of the trace (5.18) is equivalent to minimization of $\det\left(\mathbf{H}^{\mathrm{T}}\mathbf{H}\right)^{-1}$ [74].

A large number of optimal geometries have by now been derived. [72] provides a good summary, which is recapitulated in Appendix I.

5.2.4 Kolmogorov-Smirnov test

Consider a sample $\mathbf{x}=\{x_1,\ldots,x_n\}$ of the length n, which presents a realization of some random variable, whose cumulative density function (CDF) is $G(x)$. Denote $F_n(x)$ empirical CDF of the sample $\mathbf{x}$. From the probabilistic theory it is known that $F_n(x)\to G(x),\ n\to\infty$. Assume that one needs to test hypothesis

$$H: G(\cdot)=F(\cdot). \tag{5.19}$$

Kolmogorov's statistics D_n is defined as [75]

$$D_n=\sup_{-\infty<x<\infty}\left|F_n(x)-F(x)\right|. \tag{5.20}$$

If hypothesis H is true, i. e. $G(x)=F(x)$, than $F_n(x)\to F(x),\ n\to\infty$, and $D_n\to 0,\ n\to\infty$. If, on the contrary, $G(x)\neq F(x)$, than

$$\sup_{-\infty<x<\infty}\left|F_n(x)-F(x)\right|\to\sup_{-\infty<x<\infty}\left|G(x)-F(x)\right|>0. \tag{5.21}$$

Kolmogorov showed that for all continuous distributions $G(x)$ the statistics D_n is distributed equally. Further Smirnov derived an approximation of the statistics for large samples in the form

$$\lim_{n\to\infty}P\left(\sqrt{n}D_n<y\right)=K(y)=1+2\sum_{k=1}^{\infty}(-1)^k e^{-2k^2y^2}. \tag{5.22}$$

The function $K(y)$ and distribution functions of Kolmogorov's statistics for small n can be found in the dedicated statistical tables [76].

Practical algorithm of the test is given below.

Denote $\overline{x}=\left\{x_{(1)},\ldots,x_{(n)}\right\}$ an ordered sample x

0. Declare acceptable false alarm rate α

1. Compute $D_n=\max_{1\le k\le n}\left[\frac{k}{n}-F\left(x_{(k)}\right),F\left(x_{(k)}\right)-\frac{k-1}{n}\right]$

2. Reject H if $\sqrt{n}D_n>K_\alpha$

(5.23)

Theoretically, Kolmogorov's approach is capable of detecting any deviation of the sample's distribution $G(x)$ from $F(x)$ if number of measurements is sufficiently large. However, this cannot possibly be achieved in practice, because the length of the sample is always limited, and because any assumption of the distribution function $F(x)$ already presents an approximation.

5.2.5 Extension of parity space approach with Kolmogorov-Smirnov test

To the author's opinion, a very natural extension of the parity space method, described in Section 5.2.2, would be making decision based on some history of decision variables $\{D(t_i)\}_{i=1}^N$, rather than based solely on the current time instance. Denote $G(x)$ true CDF of the sample $\{D(t_i)\}_{i=1}^N$. In normal

mode, i. e. when no failures are present, $D(t_i)$ are independent $\chi^2(m-n)$ distributed random variables. Thus, detecting the failure could be reduced to testing the hypothesis

$$H: G(x) = CDF_{\chi^2(m-n)}(x), \tag{5.24}$$

which leads to the following fault detection algorithm.

Fault detection

0. Declare acceptable false alarm rate α
1. Compute $\{D(t_i)\}_{i=1}^N$ using the latest N measurements
2. Use Kolmogorov-Smirnov approach to test the hypotesis
$$\left\{D(t_i) = 1/\sigma_r^2 \cdot \mathbf{p}^{\mathrm{T}}(t_i)\mathbf{p}(t_i)\right\}_{i=1}^N \sim \chi^2(m-n)$$
3. Declare that fault accured if the Kolmogorov's statistics $D_N \geq K_\alpha$, where $P(D_N < K_\alpha) = 1-\alpha$.

(5.25)

Fault isolation can then be performed as follows.

Fault isolation

1. Eliminate k^{th} measurement z_k
2. Compute parity vector $\mathbf{p}^k$ using the rest measurements
3. Compute decision variables
$$\left\{D^k(t_i) = 1/\sigma_r^2 \cdot \left(\mathbf{p}^k\right)^{\mathrm{T}}(t_i)\mathbf{p}^k(t_i)\right\}_{i=1}^N$$
4. Use Kolmogorov-Smirnov approach to test if the sample $\left\{D^k(t_i)\right\}_{i=1}^N$ is $\chi^2(m-n-1)$ distributed
5. In case $\exists$ unique k such that $D_N^k < K_\alpha$ declare that k^{th} sensor failed
6. In case there are more than one k such that $D_N^k < K_\alpha$, or all the $D_N^k > K_\alpha$, declare inability to isolate the fault, or, alternatevely, declare faulty the sensor, whose elimination minimizes D_N^k

(5.26)

Advantages of the presented FDI modification are

1. Possibility to detect much smaller noise-like errors and changes in the distribution of measurement noise
2. Higher probability of correct isolation
3. Lower probability of false alarm
4. Lower probability of missed detection

Though the method appears sensitive to instrumental errors and is more computationally complex. Simulation and comparison of the standard and modified parity space methods, as well as demonstration of advantages of the modification, is presented in the following section.

5.2.6 Simulation and comparison

In the simulation, presented in the current section, five-sensor skewed redundant configuration was considered. The design matrix of the configuration is given by

$$\mathbf{H} = \begin{pmatrix} 0.5774 & 0.5774 & 0.5774 \\ -0.3707 & 0.7275 & 0.5774 \\ -0.8064 & -0.1277 & 0.5774 \\ -0.1277 & -0.8064 & 0.5774 \\ 0.7275 & -0.3707 & 0.5774 \end{pmatrix}. \tag{5.27}$$

Perfect measurements of inertial sensors were generated in the flight simulator. The corresponding trajectory profile is given in Appendix D.1.2. Errors of inertial sensors were modeled as Gaussian white noises with the variance specific to industrial-grade IMU (see Appendix D.2).

Figures 38, 39 show performance of the standard and modified parity space methods, respectively, in a situation, when $0.09\ [\mathrm{m/s^2}]$ jump of a bias of the 4th accelerometer happened between 600 and 2000 seconds. The modeled error appears relatively small, and its magnitude is comparable to the standard deviation of the sensor's noise. Frequencies of false alarm, missed detection, correct isolation, and wrong isolation are listed in Table 10.

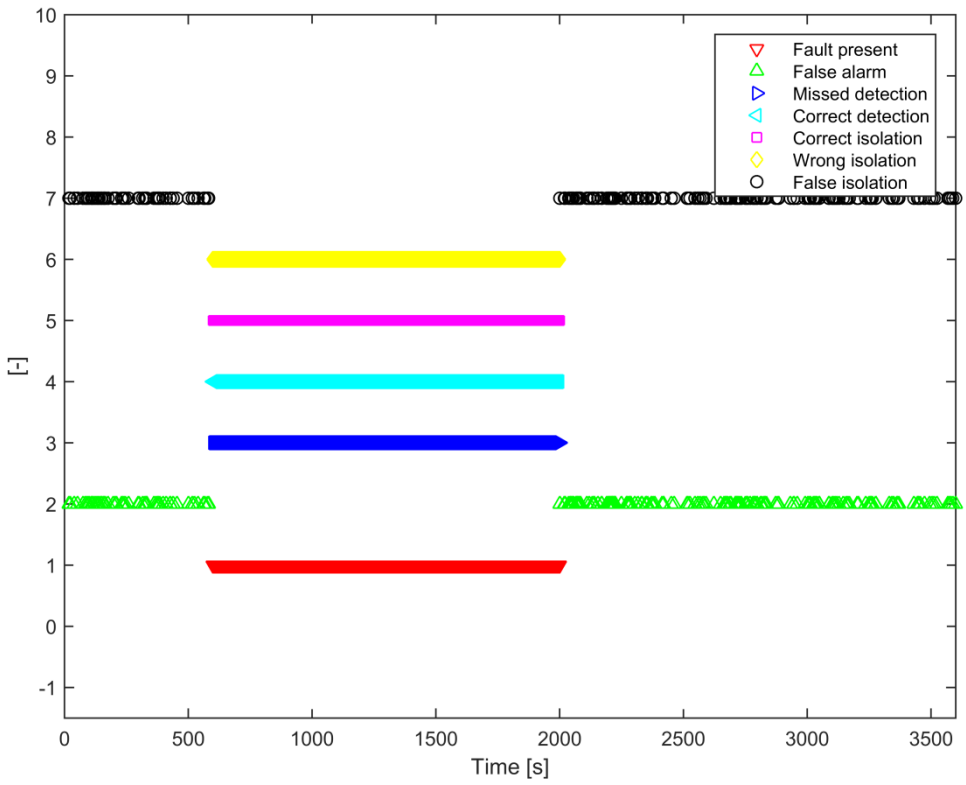

Fig. 38–Performance of standard parity space FDI

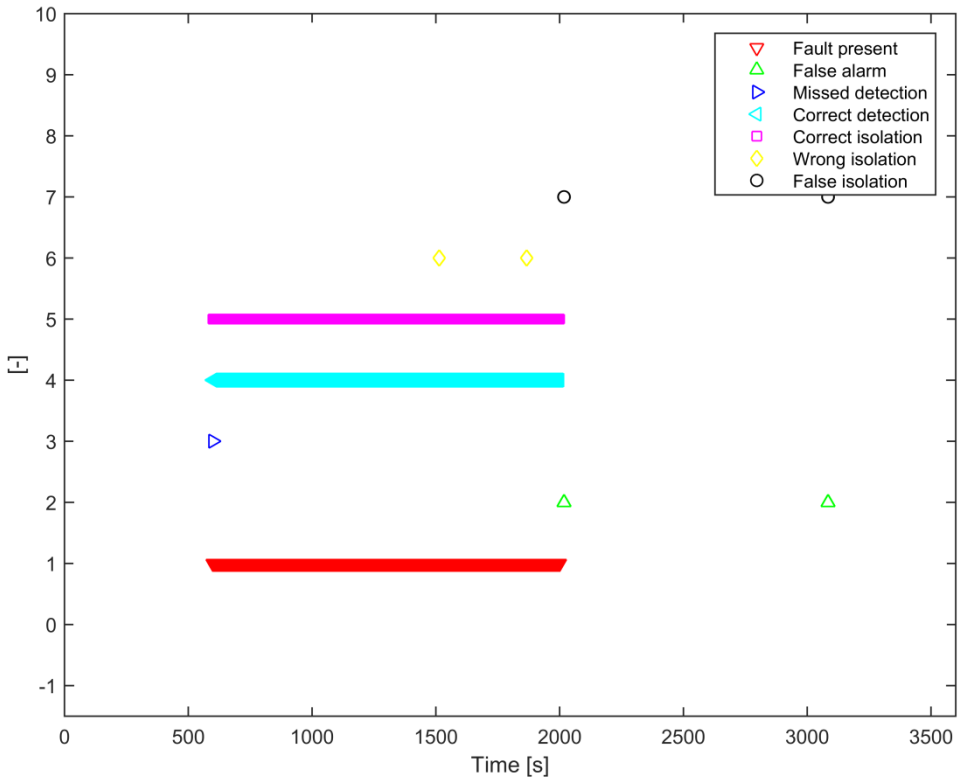

Fig. 39–Performance of modified parity space FDI

Table 10

	Standard parity space	**Modified parity space**
False alarm	9.95e-4	9.09e-4
Missed detection	0.8991	7.14e-6
Correct isolation	0.0655	0.9986
Wrong isolation	0.0354	0.0014

Figures 40, 41 show performance of the standard and modified parity space methods, respectively, in a situation, when $0.12\sin(10t)\ [m/s^2]$ error signal was added to the output of the 4th accelerometer between 600 and 2000 seconds. The modeled error appears relatively small, and its magnitude is comparable to the standard deviation of the sensor's noise. Frequencies of false alarm, missed detection, correct isolation, and wrong isolation are listed in Table 11.

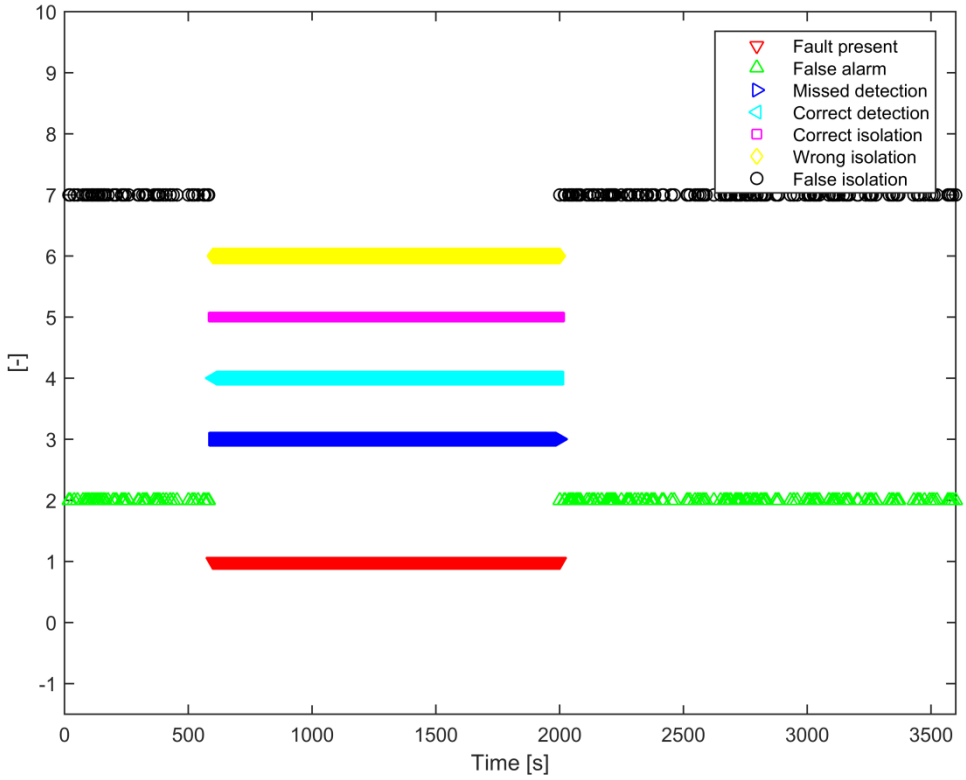

Fig. 40–Performance of standard parity space FDI

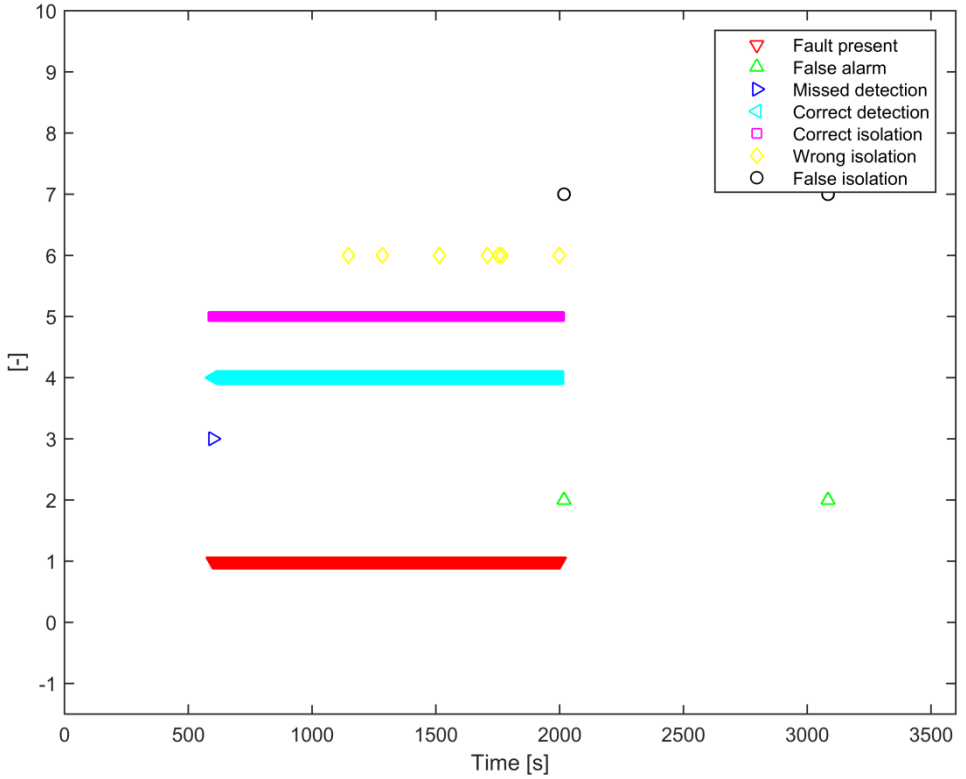

Fig. 41–Performance of modified parity space FDI

Table 11

	Standard parity space	Modified parity space
False alarm	9.95e-4	9.09e-4
Missed detection	0.8825	7.14e-6
Correct isolation	0.0816	0.9950
Wrong isolation	0.0359	0.005

Results of the simulation show that there exists a class of errors that cannot be efficiently detected by standard parity space method. The modification of the method, suggested in Section 5.2.5, allows to overcome the problem and makes the method much more sensitive to small errors. Table 10 and Table 11 distinctly demonstrate the advantages, discussed in Section 5.2.5, namely, reduced probabilities of false alarm, missed detection, and wrong isolation, as well as an increase in probability of correct isolation. Consequently, the modified method shall be considered for use in the applications, which require high level of sensitivity, while the standard shall be preferred in the situations, when only large errors are probable.

5.2.7 Problems of low-cost applications

All the sensors have instrumental errors, which are of deterministic nature. For example, a bias. In tactical- and navigation-grade systems bias-like instrumental errors are relatively small and do not usually exceed the magnitude of the standard deviation of the sensors' noise [60, 77]. However, low-cost systems can happen to feature sensors, whose bias is several times larger, than the standard deviation of noise [78]. This errors are never known and even vary significantly from turn-on to turn-off. Presence of large deterministic errors can cause considerable shift of the normal mode cumulative distribution function, and thus lead to poor performance of the FDI algorithms, discussed above.

If standard parity space method is considered, then the presence of a bias causes much higher false alarm and false isolation rates, as well as decreases probability of correct isolation. Consequently, threshold value needs to be changed in order to achieve reasonable performance. Moreover, optimal tuning appears impossible, because the bias can vary from turn-on to turn-off.

In case of testing a sample by the means of Kolmogorov-Smirnov approach, the bias will cause a shift of CDF, and thus the null hypothesis will likely to be rejected permanently. Moreover, the longer the sample is, the smaller the bias needs to be to cause rejection of the null hypothesis.

Apparently, [67] is the first work that considered the problems of low-cost inertial systems. However, [67] makes stronger emphasis on cross-correlation of the noises, rather than on presence of deterministic errors. The FDI approaches, suggested in [67], suppose real-time estimation of noise standard deviation and cross-correlations. Thus, the hypothesis, being tested by FDI algorithms, appears to be modified during operation.

The perspective of the current work, however, differs from [67]. The FDI approaches, being presented, are not supposed to determine normal mode conditions during operation. The actual purpose of FDI is to alarm the user in case performance of some sensor does not agree with the specification, provided by the manufacturer. Thus, unlike in [67], the hypothesis, being tested, remains permanent. Moreover, the methodologies, proposed in [67], suppose, similarly to parity space method, making decision based on only one time instance, rather than on a history of data.

5.2.8 Modification of the methods for use in low-cost systems

5.2.8.1 Standard parity space method

Assume, that the measurements of the redundant system are biased, and that its maximum possible value is available from specification. Then, the following modification of the algorithm (5.11) can immediately be proposed.

Fault detection

0. Declare acceptable false alarm probability α
1. Use the latest N measurements to compute the mean $\bar{\mathbf{p}}$ of parity vector $\mathbf{p}=\mathbf{Pz}$
2. At each moment of time compute $1/\sigma_r^2(\mathbf{p}-\bar{\mathbf{p}})^{\mathrm{T}}(\mathbf{p}-\bar{\mathbf{p}})$
3. Declare that fault occured if
a) either $D>T_\alpha$, where $P(D>T_\alpha)=\alpha$
b) or if $\exists i$ such that $\lvert\bar{p}_i\rvert>T_i^s$

(5.28)

The threshold values T_i^s for components of $\bar{\mathbf{p}}$ can be computed based on the specification and parity matrix $\mathbf{P}$ as follows:

$$T_i^s=\left(\sum_{j=1}^{m-n}\lvert p_{ij}\rvert\right)\cdot\max\lvert i^{th}\ \text{sensor bias}\rvert. \tag{5.29}$$

Therein p_{ij} denote the elements of parity matrix $\mathbf{P}$, and $\max\lvert i^{th}\ \text{sensor bias}\rvert$ is the maximum bias value, specified by manufacturer of the system.

Fault isolation algorithm (5.16) does not need to be modified.

5.2.8.2 KS modified parity space method

Consider, that measurements of redundant sensor system incorporate biases. Then, the equation of the output $\mathbf{z}$ takes the form

$$\mathbf{z}(t)=\mathbf{H}\cdot\mathbf{x}(t)+\mathbf{b}_z+\mathbf{r}. \tag{5.30}$$

Consequently,

$$\mathbf{p}(t)=\mathbf{P}\cdot\mathbf{z}(t)=\mathbf{H}\cdot\mathbf{b}_z+\mathbf{P}\cdot\mathbf{r}. \tag{5.31}$$

Thus, random vector $\mathbf{p}(t)$ is normally distributed with constant mean $\mathbf{b}_p=\mathbf{P}\cdot\mathbf{b}_z$ and covariance matrix $\sigma_r^2\mathbf{I}$. The idea of a modification consists in making fault detection insensitive to the constant bias.

Consider moments of time $\{t_i\}_{i=1}^{N}$, $t_i < t_{i+1}$. Then the first differences $\{\delta\mathbf{p}_i = \mathbf{p}(t_{i+1}) - \mathbf{p}(t_i)\}_{i=1}^{N-1}$ of parity vector have zero mean and covariance matrix

$$\mathrm{E}\left[\delta\mathbf{p}_i \delta\mathbf{p}_i^{\mathrm{T}}\right] = 2\sigma_r^2 \mathbf{I}. \tag{5.32}$$

However, components δp_i^s, $s = 1,\ldots,m-n$ of vector $\delta\mathbf{p}_i$ are time-correlated, and

$$\mathrm{E}[\left(\delta p_1^s \ldots \delta p_{N-1}^s\right)^{\mathrm{T}} \left(\delta p_1^s \ldots \delta p_{N-1}^s\right)] = \mathbf{W} = \sigma_r^2 \begin{pmatrix} 2 & -1 & 0 & \mathbf{0}_{1\times} & 0 \\ -1 & 2 & -1 & \mathbf{0}_{1\times} & 0 \\ \mathbf{0}_{\times 1} & \ddots & \ddots & \ddots & \mathbf{0}_{\times 1} \\ 0 & \mathbf{0}_{1\times} & -1 & 2 & -1 \\ 0 & \mathbf{0}_{1\times} & 0 & -1 & 2 \end{pmatrix}. \tag{5.33}$$

The matrix $\mathbf{W}$ can be decomposed into Cholesky factors:

$$\mathbf{W} = \mathbf{U}^{\mathrm{T}}\mathbf{U}. \tag{5.34}$$

Therefore, transformed random vectors

$$\boldsymbol{\rho}^s = \left(\rho_1^s \ldots \rho_{N-1}^s\right)^{\mathrm{T}} = \left(\mathbf{U}^{\mathrm{T}}\right)^{-1} \left(\delta p_1^s \ldots \delta p_{N-1}^s\right)^{\mathrm{T}},\ s = 1,\ldots,m-n, \tag{5.35}$$

appear normally distributed with zero mean and covariance matrix

$$\mathrm{E}[\boldsymbol{\rho}^s (\boldsymbol{\rho}^s)^{\mathrm{T}}] = \mathbf{I}. \tag{5.36}$$

Consider now vectors $\delta\mathbf{p}_{uncorr}^i = \left(\rho_i^1 \quad \ldots \quad \rho_i^{m-n}\right)^{\mathrm{T}}$. Their components are independent normally distributed random numbers with zero means and unit variances, and, consequently, the random variable $D_i^1 = (\delta\mathbf{p}_{uncorr}^i)^{\mathrm{T}} \delta\mathbf{p}_{uncorr}^i$ is $\chi^2(m-n)$ distributed. By construction, distribution of D_i^1 is completely independent of the magnitude of sensors' biases.

The following algorithm of fault detection follows from the properties of D_i^1.

Fault detection

0. Declare acceptable false alarm rate α
1. Compute the mean $\bar{\mathbf{p}}$ of parity vector $\mathbf{p} = \mathbf{Pz}$, $\delta\mathbf{p}_{uncorr}^i$, D_i^1, $i = 1,\ldots,N-1$ using the latest N measurements
2. Use KS approach to test null hypothesis, i. e. to verify that $\left\{D_i^1\right\}_{i=1}^{N-1} \sim \chi^2(m-n)$
3. Reject null hypothesis and declare fault if
   a) either the Kolmogorov's statistics D_{N-1} exceeds K_α, where $P(D_{N-1} < K_\alpha) = 1-\alpha$
   b) or if $\exists i$ such that $\left|\bar{p}_i\right| > T_i^s$

(5.37)

The threshold values T_i^s can be determined using (5.29).

Modified fault isolation procedure takes the following form.

Fault isolation

1. Eliminate measurements of the k^{th} sensor
2. Perform fault detection procedure for the remaining $m-1$ sensors
5. In case $\exists$ unique k, such that after elimination of the k^{th} sensor fault detection algorithm does not generate alarm, declare that k^{th} sensor is faulty
6. In case there are more than one sensor, whose elimination leads to disappearing of alarm, declare inability to isolate, or, alternatively, declare faulty the sensor k, whose elimination minimizes Kolmogorov's statistics at the KS test step of the fault detection
7. In case elimination of any sensor does not lead to disappearing of alarm declare inability to isolate, or, alternatively, declare faulty the sensor k, whose elimination minimizes Kolmogorov's statistics at the KS test step of the fault detection

(5.38)

5.2.9 Monte Carlo simulation and discussion

In the simulation, presented in the current section, five-sensor skewed redundant configuration was considered. The design matrix of the configuration is given by (5.27). Perfect measurements of inertial sensors were generated in the flight simulator. The corresponding trajectory profile is given in Appendix D.1.2. Errors of inertial sensors were assumed to be composed of a bias, bias instability, and white noise. Simulated parameters were specific to industrial-grade IMU and are given in Appendix D.2. One thousand of error profiles were generated using different random number generator seeds. In the simulation it was assumed that an output of the 4th accelerometer was superposed with an error signal

$$A \cdot \sin(2\pi f \cdot t). \tag{5.39}$$

One thousand simulations of the FDI algorithms, described in Section 5.2.8, were carried out for each pair (A, f) of the error signal parameters. Parameter α of the algorithms was set to 10^{-3}. Empirical probabilities of missed detection and correct isolation are presented in Table 12 and Table 13, respectively. Each of the entries was computed as a mean of one thousand realizations of a simulation.

Table 12–Probability of missed detection [%] rounded to 0.01 %, KS test/parity space

A [m/s^2] ; f [Hz]	**25**	**8.3**	**2.8**	**0.9**	**0.3**
0.01	99.92/99.88	99.92/99.88	99.92/99.88	99.92/99.88	99.93/99.86
0.03	98.99/99.75	98.91/99.76	98.94/99.75	99.00/99.76	99.85/99.48
0.09	0.04/94.77	0.01/95.87	0.02/95.80	0.06/95.87	70.73/81.75
0.27	0.00/49.93	0.00/35.79	0.00/35.85	0.00/36.08	3.19/17.72
0.81	0.00/48.58	0.00/16.60	0.00/11.14	0.00/11.21	0.00/0.91
2.43	0.00/24.71	0.00/14.64	0.00/3.25	0.00/2.92	0.00/0.00
7.29	0.00/8.23	0.00/4.83	0.00/0.91	0.00/0.29	0.00/0.00

Table 13–Probability of correct isolation [%] rounded to 0.01 %, KS test/parity space

A [m/s^2] ; f [Hz]	**25**	**8.3**	**2.8**	**0.9**	**0.3**
0.01	0.02/0.03	0.02/0.03	0.02/0.03	0.02/0.03	0.01/0.03
0.03	0.26/0.08	0.28/0.07	0.27/0.07	0.25/0.07	0.04/0.17
0.09	68.66/2.48	73.56/1.90	72.07/1.93	69.12/1.89	11.55/6.78
0.27	99.94/38.56	99.94/43.95	99.94/43.98	99.94/43.85	91.78/47.23
0.81	99.94/50.64	99.94/81.06	99.94/82.80	99.94/82.75	99.94/85.81
2.43	99.94/66.69	99.94/84.06	99.94/94.32	99.94/94.36	99.94/95.54
7.29	99.94/87.71	99.94/89.47	99.94/95.62	99.94/98.26	99.94/98.58

The results of the Monte Carlo simulation demonstrate that extension of the standard parity space method with Kolmogorov-Smirnov's approach to hypothesis testing allows to detect successfully larger class of error signals. Tables 12, 13 distinctly show that detection and isolation of relatively small time-varying error signals improve dramatically. Though, if error signal is constant, i. e. presents a sudden shift of a bias, both methods were discovered to perform similarly, and difference in sensitivity appeared insignificant. It is worth to be mentioned explicitly that making algorithms insensitive to a bias presents, in general, a tradeoff between detection performance and robustness. So, the modifications, introduced in Section 5.2.8, appear to be the actual reason why both algorithms perform similarly in case error signals are constant.

5.2.10 Instantaneous vs. history-based failure detection

The conventional approach to fault detection (5.11), known also as χ^2 test, makes decision based only on single measurement and thus performs well only if errors are large. Though it cannot detect error signals, whose magnitude is comparable to noise amplitude. In contrast, Kolmogorov-Smirnov's approach appears much more sensitive and is not restricted to constant errors. However, KS test can perform poorly if the sample being tested contains just a few outliers. This happens because the outliers can, with some small probability, occur to be a realization of noise, and thus the test does not raise the alarm if their number is small compared to the length of the sample. Therefore, it is natural to ask, how many of the measurements in the sample shall be erroneous in order to cause KS test to raise the alarm?

Consider a sample of a length n. Assume that $n_1 = cn$ sequential measurements in the sample are erroneous. Moreover, assume that errors have the same sign and are large compared to noise standard deviation. Then, by definition of Kolmogorov's statistics,

$$D_n \approx n_1 / n = c. \tag{5.40}$$

For large samples the null hypothesis is rejected if

$$\sqrt{n} D_n \approx c\sqrt{n} > K_\alpha. \tag{5.41}$$

Consequently, the minimum number of outliers required to reject the null hypotheses is

$$c_{min} = K_\alpha / \sqrt{n} + \varepsilon, \tag{5.42}$$

where ε is some small number. Assume now that measurements are collected at a frequency of f [Hz]. Then the time to alert is related to c_{min} as follows:

$$t_{alert} = \frac{c_{min} \cdot n}{f} = \frac{K_\alpha \cdot \sqrt{n}}{f}. \tag{5.43}$$

The table below tabulates time to alert values for the false alarm rate $\alpha = 0.001$.

Table 14–Time to alert, [s]

f; n	**50**	**100**	**200**	**500**
50 [Hz]	0.276	0.390	0.552	0.872
100 [Hz]	0.138	0.195	0.276	0.436
200 [Hz]	0.067	0.096	0.138	0.218
500 [Hz]	0.028	0.039	0.055	0.087

In the Table 14 it is seen that the longer the history under test is, the larger time to alert becomes. At the same time increasing sampling frequency makes time to alert shorter. Therefore, a suitable value can be ensured by finding a tradeoff between sampling frequency and the length of the sample being tested. Since large errors present the highest danger to the system, their fast detectability is of an utmost importance. This problem can be efficiently solved by the means of the conventional instantaneous χ^2 test (5.11), which presents, in fact, a limit case of Kolmogorov-Smirnov's test. The Kolmogorov-Smirnov's approach, in turn, can further be employed to detect errors and malfunctions that cannot be distinguished by the means of instantaneous testing. Consequently, much better detection performance can be achieved by combining the two methods and making use of the strengths of both of them.

5.3 Model-based failure detection and integrity monitoring

5.3.1 Applicability of classical techniques

Model-based failure detection supposes usage of system's dynamics and external aiding information both for improving performance and for monitoring integrity of navigation system. The core idea of the concept consists in using observability properties of linear system in order to detect and, if possible, isolate faults of system's components.

By now the problem of model-based failure detection has been addressed by many researchers, and the achievements have been summarized in several survey papers [79-81] and books [82-84]. To the author's opinion the best chronological description of the development of the field is given in [85].

The total amount of available literature appears, in fact, enormous, and that is why only the most important publications will be cited here.

From the author's point of view, the following approaches shall be highlighted if integrated navigation applications are considered:

1. analytical redundancy [86, 87],
2. Generalized Likelihood Ratio (GLR) [88],
3. parity relation [89, 90],
4. innovation-based detection [91].

Analytical redundancy and parity relation approaches appear mature, but are restricted to the case of linear time-invariant systems. The limitation, unfortunately, does not allow them to perform optimally in modern integrated navigation systems, which are known to exploit time-varying propagation of errors and optimal gain filters.

GLR approach is not restricted to time-invariant systems and thus can, in principle, be applied to monitoring of an integrated navigation filter. However, implementation of this approach in a real system appears problematic, because it requires to run a growing bunch of Kalman filters on board. Moreover, high performance can only be achieved if linear dynamic system is completely observable, which does not usually happen in navigation applications. Consequently, in the light of high computational complexity, the rationality of applying this approach can still be doubted.

Innovation-based integrity monitoring, in turn, appears very simple and is known to be implemented in various applications [92-94]. To the author's opinion it presents at the moment the best choice for designers of navigation systems. An extension of this very-well established and simple technique will be proposed and discussed below.

5.3.2 Innovation history monitoring using Kolmogorov-Smirnov test

Consider the discrete Kalman filter (2.31), and assume that all the measurements are scalars. A usual way to check if the filter performs well is to compute innovation $s_k^2 = (y_k - \mathbf{H}_k \hat{\mathbf{z}}_k^-)^2$ and compare it with the threshold T. Then, if

$$s_k^2 > T, \tag{5.44}$$

a fault is declared. Otherwise, the performance is considered normal.

Such a simple approach follows from the well-known property of the Kalman filter, namely

$$s_k \sim N\left(0, \mathbf{H}_k \mathbf{P}_k \mathbf{H}_k^{\mathrm{T}} + R_k\right). \tag{5.45}$$

(5.45), in turn, implies that $s_k^2 / (\mathbf{H}_k \mathbf{P}_k \mathbf{H}_k^{\mathrm{T}} + R_k)$ is χ^2 distributed, and thus the threshold T can easily be computed based on predefined false alarm rate α as follows

$$T = \left(\mathbf{H}_k \mathbf{P}_k \mathbf{H}_k^{\mathrm{T}} + R_k\right) \cdot T_\alpha, \tag{5.46}$$

where

$$P\left(\chi^2 < T_\alpha\right) = 1-\alpha. \tag{5.47}$$

In fact, the procedure of decision making in this case is similar to the one discussed in Section 5.2.2. Similar to Section 5.2.5, the procedure of fault detection can be modified by taking into account some history of innovations, rather than a single current innovation s_k.

Assume that aiding information is available at a rate, higher than Kalman filter update rate. Then the measurements collected during time interval between two consecutive updates could be used for monitoring integrity of the filter. Consider innovation sequence $\{s_i\}_{i=1}^N$, computed from these measurements and propagated error state. Unlike in a situation, when the filter does update whenever new measurement becomes available, the sequence of innovations appears time-correlated, and thus modification of the algorithm becomes less straightforward, than in Section 5.2.5. As a matter of fact, the correlation emerges, because the sequence of error state estimates is propagated starting from the same initial condition. The approach is illustrated on Figure 42.

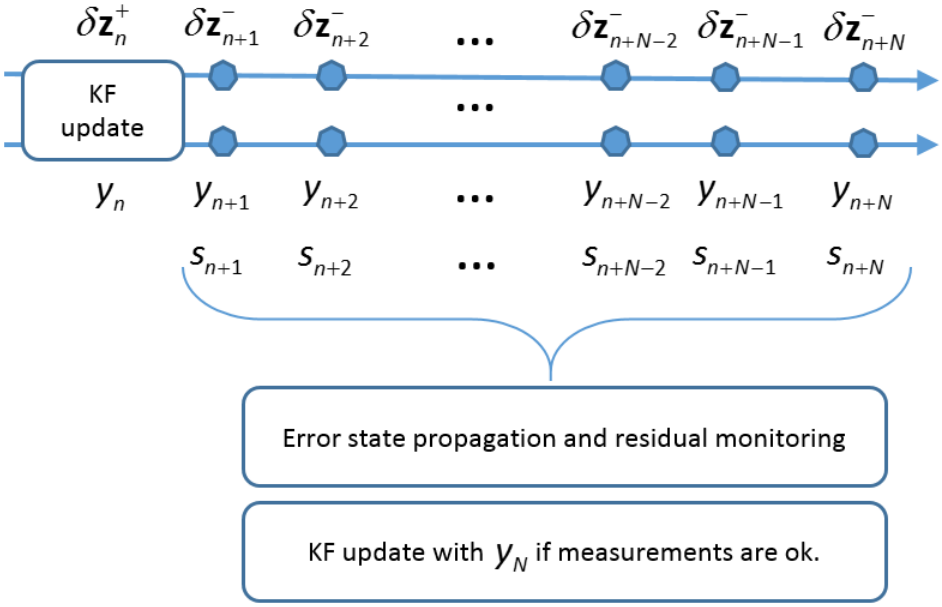

Fig. 42–Kalman filter innovation history monitoring.

Assume that measurement noise variance $R_k = \sigma_{r,k}^2$. Then

$$\begin{aligned}
&\mathrm{E}\left[s_i\right] = 0,\ \forall i,\\
&\mathrm{E}\left[s_i s_j^{\mathrm{T}}\right] = \mathbf{H}_i\mathbf{P}_i\mathbf{H}_i^{\mathrm{T}} + \sigma_{r,k}^2,\ i = j,\\
&\mathrm{E}\left[s_i s_j^{\mathrm{T}}\right] = \mathrm{E}\left[\left(y_i - \mathbf{H}_i\hat{\mathbf{z}}_i\right)\left(y_j - \mathbf{H}_j\hat{\mathbf{z}}_j\right)^{\mathrm{T}}\right] = \mathrm{E}\left[\left(\mathbf{H}_i\mathbf{z}_i + r_i - \mathbf{H}_i\hat{\mathbf{z}}_i\right)\left(\mathbf{H}_j\mathbf{z}_j + r_j - \mathbf{H}_j\hat{\mathbf{z}}_j\right)^{\mathrm{T}}\right] =\\
&= \mathrm{E}\left[\left(\mathbf{H}_i\left(\mathbf{z}_i - \hat{\mathbf{z}}_i\right) + r_i\right)\left(\mathbf{H}_j\left(\mathbf{z}_j - \hat{\mathbf{z}}_j\right) + r_j\right)^{\mathrm{T}}\right] = \mathrm{E}\left[\left(\mathbf{H}_i\left(\mathbf{z}_i - \hat{\mathbf{z}}_i\right) + r_i\right)\left(\mathbf{H}_j\boldsymbol{\Phi}_{j,i}\left(\mathbf{z}_i - \hat{\mathbf{z}}_i\right) + r_j\right)^{\mathrm{T}}\right] =\\
&= \mathrm{E}\left[\left(\mathbf{H}_i\delta\mathbf{z}_i + r_i\right)\left(\mathbf{H}_j\boldsymbol{\Phi}_{j,i}\delta\mathbf{z}_i + r_j\right)^{\mathrm{T}}\right] = \mathbf{H}_i\mathbf{P}_i\boldsymbol{\Phi}_{j,i}^{\mathrm{T}}\mathbf{H}_j^{\mathrm{T}},\ i \neq j.
\end{aligned} \tag{5.48}$$

Therefore, the matrix

$$\mathbf{C} = \begin{pmatrix} c_{11} & \cdots & c_{1N} \\ \vdots & \ddots & \vdots \\ c_{N1} & \cdots & c_{NN} \end{pmatrix}, \tag{5.49}$$

where $c_{ij} = \mathrm{E}[s_i s_j^{\mathrm{T}}]$ presents a covariance matrix of the random vector $\mathbf{s} = \begin{pmatrix} s_1 & \dots & s_N \end{pmatrix}^{\mathrm{T}}$, whose components are normally distributed. The matrix $\mathbf{C}$ can be decomposed into Cholesky factors

$$\mathbf{C} = \mathbf{U}^{\mathrm{T}}\mathbf{U}, \tag{5.50}$$

and then the transformation $(\mathbf{U}^{\mathrm{T}})^{-1}$ of the vector $\mathbf{s}$ yields random vector

$$\boldsymbol{\rho} = \left(\mathbf{U}^{\mathrm{T}}\right)^{-1}\mathbf{s}, \tag{5.51}$$

which is normally distributed with zero mean and identity covariance matrix. Consequently, its components are independent and identically distributed. These properties allow to reduce the problem of fault detection to testing a hypothesis that the sample $\{\rho_i\}_{i=1}^{N}$ comes from a standard normal distribution. In fact, the proposed method is simply intended to check, how well the measurement agrees with the propagated quantity.

Practical fault detection algorithm is summarized below.

Fault detection

0. Declare acceptable false alarm rate α
1. Compute $\{s_k\}_{k=1}^{N}$ using the latest N measurements that were collected after the latest Kalman filter update step
2. Compute covariance matrix $\mathbf{C}$ of the vector $\mathbf{s} = \begin{pmatrix} s_1 & \dots & s_N \end{pmatrix}^{\mathrm{T}}$ and decorrelating transformation $(\mathbf{U}^{\mathrm{T}})^{-1}$, where $\mathbf{C} = \mathbf{U}^{\mathrm{T}}\mathbf{U}$
3. Compute decorrelated innovation vector $\boldsymbol{\rho} = (\mathbf{U}^{\mathrm{T}})^{-1}\mathbf{s}$
4. Compute Kolmogorov's statistics D_N for the sample $\{\rho_k\}_{k=1}^{N}$
5. Reject null hypothesis, declare fault, and skip KF update if
   a) either the Kolmogorov's statistics D_N exceeds K_α, where $P(D_N < K_\alpha) = 1 - \alpha$
   b) absolute value of the current innovation $s(t_N)$ exceeds three sigma threshold, i. e. $|s(t_N)|^2 > 9\left(\mathbf{H}(t_N)\mathbf{P}(t_N)\mathbf{H}^{\mathrm{T}}(t_N) + \sigma_r^2\right)$

(5.52)

The step 5.b of the algorithm (5.52) is important, because KS test, as well as Anderson-Darling [95] and other nonparametric statistical tests, are, as was shown in the Section 5.2.10, not sensitive to a small number of outliers. Thus, if a failure happens to occur exactly at the moment of Kalman filter update, it will likely to be missed by statistical test. This will lead to performing Kalman filter update with inconsistent measurement information, and the estimate of navigation error state will get corrupted. Moreover, if further the corrupted estimate is fed back to the navigation solution, the total state estimate will, as well, get corrupted, and both strapdown navigation solution and navigation error state will not be propagated correctly further. Obviously, this can cause severe irreversible

consequences and endanger system's integrity. That is why the algorithm (5.52) suggests to combine instantaneous and history based detection strategies.

5.3.3 Discussion

If linear dynamic system is not completely observable, innovation monitoring can only be used to detect failures, but not to isolate them. This problem is not specific only to FDI approaches based on innovation monitoring, but is common to all the techniques, discussed in Section 5.3.1. The reason for that consists in the fact that in incompletely observable linear systems two different failures can cause similar behavior of the filter, and thus appear indistinguishable from each other. That is why in integrated navigation applications model-based approaches cannot replace hardware redundancy completely, and the most crucial parts of the system, such as inertial sensors, for example, must be made redundant. Therefore, the model-based techniques shall primarily be considered for detecting faults in aiding information. Moreover, reliable operation of these techniques can be ensured only if error propagation model is accurate, which, in turn, requires availability of trustworthy inertial measurements, because system matrix of the navigation error propagation equations (2.9) depends explicitly on both navigation solution and specific force.

The abovementioned aspects of model-based FDI approaches encourage to suggest the following concept of fault-tolerant integrated navigation system:

1. The system shall feature redundant number of accelerometers and gyroscopes
2. Failures of redundant IMU shall be detected on the sensor level by the means of the algorithms, discussed in Section 5.2
3. The most critical aiding systems must be duplicated
4. Failures of aiding system can be monitored at the system level by the means of the algorithms, discussed in Section 5.3.2

Usage of system level approaches allows to reduce the minimum number of identical aiding systems, required for successful FDI. For example, instead of installing three barometric altimeters and detecting/isolating their errors on the sensor level, one can consider installing just two and performing FDI by the means of system level techniques. Thus, the main advantages of using system level FDI are reduced weight and cost, while the disadvantage consists in the increase of computational burden.

5.3.4 Simulation

In the simulation, presented in the current section, five-sensor skewed redundant configuration was considered. The design matrix of the configuration is given by (5.27). Perfect measurements of inertial sensors were generated in the flight simulator. The corresponding trajectory and wind profiles are given in Appendix D.1.2. Errors of inertial sensors were assumed to be composed of a bias, bias instability, and white noise. Simulated parameters were specific to industrial-grade IMU and a given in Appendix D.2.

The INS was aided by ADS and magnetometer. Kalman filter updates were performed once in a second. Measurements of the IMU and magnetometer were assumed failure-free, while components of ADS could be faulty. The following failure scenario was assumed:

1. Barometric altimeter switch-off between 300 and 500 seconds,
2. TAS switch-off between 700 and 1000 seconds,
3. AOA switch-off between 1500 and 1900 seconds,
4. AOS switch-off between 2900 and 3300 seconds.

Figures 43, 44 show the innovation sequences and fault detection performance of the algorithm (5.52) in normal mode, i. e. if measurements are failure-free throughout operation time. Vertical lines on the Figures mark the moments of time, when wind gusts occur. It is seen that a sudden change of the wind conditions changes considerably distribution of TAS, AOA, and AOS innovations. This is successfully detected by the monitoring system and Kalman filter updates are skipped, which leads to the growth of innovation variances. After the measurements become consistent with the navigation solution again, Kalman filter updates are unsuspended.

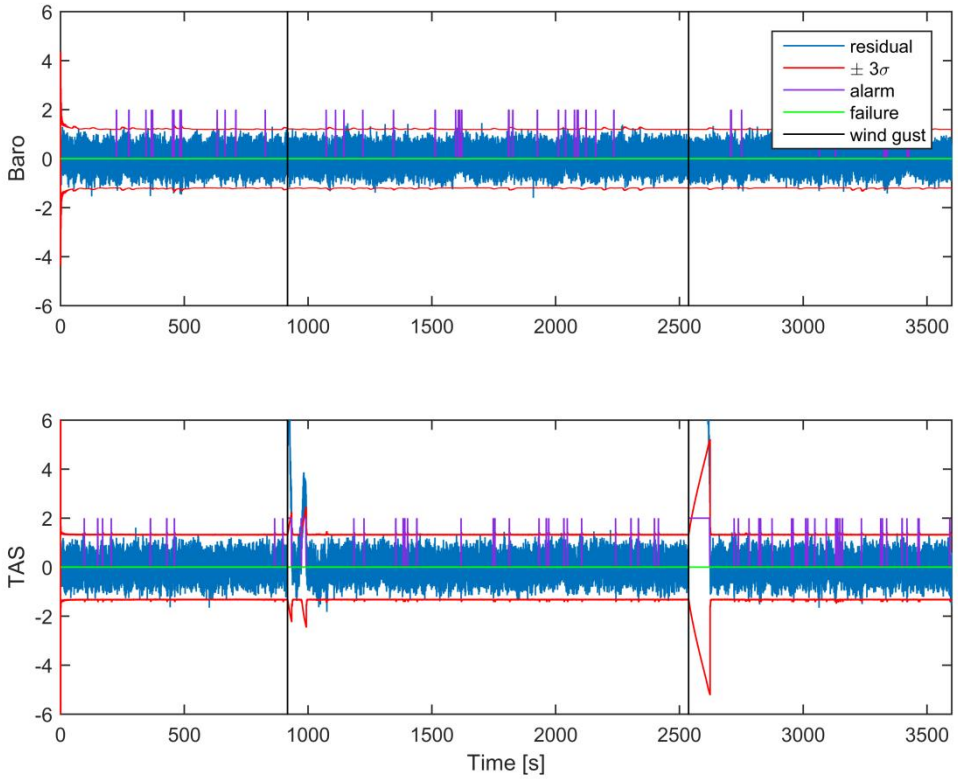

Fig. 43–Altimeter and TAS innovations in normal mode

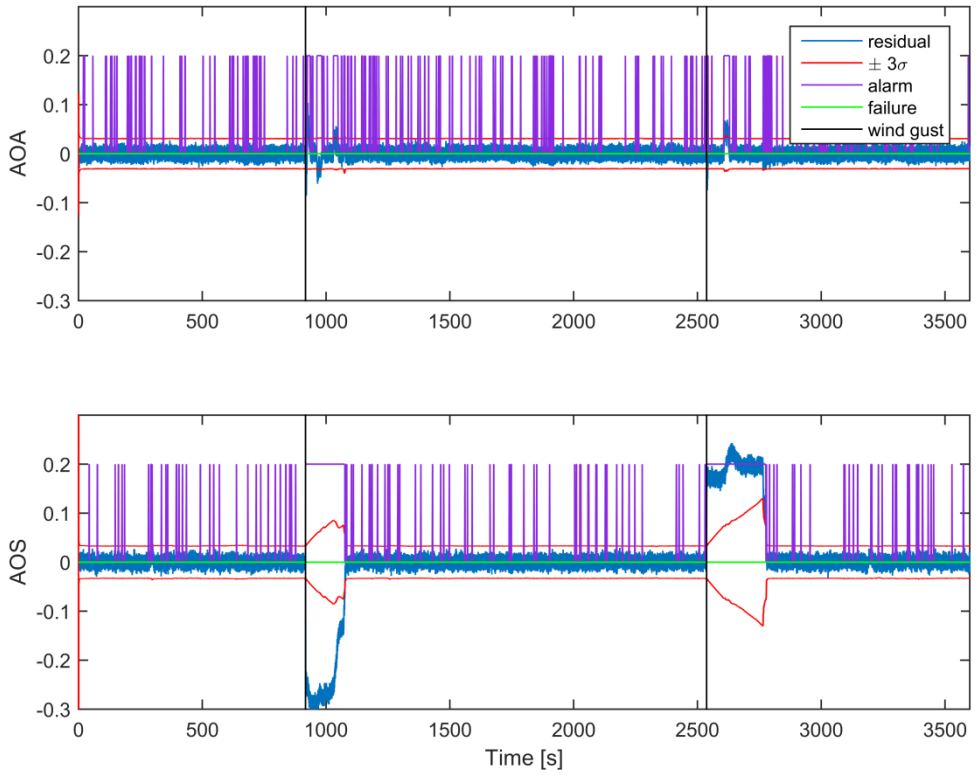

Fig. 44–AOA and AOS innovations in normal mode

Figures 45, 46 show the innovation sequences and fault detection performance of the algorithm (5.52) in the abovementioned failure scenario.

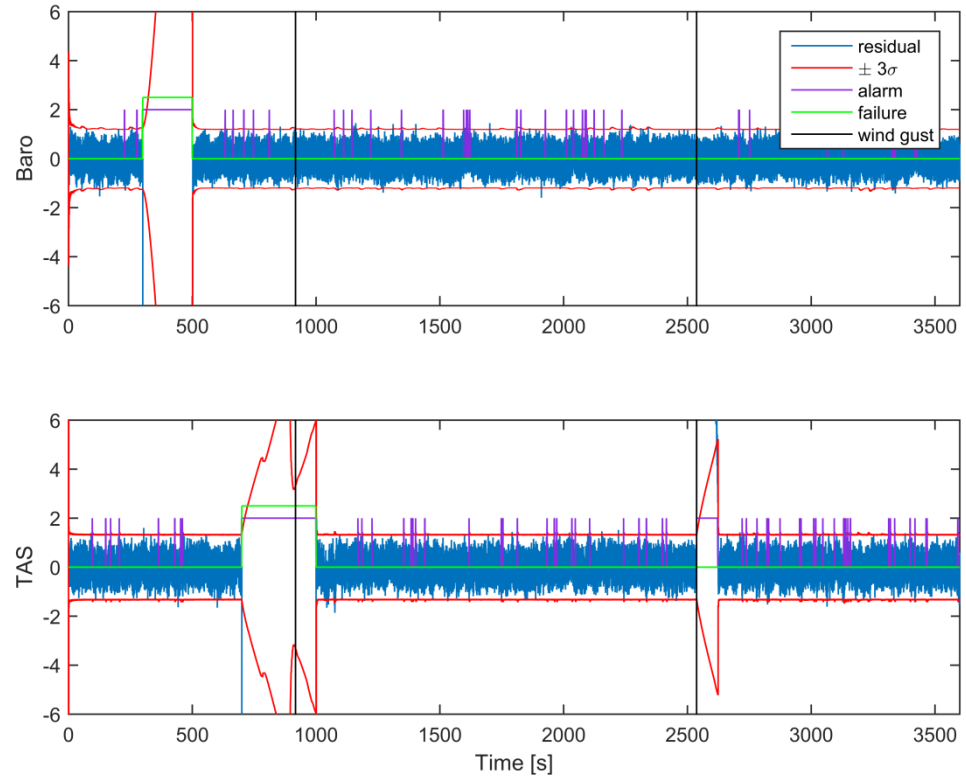

Fig. 45–Altimeter and TAS innovations in failure mode

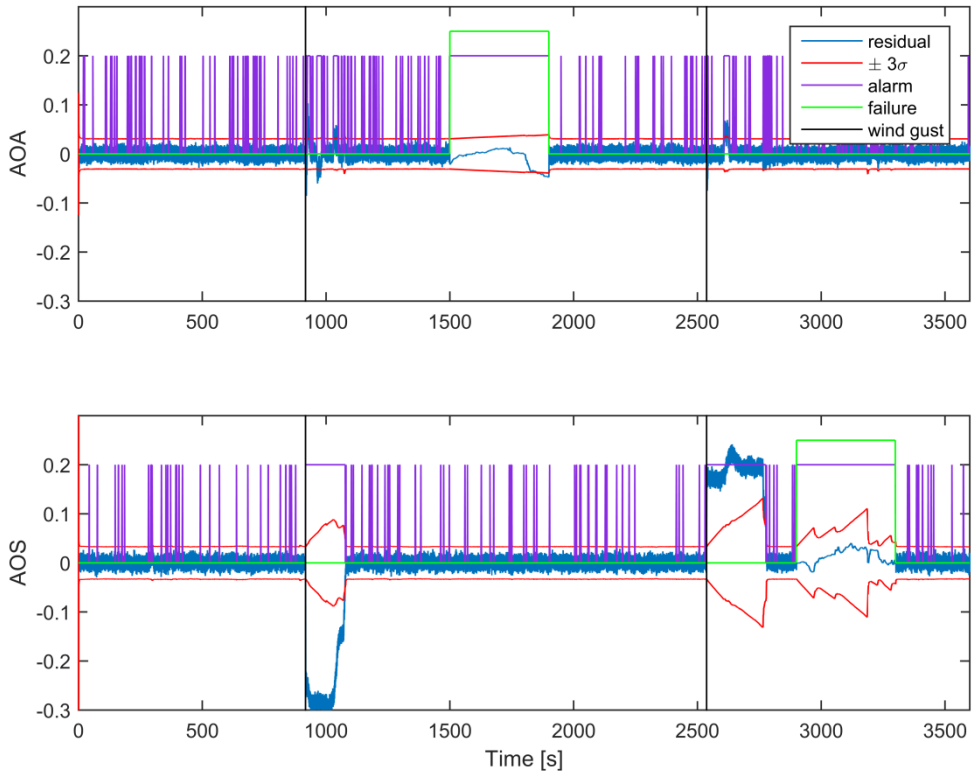

Fig. 46–AOA and AOS innovations in failure mode

Behavior of the errors of orientation, position, and velocity, as well as estimates of inertial sensors' errors, agrees completely with the analysis, presented in Chapter 3, and thus is omitted here. The FD algorithm (5.52) is seen to provide a very high probability of detection and acceptable false alarm rate. Moreover, it appears highly sensitive to small errors and changes in the distribution of innovation sequence. It is worth to be pointed explicitly that errors of AOA and AOS would not be detected by the standard χ^2 test (5.44), because their absolute values remain most of the time less, than the standard deviation of corresponding measurement noises.

5.4 Conclusions

In Chapter 5 a modification of the well-established FDI algorithms was proposed. The main idea of the modification consists in using some history of measurements for detection and isolation of faults. Results of the simulation, presented in Sections 5.2.6, 5.2.9, and 5.3.4, distinctly demonstrated that usage of Kolmogorov-Smirnov's approach to hypothesis testing allowed to expand considerably the class of errors, successfully detected by monitoring system. The advantages of the modified techniques are

1. capability to detect time-varying errors,
2. sensitivity to small errors, i. e. the errors of an order of measurement noise,
3. capability to detect changes in measurement noise distribution,
4. in AD-AHRS application, improvement of filter performance and consistency by suspending Kalman fitter updates, when wind conditions are changing.

Disadvantages of the modification are

1. increased computational burden,
2. increase of time to alert,
3. requirement of reliable error propagation model,
4. need to extend error state vector and model stochastic errors, especially strongly correlated noises, properly in the filter [96].

Increase of time to alert, in fact, is the major disadvantage of the proposed modification. This is especially critical if error happens to be extremely large. The conventional approach (5.11), though, appears efficient for large errors, but is completely insensitive to time-varying errors of an order of noise standard deviation. This problem as well can threaten integrity of the navigation filter in long-term perspective and thus must not be ignored. Therefore, the best solution, from the author's point of view, is to combine the approaches and to make use of the strengths of both instantaneous and history-based detection strategies.

The system designer could, as well, consider replacing Kolmogorov-Smirnov's test by the test of Anderson-Darling. Though, when the length of a sample is relatively small, i. e. one hundred or less, difference in performance appears negligible.

5.5 Proposal for a minimum fault-tolerant design of AHRS

Figure 47 proposes the minimum robust design of a fault-tolerant AHRS. Robustness is understood in the sense that all the aiding sources are onboard-autonomous and thus cannot be spoofed or jammed like, for example, radio navigation systems and GNSS.

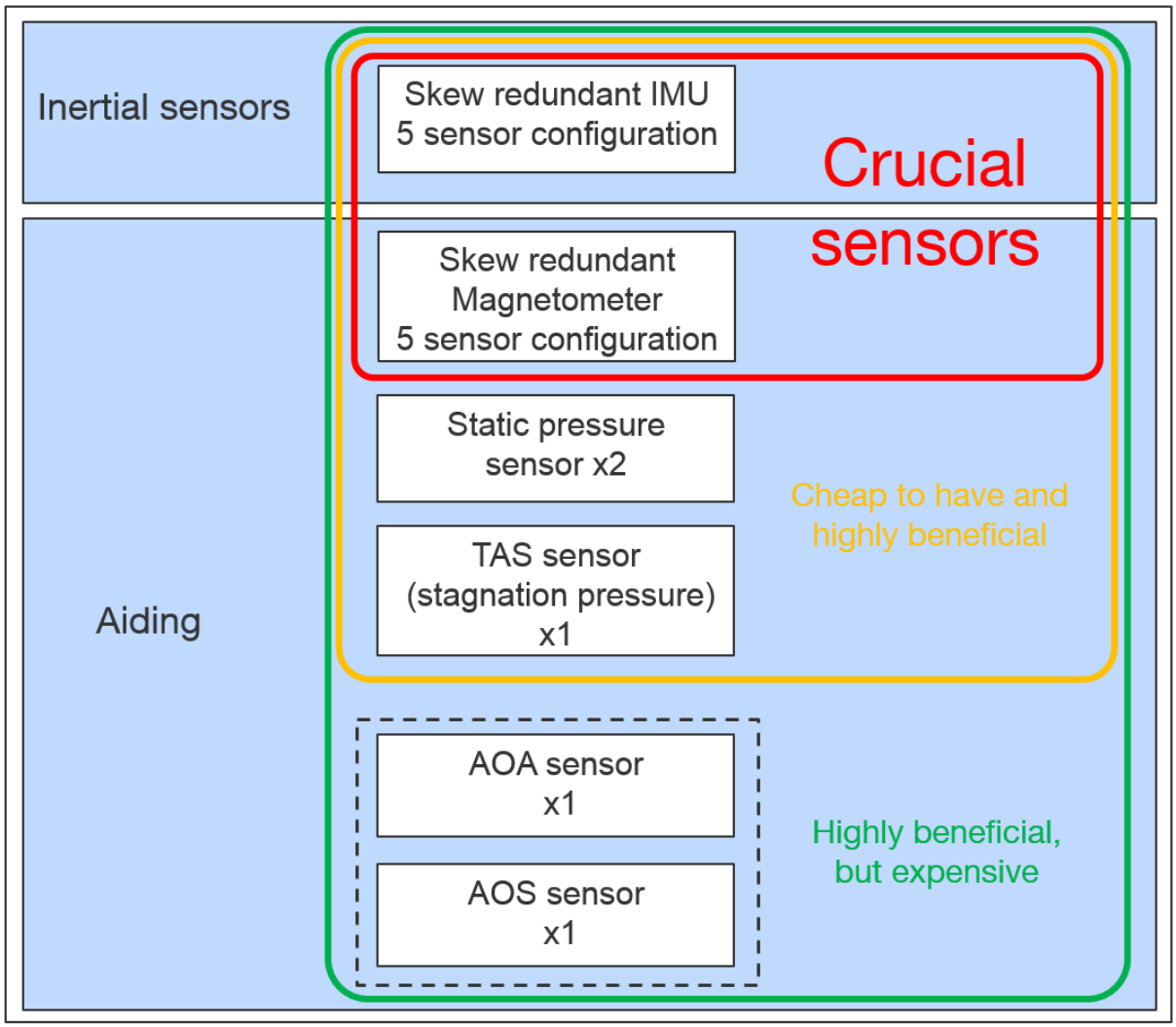

Fig. 47–Minimum robust design of fault-tolerant AHRS

IMU and magnetometer are the most crucial for attitude and heading determination. In fact, measurements of specific force, angular rate, and the Earth's magnetic field is the minimum set of information, required for robust orientation computation. Implementation of this concept is discussed in detail in Section 4.1. Despite its simplicity and high popularity, the approach has got limitations that do not allow to achieve accuracy level comparable to performance of integrated INS/GNSS. The main disadvantage of the method is degradation of orientation accuracy during dynamic flight or turbulence. Therefore, the approach shall be recommended as a back-up solution when all the other aiding sources are unavailable. In order to ensure fail-operational performance, IMU and magnetometer shall be made skew-redundant, and FDI shall be performed on redundant IMU/magnetometer levels by the means of parity space or modified parity space approaches. Installation of $4+N$ sensors of the same

type will allow to remain operational if N sensors fail. Thus, the minimum of five 1-axis accelerometers, gyroscopes, and magnetometers is required in order to remain operational in spite of failure of one of them.

Barometric altitude is the most valuable information in terms of observability properties and cost. Attitude errors are observable during maneuvering. Hence, the vehicle has an opportunity to make use of occasional turning and therefore improve considerably accuracies of roll and pitch estimates. Thus, this type of aiding appears highly useful for flying platforms that maneuver frequently, like, for example, remotely controlled airplanes, operated in visual range. Since information on altitude appears extremely beneficial, altimeter should be made redundant. FDI can then be performed on the system level and thus just two altimeters are enough to allow both fault detection and isolation.

TAS, AOA, and AOS are required to provide observability of attitude errors during cruise flight. Thought, each of the abovementioned sensors cannot provide necessary observability properties on its own, i.e. when it appears the only source of aiding. Moreover, AOA and AOS sensors present either a multihole probe, or aerodynamic vanes, and appear highly expensive, because the first design requires a long and complex calibration procedure, and the second supposes a very precise mechanical manufacturing. However, since the set of three sensors, namely TAS, AOA, and AOS, already appears partially redundant from observability point of view, duplication of these systems does not appear crucial. Even if two out of three measurements become unavailable, the system still has an option of increasing maneuvering rate and keeping AHRS performance by the means of altitude aiding.

5.6 Never give-up concept of operation

Figure 48 illustrates a concept of fault-tolerant operation of the AHR/back-up navigation system design proposed in Section 5.5. Since IMU, magnetometer, and altimeter are made redundant, simultaneous loss of 1 accelerometer, 1 gyroscope, 1 magnetometer, and 1 altimeter will not influence performance of the system. Loss of one of the ADS sensors, in turn, will degrade navigation performance, but will have minor effect on accuracy of orientation. Further loss of the second ADS sensor will make attitude errors unobservable during straight and leveled flight. In order to keep high accuracy of attitude estimates the vehicle then can start maneuvering more frequently and exploit information provided by altimeter. If all the altimeters (static pressure ports) fail, the system can still use the traditional approach and compute orientation from IMU and magnetometer measurements. Though, performance will degrade considerably. A scenario, in which TAS, AOA, and AOS sensors remain operational in spite of failure of all the altimeters is not considered, because altimeter, TAS, AOA, and AOS sensors usually use the same static pressure ports. Consequently, failure of all the static pressure ports implies failure of TAS, AOA, and AOS sensors as well. If two accelerometers, or two gyroscopes, or two magnetometers fail simultaneously, the system still can operate, but its integrity cannot be monitored further, and the faulty sensor cannot be isolated. Thus, the system ceases to be fail-safe and any further failure can lead to a disaster. Moreover, the navigation solution may get considerably corrupted, since faulty measurements of specific force or angular rate will still be used in

least-squares estimation. In fact, the estimation of inertial measurements from redundant number of measured projections can be made more robust to outliers if least squares is replaced by least absolute deviations approach [97], or by guaranteed estimation [98, 99].

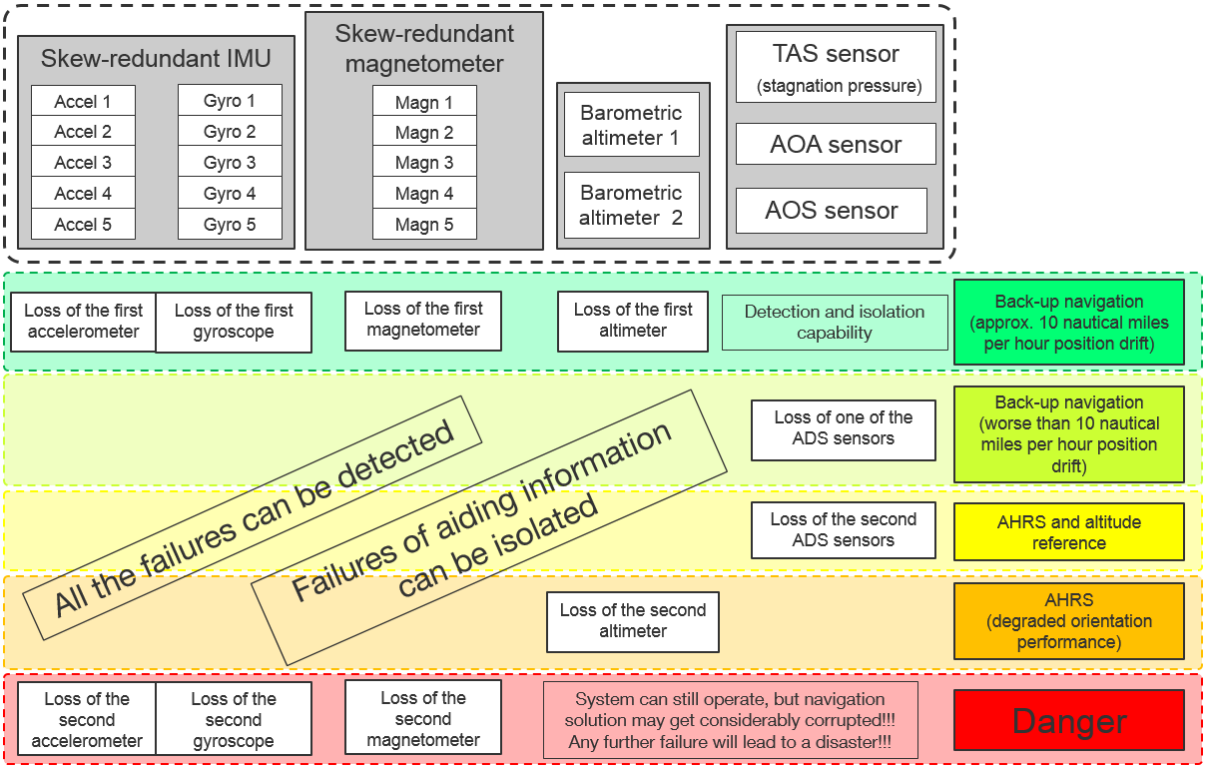

Fig. 48–Operation concept of the minimum design

Table 15 summarizes the system's operation characteristics in the event of the specified failure.

Table 15

	Operation type	
Failure type	Fail-safe	Fail-operational
1 accelerometer	✓	✓
2 accelerometers		✓
≥3 accelerometers		
1 gyroscope	✓	✓
2 gyroscopes		✓
≥3 gyroscopes		
1 magnetometer	✓	✓
2 magnetometers		✓
≥3 magnetometers		
1 altimeter	✓	✓
2 altimeters	✓	✓

TAS sensor	✓	✓
AOA sensor	✓	✓
AOS sensor	✓	✓

A check in the "fail-safe" column means that the system remains capable to compute reliable orientation solution, despite the specified failure. A check in the "fail-operational" column indicates that the system remains, in principle, capable to compute orientation solution, but an error may happen to be extremely large, because of system's inability to isolate faulty sensor.

5.7 Reliability analysis of the proposed design

In order to evaluate reliability of the proposed AHR/back-up navigation system design, the following probabilities will be derived:

1. Probability that the system provides the highest performance P_{HP},
2. Probability that the system ceases to be fail-operational and fail-safe P_{danger},
3. Probability that the system fails completely P_{fail}.

Assume that probabilities of failure of the system's components are known. Denote P_A, P_G, P_M, P_B, and P_{AD} probabilities of failures of accelerometers, gyroscopes, magnetic sensors, altimeters, and air data sensors, respectively.

The system provides the highest performance if

1. TAS, AOA, and AOS sensors operate normally,
2. Less than 1 altimeter failed,
3. Less than 1 accelerometer failed,
4. Less than 1 gyroscope failed,
5. Less than 1 accelerometer failed.

Corresponding probabilities are derived below.

$$
\begin{aligned}
&P\left(\text{TAS, AOA, AOS operate normally}\right)=\left(1-P_{AD}\right)^3,\\
&P\left(\text{less than 1 altimeter failed}\right)=\\
&\quad=P\left(\text{2 altimeters operate normally}\right)+P\left(\text{1 out of 2 altimeters failed}\right)=\\
&\quad=\left(1-P_B\right)^2+C_2^1\left(1-P_B\right)P_B,\\
&P\left(\text{less than 1 accelerometer failed}\right)=\\
&\quad=P\left(\text{5 accelerometers operate normally}\right)+P\left(\text{1 out of 5 accelerometers failed}\right)=\\
&\quad=\left(1-P_A\right)^5+C_5^1\left(1-P_A\right)P_A,\\
&P\left(\text{less than 1 gyroscope failed}\right)=\left(1-P_G\right)^5+C_5^1\left(1-P_G\right)P_G,\\
&P\left(\text{less than 1 magnetometer failed}\right)=\left(1-P_M\right)^5+C_5^1\left(1-P_M\right)P_M.
\end{aligned}
\tag{5.53}
$$

Consequently,

$$\boxed{\begin{aligned}P_{HP} = &\left[\left(1-P_A\right)^5 + C_5^1\left(1-P_A\right)P_A\right]\cdot\left[\left(1-P_G\right)^5 + C_5^1\left(1-P_G\right)P_G\right]\cdot\left[\left(1-P_M\right)^5 + C_5^1\left(1-P_M\right)P_M\right]\cdot \\ &\cdot\left[\left(1-P_B\right)^2 + C_2^1\left(1-P_B\right)P_B\right]\cdot\left(1-P_{AD}\right)^3.\end{aligned}} \tag{5.54}$$

Herein $C_n^k = \dfrac{n!}{k!(n-k)!}$ denote binomial coefficients.

The system ceases to be fail-operational and fail-safe if either

1. 2 out of 5 accelerometers failed, 4 or more gyroscopes and magnetometers operate normally,
2. Or 2 out of 5 gyroscopes failed, 4 or more accelerometers and magnetometers operate normally,
3. Or 2 out of 5 magnetometers failed, 4 or more accelerometers and gyroscopes operate normally.

$$\begin{aligned}&P\left(\text{2 out of 5 accelerometers failed}\right) = C_5^2\left(1-P_A\right)^3 P_A^2, \\ &P\left(\text{2 out of 5 gyroscopes failed}\right) = C_5^2\left(1-P_G\right)^3 P_G^2, \\ &P\left(\text{2 out of 5 magnetometers failed}\right) = C_5^2\left(1-P_M\right)^3 P_M^2.\end{aligned} \tag{5.55}$$

Thus,

$$\boxed{\begin{aligned}P_{danger} = &C_5^2\left(1-P_A\right)^3 P_A^2\cdot\left[\left(1-P_G\right)^5 + C_5^1\left(1-P_G\right)P_G\right]\cdot\left[\left(1-P_M\right)^5 + C_5^1\left(1-P_M\right)P_M\right] + \\ &+ C_5^2\left(1-P_G\right)^3 P_G^2\cdot\left[\left(1-P_A\right)^5 + C_5^1\left(1-P_A\right)P_A\right]\cdot\left[\left(1-P_M\right)^5 + C_5^1\left(1-P_M\right)P_M\right] + \\ &+ C_5^2\left(1-P_M\right)^3 P_M^2\cdot\left[\left(1-P_A\right)^5 + C_5^1\left(1-P_A\right)P_A\right]\cdot\left[\left(1-P_G\right)^5 + C_5^1\left(1-P_G\right)P_G\right].\end{aligned}} \tag{5.56}$$

The system fails completely if either

1. More than 2 accelerometers fail,
2. More than 2 gyroscopes fail,
3. More than 2 magnetometers fail.

$$\begin{aligned}&P_1 = P\left(\text{2 or less accelerometers failed}\right) = \left[\left(1-P_A\right)^5 + C_5^1\left(1-P_A\right)^4 P_A + C_5^2\left(1-P_A\right)^3 P_A^2\right], \\ &P_2 = P\left(\text{2 or less gyroscopes failed}\right) = \left[\left(1-P_G\right)^5 + C_5^1\left(1-P_G\right)^4 P_G + C_5^2\left(1-P_G\right)^3 P_G^2\right], \\ &P_3 = P\left(\text{2 or less magnetometers failed}\right) = \left[\left(1-P_M\right)^5 + C_5^1\left(1-P_M\right)^4 P_M + C_5^2\left(1-P_M\right)^3 P_M^2\right].\end{aligned} \tag{5.57}$$

Consequently,

$$\boxed{P_{fail} = 1 - P_1 P_2 P_3.} \tag{5.58}$$

Assuming, for example, that $P_A = P_G = P_M = P_B = P_{AD} = 10^{-4}$ yields

$$\begin{aligned}&P_{HP} \approx 0.9997, \\ &P_{danger} = 3\cdot 10^{-7}, \\ &P_{fail} = 1.2\cdot 10^{-10}.\end{aligned} \tag{5.59}$$

In contrast, for a traditional non redundant system, featuring 3 accelerometers, 3 gyroscopes, and 3 magnetometers (flux sensors), any failure leads to complete failure of the system, and

$$P_{fail}^{trad} = 1-\left(1-P_A\right)^3\left(1-P_G\right)^3\left(1-P_M\right)^3 \approx 9\cdot 10^{-4}. \tag{5.60}$$

This comparison distinctly shows that installing redundant number of the most crucial sensors is highly important for ensuring fail-safe operation of the system.

In operations research [100, 101] reliability of the system is usually studied in terms of distribution of time to failure. A common model is exponential failure distribution

$$P\left(T<t\right)=1-e^{-\lambda t}, \tag{5.61}$$

where λ is related to mean time to failure $\bar{t}$ as $\bar{t}=1/\lambda$. If mean times to failure are known from experiment, P_A, P_G, P_M, P_B, and P_{AD} can be substituted in formulae (5.54), (5.56), (5.57), (5.58) by

$$\begin{aligned} &P_A(t)=1-e^{-\lambda_A t},\ P_G(t)=1-e^{-\lambda_G t},\\ &P_M(t)=1-e^{-\lambda_M t},\ P_B(t)=1-e^{-\lambda_B t},\\ &P_{AD}(t)=1-e^{-\lambda_{AD} t}. \end{aligned} \tag{5.62}$$

This will yield dependencies of the probabilities of high performance $P_{HP}(t)$, danger mode $P_{danger}(t)$, and complete failure $P_{fail}(t)$ on time of operation.

6 Summary of results and conclusions

Results, contributions, and findings of this thesis can be logically divided into five groups.

The *central applied result* consists in

Proposing robust fault-tolerant design of AHR/back-up navigation system.

The design suggests several important advantages, compared to classical AHRS, or integrated INS/GNSS.

The first advantage consists in using *solely autonomous measurement systems*, such as IMU, Air Data System and magnetometer, which, unlike GNSS signals, cannot be remotely spoofed, jammed, or deliberately disabled. This makes the system *more robust* and allows to achieve *higher reliability*, which is especially important in civil UAV applications.

The second advantage is a *much higher accuracy of the orientation solution*, compared to the classical autonomous AHRS design, discussed in the Section 4.1. In fact, *integration of INS with ADS and magnetometer and usage of optimal (Kalman) filtering* allow to *determine orientation almost as accurately as integrated INS/GNSS systems*, featuring the same class of inertial sensors. Moreover, the approach suggests *considerably improved accuracy of position determination*, and even with industrial-grade IMU it appears possible to achieve only 10 nautical miles per hour position drift rate. This is especially remarkable, because *navigation-grade inertial systems, featuring highly accurate RLG gyroscopes and quartz accelerometers*, usually provide the user with position estimate, which degrades at a rate of *1 nautical mile per hour*. Thus, *position solution*, computed using an output of *1000 times less accurate inertial sensors*, appears *only 10 times less accurate*. This quality constitutes the third significant advantage of the proposed design.

The fourth advantage is *fault-tolerance*, provided by the means of *minimum redundancy*. It was argued that *IMU and magnetometer* were the *most crucial* sensors for attitude and heading estimation. Therefore, they shall be made redundant. Fault detection and isolation can then be done on redundant IMU/magnetometer levels by the means of either parity space method, or parity space extended by Kolmogorov-Smirnov test approach, or by a combination of both. *Barometric altimeter* was shown to be *highly beneficial from observability point of view*. Since altimeter is relatively cheap, redundancy can, in general, be easily afforded. *Fault detection and isolation* then can be done on *system level* by the means of Kalman filter innovation monitoring. In this case *two altimeters appear enough to both detect and isolate the erroneous one*. *TAS, AOA, and AOS* are highly expensive, and their contribution to the navigation system consists in making *attitude errors observable both at cruise flight and during maneuvering*. Making these sensors redundant can be desirable in some applications, but is not crucial,

because the *complete set of three sensors is already partially redundant from observability point of view*. In case of *simultaneous failure of two air data aiding sources*, though, a UAV or a pilot could consider *adjusting flight trajectory and maneuvering more frequently in order to maintain AHRS/navigation performance by the means of aiding by barometric altitude*. A more detailed explanation of the concept is provided in Sections 5.5, 5.6 and is illustrated by Figures 47, 48.
In summary it shall be said that *the proposed design presents low size, weight, power, and cost (SWaP-C) robust autonomous fault-tolerant navigation system with the best in-IMU-class performance, which, in the events of failures, can gracefully degrade to AHRS mode*.

Another important result, in the author's opinion, is a presentation of a
Systematic study of a problem of Air Data, Magnetometer, and INS integration.
The problem of integrating INS, ADS, and 3-axis magnetometer into a robust autonomous attitude and heading reference/back-up navigation system *was systematically studied by the means of formal mathematical techniques*. Firstly, the necessary mathematical background was presented, *high-fidelity measurement equations were derived*, and *analytical observability analysis of the system was conducted*. Knowledge of *explicit forms of observable linear combinations of error states made behavior of the Kalman filter highly predictable and encouraged to recommend occasional maneuvering to improve navigation performance*. Besides that *heading error* was proven to be *completely unobservable in case of aiding INS by the b-frame measurement of vehicle's velocity*. *Results of the analytical analysis of the system were demonstrated in simulation and suggested improvements of accuracy and robustness in navigation systems, featuring low-cost inertial sensors, and contributed to the AHR/back-up navigation system design, discussed above*. The findings and conclusions are presented in Sections 3.2.12, 3.3.7, and 3.6 in detail.

Based on the systematic study
Several alternative autonomously aided AHRS mechanizations were derived and compared.
These AHRS mechanizations present a sequential extension of the conventional approach, discussed in the Section 4.1. *Performance of the mechanizations* was *demonstrated* and *compared* by the means of simulation. *Achievable accuracies were identified and tabulated for each of the mechanizations and IMUs of different grades.* It was shown that *integration even of a low-cost MEMS-based INS with ADS and magnetometer* could suggest *high level of robustness* and could allow to *satisfy aviation authorities' accuracy requirements*. Therefore, it was demonstrated that *dependency on GNSS signal availability could be relaxed* in many applications. *Processing of real experimental data confirmed results of simulations and conclusions*. Extensive discussion and detailed explanation of the findings are given in the Section 4.6.

Further,

Usage of redundancy concept in an integrated navigation systems was considered.

The facts that *integrated navigation system is not usually time-invariant and completely observable* are the *loose-ends of system-level redundancy concepts*. *Limited applicability of system-level concept* to integrated navigation applications, therefore, encouraged to propose *homogeneous redundancy of the most crucial parts of the system*, such as IMU and some of the aiding systems. Under assumption that *IMU is redundant* and its failures are detected and isolated on sensor-level, *Kalman filter innovation sequence monitoring* was shown to indicate efficiently *failures of aiding systems*. *Classical sensor- and system-level fault detection methods*, namely one-instance parity space and one instance Kalman filter innovation monitoring, *were suggested to be improved*. The improvement consists in using *nonparametric hypothesis testing (Kolmogorov-Smirnov's approach) of a history of parity vectors and Kalman filter innovations*. *It was demonstrated that the modification enabled to detect wider class of errors and improved considerably fault detection and isolation performances*. Sections 5.1, 5.2.6, 5.2.9, 5.3.1, 5.3.3, and 5.4 present the related contributions in detail.

As a side effect of the observability analysis, conducted in the Chapter 3,

A unified methodology of observability investigation in linear time-varying systems was developed.

Mathematical relation between observability Gramian and observability matrix was established. It was shown that *under particular assumptions*, which are usually fulfilled in applied problems, *rows of observability matrix span row space of observability Gramian* and thus define a basis in a linear space of observable costates. This result allows to *alternatively use observability matrix to determine observable and unobservable spaces as well as to check for complete observability*. Usage of *observability matrix* is especially favorable, when analysis is performed *analytically*, because Gramian-based approach is in this case problematic due to necessity to compute transition matrix of linear dynamic system. Based on presented relation, a unified approach to investigate observability in linear time-varying systems was suggested. The approach includes both *analytical and numerical methods* as well as a *strategy to verify analytical derivations by the means of numerical computation*. *Efficiency of the unified approach was demonstrated by conducting observability investigation in a problem of calibration of a strapdown inertial navigation system on low-grade turntables*.

In addition to that

A relation between deterministic observability concept and Kalman filtering was investigated.

It was shown that for linear systems without input noise covariance of the Kalman filter estimate presents an inverse of a sum of weighted observability Gramian and purely propagated inverse covariance of the state. Furthermore, it was demonstrated, how the *filter treats* the space of *unobservable linear combinations*.

The contributions related to observability theory are presented in Section 3.1 and Appendices A, E, and B.

Finally, it was demonstrated that

Suitable choice of filter mechanization could provide certain benefits for integrated navigation systems featuring low-cost inertial sensors.

For example, it was shown that mechanizing navigation filter of ADS aided INS in b-frame, rather than in n-frame, made behavior of covariance matrix much more robust to errors of total navigation state. Though, for INS, aided by altitude measurements, the situation appeared opposite, and n-frame mechanization demonstrated better performance. *Therefore it was argued that optimal mechanization could be application-specific and observability-dependent. Moreover, it was suggested that filter mechanization was chosen in such a way as to eliminate dependencies of measurement matrix on inaccurately estimated navigation parameters.*

Extensive discussion and simulation results are available in Appendix H.

Appendix A. Proof of the Theorem 4.

A series of facts, presented below, will be needed to prove Theorem 4.

Proposition 1. Costates defined by rows of observability matrix are observable in the sense of Definition 3.

Proof: Without loss of generality consider a case of scalar output. Define $u(\tau):[t_0,t]\to\mathbb{R}$ as

$$u(\tau)=y(t)/\int_{t_0}^{t}y(s)ds. \tag{A.1}$$

Then

$$h(t)x(t)=\int_{t_0}^{t}u(\tau)y(\tau)d\tau. \tag{A.2}$$

If t_0 is chosen in such a way that

$$\int_{t_0}^{t}y(s)ds\neq 0, \tag{A.3}$$

function $u(\tau)$ becomes continuous. In case $\forall\tau\le t\ \ y(\tau)=0$ definition of $u(\tau)$ remains correct since by mean value theorem for definite integrals

$$\int_{t_0}^{t}y(s)ds=y(\xi)(t-t_0),\ \ \xi\in[t_0,t], \tag{A.4}$$

and

$$u(\tau)=y(t)/\int_{t_0}^{t}y(s)ds=y(t)/\big(y(\xi)(t-t_0)\big)=y(t)/\big(y(t)(t-t_0)\big)=1/(t-t_0). \tag{A.5}$$

In order to compute derivatives of the output consider

$$u_i(\tau)=y^{(i)}(t)/\int_{t_0}^{t}y(s)ds. \tag{A.6}$$

In case $\forall\tau\le t\ \ y(\tau)=0$ definition remains correct since value of the function appears to be identically equal to the value of derivative (to zero). *End of Proof.*

Here and further $\mathbf{l}_i(\tau)$ denotes $(i+1)^{th}$ row of observability matrix $\mathbf{L}(\tau)$. In case of scalar output $0\le i\le n-1$. In case of vector output $0\le i\le nm-1$.

Proposition 2. *Let* $\dim \mathbf{y}(\tau)=1$ *and* $\operatorname{rank}\mathbf{L}(\tau)=r$ *for* $\forall \tau\in[t_*,t]$. *Then for* $\forall[t_1,t_2]\subset[t_*,t]$, $t_1<t_2$, $\exists\tau^*\in[t_1,t_2]$ *such that for* $\forall\ 0\le i\le r-1$ $\left\|\mathbf{l}_i(\tau^*)\right\|\neq 0$.

Proof: Suppose that $\exists[t_1,t_2]\subset[t_*,t]$, $t_1<t_2$, such that there exists $0\le i_0\le r-1$ and $\left\|\mathbf{l}_{i_0}(\tau)\right\|=0$ $\forall\tau\in[t_1,t_2]$. Then, by definition of observability matrix, $\left\|\mathbf{l}_j(\tau)\right\|=0$ for $\forall j>i_0$ and $\forall\tau\in[t_1,t_2]$. Thus $\operatorname{rank}\mathbf{L}(\tau)<r$ on $[t_1,t_2]$ which contradicts the assumption. *End of Proof.*

Proposition 3. *Let* $\dim \mathbf{y}(\tau)=1$ *and* $\operatorname{rank}\mathbf{L}(\tau)=r$ *for* $\forall \tau\in[t_*,t]$. *Then for* $\forall[t_1,t_2]\subset[t_*,t]$, $t_1<t_2$, $\exists\tau^*\in[t_1,t_2]$ *such that*

$$\operatorname{rank}\begin{pmatrix}\mathbf{l}_0(\tau^*)\\ \vdots\\ \mathbf{l}_{r-1}(\tau^*)\end{pmatrix}=r. \tag{A.7}$$

Proof: Consider $\forall[t_1,t_2]\subset[t_*,t]$. By Proposition 2 $\exists\tau_0^*\in[t_1,t_2]$ such that $\left\|\mathbf{l}_0(\tau_0^*)\right\|\neq 0$. Moreover, since $\mathbf{l}_0(\tau)$ is continuous, there exists $[t_1^0,t_2^0]\ni\tau_0^*$, $[t_1^0,t_2^0]\subset[t_1,t_2]$, $t_1^0<t_2^0$, such that $\left\|\mathbf{l}_0(\tau)\right\|\neq 0$ $\forall\tau\in[t_1^0,t_2^0]$. Again, by Proposition 2, $\exists\tau_1^*\in[t_1^0,t_2^0]$ such that $\left\|\mathbf{l}_1(\tau_1^*)\right\|\neq 0$. But since $\mathbf{l}_1(\tau)$ is continuous, there exists $[t_1^1,t_2^1]\ni\tau_1^*$, $[t_1^1,t_2^1]\subset[t_1^0,t_2^0]$, $t_1^1<t_2^1$ such that $\left\|\mathbf{l}_1(\tau)\right\|\neq 0$ $\forall\tau\in[t_1^1,t_2^1]$. Rows $\mathbf{l}_0(\tau)$ and $\mathbf{l}_1(\tau)$ are linearly independent on some $[t_1^{1,0},t_2^{1,0}]\subset[t_1^1,t_2^1]$, because otherwise, by definition of observability matrix, rows $\mathbf{l}_2(\tau),\ldots,\mathbf{l}_{n-1}(\tau)$ would be proportional to $\mathbf{l}_0(\tau)$ and $\operatorname{rank}\mathbf{L}(\tau)$ would be equal to one $\forall\tau\in[t_1^1,t_2^1]$, which contradicts hypotheses of the proposition. Applying the same reasoning sequentially to rows $\mathbf{l}_2(\tau),\ldots,\mathbf{l}_{r-1}(\tau)$ starting from interval $[t_1^{1,0},t_2^{1,0}]$ we obtain that there exists $[t_1^{r-1,0},t_2^{r-1,0}]$, where the first r rows of observability matrix are linearly independent. τ^* can be chosen arbitrarily from the closed interval $[t_1^{r-1,0},t_2^{r-1,0}]$. *End of Proof.*

Denote T a set of all $\tau^*\in[t_*,t]$ such that

$$\operatorname{rank}\begin{pmatrix}\mathbf{l}_0(\tau^*)\\ \vdots\\ \mathbf{l}_{r-1}(\tau^*)\end{pmatrix}=r. \tag{A.8}$$

Proposition 4. *Let* $\dim \mathbf{y}(\tau)=1$ *and* $\operatorname{rank}\mathbf{L}(\tau)=r$ $\forall\tau\in[t_*,t]$. *Then* $\forall\delta>0$ $\bigcup_{\tau^*\in T}U_\delta(\tau^*)\supset[t_*,t]$.

Proof: Let there exist $\delta_0>0$ and $\tau_0\in[t_*,t]$ such that

$$\tau_0\notin\bigcup_{\tau^*\in T}U_\delta(\tau^*).$$

Obviously, $\tau_0\notin T$. Consider $\forall\delta_1<\delta_0$ and closed interval $\Delta=[\tau_0,\tau_0+\delta_1]\subset[t_*,t]$, if $\tau_0\in[t_*,t)$, and $\Delta=[\tau_0-\delta_1,\tau_0]\subset[t_*,t]$, if $\tau_0=t$. Then, by Proposition 3, there exists $\tau^*\in\Delta$ such that

$$\operatorname{rank}\begin{pmatrix} \mathbf{l}_0(\tau^*) \\ \vdots \\ \mathbf{l}_{r-1}(\tau^*) \end{pmatrix} = r.$$

Hence $\tau_0 \in U_{\delta_0}(\tau^*)$, which contradicts initial assumption. *End of Proof.*

Proposition 5. *Let* $\dim \mathbf{y}(\tau) = 1$ *and assume that system and measurement matrices are analytic on* $[t_*, t]$. *Then set* $T_1 = [t_*, t] \setminus T$ *is finite.*

Proof: Suppose that the set T_1 consists of infinite number of points. Then $\forall \delta > 0$ $\{U_\delta(\tau^*)\}_{\tau^* \in T}$ is a cover of $[t_*, t]$. Closed interval is compact, and thus, there exists a finite subcover $\{U_\delta(\tau_i^*)\}_{i=1,\, \tau_i^* \in T}^{N}$ $\forall \delta > 0$. For some i_0 a neighborhood $U_\delta(\tau_{i_0}^*)$ contains infinite number of points from T_1. Consider closure of $[t_*, t] \bigcap U_\delta(\tau_{i_0}^*) = \Delta_0$, which is a closed interval, and a sequence of closed intervals Δ_i, $0 < i < \infty$, where Δ_i is half of Δ_{i-1}, which contains infinite number of points from T_1. Sequence $\Delta_0 \supset \Delta_1 \supset \ldots \supset \Delta_i \supset \ldots$ is nested and length of Δ_i converges to zero given $i \to \infty$. By Cantor's intersection theorem [102] $\exists c \in \bigcap_{i=0}^{\infty} \Delta_i$. Consider now function $f(\tau) = \det\left(\mathbf{L}^r (\mathbf{L}^r)^{\mathrm{T}}\right)$, where

$$\mathbf{L}^r = \begin{pmatrix} \mathbf{l}_0(\tau) \\ \vdots \\ \mathbf{l}_{r-1}(\tau) \end{pmatrix}. \tag{A.9}$$

$f(\tau)$ is analytic, $f(\tau) \geq 0$, and $f(\tau) = 0$ if and only if rows $\mathbf{l}_0(\tau), \ldots, \mathbf{l}_{r-1}(\tau)$ are linearly dependent [103]. By construction, any $U_\delta(c)$ contains infinite number of points, where $f(\tau) = 0$.

Assume that $f(c) = 0$. Then c is a limit point of a set of zeros of $f(\tau)$, and, consequently, $f(\tau) \equiv 0$. This leads to a contradiction with Proposition 3.

In case $f(c) \neq 0$, there exists a neighborhood $U_{\delta_2}(c)$ such that $\left| f(U_{\delta_2}(c)) \right| > \varepsilon_2$. But any neighborhood of c by construction contains infinite number of points, where $f(\tau) = 0$. This again leads to a contradiction. *End of Proof.*

Lemma 1. *Let a square matrix* $\mathbf{M}(\tau)$ *be continuous on a closed interval* $[t_*, t]$, *and let* $\det \mathbf{M}(\tau) \neq 0$ *for* $\forall \tau \in [t_*, t]$. *Then* $\mathbf{M}^{-1}(\tau)$ *is continuous on* $[t_*, t]$.

Proof: Inverse matrix is given by $\mathbf{M}^{-1}(\tau) = 1 / \det \mathbf{M}(\tau) \cdot \mathbf{C}^{\mathrm{T}}$, where $\mathbf{C}$ is a matrix of cofactors. Elements of cofactor matrix are sums of products of elements of $\mathbf{M}(\tau)$ and thus are continuous on $[t_*, t]$. Since $\det \mathbf{M}(\tau) \neq 0$ for $\forall \tau \in [t_*, t]$, $1 / \det \mathbf{M}(\tau)$ is continuous on $[t_*, t]$. A product of continuous functions is continuous, which implies continuity of elements of $\mathbf{M}^{-1}(\tau)$. *End of Proof.*

Lemma 2. *Suppose that matrix* $\mathbf{L}(\tau)$ *of dimension* $p \times n$, $p > n$ *is continuous on closed interval* $[t_*, t]$, $\operatorname{rank} \mathbf{L}(\tau) = r < n$ $\forall \tau \in [t_*, t]$, *and that there exists a set* $\{\mathbf{l}_{jk}(\tau)\}_{k=1}^{r}$, $jk \in \{0, \ldots, nm-1\}$, *of rows of*

$\mathbf{L}(\tau)$, *which are linearly independent* $\forall \tau \in [t_*, t]$. *Denote* $\mathbf{l}(\tau)$ *an arbitrary row of matrix* $\mathbf{L}(\tau)$. *Then* $\mathbf{l}(\tau) = \sum_{k=1}^{r} c_k(\tau) \cdot \mathbf{l}_{jk}(\tau)$, *where* $c_k(\tau)$ *are continuous on* $[t_*, t]$ *functions.*

Proof: Coefficients of expansion are given by

$$\begin{pmatrix} c_1(\tau) & \dots & c_r(\tau) \end{pmatrix} = \mathbf{l}(\tau) \cdot \mathbf{P}^{\mathrm{T}} \left(\mathbf{P}\mathbf{P}^{\mathrm{T}} \right)^{-1} \tag{A.10}$$

where

$$\mathbf{P}(\tau) = \begin{pmatrix} \mathbf{l}_{j1}(\tau) \\ \vdots \\ \mathbf{l}_{jr}(\tau) \end{pmatrix}. \tag{A.11}$$

$\mathbf{l}_{j1}(\tau), \dots, \mathbf{l}_{jr}(\tau)$ are linearly independent for $\forall \tau \in [t_*, t]$. Hence $\mathbf{P}\mathbf{P}^{\mathrm{T}}$ is invertible on $[t_*, t]$. By Lemma 1 inverse matrix of $\mathbf{P}\mathbf{P}^{\mathrm{T}}$ is continuous, which implies continuity of coefficients $c_k(\tau)$. *End of Proof.*

Lemma 3. Suppose that matrices $\mathbf{A}(\tau)$ *and* $\mathbf{H}(\tau)$ *are analytic, and that rank of observability matrix* $\mathbf{L}(\tau)$ *is constant on* $[t_*, t]$ *and equals to* $r < n$. *Suppose that there exists a set of* r *rows* $\{\mathbf{l}_{js}(\tau)\}_{s=1}^{r}$, $js \in \{0, \dots, nm-1\}$, *of* $\mathbf{L}(\tau)$, *which are linearly independent* $\forall \tau \in [t_*, t]$ *and that ranks of observability matrices* $\mathbf{L}^1(\tau), \dots, \mathbf{L}^m(\tau)$, *generated by rows of* $\mathbf{H}(\tau)$, *are constant on* $[t_*, t]$. *Then vector* $\mathbf{z} = \left(\mathbf{l}_{j1}(\tau)\mathbf{x}, \dots, \mathbf{l}_{jr}(\tau)\mathbf{x} \right)^{\mathrm{T}}$ *satisfies a system of linear differential equations*

$$\dot{\mathbf{z}} = \mathbf{A}_{1,r\times r}(\tau)\mathbf{z}, \tag{A.12}$$

and matrix $\mathbf{A}_{1,r\times r}(\tau)$ *is continuous on* $[t_*, t]$.

Proof: Assume that $\max\{\mathbf{l}_{js}(\tau)\}_{s=1}^{r} \le (n-1)m - 1$. Then for $\forall s \in \{1, \dots, r\}$

$$\dot{z}_{js} = \frac{d}{d\tau}(\mathbf{l}_{js}(\tau)\mathbf{x}) = \left(\dot{\mathbf{l}}_{js}(\tau) + \mathbf{l}_{js}(\tau)\mathbf{A}(\tau) \right)\mathbf{x}. \tag{A.13}$$

Note that $\dot{\mathbf{l}}_{js}(\tau) + \mathbf{l}_{js}(\tau)\mathbf{A}(\tau)$ is one of the rows of observability matrix $\mathbf{L}(\tau)$, and thus

$$\dot{\mathbf{l}}_{js}(\tau) + \mathbf{l}_{js}(\tau)\mathbf{A}(\tau) = \sum_{k=1}^{r} c_k(\tau)\mathbf{l}_{jk}(\tau). \tag{A.14}$$

By Lemma 2 $c_k(\tau)$ are continuous on $[t_*, t]$. From (A.13) and (A.14) it follows that

$$\dot{z}_{js} = \left(\sum_{k=1}^{r} c_k(\tau)\mathbf{l}_{jk}(\tau) \right)\mathbf{x} = \sum_{k=1}^{r} c_k(\tau) z_{jk}(\tau), \tag{A.15}$$

and consequently vector $\mathbf{z}$ satisfies (A.12).
Consider now that some js satisfies $(n-1)m - 1 \le js \le nm - 1$. Then

$$\dot{z}_{js} = \frac{d}{d\tau}(\mathbf{l}_{js}(\tau)\mathbf{x}) = \left(\dot{\mathbf{l}}_{js}(\tau) + \mathbf{l}_{js}(\tau)\mathbf{A}(\tau) \right)\mathbf{x}, \tag{A.16}$$

but $\mathbf{l}_{js+m}(\tau)=\dot{\mathbf{l}}_{js}(\tau)+\mathbf{l}_{js}(\tau)\mathbf{A}(\tau)$ does not appear to be a row of $\mathbf{L}(\tau)$. However, $\mathbf{l}_{js+m}(\tau)$ appears to be generated by some row of $\mathbf{H}(\tau)$. Observability matrix $\mathbf{L}^*(\tau)$ corresponding to the generating row of $\mathbf{H}(\tau)$ has constant rank on $[t_*,t]$. By Proposition 5 $[t_*,t]\setminus T_1=[t_*,t_1)\cup(t_1,t_2)\cup\ldots\cup(t_N,t]$, where

$$T_1=\{\tau^*\in[t_*,t]:\operatorname{rank}\begin{pmatrix}\mathbf{l}_0^*(\tau)\\ \vdots\\ \mathbf{l}_r^*(\tau)\end{pmatrix}<r\}. \tag{A.17}$$

On each $\Delta_1=[t_*,t_1)$, $\Delta_i=(t_{i-1},t_i)$, $\Delta_{N+1}=(t_N,t]$

$$\mathbf{l}_r^*(\tau)=\sum_{s=0}^{r-1}\alpha_s^r(\tau)\mathbf{l}_s^*(\tau). \tag{A.18}$$

By Lemma 2 $\alpha_s^r(\tau)$ are continuous on Δ_i. Consequently, by definition of observability matrix, the same holds for $\mathbf{l}_k^*(\tau)$, $r<k\le n-1$, and $\mathbf{l}_{js+m}(\tau)$. That is why on each Δ_i

$$\mathbf{l}_{js+m}(\tau)=\sum_{s=0}^{r-1}\alpha_s^r(\tau)\mathbf{l}_s^*(\tau)=\sum_{s=0}^{r-1}\alpha_s^r(\tau)\sum_{k=1}^{r}c_k^s(\tau)\mathbf{l}_{jk}(\tau)=\sum_{k=1}^{r}\left(\sum_{s=0}^{r-1}\alpha_s^r(\tau)c_k^s(\tau)\right)\mathbf{l}_{jk}(\tau). \tag{A.19}$$

Coefficients of expansion $\beta_k^{js+m}(\tau)=\sum_{s=0}^{r-1}\alpha_s^r(\tau)c_k^s(\tau)$ can be computed from

$$\left(\beta_1^{js+m}(\tau)\quad\ldots\quad\beta_r^{js+m}(\tau)\right)=\mathbf{l}_{js+m}(\tau)\cdot\mathbf{P}^{\mathrm{T}}\left(\mathbf{P}\mathbf{P}^{\mathrm{T}}\right)^{-1}, \tag{A.20}$$

where

$$\mathbf{P}(\tau)=\begin{pmatrix}\mathbf{l}_{j1}(\tau)\\ \vdots\\ \mathbf{l}_{jr}(\tau)\end{pmatrix}. \tag{A.21}$$

By Lemma 1 $\beta_k^{js+m}(\tau)$ are continuous on $[t_*,t]$ functions and consequently expansion $\mathbf{l}_{js+m}(\tau)=\sum_{k=1}^{r}\beta_k^{js+m}(\tau)\mathbf{l}_{jk}(\tau)$ holds at $\forall\tau\in[t_*,t]$. Hence

$$\dot{z}_{js}=\sum_{k=1}^{r}\beta_k^{js+m}(\tau)\mathsf{z}_{jk} \tag{A.22}$$

and vector $\mathbf{z}$ satisfies (A.12). *End of Proof.*

Proof of the Theorem 4: Consider $\boldsymbol{\eta}(t)$ such that $\mathbf{L}(t)\boldsymbol{\eta}(t)=\mathbf{0}$. Then for $\forall t_0\in[t_*,t)$

$$\begin{aligned}\mathbf{W}(t,t_0)\boldsymbol{\eta}(t)&=\int_{t_0}^{t}\boldsymbol{\Phi}^{\mathrm{T}}(\tau,t)\mathbf{H}^{\mathrm{T}}(\tau)\mathbf{H}(\tau)\boldsymbol{\Phi}(\tau,t)d\tau\cdot\boldsymbol{\eta}(t)\\ &=\int_{t_0}^{t}\boldsymbol{\Phi}^{\mathrm{T}}(\tau,t)\mathbf{H}^{\mathrm{T}}(\tau)\mathbf{H}(\tau)\boldsymbol{\Phi}(\tau,t)\boldsymbol{\eta}(t)d\tau=\int_{t_0}^{t}\boldsymbol{\Phi}^{\mathrm{T}}(\tau,t)\mathbf{H}^{\mathrm{T}}(\tau)\mathbf{y}_1(\tau)d\tau,\end{aligned} \tag{A.23}$$

where $\mathbf{y}_1(\tau)$ is output function, generated by boundary condition $\mathbf{x}(t)=\boldsymbol{\eta}(t)$. By Lemma 3, components of vector function $\mathbf{y}_1(\tau)$ can be computed as a linear combination of the solution of

equation (A.12). Note that $\mathbf{L}(t)\boldsymbol{\eta}(t)=\mathbf{0}$ implies $\mathbf{z}(t)=\mathbf{0}$, and matrix $\mathbf{A}_{1,r\times r}(\tau)$ of Equation (A.12) is continuous on $[t_*,t]$. Thus, there exists only a trivial solution $\mathbf{z}(\tau)\equiv\mathbf{0}$. Consequently, $\mathbf{y}_1(\tau)\equiv\mathbf{0}$ on $[t_*,t]$, and $\mathbf{W}(t,t_0)\boldsymbol{\eta}(t)=0$. This means that

$$\dim \operatorname{Ker}\mathbf{W}(t,t_0)\geq n-r,\ \forall t_0\in[t_*,t). \tag{A.24}$$

(A.24) implies that

$$\dim \operatorname{Im}\mathbf{W}(t,t_0)\leq r,\ \forall t_0\in[t_*,t). \tag{A.25}$$

But, by Proposition 1,

$$\dim \operatorname{Im}\mathbf{W}(t,t_0)\geq r,\ \forall t_0\in[t_*,t). \tag{A.26}$$

Thus, $\dim \operatorname{Im}\mathbf{W}(t,t_0)=r,\ \forall t_0\in[t_*,t)$, and transposed rows of observability matrix $\mathbf{L}(t)$ span $\bigcup_{t_*<t_0<t}\operatorname{Im}\mathbf{W}(t,t_0)$. *End of Proof.*

Appendix B. Observability and Kalman filtering.

The notion of observability is deterministic and appears to be defined by a pair of system and measurement matrices. Kalman filter, in turn, has probabilistic nature, and thus besides observability, properties of input and measurement noises contribute significantly to behavior of the filter's output, i. e. to behavior of estimated mean and conditional covariance matrix. Even though importance of deterministic observability for Kalman filter performance is in general understood by engineering society, exact relation between the filter and observability concept seems to be missing in classic books on control and estimation theory [16, 17, 20, 21, 104-106], as well as in the works that are dedicated to investigation of observability in various navigation applications [107-111]. Therefore in this chapter further insights into the relation between observability and Kalman filtering are presented.

B.1 Solution of covariance equation in "zero noise" case

Consider linear system

$$\begin{aligned}\dot{\mathbf{x}}(t) &= \mathbf{A}(t)\mathbf{x}(t) + \mathbf{\Gamma}(t)\mathbf{q}(t),\\ \mathbf{y}(t) &= \mathbf{H}(t)\mathbf{x}(t) + \mathbf{r}(t).\end{aligned} \tag{B.1}$$

Assume that $\mathbf{x}(t_0) \sim N(\tilde{\mathbf{x}}(t_0), \mathbf{P}(t_0))$, and that $\mathbf{q}(t)$ and $\mathbf{r}(t)$ are Gaussian white noises, such that

$$\begin{aligned}&\mathrm{E}\left[\mathbf{q}(t)\right] = 0,\ \mathrm{E}\left[\mathbf{q}(t)\mathbf{q}^{\mathrm{T}}(\tau)\right] = \mathbf{Q}(t)\delta(t-\tau),\\ &\mathrm{E}\left[\mathbf{r}(t)\right] = 0,\ \mathrm{E}\left[\mathbf{r}(t)\mathbf{r}^{\mathrm{T}}(\tau)\right] = \mathbf{R}(t)\delta(t-\tau),\\ &\mathrm{E}\left[\mathbf{x}(t_0)\mathbf{r}^{\mathrm{T}}(t)\right] = 0,\ \mathrm{E}\left[\mathbf{x}(t_0)\mathbf{q}^{\mathrm{T}}(t)\right] = 0,\\ &\mathrm{E}\left[\mathbf{r}(t)\mathbf{q}^{\mathrm{T}}(\tau)\right] = 0.\end{aligned} \tag{B.2}$$

Then covariance matrix of conditional expectation $\mathrm{E}[\mathbf{x}(t)\,|\,\mathbf{y}(t)]$ is subject to matrix Riccati equation (see Section 2.6.2)

$$\dot{\mathbf{P}}(t) = \mathbf{A}(t)\mathbf{P}(t) + \mathbf{P}(t)\mathbf{A}^{\mathrm{T}}(t) + \mathbf{\Gamma}(t)\mathbf{Q}(t)\mathbf{\Gamma}^{\mathrm{T}}(t) - \mathbf{P}(t)\mathbf{H}^{\mathrm{T}}(t)\mathbf{R}^{-1}(t)\mathbf{H}(t)\mathbf{P}(t),\ \mathbf{P}(t_0) = \mathbf{P}_0. \tag{B.3}$$

It is well known [24] that the quadratic equation (B.3) can be replaced by the following linear matrix equation of higher dimensionality

$$\begin{pmatrix}\dot{\mathbf{\Psi}}_1\\ \dot{\mathbf{\Psi}}_2\end{pmatrix} = \begin{pmatrix}\mathbf{A}(t) & \mathbf{\Gamma}(t)\mathbf{Q}(t)\mathbf{\Gamma}^{\mathrm{T}}(t)\\ \mathbf{H}^{\mathrm{T}}(t)\mathbf{R}^{-1}(t)\mathbf{H}(t) & -\mathbf{A}^{\mathrm{T}}(t)\end{pmatrix}\begin{pmatrix}\mathbf{\Psi}_1\\ \mathbf{\Psi}_2\end{pmatrix},\ \mathbf{\Psi}_1(t_0) = \mathbf{P}_0,\ \mathbf{\Psi}_2(t_0) = \mathbf{I}. \tag{B.4}$$

The solution of (B.3) can be expressed in terms of the solution of (B.4) as

$$\mathbf{P}(t) = \boldsymbol{\Psi}_1(t)\boldsymbol{\Psi}_2^{-1}(t). \tag{B.5}$$

In case $\mathbf{Q}(t) \equiv \mathbf{0}$ the solution of (B.4) takes the form

$$\begin{aligned} \boldsymbol{\Psi}_1(t) &= \boldsymbol{\Phi}(t, t_0)\mathbf{P}_0, \\ \boldsymbol{\Psi}_2(t) &= \boldsymbol{\Phi}^{\mathrm{T}}(t_0, t) + \left(\int_{t_0}^{t} \boldsymbol{\Phi}^{\mathrm{T}}(\tau, t)\mathbf{H}^{\mathrm{T}}(\tau)\mathbf{R}^{-1}(\tau)\mathbf{H}(\tau)\boldsymbol{\Phi}(\tau, t_0)d\tau \right) \cdot \mathbf{P}_0, \end{aligned} \tag{B.6}$$

where $\boldsymbol{\Phi}(t, t_0)$ is transition matrix of the system (B.1).

Note that

$$\begin{aligned} &\int_{t_0}^{t} \boldsymbol{\Phi}^{\mathrm{T}}(\tau, t)\mathbf{H}^{\mathrm{T}}(\tau)\mathbf{R}^{-1}(\tau)\mathbf{H}(\tau)\boldsymbol{\Phi}(\tau, t_0)d\tau = \\ &= \int_{t_0}^{t} \boldsymbol{\Phi}^{\mathrm{T}}(\tau, t)\mathbf{H}^{\mathrm{T}}(\tau)\mathbf{R}^{-1}(\tau)\mathbf{H}(\tau)\boldsymbol{\Phi}(\tau, t)d\tau \cdot \boldsymbol{\Phi}(t, t_0) = \mathbf{W}_{\mathbf{R}}(t, t_0)\boldsymbol{\Phi}(t, t_0), \end{aligned} \tag{B.7}$$

and

$$\mathbf{W}_{\mathbf{R}}(t, t_0) = \int_{t_0}^{t} \boldsymbol{\Phi}^{\mathrm{T}}(\tau, t)\mathbf{H}^{\mathrm{T}}(\tau)\mathbf{R}^{-1}(\tau)\mathbf{H}(\tau)\boldsymbol{\Phi}(\tau, t)d\tau \tag{B.8}$$

presents observability Gramian of a system

$$\begin{aligned} \dot{\mathbf{x}}(t) &= \mathbf{A}(t)\mathbf{x}(t) + \boldsymbol{\Gamma}(t)\mathbf{q}(t), \\ \mathbf{y}_1(t) &= \mathbf{H}_1(t)\mathbf{x}(t) + \mathbf{r}_1(t), \end{aligned} \tag{B.9}$$

where

$$\mathbf{y}_1(t) = \mathbf{U}(t)\mathbf{y}(t),\ \mathbf{H}_1(t) = \mathbf{U}(t)\mathbf{H}(t),\ \mathbf{r}_1(t) = \mathbf{U}(t)\mathbf{r}(t), \tag{B.10}$$

and the matrix $\mathbf{U}(t)$ satisfies

$$\mathbf{R}^{-1}(t) = \mathbf{U}^{\mathrm{T}}(t)\mathbf{U}(t). \tag{B.11}$$

Covariance matrix of the measurement noise $\mathbf{r}_1(t)$ in (B.9) is identity matrix, and therefore the quantity $\mathbf{W}_{\mathbf{R}}(t, t_0)$ can be understood as a „weighted“ observability Gramian, i. e. observability Gramian of a system, whose measurement noise was decorrelated and normalized by the means of a linear transformation of an output.

Consequently,

$$\begin{aligned} \mathbf{P}^{-1}(t) &= \boldsymbol{\Psi}_2(t)\boldsymbol{\Psi}_1^{-1}(t) = \left(\boldsymbol{\Phi}^{\mathrm{T}}(t_0, t) + \mathbf{W}_{\mathbf{R}}(t, t_0)\boldsymbol{\Phi}(t, t_0)\mathbf{P}_0 \right)\mathbf{P}_0^{-1}\boldsymbol{\Phi}(t_0, t) = \\ &= \boldsymbol{\Phi}^{\mathrm{T}}(t_0, t)\mathbf{P}_0^{-1}\boldsymbol{\Phi}(t_0, t) + \mathbf{W}_{\mathbf{R}}(t, t_0), \end{aligned} \tag{B.12}$$

and the solution of (B.3) takes the form

$$\boxed{\mathbf{P}(t) = \left(\boldsymbol{\Phi}^{\mathrm{T}}(t_0, t)\mathbf{P}_0^{-1}\boldsymbol{\Phi}(t_0, t) + \mathbf{W}_{\mathbf{R}}(t, t_0) \right)^{-1}} \tag{B.13}$$

The formula (B.13) states that in zero noise case inverse of covariance of the conditional expectation presents a sum of the propagated inverse of the covariance of $\mathbf{x}(t)$ *and the weighted observability Gramian.*

Similar to normal observability Gramian (3.5), the weighted observability Gramian is subject to Lyapunov equation

$$\dot{\mathbf{W}}_{\mathbf{R}}(t,t_0) = -\mathbf{A}^{\mathrm{T}}(t)\mathbf{W}_{\mathbf{R}}(t,t_0) - \mathbf{W}_{\mathbf{R}}(t,t_0)\mathbf{A}(t) + \mathbf{H}^{\mathrm{T}}(t)\mathbf{R}^{-1}(t)\mathbf{H}(t),\ \mathbf{W}_{\mathbf{R}}(t_0,t_0) = \mathbf{0}. \tag{B.14}$$

B.2 Kalman filter and Kalman canonical decomposition

Assume that in the system (B.1) matrices $\mathbf{A}$ and $\mathbf{H}$ are constant. Then there exists invertible matrix $\mathbf{T}$, such that coordinate transformation

$$\begin{pmatrix} \boldsymbol{\xi} \\ \boldsymbol{\eta} \end{pmatrix} = \mathbf{T}\mathbf{x} \tag{B.15}$$

converts the system (B.1) to the form

$$\begin{aligned} \dot{\boldsymbol{\xi}}(t) &= \mathbf{A}_{11}\boldsymbol{\xi}(t) + \mathbf{v}_1(t), \\ \dot{\boldsymbol{\eta}}(t) &= \mathbf{A}_{21}\boldsymbol{\xi}(t) + \mathbf{A}_{22}\boldsymbol{\eta}(t) + \mathbf{v}_2(t), \\ \mathbf{y}(t) &= \mathbf{H}_{11}\boldsymbol{\xi}(t) + \mathbf{r}(t), \end{aligned} \tag{B.16}$$

where $\dim\boldsymbol{\xi}$ equals to dimension of observable subspace, and subsystem

$$\begin{aligned} \dot{\boldsymbol{\xi}}(t) &= \mathbf{A}_{11}\boldsymbol{\xi}(t) + \mathbf{v}_1(t), \\ \mathbf{y}(t) &= \mathbf{H}_{11}\boldsymbol{\xi}(t) + \mathbf{r}(t), \end{aligned} \tag{B.17}$$

is completely observable. Transformation of an arbitrary linear time invariant system to the form (B.16) is called Kalman canonical decomposition, and the vectors $\boldsymbol{\xi}$ and $\boldsymbol{\eta}$ present observable and unobservable linear combinations of the components of the initial state vector $\mathbf{x}$, respectively [16, 104]. In (B.16)

$$\begin{pmatrix} \mathbf{v}_1(t) \\ \mathbf{v}_2(t) \end{pmatrix} = \mathbf{T}\boldsymbol{\Gamma}(t)\mathbf{q}(t). \tag{B.18}$$

Expectation and the covariance of the transformed noise (B.18) are given by

$$\mathrm{E}\left[\begin{pmatrix} \mathbf{v}_1(t) \\ \mathbf{v}_2(t) \end{pmatrix}\right] = \mathbf{0},\ \ \mathrm{E}\left[\begin{pmatrix} \mathbf{v}_1(t) \\ \mathbf{v}_2(t) \end{pmatrix} \cdot \begin{pmatrix} \mathbf{v}_1^{\mathrm{T}}(t) & \mathbf{v}_2^{\mathrm{T}}(t) \end{pmatrix}\right] = \mathbf{S}(t) = \mathbf{T}\boldsymbol{\Gamma}(t)\mathbf{Q}(t)\boldsymbol{\Gamma}^{\mathrm{T}}(t)\mathbf{T}^{\mathrm{T}}. \tag{B.19}$$

Denote

$$\mathbf{P}(t) = \begin{pmatrix} \mathbf{P}_{\xi\xi}(t) & \mathbf{P}_{\xi\eta}(t) \\ \mathbf{P}_{\xi\eta}^{\mathrm{T}}(t) & \mathbf{P}_{\eta\eta}(t) \end{pmatrix},\ \mathbf{S} = \begin{pmatrix} \mathbf{S}_{\xi\xi}(t) & \mathbf{S}_{\xi\eta}(t) \\ \mathbf{S}_{\xi\eta}^{\mathrm{T}}(t) & \mathbf{S}_{\eta\eta}(t) \end{pmatrix}. \tag{B.20}$$

In the new coordinate system equation (B.3) for the covariance matrix reduces to

$$\boxed{\begin{aligned}
&\dot{\mathbf{P}}_{\xi\xi}(t) = \mathbf{A}_{11}\mathbf{P}_{\xi\xi}(t) + \mathbf{P}_{\xi\xi}(t)\mathbf{A}_{11}^{\mathrm{T}} + \mathbf{S}_{\xi\xi}(t) - \mathbf{P}_{\xi\xi}(t)\mathbf{H}_{11}^{\mathrm{T}}\mathbf{R}^{-1}(t)\mathbf{H}_{11}\mathbf{P}_{\xi\xi}(t),\\
&\dot{\mathbf{P}}_{\xi\eta}(t) = \mathbf{A}_{11}\mathbf{P}_{\xi\eta}(t) + \mathbf{P}_{\xi\xi}(t)\mathbf{A}_{21}^{\mathrm{T}} + \mathbf{P}_{\xi\eta}^{\mathrm{T}}(t)\mathbf{A}_{22}^{\mathrm{T}} + \mathbf{S}_{\xi\eta}(t) - \mathbf{P}_{\xi\xi}(t)\mathbf{H}_{11}^{\mathrm{T}}\mathbf{R}^{-1}(t)\mathbf{H}_{11}\mathbf{P}_{\xi\eta}(t),\\
&\dot{\mathbf{P}}_{\eta\eta}(t) = \mathbf{A}_{21}\mathbf{P}_{\xi\eta}(t) + \mathbf{A}_{22}\mathbf{P}_{\eta\eta}(t) + \mathbf{P}_{\xi\eta}^{\mathrm{T}}(t)\mathbf{A}_{21}^{\mathrm{T}} + \mathbf{P}_{\eta\eta}(t)\mathbf{A}_{22}^{\mathrm{T}} + \mathbf{S}_{\eta\eta}(t) - \mathbf{P}_{\xi\eta}^{\mathrm{T}}(t)\mathbf{H}_{11}^{\mathrm{T}}\mathbf{R}^{-1}(t)\mathbf{H}_{11}\mathbf{P}_{\xi\eta}(t).
\end{aligned}} \tag{B.21}$$

and thus the optimal estimator (2.34) takes the form

$$\begin{aligned}
&\dot{\tilde{\boldsymbol{\xi}}}(t) = \mathbf{A}_{11}\tilde{\boldsymbol{\xi}}(t) + \mathbf{K}_{\xi}(t)\left(\mathbf{y}(t) - \mathbf{H}_{11}\tilde{\boldsymbol{\xi}}(t)\right),\\
&\dot{\tilde{\boldsymbol{\eta}}}(t) = \mathbf{A}_{21}\tilde{\boldsymbol{\xi}}(t) + \mathbf{A}_{22}\tilde{\boldsymbol{\eta}}(t) + \mathbf{K}_{\eta}(t)\left(\mathbf{y}(t) - \mathbf{H}_{11}\tilde{\boldsymbol{\xi}}(t)\right).
\end{aligned} \tag{B.22}$$

The gains of the estimator are given by

$$\mathbf{K} = \begin{pmatrix} \mathbf{K}_{\xi}(t) \\ \mathbf{K}_{\eta}(t) \end{pmatrix} = \begin{pmatrix} \mathbf{P}_{\xi\xi}(t)\mathbf{H}_{11}^{\mathrm{T}}\mathbf{R}(t)^{-1} \\ \mathbf{P}_{\xi\eta}^{\mathrm{T}}(t)\mathbf{H}_{11}^{\mathrm{T}}\mathbf{R}(t)^{-1} \end{pmatrix}. \tag{B.23}$$

(B.22), in turn, implies the following dynamics of errors $\delta\boldsymbol{\xi} = \boldsymbol{\xi} - \tilde{\boldsymbol{\xi}}$ and $\delta\boldsymbol{\eta} = \boldsymbol{\eta} - \tilde{\boldsymbol{\eta}}$

$$\boxed{\begin{aligned}
&\delta\dot{\boldsymbol{\xi}} = \left(\mathbf{A}_{11} - \mathbf{K}_{\xi}(t)\mathbf{H}_{11}\right)\delta\boldsymbol{\xi},\\
&\delta\dot{\boldsymbol{\eta}} = \left(\mathbf{A}_{21} - \mathbf{K}_{\eta}(t)\mathbf{H}_{11}\right)\delta\boldsymbol{\xi} + \mathbf{A}_{22}\delta\boldsymbol{\eta}.
\end{aligned}} \tag{B.24}$$

Formulae (B.21), (B.23), and (B.24) allow to make several important conclusions about capabilities and performance of the Kalman filter:

1. *Uncertainties in unobservable subspace do not affect the estimates of observable states.*
2. *Since the subsystem (B.17) is completely observable,* $\delta\boldsymbol{\xi} \to \mathbf{0}$, $t \to \infty$.
3. *Kalman filter cannot estimate meaningfully unobservable states, unless all the eigenvalues of* $\mathbf{A}_{22}$ *have negative real parts.*
4. *Gains for unobservable states are zero if and only if* $\mathbf{H}_{11}\mathbf{P}_{\xi\eta}(t) \equiv \mathbf{0}$. *This can happen, for example, if* $\mathbf{P}_{\xi\eta}(t_0) = \mathbf{0}$, $\mathbf{A}_{21} = \mathbf{0}$, $\mathbf{S}_{\xi\eta}(t) \equiv \mathbf{0}$.

Proof of the second conclusion is available in the book [21], while the statement itself can be found in many other sources. Ideas introduced in the current section can partly be found in the work [112].

B.3 Solution of covariance equation in "zero noise" case for decomposed LTI system

Consider linear time invariant (LTI) system in the decomposed form (B.16) and assume that $\mathbf{Q}(t) \equiv \mathbf{0}$. In the system (B.16) matrices $\mathbf{A}$ and $\mathbf{H}$ are given by

$$\mathbf{A} = \begin{pmatrix} \mathbf{A}_{11} & \mathbf{0} \\ \mathbf{A}_{21} & \mathbf{A}_{22} \end{pmatrix}, \mathbf{H} = \begin{pmatrix} \mathbf{H}_{11} & \mathbf{0} \end{pmatrix}, \tag{B.25}$$

and therefore the transition matrix takes the form

$$\boldsymbol{\Phi}(t,t_0)=\begin{pmatrix}\boldsymbol{\Phi}_{11}(t,t_0) & \mathbf{0}\\ \boldsymbol{\Phi}_{21}(t,t_0) & \boldsymbol{\Phi}_{22}(t,t_0)\end{pmatrix}. \tag{B.26}$$

In (B.26) $\boldsymbol{\Phi}_{11}(t,t_0)$ is transition matrix of the system

$$\dot{\mathbf{x}}_1=\mathbf{A}_{11}\mathbf{x}_1, \tag{B.27}$$

$\boldsymbol{\Phi}_{22}(t,t_0)$ is transition matrix of the system

$$\dot{\mathbf{x}}_2=\mathbf{A}_{22}\mathbf{x}_2, \tag{B.28}$$

and $\boldsymbol{\Phi}_{21}(t,t_0)$ can be computed as

$$\boldsymbol{\Phi}_{21}(t,t_0)=\int_{t_0}^{t}\boldsymbol{\Phi}_{22}(t,\tau)\mathbf{A}_{21}\boldsymbol{\Phi}_{11}(\tau,t_0)d\tau. \tag{B.29}$$

Consequently, the matrix $\boldsymbol{\Psi}_1(t)$ takes the form

$$\boldsymbol{\Psi}_1(t)=\boldsymbol{\Phi}(t,t_0)\mathbf{P}(t_0)=\begin{pmatrix}\boldsymbol{\Phi}_{11}(t,t_0)\mathbf{P}_{\xi\xi}(t_0) & \boldsymbol{\Phi}_{11}(t,t_0)\mathbf{P}_{\xi\eta}(t_0)\\ \boldsymbol{\Phi}_{21}(t,t_0)\mathbf{P}_{\xi\xi}(t_0)+\boldsymbol{\Phi}_{22}(t,t_0)\mathbf{P}_{\xi\eta}^{\mathrm{T}}(t_0) & \boldsymbol{\Phi}_{21}(t,t_0)\mathbf{P}_{\xi\eta}(t_0)+\boldsymbol{\Phi}_{22}(t,t_0)\mathbf{P}_{\eta\eta}(t_0)\end{pmatrix}. \tag{B.30}$$

The integral in (B.6) can be rearranged as

$$\begin{aligned}\mathbf{N}(t,t_0)&=\int_{t_0}^{t}\boldsymbol{\Phi}^{\mathrm{T}}(\tau,t)\mathbf{H}^{\mathrm{T}}\mathbf{R}^{-1}(\tau)\mathbf{H}\boldsymbol{\Phi}(\tau,t_0)d\tau=\\ &=\begin{pmatrix}\int_{t_0}^{t}\boldsymbol{\Phi}_{11}^{\mathrm{T}}(\tau,t)\mathbf{H}_{11}^{\mathrm{T}}\mathbf{R}^{-1}(\tau)\mathbf{H}_{11}\boldsymbol{\Phi}_{11}(\tau,t_0)d\tau & \mathbf{0}\\ \mathbf{0} & \mathbf{0}\end{pmatrix}=\begin{pmatrix}\mathbf{N}_{11}(t,t_0) & \mathbf{0}\\ \mathbf{0} & \mathbf{0}\end{pmatrix},\end{aligned} \tag{B.31}$$

which allows to reduce the expression (B.6) for $\boldsymbol{\Psi}_2(t)$ to

$$\begin{aligned}\boldsymbol{\Psi}_2(t)&=\begin{pmatrix}\boldsymbol{\Phi}_{11}^{\mathrm{T}}(t_0,t) & \boldsymbol{\Phi}_{21}^{\mathrm{T}}(t_0,t)\\ \mathbf{0} & \boldsymbol{\Phi}_{22}^{\mathrm{T}}(t_0,t)\end{pmatrix}+\begin{pmatrix}\mathbf{N}_{11}(t,t_0)\mathbf{P}_{\xi\xi}(t_0) & \mathbf{N}_{11}(t,t_0)\mathbf{P}_{\xi\eta}(t_0)\\ \mathbf{0} & \mathbf{0}\end{pmatrix}=\\ &=\begin{pmatrix}\boldsymbol{\Phi}_{11}^{\mathrm{T}}(t_0,t)+\mathbf{N}_{11}(t,t_0)\mathbf{P}_{\xi\xi}(t_0) & \boldsymbol{\Phi}_{21}^{\mathrm{T}}(t_0,t)+\mathbf{N}_{11}(t,t_0)\mathbf{P}_{\xi\eta}(t_0)\\ \mathbf{0} & \boldsymbol{\Phi}_{22}^{\mathrm{T}}(t_0,t)\end{pmatrix}.\end{aligned} \tag{B.32}$$

The inverse of $\boldsymbol{\Psi}_2(t)$ can be computed by the means of Frobenius formula

$$\begin{pmatrix}\mathbf{M}_{11} & \mathbf{M}_{12}\\ \mathbf{M}_{21} & \mathbf{M}_{22}\end{pmatrix}^{-1}=\begin{pmatrix}\mathbf{M}_{11}^{-1}+\mathbf{M}_{11}^{-1}\mathbf{M}_{12}\mathbf{X}^{-1}\mathbf{M}_{21}\mathbf{M}_{11}^{-1} & -\mathbf{M}_{11}^{-1}\mathbf{M}_{12}\mathbf{X}^{-1}\\ -\mathbf{X}^{-1}\mathbf{M}_{21}\mathbf{M}_{11}^{-1} & \mathbf{X}^{-1}\end{pmatrix},\ \mathbf{X}=\mathbf{M}_{22}-\mathbf{M}_{21}\mathbf{M}_{11}^{-1}\mathbf{M}_{12}. \tag{B.33}$$

The result is given by

$$\boldsymbol{\Psi}_2^{-1}(t)=$$
$$\begin{pmatrix}\left(\boldsymbol{\Phi}_{11}^{\mathrm{T}}(t_0,t)+\mathbf{N}_{11}(t,t_0)\mathbf{P}_{\xi\xi}(t_0)\right)^{-1} & -\left(\boldsymbol{\Phi}_{11}^{\mathrm{T}}(t_0,t)+\mathbf{N}_{11}(t,t_0)\mathbf{P}_{\xi\xi}(t_0)\right)^{-1}\left(\boldsymbol{\Phi}_{21}^{\mathrm{T}}(t_0,t)+\mathbf{N}_{11}(t,t_0)\mathbf{P}_{\xi\eta}(t_0)\right)\boldsymbol{\Phi}_{22}^{\mathrm{T}}(t,t_0)\\ \mathbf{0} & \boldsymbol{\Phi}_{22}^{\mathrm{T}}(t,t_0)\end{pmatrix}. \tag{B.34}$$

Then multiplication of (B.30) by (B.34) yields the following solution of the equation (B.3) for covariance matrix

$$
\begin{aligned}
&\mathbf{P}_{\xi\xi}(t)=\mathbf{\Phi}_{11}(t,t_0)\mathbf{P}_{\xi\xi}(t_0)\left(\mathbf{\Phi}_{11}^{\mathrm{T}}(t_0,t)+\mathbf{N}_{11}(t,t_0)\mathbf{P}_{\xi\xi}(t_0)\right)^{-1},\\
&\mathbf{P}_{\xi\eta}(t)=-\mathbf{\Phi}_{11}(t,t_0)\mathbf{P}_{\xi\xi}(t_0)\left(\mathbf{\Phi}_{11}^{\mathrm{T}}(t_0,t)+\mathbf{N}_{11}(t,t_0)\mathbf{P}_{\xi\xi}(t_0)\right)^{-1}\left(\mathbf{\Phi}_{21}^{\mathrm{T}}(t_0,t)+\mathbf{N}_{11}(t,t_0)\mathbf{P}_{\xi\eta}(t_0)\right)\mathbf{\Phi}_{22}^{\mathrm{T}}(t,t_0)+\\
&\quad+\mathbf{\Phi}_{11}(t,t_0)\mathbf{P}_{\xi\eta}(t_0)\mathbf{\Phi}_{22}^{\mathrm{T}}(t,t_0),\\
&\mathbf{P}_{\eta\xi}(t)=\mathbf{P}_{\xi\eta}^{\mathrm{T}}(t)=\left(\mathbf{\Phi}_{21}(t,t_0)\mathbf{P}_{\xi\xi}(t_0)+\mathbf{\Phi}_{22}(t,t_0)\mathbf{P}_{\xi\eta}^{\mathrm{T}}(t_0)\right)\left(\mathbf{\Phi}_{11}^{\mathrm{T}}(t_0,t)+\mathbf{N}_{11}(t,t_0)\mathbf{P}_{\xi\xi}(t_0)\right)^{-1},\\
&\mathbf{P}_{\eta\eta}(t)=-\left(\mathbf{\Phi}_{21}(t,t_0)\mathbf{P}_{\xi\xi}(t_0)+\mathbf{\Phi}_{22}(t,t_0)\mathbf{P}_{\xi\eta}^{\mathrm{T}}(t_0)\right)\left(\mathbf{\Phi}_{11}^{\mathrm{T}}(t_0,t)+\mathbf{N}_{11}(t,t_0)\mathbf{P}_{\xi\xi}(t_0)\right)^{-1}\cdot\\
&\quad\cdot\left(\mathbf{\Phi}_{21}^{\mathrm{T}}(t_0,t)+\mathbf{N}_{11}(t,t_0)\mathbf{P}_{\xi\eta}(t_0)\right)\mathbf{\Phi}_{22}^{\mathrm{T}}(t,t_0)+\left(\mathbf{\Phi}_{21}(t,t_0)\mathbf{P}_{\xi\eta}(t_0)+\mathbf{\Phi}_{22}(t,t_0)\mathbf{P}_{\eta\eta}(t_0)\right)\mathbf{\Phi}_{22}^{\mathrm{T}}(t,t_0).
\end{aligned}
\tag{B.35}
$$

The formulae (B.35) present an explicit expression of the state covariance matrix in terms of the transition and the measurement matrices of the system (B.16).

Alternatively, (B.35) can be written in an implicit form, which allows to shorten the notation considerably.

$$
\begin{aligned}
&\mathbf{P}_{\xi\xi}(t)=\left(\mathbf{\Phi}_{11}^{\mathrm{T}}(t_0,t)\mathbf{P}_{\xi\xi}^{-1}(t_0)\mathbf{\Phi}_{11}(t_0,t)+\mathbf{W}_{\mathbf{R},11}(t,t_0)\right)^{-1},\\
&\mathbf{P}_{\xi\eta}^{\mathrm{T}}(t)=\left(\mathbf{\Phi}_{21}(t,t_0)+\mathbf{\Phi}_{22}(t,t_0)\mathbf{P}_{\xi\eta}^{\mathrm{T}}(t_0)\mathbf{P}_{\xi\xi}^{-1}(t_0)\right)\mathbf{\Phi}_{11}(t_0,t)\mathbf{P}_{\xi\xi}(t),\\
&\mathbf{P}_{\eta\eta}(t)=\mathbf{\Phi}_{22}(t,t_0)\left(\mathbf{P}_{\eta\eta}(t_0)-\mathbf{P}_{\xi\eta}^{\mathrm{T}}(t_0)\mathbf{P}_{\xi\xi}^{-1}(t_0)\mathbf{P}_{\xi\eta}(t_0)\right)\mathbf{\Phi}_{22}^{\mathrm{T}}(t,t_0)+\mathbf{P}_{\xi\eta}^{\mathrm{T}}(t)\mathbf{P}_{\xi\xi}^{-1}(t)\mathbf{P}_{\xi\eta}(t)
\end{aligned}
\tag{B.36}
$$

Herein

$$
\mathbf{W}_{\mathbf{R},11}(t,t_0)=\int_{t_0}^{t}\mathbf{\Phi}_{11}^{\mathrm{T}}(\tau,t)\mathbf{H}_{11}^{\mathrm{T}}\mathbf{R}^{-1}(\tau)\mathbf{H}_{11}\mathbf{\Phi}_{11}(\tau,t)d\tau. \tag{B.37}
$$

The obtained solution unveils the following useful properties of the Kalman filter for LTI systems with no input noise:

1. *Covariance of the unobservable states* $\mathbf{P}_{\eta\eta}(t)$ *remains constant over time if* $\mathbf{A}_{21}=\mathbf{0}$, $\mathbf{A}_{22}=\mathbf{0}$, *and* $\mathbf{P}_{\xi\eta}(t_0)=\mathbf{0}$.
2. $\mathbf{A}_{21}=\mathbf{0}$ *and* $\mathbf{P}_{\xi\eta}(t_0)=\mathbf{0}$ *implies* $\mathbf{P}_{\eta\eta}(t)=\mathbf{\Phi}_{22}(t,t_0)\mathbf{P}_{\eta\eta}(t_0)\mathbf{\Phi}_{22}^{\mathrm{T}}(t,t_0)$, *and covariance of the unobservable states appears to be defined completely by the matrix* $\mathbf{A}_{22}$.
3. *If coordinates in the unobservable subspace can be chosen in such a way that*

$$
\mathbf{\eta}=\begin{pmatrix}\mathbf{\eta}_1\\ \mathbf{\eta}_2\end{pmatrix},\ \mathbf{A}_{22}=\begin{pmatrix}\mathbf{A}_{22}^{11} & \mathbf{0}\\ \mathbf{A}_{22}^{21} & \mathbf{A}_{22}^{22}\end{pmatrix},\ \mathbf{A}_{21}=\begin{pmatrix}\mathbf{0}\\ \mathbf{A}_{21}^{2}\end{pmatrix}, \tag{B.38}
$$

Then the covariance of the $\mathbf{\eta}_1$ *takes the form* $\mathbf{P}_{\eta_1\eta_1}(t)=\mathbf{\Phi}_{22}^{11}(t,t_0)\mathbf{P}_{\eta_1\eta_1}(t_0)\left(\mathbf{\Phi}_{22}^{11}(t,t_0)\right)^{\mathrm{T}}$, *provided that* $\mathbf{P}_{\xi\eta_1}(t_0)=\mathbf{0}$. *Herein* $\mathbf{\Phi}_{22}^{11}(t,t_0)$ *is transition matrix of the system* $\dot{\mathbf{\eta}}_1=\mathbf{A}_{22}^{11}\mathbf{\eta}_1$.

B.4 Example

Consider INS, aided by information on vehicle's velocity during straight and leveled flight. Under the assumptions, introduced in the Section 3.2.2, error propagation equations for the error vector

$$\mathbf{x} = \begin{pmatrix} \delta\mathbf{v}_n^{\mathsf{T}} & \psi_{n\tilde{n}}^{\mathsf{T}} & \delta\mathbf{f}_b^{\mathsf{T}} & \delta\boldsymbol{\omega}_{ib}^{\mathsf{T}} \end{pmatrix}^{\mathsf{T}} \tag{B.39}$$

can be written in the form

$$\dot{\mathbf{x}}(t) = \mathbf{A}\mathbf{x}(t) + \mathbf{q}(t), \tag{B.40}$$

where

$$\mathbf{A} = \begin{pmatrix} \mathbf{0} & -\left[\mathbf{R}_{\tilde{n}b}\tilde{\mathbf{f}}_b\times\right] & \mathbf{R}_{\tilde{n}b} & \mathbf{0} \\ \mathbf{0} & \mathbf{0} & \mathbf{0} & \mathbf{R}_{\tilde{n}b} \\ \mathbf{0} & \mathbf{0} & \mathbf{0} & \mathbf{0} \\ \mathbf{0} & \mathbf{0} & \mathbf{0} & \mathbf{0} \end{pmatrix}, \; \mathbf{R}_{\tilde{n}b} \approx \begin{pmatrix} \cos\psi & -\sin\psi & 0 \\ \sin\psi & \cos\psi & 0 \\ 0 & 0 & 1 \end{pmatrix}, \; \tilde{\mathbf{f}}_b \approx \begin{pmatrix} 0 \\ 0 \\ -g \end{pmatrix}. \tag{B.41}$$

The measurement equation takes the form

$$\begin{aligned} &\mathbf{y} = \delta\mathbf{v}_n = \mathbf{H}\mathbf{x} + \mathbf{r}(t), \\ &\mathbf{H} = \begin{pmatrix} \mathbf{I}_{3\times3} & \mathbf{0}_{3\times3} & \mathbf{0}_{3\times3} & \mathbf{0}_{3\times3} \end{pmatrix}. \end{aligned} \tag{B.42}$$

Analytical observability analysis, introduced in the Section 3.1.2, yields the following observable combinations

$$\begin{aligned} &\xi_1 = \delta v_{n1}, \\ &\xi_2 = -g\psi_{n\tilde{n}2} + \cos\psi\cdot\delta f_{b1} - \sin\psi\cdot\delta f_{b2}, \\ &\xi_3 = -g\sin\psi\cdot\delta\omega_{b1} - g\cos\psi\cdot\delta\omega_{b2}, \\ \\ &\xi_4 = \delta v_{n2}, \\ &\xi_5 = g\psi_{n\tilde{n}1} + \sin\psi\cdot\delta f_{b1} + \cos\psi\cdot\delta f_{b2}, \\ &\xi_6 = g\cos\psi\cdot\delta\omega_{b1} - g\sin\psi\cdot\delta\omega_{b2}, \\ \\ &\xi_7 = \delta v_{n3}, \\ &\xi_8 = \delta f_{b3}. \end{aligned} \tag{B.43}$$

Linear combinations of components of $\mathbf{x}$, which remain unobservable, are

$$\begin{aligned} &\eta_1 = \psi_{n\tilde{n}3}, \\ \\ &\eta_2 = -\sin\psi/g\cdot\psi_{n\tilde{n}1} + \cos\psi/g\cdot\psi_{n\tilde{n}2} + \delta f_{b1}, \\ &\eta_3 = -\cos\psi/g\cdot\psi_{n\tilde{n}1} - \sin\psi/g\cdot\psi_{n\tilde{n}2} + \delta f_{b2}, \\ \\ &\eta_5 = \delta\omega_{b3}. \end{aligned} \tag{B.44}$$

Denote $(\boldsymbol{\xi}^{\mathsf{T}}\ \boldsymbol{\eta}^{\mathsf{T}})^{\mathsf{T}} = (\xi_1\ldots\xi_8\ \eta_1\ldots\eta_4)^{\mathsf{T}}$ and consider coordinate transformation $\mathbf{z} = \mathbf{T}\mathbf{x}$, where

$$\mathbf{T}=\frac{\partial(\boldsymbol{\xi}^{\mathrm{T}}\ \boldsymbol{\eta}^{\mathrm{T}})^{\mathrm{T}}}{\partial\mathbf{x}^{\mathrm{T}}}=$$

$$=\begin{pmatrix}
1 & 0 & 0 & 0 & 0 & 0 & 0 & 0 & 0 & 0 & 0 & 0\\
0 & 0 & 0 & 0 & -g & 0 & \cos\psi & -\sin\psi & 0 & 0 & 0 & 0\\
0 & 0 & 0 & 0 & 0 & 0 & 0 & 0 & 0 & -g\sin\psi & -g\cos\psi & 0\\
0 & 1 & 0 & 0 & 0 & 0 & 0 & 0 & 0 & 0 & 0 & 0\\
0 & 0 & 0 & g & 0 & 0 & \sin\psi & \cos\psi & 0 & 0 & 0 & 0\\
0 & 0 & 0 & 0 & 0 & 0 & 0 & 0 & 0 & g\cos\psi & -g\sin\psi & 0\\
0 & 0 & 1 & 0 & 0 & 0 & 0 & 0 & 0 & 0 & 0 & 0\\
0 & 0 & 0 & 0 & 0 & 0 & 0 & 0 & 1 & 0 & 0 & 0\\
0 & 0 & 0 & 0 & 0 & 1 & 0 & 0 & 0 & 0 & 0 & 0\\
0 & 0 & 0 & -\frac{1}{g}\sin\psi & \frac{1}{g}\cos\psi & 0 & 1 & 0 & 0 & 0 & 0 & 0\\
0 & 0 & 0 & -\frac{1}{g}\cos\psi & -\frac{1}{g}\sin\psi & 0 & 0 & 1 & 0 & 0 & 0 & 0\\
0 & 0 & 0 & 0 & 0 & 0 & 0 & 0 & 0 & 0 & 0 & 1
\end{pmatrix}. \tag{B.45}$$

Coordinate transformation $\mathbf{T}$ converts the original system to the form

$$\begin{aligned}\dot{\mathbf{z}}&=\mathbf{A}_1\mathbf{z}+\mathbf{v}(t),\\ \mathbf{y}&=\mathbf{H}_1\mathbf{z}+\mathbf{r}(t).\end{aligned} \tag{B.46}$$

The new system and measurement matrices are related to the matrices of the original system as

$$\mathbf{A}_1=\mathbf{TAT}^{-1}=\begin{pmatrix}
0 & 1 & 0 & 0 & 0 & 0 & 0 & 0 & 0 & 0 & 0 & 0\\
0 & 0 & 1 & 0 & 0 & 0 & 0 & 0 & 0 & 0 & 0 & 0\\
0 & 0 & 0 & 0 & 0 & 0 & 0 & 0 & 0 & 0 & 0 & 0\\
0 & 0 & 0 & 0 & 1 & 0 & 0 & 0 & 0 & 0 & 0 & 0\\
0 & 0 & 0 & 0 & 0 & 1 & 0 & 0 & 0 & 0 & 0 & 0\\
0 & 0 & 0 & 0 & 0 & 0 & 0 & 0 & 0 & 0 & 0 & 0\\
0 & 0 & 0 & 0 & 0 & 0 & 0 & 1 & 0 & 0 & 0 & 0\\
0 & 0 & 0 & 0 & 0 & 0 & 0 & 0 & 0 & 0 & 0 & 0\\
0 & 0 & 0 & 0 & 0 & 0 & 0 & 0 & 0 & 0 & 0 & 1\\
0 & 0 & -\frac{\cos\psi}{g^2} & -\frac{\sin\psi}{g^2} & 0 & 0 & 0 & 0 & 0 & 0 & 0 & 0\\
0 & 0 & \frac{\sin\psi}{g^2} & -\frac{\cos\psi}{g^2} & 0 & 0 & 0 & 0 & 0 & 0 & 0 & 0\\
0 & 0 & 0 & 0 & 0 & 0 & 0 & 0 & 0 & 0 & 0 & 0
\end{pmatrix},$$

$$\mathbf{H}_1=\mathbf{HT}^{-1}=\begin{pmatrix}
1 & 0 & 0 & 0 & 0 & 0 & 0 & 0 & 0 & 0 & 0 & 0\\
0 & 0 & 0 & 1 & 0 & 0 & 0 & 0 & 0 & 0 & 0 & 0\\
0 & 0 & 0 & 0 & 0 & 0 & 1 & 0 & 0 & 0 & 0 & 0
\end{pmatrix}. \tag{B.47}$$

In terms of the Kalman canonical decomposition (B.16)

$$\mathbf{A}_{11}=\begin{pmatrix}0&1&0&0&0&0&0&0\\0&0&1&0&0&0&0&0\\0&0&0&0&0&0&0&0\\0&0&0&0&1&0&0&0\\0&0&0&0&0&1&0&0\\0&0&0&0&0&0&0&0\\0&0&0&0&0&0&0&1\\0&0&0&0&0&0&0&0\end{pmatrix},\ \mathbf{A}_{22}=\begin{pmatrix}0&0&0&1\\0&0&0&0\\0&0&0&0\\0&0&0&0\end{pmatrix},$$

$$\mathbf{A}_{21}=\begin{pmatrix}0&0&0&0&0&0&0&0\\0&-\frac{\cos\psi}{g^2}&-\frac{\sin\psi}{g^2}&0&0&0&0&0\\0&\frac{\sin\psi}{g^2}&-\frac{\cos\psi}{g^2}&0&0&0&0&0\\0&0&0&0&0&0&0&0\end{pmatrix}, \tag{B.48}$$

$$\mathbf{H}_{11}=\begin{pmatrix}1&0&0&0&0&0&0&0\\0&0&0&1&0&0&0&0\\0&0&0&0&0&0&1&0\end{pmatrix}.$$

Assume at first that input noise is zero. Then formulae (B.47), (B.48) show that errors of heading channel are independent of other components of the error state and that dynamics of the vector $\boldsymbol{\eta}_1=\begin{pmatrix}\psi_{n\tilde{n}3} & \delta\omega_{b3}\end{pmatrix}^{\mathrm{T}}$ is subject to

$$\dot{\boldsymbol{\eta}}_1=\begin{pmatrix}0&1\\0&0\end{pmatrix}\cdot\boldsymbol{\eta}_1. \tag{B.49}$$

Consequently, by conclusion 3 of the Appendix B.3, covariance of $\boldsymbol{\eta}_1$ takes the form

$$\mathbf{P}_{\boldsymbol{\eta}_1\boldsymbol{\eta}_1}(t)=\boldsymbol{\Phi}_{\boldsymbol{\eta}_1}(t,t_0)\mathbf{P}_{\boldsymbol{\eta}_1\boldsymbol{\eta}_1}(t_0)\left(\boldsymbol{\Phi}_{\boldsymbol{\eta}_1}(t,t_0)\right)^{\mathrm{T}}. \tag{B.50}$$

Herein $\boldsymbol{\Phi}_{\boldsymbol{\eta}_1}(t,t_0)$ is transition matrix of the system (B.49). Assume, for example, that

$$\mathbf{P}_{\boldsymbol{\eta}_1\boldsymbol{\eta}_1}(t_0)=\begin{pmatrix}\sigma^2_{\psi_{n\tilde{n}3}}&0\\0&\sigma^2_{\delta\omega_{b3}}\end{pmatrix}. \tag{B.51}$$

Then the equation (B.50) yields

$$\begin{aligned}&\mathbf{P}_{\boldsymbol{\eta}_1\boldsymbol{\eta}_1}(t)=\\&=\begin{pmatrix}1&t-t_0\\0&1\end{pmatrix}\begin{pmatrix}\sigma^2_{\psi_{n\tilde{n}3}}&0\\0&\sigma^2_{\delta\omega_{b3}}\end{pmatrix}\begin{pmatrix}1&0\\t-t_0&1\end{pmatrix}=\\&=\begin{pmatrix}\sigma^2_{\psi_{n\tilde{n}3}}+\sigma^2_{\delta\omega_{b3}}(t-t_0)^2&\sigma^2_{\delta\omega_{b3}}(t-t_0)\\\sigma^2_{\delta\omega_{b3}}(t-t_0)&\sigma^2_{\delta\omega_{b3}}\end{pmatrix}.\end{aligned} \tag{B.52}$$

Assume now that input noise is present in (B.40) and let

$$
\begin{aligned}
&\psi = \pi/3,\ g = 9.81,\\
&\mathrm{E}\left[\mathbf{r}(t)\mathbf{r}^{\mathrm{T}}(\tau)\right] = \mathbf{R}\cdot\delta(t-\tau),\ \mathbf{R} = \mathrm{diag}(0.25,\ 0.25, 0.25),\\
&\mathrm{E}\left[\mathbf{q}(t)\mathbf{q}^{\mathrm{T}}(\tau)\right] = \mathbf{Q}\cdot\delta(t-\tau),\\
&\mathbf{Q} = \mathrm{diag}(7\cdot10^{-6}, 7\cdot10^{-6}, 7\cdot10^{-6}, 8\cdot10^{-7}, 8\cdot10^{-7}, 8\cdot10^{-7},\\
&\qquad 1\cdot10^{-8}, 1\cdot10^{-8}, 1\cdot10^{-8}, 1\cdot10^{-12}, 1\cdot10^{-12}, 1\cdot10^{-12}),\\
&\mathbf{P}_0 = \mathrm{diag}(1,\ 1,\ 1,\ 4\cdot10^{-4}, 4\cdot10^{-4}, 4\cdot10^{-4},\\
&\qquad 1\cdot10^{-3}, 1\cdot10^{-3}, 1\cdot10^{-3}, 1\cdot10^{-8}, 1\cdot10^{-8}, 1\cdot10^{-8}).
\end{aligned}
\tag{B.53}
$$

Then equation for conditional covariance $\mathbf{P}_{zz}(t)$ of the vector $\mathbf{z}$ takes the form

$$
\dot{\mathbf{P}}_{zz}(t) = \mathbf{A}_1\mathbf{P}_{zz}(t) + \mathbf{P}_{zz}(t)\mathbf{A}_1^{\mathrm{T}} + \mathbf{TQT}^{\mathrm{T}} - \mathbf{P}_{zz}(t)\mathbf{H}_1^{\mathrm{T}}\mathbf{R}^{-1}\mathbf{H}_1\mathbf{P}_{zz}(t),\ \mathbf{P}_{zz}(t_0) = \mathbf{TP}_0\mathbf{T}^{\mathrm{T}}. \tag{B.54}
$$

Solving (B.54) numerically and substituting the result into (B.23) yields Kalman filter gains for components of the vector $\mathbf{z}$. Since $\dim\mathbf{z} = 12$ and $\dim\mathbf{y} = 3$, gain matrix $\mathbf{K}$ is of a size 12×3. Plots of the elements of $\mathbf{K}$ are given on the Figures 49–52. $K_{i,j}$ denotes an element of $\mathbf{K}$ staying in the i^{th} row and the j^{th} column. The elements in the rows 9 to 12 are Kalman gains for unobservable states.

As was shown above, errors of heading channel are unobservable and independent of other error states. In accordance with that corresponding Kalman filter gains $K_{9,j}$ and $K_{12,j}$, $j = 1,2,3$, are seen to be equal to zero. Dynamics of unobservable states η_2 and η_3, in turn, is influenced considerably by observable states, and thus the gains for them have nonzero values and can hardly be considered negligible.

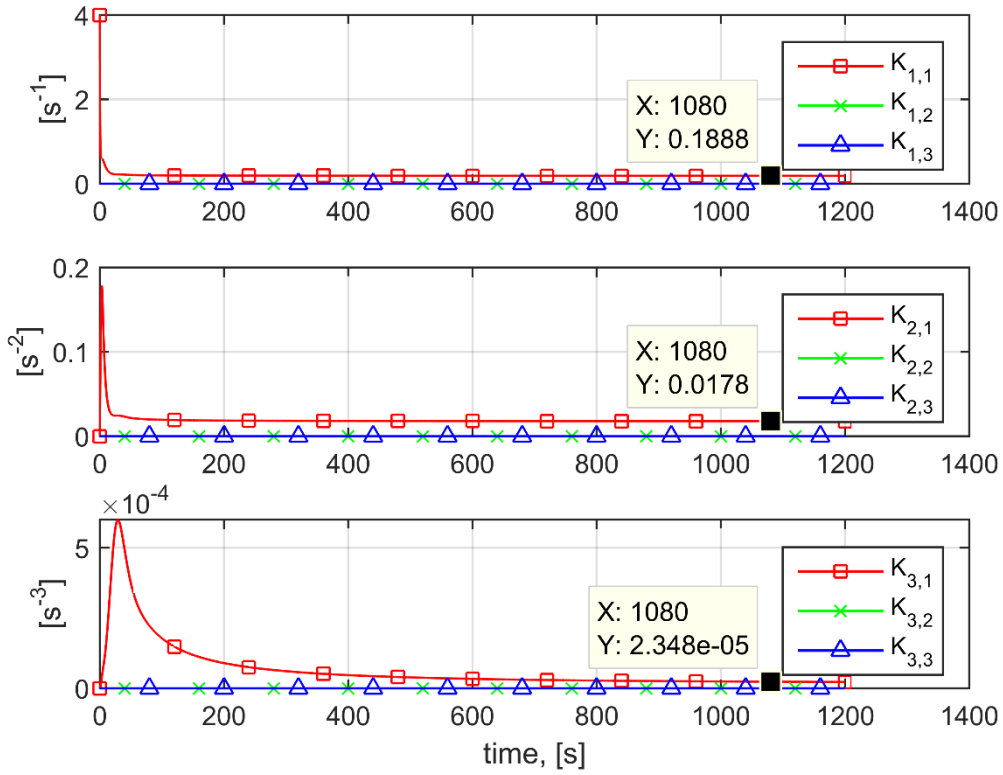

Fig. 49

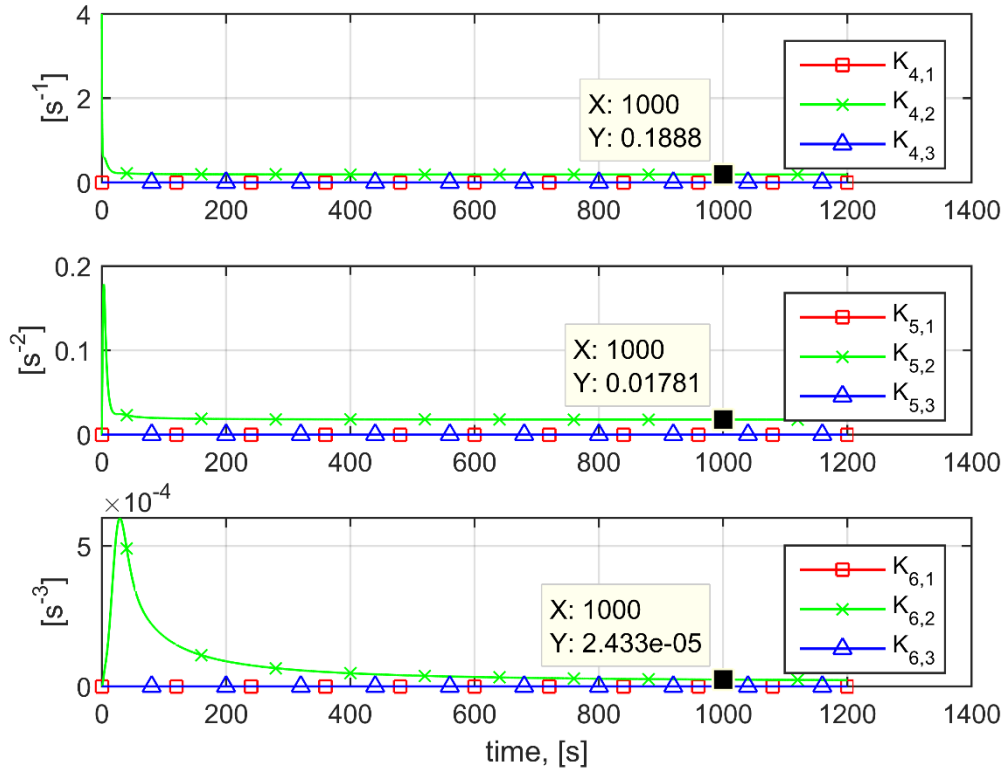
[s-1]
X: 1000
Y: 0.1888
K4,1
K4,2
K4,3
[s-2]
X: 1000
Y: 0.01781
K5,1
K5,2
K5,3
×10-4
[s-3]
X: 1000
Y: 2.433e-05
K6,1
K6,2
K6,3
time, [s]

Fig. 50

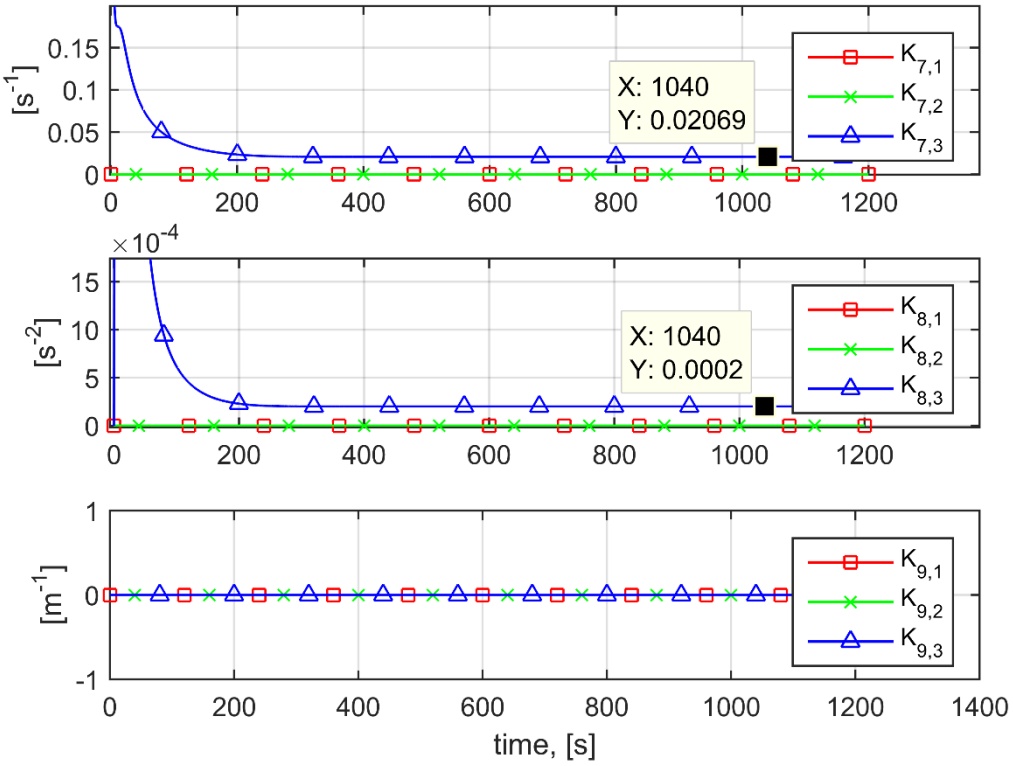
[s-1]
X: 1040
Y: 0.02069
K7,1
K7,2
K7,3
×10-4
[s-2]
X: 1040
Y: 0.0002
K8,1
K8,2
K8,3
[m-1]
K9,1
K9,2
K9,3
time, [s]

Fig. 51

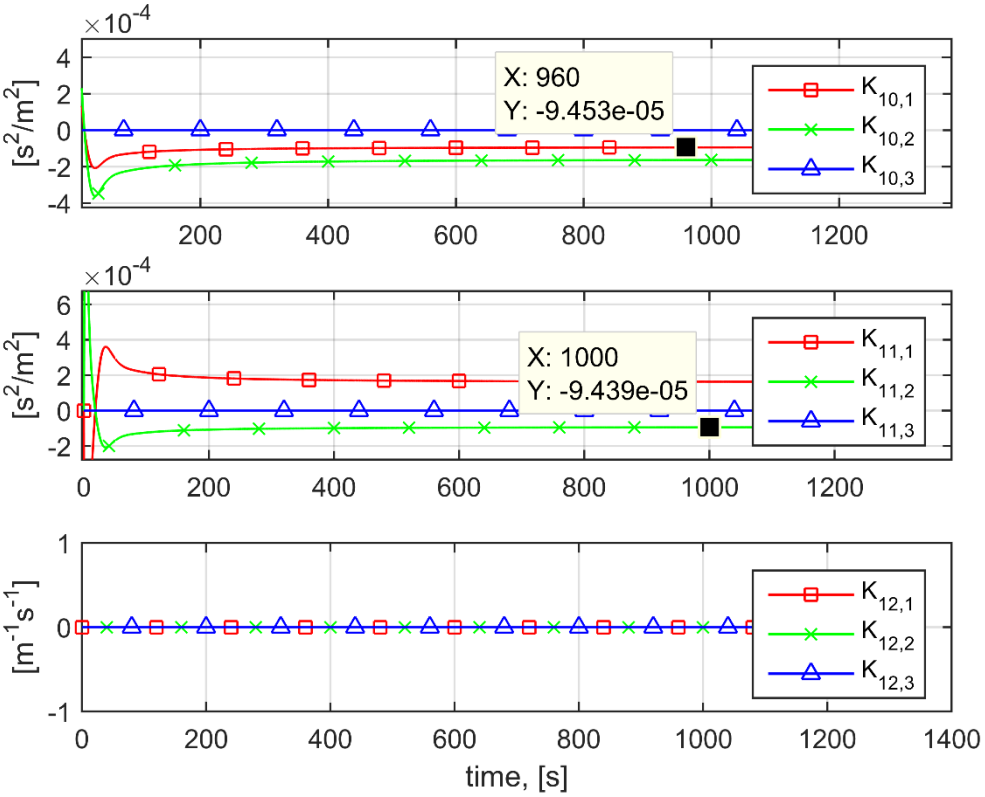
×10^-4
[s^2/m^2]
X: 960
Y: -9.453e-05
K10,1
K10,2
K10,3
×10^-4
[s^2/m^2]
X: 1000
Y: -9.439e-05
K11,1
K11,2
K11,3
[m^-1s^-1]
K12,1
K12,2
K12,3
time, [s]

Fig. 52

Appendix C. Performance classes according to RTCA DO-334.

Table 16–Attitude performance requirements according to RTCA DO-334

Category	Attitude accuracy	
	Static Conditions	**Dynamic conditions**
A1	0.1 deg	0.2 deg
A2	0.2 deg	0.5 deg
A3	0.5 deg	1.0 deg
A4	1.0 deg	2.5 deg
A5	1.0 deg	2.5* deg

Table 17–Heading performance requirements according to RTCA DO-334

Category	Source of heading information	Heading accuracy	
		Static conditions	**Dynamic conditions**
H1	Non magnetic, i. e. gyrocompassing system	1.0 deg	2.0 deg
H2	Magnetic slaving	1.0 deg	2.0 deg
H3	Magnetic slaving	1.5 deg	4.0 deg
H4	Magnetic slaving	2.0 deg	6.0 deg
H5	Magnetic slaving	2.0 deg	6.0 deg (10 deg during maneuvers up to ±30 deg roll. No requirements outside ±30 deg roll.)
		Heading drift accuracy under all conditions	
H6	Degraded mode	2 deg in 6 hours	
H7	Degraded mode	2 deg in 3 hours	
H8	Degraded mode	5 deg in 1 hour	
H9	Degraded mode	30 deg in 1 hour	
H10	Degraded mode	5 deg in 10 minutes	
H11	Degraded mode	10 deg in 10 minutes	
HX	No heading capability	n/a	

Appendix D. Simulation environment.

D.1 Trajectory generation

Trajectories, used in the simulations, were generated in a flight simulator following [113, 114].

D.1.1 Trajectory for demonstration of observability properties

Analytical observability analysis, presented in Chapter 3, considered the most typical flight situations, encountered by a general aviation aircraft, namely, straight and leveled unaccelerated flight, steady climb, and steady turn. Height and heading profiles of the trajectory, used for observability demonstration, are shown on Figure 53. The trajectory is seen to cover all the situations, considered in the conducted observability investigation.

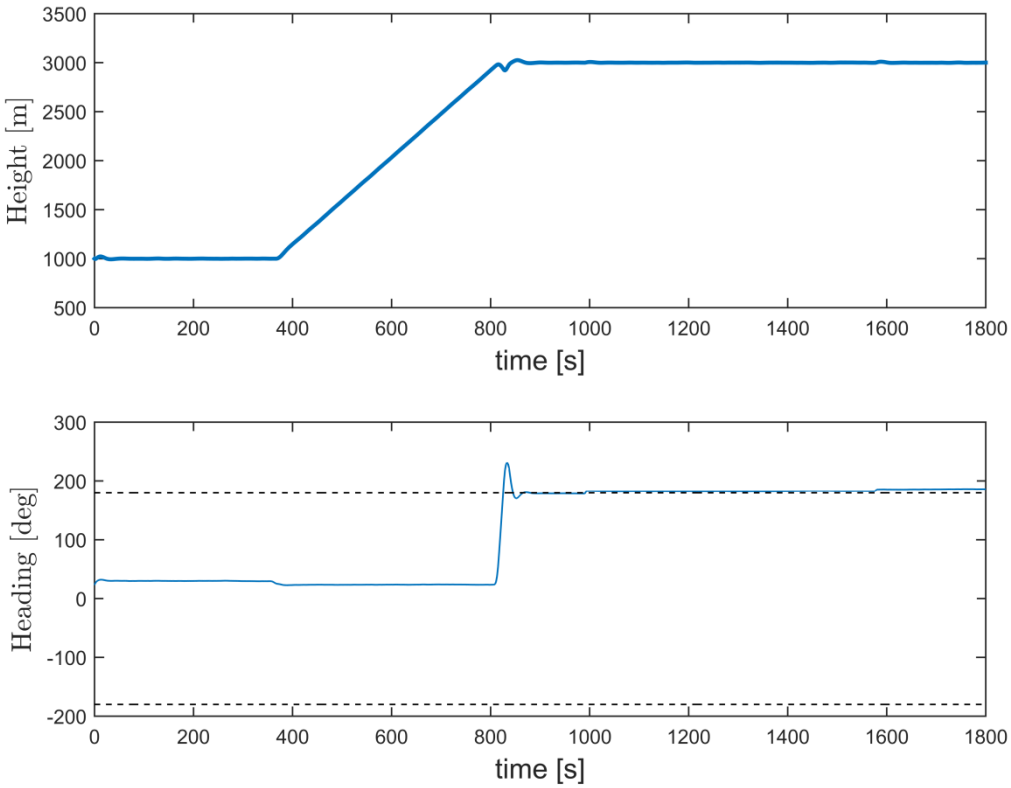

Fig. 53

D.1.2 Trajectory for simulation of FDI methodologies

Simulations, presented in Chapter 5, consider the flight trajectory, whose position and orientation profiles are given by Figures 54, 55, respectively.

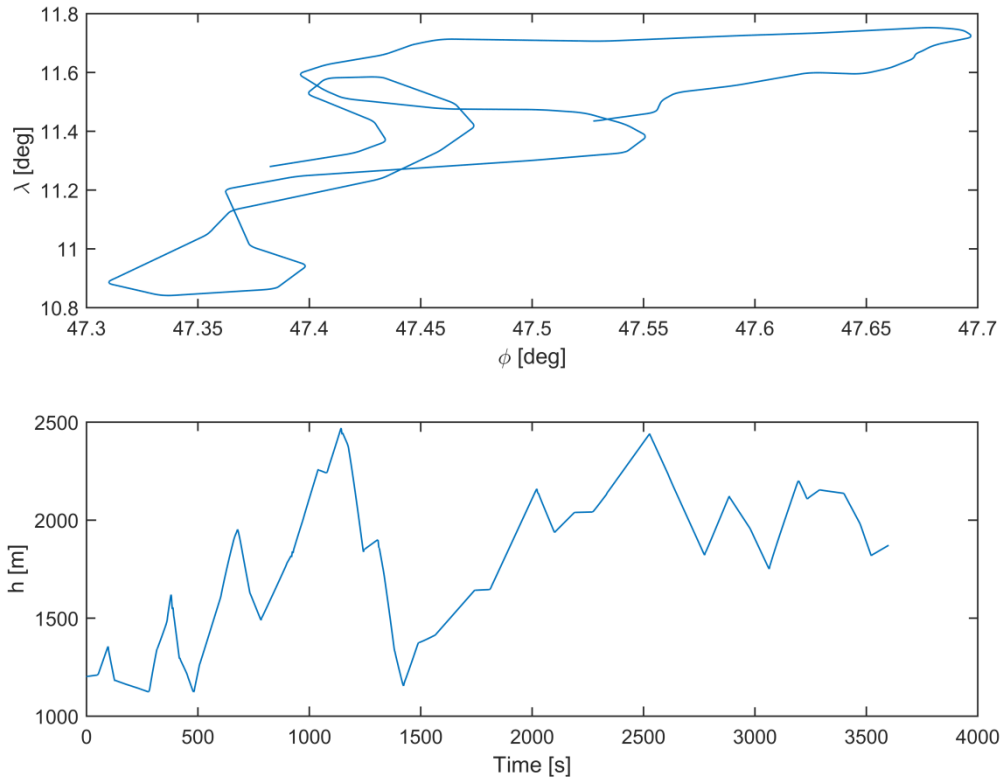
11.8
11.6
11.4
11.2
11
10.8
λ [deg]
47.3
47.35
47.4
47.45
47.5
47.55
47.6
47.65
47.7
ϕ [deg]
2500
2000
1500
1000
h [m]
0
500
1000
1500
2000
2500
3000
3500
4000
Time [s]

Fig. 54

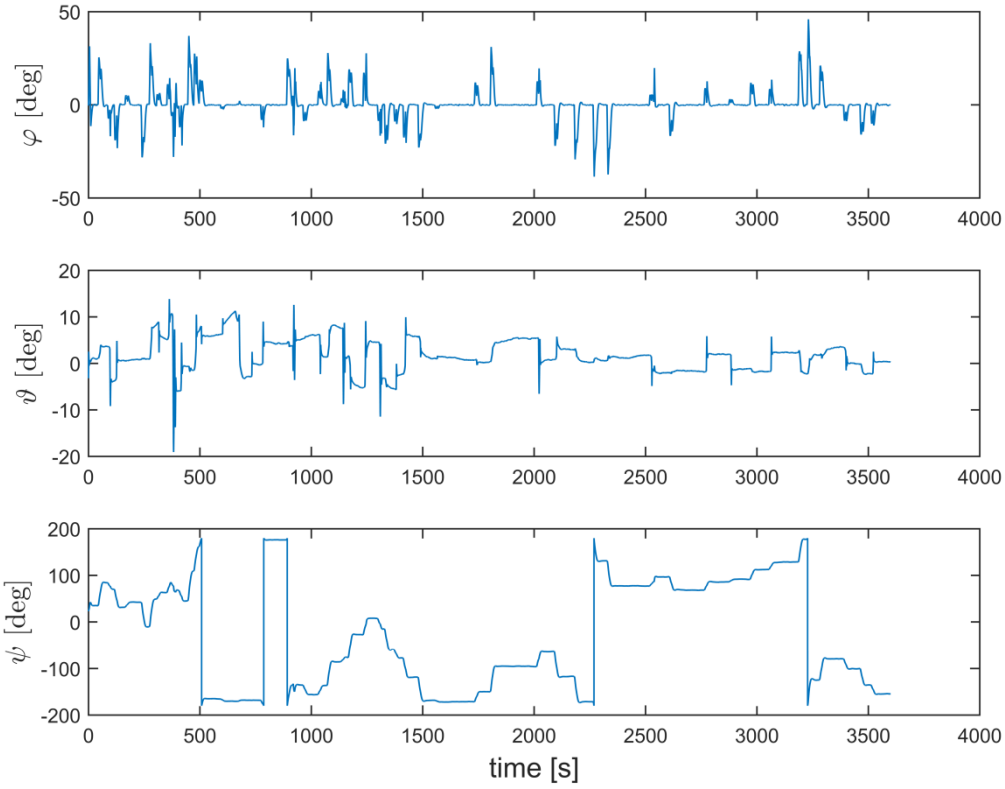
50
0
-50
φ [deg]
20
10
0
-10
-20
ϑ [deg]
200
100
0
-100
-200
ψ [deg]
0
500
1000
1500
2000
2500
3000
3500
4000
time [s]

Fig. 55

D.1.3 Highly dynamic (aerobatic) trajectory

Figures 56, 57 show position and orientation profiles of the highly dynamic trajectory, generated by the means of X-Plane 10 flight simulator and embedded F22 fighter aircraft model, respectively. Figure 58, in turn, shows AOA and AOS profiles, corresponding to this trajectory.

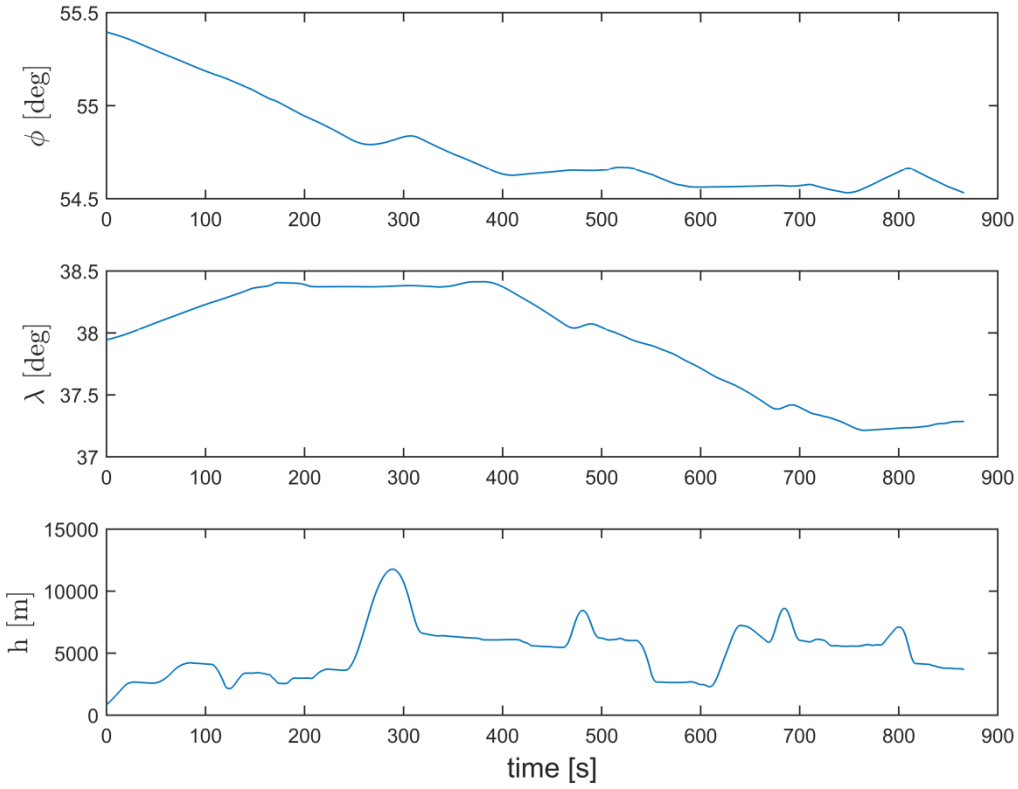

Fig. 56–Latitude ϕ, longitude λ, and height h profiles

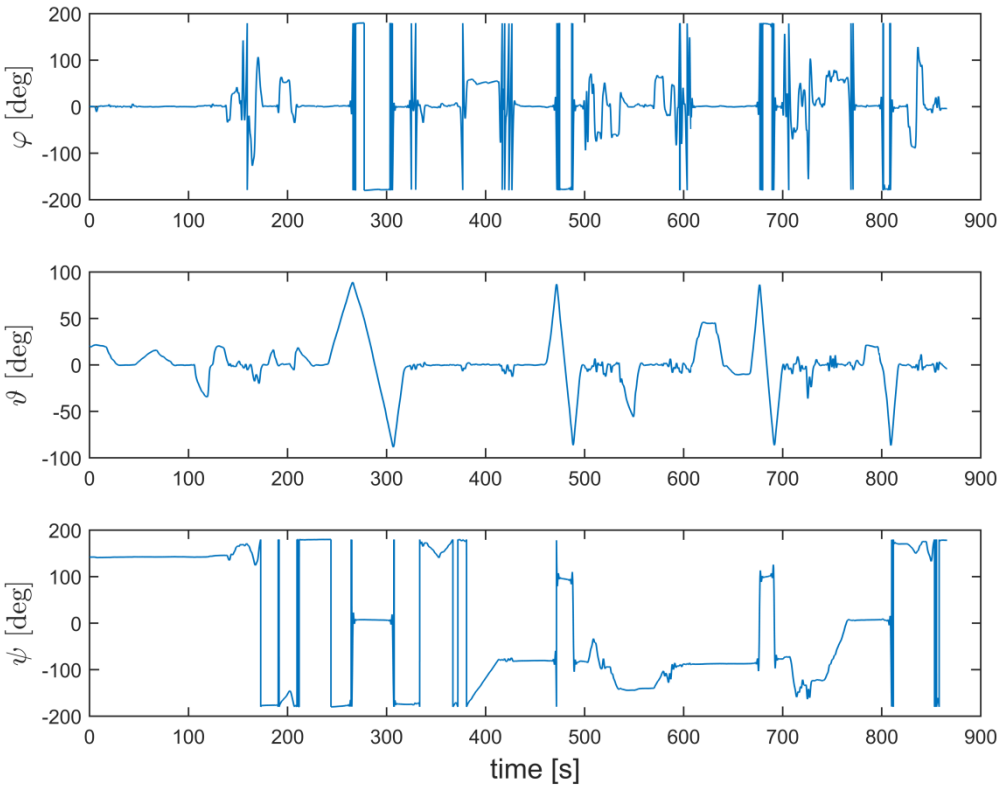

Fig. 57–Orientation angles: roll φ, pitch ϑ, and yaw ψ

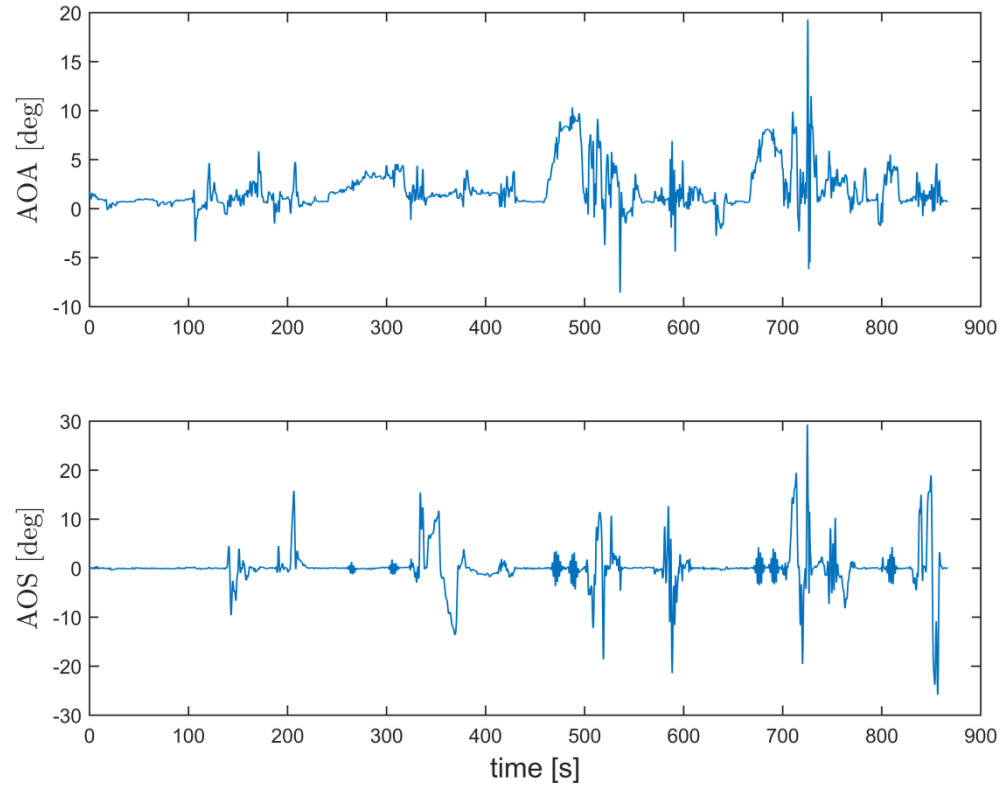

Fig. 58–Angle of attack and angle of sideslip

D.2 IMU error model

Errors of inertial sensors were assumed to feature a bias ($\mathbf{b}_\bullet$), bias instability ($\boldsymbol{\xi}_\bullet$) [115], and Gaussian white noise $\mathbf{v}_\bullet$ [17]:

$$\begin{aligned} \delta\boldsymbol{\omega}_{ib} &= \mathbf{b}_g + \boldsymbol{\xi}_g + \mathbf{v}_g, \\ \delta\mathbf{f}_b &= \mathbf{b}_a + \boldsymbol{\xi}_a + \mathbf{v}_a. \end{aligned} \tag{D.1}$$

Relative parameters were taken from specifications of the sensors available on the market. A reference specification of the industrial-grade IMU is [78], of the tactical-grade [77], of the navigation-grade IMU is [60]. Bias, bias instability, and random walk parameters a summarized in the table below. Numerical modeling of bias instability is discussed in [96].

Table 18. Parameters of the simulated sensor errors.

	Industrial-grade	**Tactical grade**	**Navigation-grade**
Bias	< 0.2 deg/s; < 16 mg	< 10 deg/h; < 3 mg	< 0.003 deg/h; < 25 μg
Random Walk	0.3 deg/sqrt(Hz); 0.029 m/sec/sqrt(h)	0.3 deg/sqrt(h); 0.25 mg/sqrt(Hz)	0.0025 deg/sqrt(h); 8 μg/sqrt(Hz)
Bias Instability	6.25 deg/h; 0.1 mg	0.1 deg/h ; 10 μg	0.002 deg/h; 10 μg

D.3 Modeling of wind

Wind profile, which is used as an input to the flight simulator, is modeled as a sum of random walk [17], Dryden turbulence model [116], Gaussian white noise [17], and deterministic wind gusts [116]. The wind profile, used to generate the trajectory, shown on Figure 53, is given by Figure 59. Figure 60 shows the wind profiled, which was used to generate the trajectory, given by Figure 54.

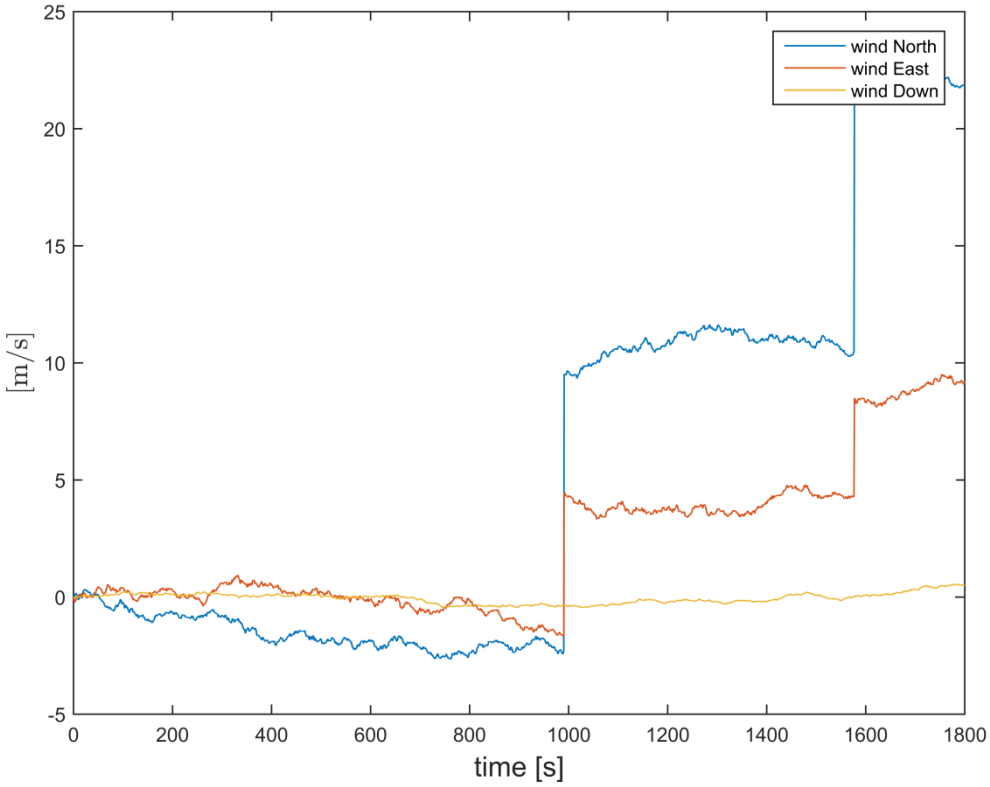
wind North
wind East
wind Down
[m/s]
time [s]
25
20
15
10
5
0
-5
0
200
400
600
800
1000
1200
1400
1600
1800

Fig. 59

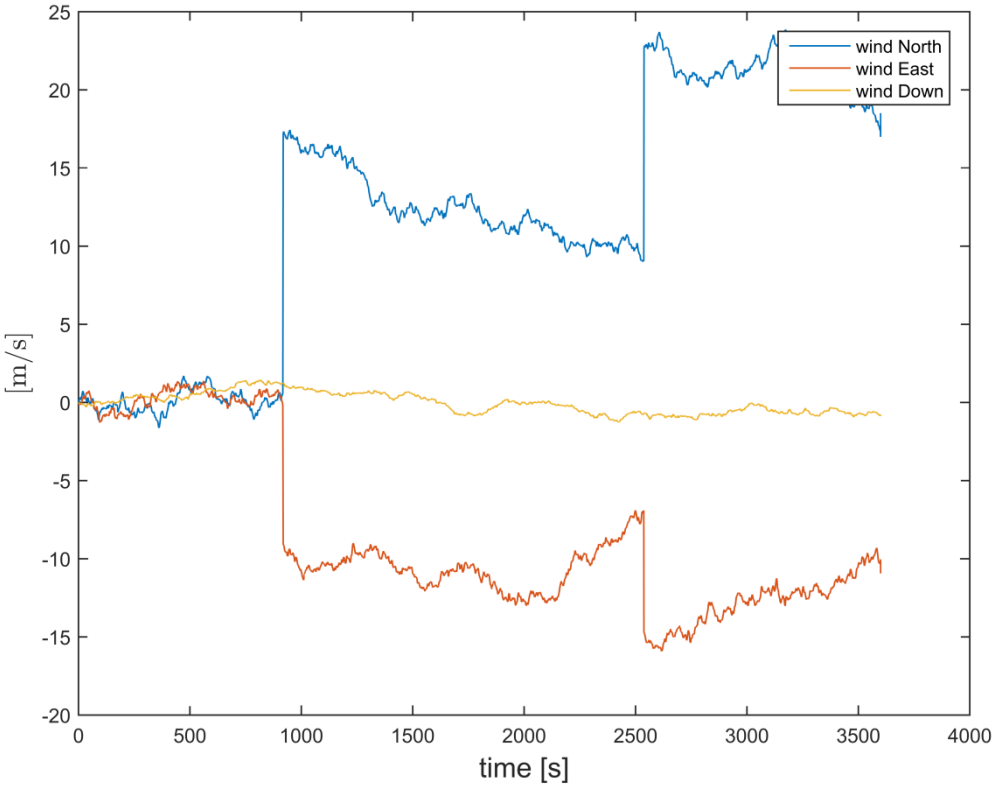
wind North
wind East
wind Down
[m/s]
time [s]
25
20
15
10
5
0
-5
-10
-15
-20
0
500
1000
1500
2000
2500
3000
3500
4000

Fig. 60

D.4 Modeling of magnetic field disturbances

Each of the components of the magnetic field disturbance $\delta\mathbf{B}_n^{\text{mod}}$ is modeled as a sum of two scaled realizations of random walk process:

$$\delta B_{nk}^{mod}(\phi,\lambda) = C\cdot\left(\xi_{1k}(\phi)+\xi_{2k}(\lambda)\right),\ k=1,2,3. \tag{D.2}$$

The Figure 61 shows components of $\delta\mathbf{B}_n^{\text{mod}}(\phi(t),\lambda(t))$ along the flight trajectory discussed in Appendix D.1.1.

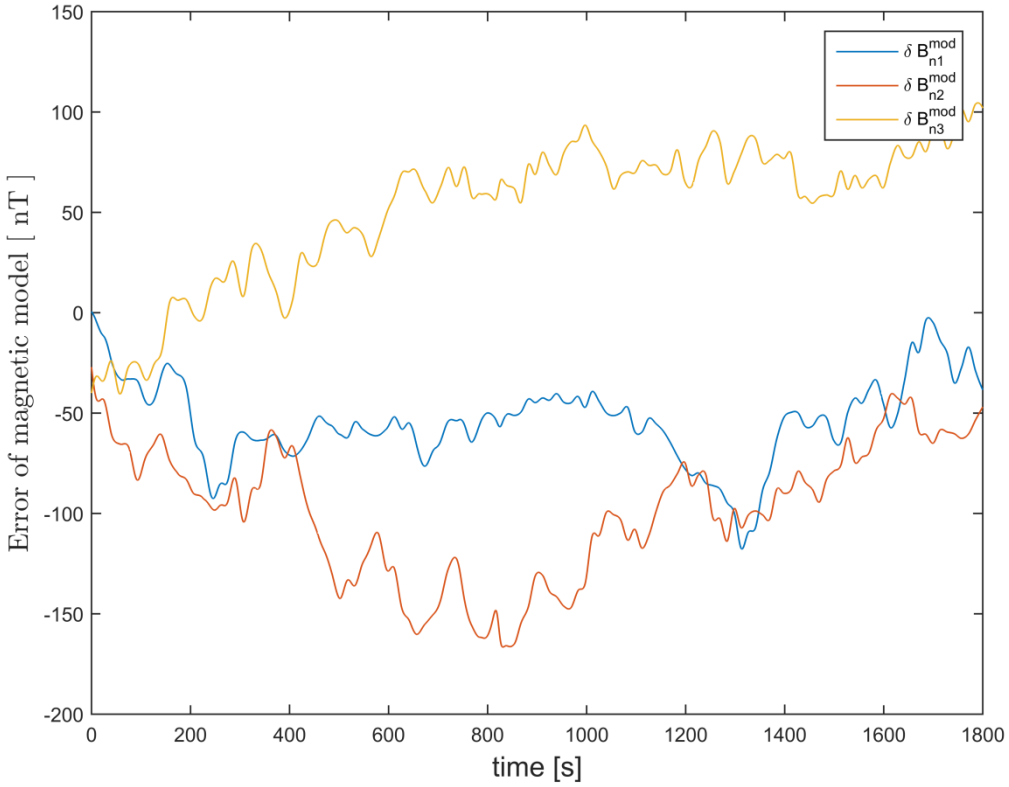

Fig. 61

D.5 Modeling of errors of aiding sensors

Errors of aiding sensors were assumed zero-mean Gaussian white noises. Magnitudes of noise standard deviations were set to 0.6 deg for AOA and AOS, 0.3 m/s for TAS, and 0.3 m for barometric altitude. These values correspond to noise amplitudes observed by experiment with SpaceAge Control 100400 miniature air data boom [27] in a wind tunnel at TU München. Standard deviation of the noise of magnetometer was set to 10 nT. This value agrees with performance of Honeywell HMR2300 3-axis digital magnetometer [117].

D.6 Optimal filter

Closed-loop error state Kalman filter [21] is used as an optimal estimator. Error state and error state covariance are propagated at the rate of inertial sensors. Kalman filter updates are performed at a frequency of 1 Hz.

D.7 Initialization of covariance matrix

Navigation filters are initialized simply with over-bounded, diagonal navigation error state covariance matrix. More sophisticated approach that allows to achieve higher statistical consistency of the navigation solution is derived and discussed in [96].

D.7.1 Initialization of the filter in Section 3.5.1

Navigation error state vector is given by (3.34). Diagonal elements of the initial covariance matrix are given below.

$$\begin{aligned}
&p_{1,1}(0)=10^{-12},\ p_{2,2}(0)=10^{-12},\ p_{3,3}(0)=1,\\
&p_{4,4}(0)=1,\ p_{5,5}(0)=1,\ p_{6,6}(0)=1,\\
&p_{7,7}(0)=10^{-4},\ p_{8,8}(0)=10^{-4},\ p_{9,9}(0)=2\cdot10^{-4},\\
&p_{10,10}(0)=2.25\cdot10^{-4},\ p_{11,11}(0)=2.25\cdot10^{-4},\ p_{12,12}(0)=2.25\cdot10^{-4},\\
&p_{13,13}(0)=4\cdot10^{-4},\ p_{14,14}(0)=4\cdot10^{-4},\ p_{15,15}(0)=4\cdot10^{-4},\\
&p_{16,16}(0)=1,\ p_{17,17}(0)=2500,\ p_{18,18}(0)=10^{-4},\\
&p_{19,19}(0)=100,\ p_{20,20}(0)=100,\ p_{21,21}(0)=10.
\end{aligned} \tag{D.3}$$

D.7.2 Initialization of the filter in Section 3.5.2

Navigation error state vector is given by (3.77). The first 15 element of initial covariance matrix are the same as in (D.3), but

$$\begin{aligned}
&p_{16,16}(0)=625,\ p_{17,17}(0)=625,\ p_{18,18}(0)=625,\\
&p_{19,19}(0)=90000,\ p_{20,20}(0)=90000,\ p_{21,21}(0)=90000.
\end{aligned} \tag{D.4}$$

D.7.3 Initialization of the filter in Section 4.4

D.7.3.1 IMU+Magnetometer

Navigation error state vector takes the form

$$\mathbf{x}=\left(\psi_{n\tilde{n}}^{\mathrm{T}}\quad \delta\mathbf{f}_b^{\mathrm{T}}\quad \delta\boldsymbol{\omega}_{ib}^{\mathrm{T}}\quad (\delta\mathbf{B}_n^{\mathrm{mod}})^{\mathrm{T}}\right)^{\mathrm{T}}. \tag{D.5}$$

Diagonal elements of the initial covariance matrix are given by

Tactical - grade IMU	**Industrial - grade IMU**
$p_{1,1}(0)=10^{-4},\ p_{2,2}(0)=10^{-4},\ p_{3,3}(0)=10^{-2},$	$p_{1,1}(0)=10^{-4},\ p_{2,2}(0)=10^{-4},\ p_{3,3}(0)=10^{-2},$
$p_{4,4}(0)=0.2,\ p_{5,5}(0)=0.2,\ p_{6,6}(0)=0.2,$	$p_{4,4}(0)=0.2,\ p_{5,5}(0)=0.2,\ p_{6,6}(0)=0.2,$
$p_{7,7}(0)=10^{-8},\ p_{8,8}(0)=10^{-8},\ p_{9,9}(0)=10^{-8},$	$p_{7,7}(0)=10^{-8},\ p_{8,8}(0)=10^{-8},\ p_{9,9}(0)=10^{-8},$
$p_{10,10}(0)=p_{11,11}(0)=p_{12,12}(0)=9\cdot10^{4},$	$p_{10,10}(0)=p_{11,11}(0)=p_{12,12}(0)=9\cdot10^{4},$

(D.6)

D.7.3.2 IMU+Barometric altimeter+Magnetometer

Navigation error state vector takes the form

$$\mathbf{x}=\left(\delta h \quad \delta v_{n3} \quad \psi_{n\tilde{n}}^{\mathrm{T}} \quad \delta\mathbf{f}_b^{\mathrm{T}} \quad \delta\boldsymbol{\omega}_{ib}^{\mathrm{T}} \quad \delta\mathbf{B}_b^{\mathrm{T}} \quad (\delta\mathbf{B}_n^{\mathrm{mod}})^{\mathrm{T}} \quad \delta\mathbf{a}_n\right)^{\mathrm{T}}. \tag{D.7}$$

Diagonal elements of the initial covariance matrix are given by

Tactical - grade IMU	**Industrial - grade IMU**
$p_{1,1}(0)=1,\ p_{2,2}(0)=1,$	$p_{1,1}(0)=1,\ p_{2,2}(0)=1,$
$p_{3,3}(0)=10^{-4},\ p_{4,4}(0)=10^{-4},\ p_{5,5}(0)=10^{-2},$	$p_{3,3}(0)=10^{-4},\ p_{4,4}(0)=10^{-4},\ p_{5,5}(0)=10^{-2},$
$p_{6,6}(0)=p_{7,7}(0)=p_{8,8}(0)=10^{-3},$	$p_{6,6}(0)=p_{7,7}(0)=p_{8,8}(0)=10^{-3},$
$p_{9,9}(0)=p_{10,10}(0)=p_{11,11}(0)=10^{-8},$	$p_{9,9}(0)=p_{10,10}(0)=p_{11,11}(0)=10^{-8},$
$p_{12,12}(0)=p_{13,13}(0)=p_{14,14}(0)=625,$	$p_{12,12}(0)=p_{13,13}(0)=p_{14,14}(0)=625,$
$p_{15,15}(0)=p_{16,16}(0)=p_{17,17}(0)=9\cdot10^{4},$	$p_{15,15}(0)=p_{16,16}(0)=p_{17,17}(0)=9\cdot10^{4},$
$p_{18,18}(0)=p_{19,19}(0)=p_{20,20}(0)=0.2.$	$p_{18,18}(0)=p_{19,19}(0)=p_{20,20}(0)=0.2.$

(D.8)

D.7.3.3 IMU+Barometric altimeter+Magnetometer+Air Data

Navigation error state vector takes the form

$$\mathbf{x}=\left(\delta\boldsymbol{\lambda}^{\mathrm{T}} \quad \delta\mathbf{v}_n^{\mathrm{T}} \quad \psi_{n\tilde{n}}^{\mathrm{T}} \quad \delta\mathbf{f}_b^{\mathrm{T}} \quad \delta\boldsymbol{\omega}_{ib}^{\mathrm{T}} \quad (\delta\mathbf{v}_n^{W})^{\mathrm{T}} \quad \delta\mathbf{B}_b^{\mathrm{T}} \quad (\delta\mathbf{B}_n^{\mathrm{mod}})^{\mathrm{T}}\right)^{\mathrm{T}}. \tag{D.9}$$

Diagonal elements of the initial covariance matrix are given by

Tactical - grade IMU	**Industrial - grade IMU**
$p_{1,1}(0)=10^{-12},\ p_{2,2}(0)=10^{-12},\ p_{3,3}(0)=1,$	$p_{1,1}(0)=10^{-12},\ p_{2,2}(0)=10^{-12},\ p_{3,3}(0)=1,$
$p_{4,4}(0)=p_{5,5}(0)=p_{6,6}(0)=1,$	$p_{4,4}(0)=p_{5,5}(0)=p_{6,6}(0)=1,$
$p_{7,7}(0)=1\,p_{8,8}(0)=10^{-4},\ p_{9,9}(0)=2\cdot10^{-4},$	$p_{7,7}(0)=p_{8,8}(0)=4\cdot10^{-4},\ p_{9,9}(0)=10^{-3},$
$p_{10,10}(0)=p_{11,11}(0)=p_{12,12}(0)=2.25\cdot10^{-4},$	$p_{10,10}(0)=p_{11,11}(0)=p_{12,12}(0)=10^{-3},$
$p_{13,13}(0)=p_{14,14}(0)=p_{15,15}(0)=4\cdot10^{-10},$	$p_{13,13}(0)=p_{14,14}(0)=p_{15,15}(0)=10^{-6},$
$p_{16,16}(0)=p_{17,17}(0)=100,\ p_{18,18}(0)=10,$	$p_{16,16}(0)=p_{17,17}(0)=100,\ p_{18,18}(0)=10,$
$p_{19,19}(0)=p_{20,20}(0)=p_{21,21}(0)=625,$	$p_{19,19}(0)=p_{20,20}(0)=p_{21,21}(0)=625,$
$p_{22,22}(0)=p_{23,23}(0)=p_{24,24}(0)=9\cdot10^{4}.$	$p_{22,22}(0)=p_{23,23}(0)=p_{24,24}(0)=9\cdot10^{4}.$

(D.10)

D.7.4 Initialization of the filter in Section 5.3.4

Covariance matrix is initialized by (D.10).

D.8 System noise matrix

Description of structures of corresponding navigation error state vectors is given in Appendix D.7. In all the simulated scenarios system noise matrix was assumed constant and diagonal.

D.8.1 System noise matrix of the filter in Section 3.5.1

Diagonal elements of the *continuous* system noise matrix are given below.

$$\begin{aligned}
&q_{1,1} = q_{2,2} = q_{3,3} = 0,\\
&q_{4,4} = q_{5,5} = q_{6,6} = 7\cdot 10^{-6},\\
&q_{7,7} = q_{8,8} = q_{9,9} = 10^{-8},\\
&q_{10,10} = q_{11,11} = q_{12,12} = 10^{-9},\\
&q_{13,13} = q_{14,14} = q_{15,15} = 10^{-14},\\
&q_{16,16} = 10^{-3},\ q_{17,17} = 10^{-2},\ q_{18,18} = 10^{-10},\\
&q_{19,19} = 0.02,\ q_{20,20} = 0.02,\ q_{21,21} = 10^{-3}.
\end{aligned} \tag{D.11}$$

D.8.2 System noise matrix of the filter in Section 3.5.2

The first 15 diagonal elements of the system noise matrix are given by (D.11), but

$$\begin{aligned}
&q_{16,16} = q_{17,17} = q_{18,18} = 5\cdot 10^{-2},\\
&q_{19,19} = q_{20,20} = q_{21,21} = 18\cdot 10^{3}.
\end{aligned} \tag{D.12}$$

D.8.3 System noise matrix of the filter in Section 4.4

D.8.3.1 IMU+Magnetometer

Tactical-grade IMU	**Industrial-grade IMU**
$q_{1,1} = q_{2,2} = q_{3,3} = 10^{-8},$	$q_{1,1} = q_{2,2} = q_{3,3} = 10^{-6},$
$q_{4,4} = q_{5,5} = q_{6,6} = 0.5,$	$q_{4,4} = q_{5,5} = q_{6,6} = 0.5,$
$q_{7,7} = q_{8,8} = q_{9,9} = 10^{-14},$	$q_{7,7} = q_{8,8} = q_{9,9} = 10^{-10},$
$q_{10,10} = q_{11,11} = q_{12,12} = 18\cdot 10^{3}.$	$q_{10,10} = q_{11,11} = q_{12,12} = 18\cdot 10^{3}.$

(D.13)

D.8.3.2 IMU+Barometric altimeter+Magnetometer

Tactical-grade IMU	**Industrial-grade IMU**
$q_{1,1} = 0,\ q_{2,2} = 7\cdot 10^{-6},$	$q_{1,1} = 0,\ q_{2,2} = 7\cdot 10^{-4},$
$q_{3,3} = q_{4,4} = q_{5,5} = 10^{-8},$	$q_{3,3} = q_{4,4} = q_{5,5} = 10^{-6},$
$q_{6,6} = q_{7,7} = q_{8,8} = 10^{-8},$	$q_{6,6} = q_{7,7} = q_{8,8} = 10^{-8},$
$q_{9,9} = q_{10,10} = q_{11,11} = 10^{-14},$	$q_{9,9} = q_{10,10} = q_{11,11} = 10^{-10},$
$q_{12,12} = q_{13,13} = q_{14,14} = 0.05,$	$q_{12,12} = q_{13,13} = q_{14,14} = 0.05,$
$q_{15,15} = q_{16,16} = q_{17,17} = 18\cdot 10^{3},$	$q_{15,15} = q_{16,16} = q_{17,17} = 18\cdot 10^{3},$
$q_{18,18} = q_{19,19} = q_{20,20} = 0.5.$	$q_{18,18} = q_{19,19} = q_{20,20} = 0.5.$

(D.14)

D.8.3.3 IMU+Barometric altimeter+Magnetometer+Air Data

Tactical - grade IMU	Industrial - grade IMU
$q_{1,1}=q_{2,2}=q_{3,3}=0,$	$q_{1,1}=q_{2,2}=q_{3,3}=0,$
$q_{4,4}=q_{5,5}=q_{6,6}=7\cdot10^{-6},$	$q_{4,4}=q_{5,5}=q_{6,6}=7\cdot10^{-6},$
$q_{7,7}=q_{8,8}=q_{9,9}=10^{-8},$	$q_{7,7}=q_{8,8}=q_{9,9}=10^{-6},$
$q_{10,10}=q_{11,11}=q_{12,12}=10^{-9},$	$q_{10,10}=q_{11,11}=q_{12,12}=10^{-8},$
$q_{13,13}=q_{14,14}=q_{15,15}=4\cdot10^{-14},$	$q_{13,13}=q_{14,14}=q_{15,15}=10^{-10},$
$q_{16,16}=q_{17,17}=0.02,\ q_{18,18}=10^{-3},$	$q_{16,16}=q_{17,17}=0.02,\ q_{18,18}=10^{-3},$
$q_{19,19}=q_{20,20}=q_{21,21}=0.05,$	$q_{19,19}=q_{20,20}=q_{21,21}=0.05,$
$q_{22,22}=q_{23,23}=q_{24,24}=18\cdot10^{3}.$	$q_{22,22}=q_{23,23}=q_{24,24}=18\cdot10^{3}.$

(D.15)

D.9 Measurement noise matrices

Barometric altitude measurement (3.19): $\mathbf{R}=1\ [\mathrm{m}^2]$.

True airspeed measurement (3.23): $\mathbf{R}=0.5\ [\mathrm{m}^2/\mathrm{s}^2]$.

Measurements of angle of attack and angle of sideslip (3.28): $\mathbf{R}=5\cdot10^{-5}\ [\mathrm{rad}^2]$.

Measurement of the Earth's magnetic field (3.71): $\mathbf{R}=225\cdot\mathbf{I}_{3\times3}\ [\mathrm{nT}^2]$.

Magnetic slaving (3.74): $\mathbf{R}=25\cdot10^{4}\ [\mathrm{nT}^2]$.

Leveling (4.5): $\mathbf{R}=9\cdot10^{-4}\ [\mathrm{m}^2/\mathrm{s}^4]$.

D.10 Simple approach to reduce effect of wind gusts

During operation of the navigation filter errors of wind velocity, which are considered in the error state vector, get significantly correlated with other navigation error states. The correlations were found to cause significant inconsistencies of the estimate of orientation shortly after occurrence of wind gust. The reason for that is excessive trust of the Kalman filter to the model of the wind, which is highly uncertain and volatile. There three possible ways to reduce impact of volatile atmosphere on the navigation filter. The first way consists in simply tuning the filter more pessimistically. This, however, will decrease considerably accuracy of the navigation solution. Another way to deal with the problem is to make use of the integrity monitoring technique suggested in Section 5.3.2 and skip Kalman filter updates if inconsistency in the innovation sequence is detected. Form the author's point of view this method is the most powerful and shall be preferred for implementation. However, implementation of this method may appear problematic due to significant increase of computational burden. If computational power of the onboard computer is limited, the following approach can be considered:

1. check the innovation of air data measurements using (5.44),
2. if the threshold T is exceeded, declare that wind situation changed, reset variances of errors of wind speed to initial condition, reset to zero elements of the covariance matrix, corresponding to cross correlations of wind speed errors and other navigation error states.

In case error state vector is given by (D.9), the procedure takes the following form:

$$
\begin{aligned}
&p_{16,16}(t) = p_{16,16}(t_0),\\
&p_{17,17}(t) = p_{17,17}(t_0),\\
&p_{18,18}(t) = p_{18,18}(t_0),\\
&p_{i,16}(t) = p_{i,17}(t) = p_{i,18}(t) = 0,\\
&p_{16,i}(t) = p_{17,i}(t) = p_{18,i}(t) = 0,\\
&i \neq 16,17,18.
\end{aligned}
\tag{D.16}
$$

The third approach was used in the simulations, presented in Chapters 3 and 4.

Appendix E. Example of application of the verification approach.

E.1 Inertial measurement unit calibration as optimal estimation

A problem of calibration of inertial measurement unit (IMU) can be formulated as a problem of optimal estimation of dynamic system's state vector [108, 118, 119]. In this case knowledge of observability properties of dynamic system is of utmost importance, since it answers the question, if the problem can in principal be solved given a particular predefined sequence of rotations on a turntable. The contribution [108] considers possibility of calibrating IMU on a low-grade single axis turntable and suggests an algorithm featuring three stages. On each of the stages one of the IMU's axes of sensitivity is aligned with turntable's rotation axis, and then IMU is rotated with a constant angular rate. It was concluded that rotating around axis, pointing upwards, did not allow to estimate all the instrumental errors, while rotating around axis, parallel to local horizontal plain, allowed. In order to demonstrate efficiency of the methodology, suggested above, a detailed observability analysis of each of the stages of the calibration algorithm is presented. Note, that [108] is extended by an analytical analysis for the case of rotation around vertical axis and an explanation, why these rotations appeared insufficient to calibrate IMU. The case of rotating around horizontal axis, in turn, was analyzed analytically in a batch manner under assumption of non-rotating Earth in [108], but without a detailed analysis of each of the stages of calibration procedure.

Following [108, 118], error propagation equations are given by

$$\begin{aligned}
&\dot{\psi}_{n\tilde{n}} = -[\boldsymbol{\omega}_{ie}^{n}\times]\cdot\psi_{n\tilde{n}} + \mathbf{R}_{nb}\left(\mathbf{b}_g + \mathbf{M}_g\boldsymbol{\omega}_{ib}\right),\\
&\dot{\mathbf{b}}_g = 0,\\
&\dot{\mathbf{M}}_g = 0,\\
&\dot{\mathbf{b}}_a = 0,\\
&\dot{\mathbf{M}}_a = 0,
\end{aligned} \tag{E.1}$$

and measurement equation takes the form

$$\mathbf{y} = -[\psi_{n\tilde{n}}\times]\cdot(0,0,1)^{\mathrm{T}} + \frac{1}{g}\mathbf{R}_{nb}\left(\mathbf{b}_a + \mathbf{M}_a\mathbf{f}_b\right). \tag{E.2}$$

Here $\boldsymbol{\omega}_{ib}$ is a vector of projections of angular rate to body-fixed coordinate frame; $\mathbf{b}_g$ is a vector of gyroscope biases; $\mathbf{M}_g$ is a matrix, whose diagonal entries are scale factor errors of gyroscopes, and non-diagonal entries are small angles of gyroscopes' axis misalignments; $\mathbf{b}_a$ is a vector of accelerometer biases; $\mathbf{M}_a$ is a matrix, whose diagonal entries are scale factor errors of accelerometers,

and non-diagonal entries are small angles of accelerometers' axis misalignments; $\psi_{n\tilde{n}}$ is a vector of orientation errors, and $\boldsymbol{\omega}_{ie}^{n}$ is vector of projections of the Earth's rotation rate to local level east-north-up frame (shorthand n-frame). $\mathbf{R}_{nb}$ is a matrix, defining rotation from n- to b-frame.

$$\mathbf{M}_g = \begin{pmatrix} m_{11}^g & m_{12}^g & m_{13}^g \\ m_{21}^g & m_{22}^g & m_{23}^g \\ m_{31}^g & m_{32}^g & m_{33}^g \end{pmatrix}, \mathbf{M}_a = \begin{pmatrix} m_{11}^a & 0 & 0 \\ m_{21}^a & m_{22}^a & 0 \\ m_{31}^a & m_{32}^a & m_{33}^a \end{pmatrix} \tag{E.3}$$

(E.1), (E.2) can be written as

$$\dot{\mathbf{z}} = \mathbf{A}(t)\mathbf{z},$$
$$\mathbf{y} = \mathbf{H}(t)\mathbf{z},$$

$$\mathbf{z} = \left(\psi_{n\tilde{n}1}\ \psi_{n\tilde{n}2}\ \psi_{n\tilde{n}3}\ b_{g1}\ b_{g2}\ b_{g3}\ b_{a1}\ b_{a2}\ b_{a3}\ m_{11}^g\ m_{12}^g\ m_{13}^g\ m_{21}^g\ m_{22}^g\ m_{23}^g\ m_{31}^g\ m_{32}^g\ m_{33}^g\ m_{11}^a\ m_{21}^a\ m_{22}^a\ m_{31}^a\ m_{32}^a\ m_{33}^a\right)^{\mathrm{T}}. \tag{E.4}$$

E.2 Case of rotation around vertical axis

E.2.1 The first stage of calibration

At the first stage of calibration

$$\mathbf{R}_{nb}(t) = \begin{pmatrix} \cos\omega t & -\sin\omega t & 0 \\ \sin\omega t & \cos\omega t & 0 \\ 0 & 0 & 1 \end{pmatrix},$$
$$\boldsymbol{\omega}_{ib} = \mathbf{R}_{nb}^{\mathrm{T}} \cdot \left(\boldsymbol{\omega}_{ie}^{n} + (0,0,\omega)^T\right), \boldsymbol{\omega}_{ie}^{n} = \left(0, \omega_{ie}\cos\phi, \omega_{ie}\sin\phi\right)^{\mathrm{T}}, \tag{E.5}$$
$$\mathbf{f}_b = \mathbf{R}_{nb}^{\mathrm{T}} \cdot \left(0,0,g\right)^T.$$

Here ω is a rate of rotation of a turntable; ϕ is local latitude; $\omega_{ie} \approx 2\pi / 24 / 3600\ [\mathrm{s}^{-1}]$ is a magnitude of the Earth's rotation rate; $g \approx 9.81\ [m/s^2]$ is gravitational acceleration. Applying procedure, described in Section 3.1.2, to the system (E.4) after substituting maneuver dependent terms with (E.5) yields constant rank observability matrix (3.8) of dimension 72×24, whose reduced row echelon form is given by

$$\mathbf{L}^{ver}_{1,rr}(t,\omega)=\begin{pmatrix}
1\,0\,0\,0\,0\,0\,0\,0\,0\,0\,0 & 0 & 0\,0 & 0 & \sin\omega t & \cos\omega t & 0 & 0\,0\,0\,0\,0\,0\\
0\,1\,0\,0\,0\,0\,0\,0\,0\,0\,0 & 0 & 0\,0 & 0 & -\cos\omega t & \sin\omega t & 0 & 0\,0\,0\,0\,0\,0\\
0\,0\,1\,0\,0\,0\,0\,0\,0\,0\,0 & 0 & 1\,0 & 0 & 0 & 0 & 0 & 0\,0\,0\,0\,0\,0\\
0\,0\,0\,1\,0\,0\,0\,0\,0\,0\,0 & \omega+\omega_{ie}\sin\phi & 0\,0 & 0 & \omega+\omega_{ie}\sin\phi & 0 & 0 & 0\,0\,0\,0\,0\,0\\
0\,0\,0\,0\,1\,0\,0\,0\,0\,0\,0 & 0 & 0\,0 & \omega+\omega_{ie}\sin\phi & 0 & \omega+\omega_{ie}\sin\phi & 0 & 0\,0\,0\,0\,0\,0\\
0\,0\,0\,0\,0\,1\,0\,0\,0\,0\,0 & 0 & 0\,0 & 0 & 0 & 0 & \omega+\omega_{ie}\sin\phi & 0\,0\,0\,0\,0\,0\\
0\,0\,0\,0\,0\,0\,1\,0\,0\,0\,0 & 0 & 0\,0 & 0 & -g & 0 & 0 & 0\,0\,0\,0\,0\,0\\
0\,0\,0\,0\,0\,0\,0\,1\,0\,0\,0 & 0 & 0\,0 & 0 & 0 & -g & 0 & 0\,0\,0\,0\,0\,0\\
0\,0\,0\,0\,0\,0\,0\,0\,1\,0\,0 & 0 & 0\,0 & 0 & 0 & 0 & 0 & 0\,0\,0\,0\,0\,g\\
0\,0\,0\,0\,0\,0\,0\,0\,0\,1\,0 & 0 & 0\,0 & 0 & 0 & 0 & 0 & 0\,0\,0\,0\,0\,0\\
0\,0\,0\,0\,0\,0\,0\,0\,0\,0\,1 & 0 & 1\,0 & 0 & 0 & 0 & 0 & 0\,0\,0\,0\,0\,0\\
0\,0\,0\,0\,0\,0\,0\,0\,0\,0\,0 & 0 & 0\,1 & 0 & 0 & 0 & 0 & 0\,0\,0\,0\,0\,0\\
0\,0\,0\,0\,0\,0\,0\,0\,0\,0\,0 & 0 & 0\,0 & 0 & 0 & 0 & 0 & 0\,0\,0\,0\,0\,0\\
\vdots & \vdots & \vdots & \vdots & \vdots & \vdots & \vdots & \vdots\\
0\,0\,0\,0\,0\,0\,0\,0\,0\,0\,0 & 0 & 0\,0 & 0 & 0 & 0 & 0 & 0\,0\,0\,0\,0\,0
\end{pmatrix}. \qquad \text{(E.6)}$$

Nonzero rows of (E.6) define some basis vector set in a space of observable costates. Multiplying them by state vector $\mathbf{z}$ yields the following observable linear combinations of error states

$$\begin{aligned}
&y^{1,ver}_1=\psi_{n\tilde{n}1}+m^g_{32}\cos\omega t+m^g_{31}\sin\omega t\\
&y^{1,ver}_2=\psi_{n\tilde{n}2}-m^g_{31}\cos\omega t+m^g_{32}\sin\omega t,\\
&y^{1,ver}_3=\psi_{n\tilde{n}3}+m^g_{21},\\
&y^{1,ver}_4=b_{g1}+m^g_{13}(\omega+\omega_{ie}\sin\phi)+m^g_{31}(\omega+\omega_{ie}\sin\phi),\\
&y^{1,ver}_5=b_{g2}+m^g_{23}(\omega+\omega_{ie}\sin\phi)+m^g_{32}(\omega+\omega_{ie}\sin\phi),\\
&y^{1,ver}_6=b_{g3}+m^g_{33}(\omega+\omega_{ie}\sin\phi),\\
&y^{1,ver}_7=b_{a1}-gm^g_{31},\ y^{1,ver}_8=b_{a2}-gm^g_{32},\\
&y^{1,ver}_9=b_{a3}+gm^a_{33},\ y^{1,ver}_{10}=m^g_{11},\\
&y^{1,ver}_{11}=m^g_{12}+m^g_{21},\ y^{1,ver}_{12}=m^g_{22}.
\end{aligned} \qquad \text{(E.7)}$$

E.2.2 The second stage of calibration

At the second stage of calibration

$$\begin{aligned}
&\mathbf{R}_{nb}(t)=\begin{pmatrix}0 & \cos\omega t & -\sin\omega t\\ 0 & \sin\omega t & \cos\omega t\\ 1 & 0 & 0\end{pmatrix},\\
&\boldsymbol{\omega}_{ib}=\mathbf{R}^{\mathrm{T}}_{nb}\cdot\left(\boldsymbol{\omega}^n_{ie}+(0,0,\omega)^T\right),\boldsymbol{\omega}^n_{ie}=\left(0,\omega_{ie}\cos\phi,\omega_{ie}\sin\phi\right)^{\mathrm{T}},\\
&\mathbf{f}_b=\mathbf{R}^{\mathrm{T}}_{nb}\cdot\left(0,0,g\right)^T.
\end{aligned} \qquad \text{(E.8)}$$

Reduced row echelon form of corresponding observability matrix is given by

$$
\mathbf{L}_{2,rr}^{ver}(t,\omega)=\begin{pmatrix}
1\,0\,0\,0\,0\,0\,0\,0\,0 & 0 & \sin\omega t & \cos\omega t & 0 & 0\,0 & 0 & 0\,0\,0\,0\,0\,0\,0\,0 \\
0\,1\,0\,0\,0\,0\,0\,0\,0 & 0 & -\cos\omega t & \sin\omega t & 0 & 0\,0 & 0 & 0\,0\,0\,0\,0\,0\,0\,0 \\
0\,0\,1\,0\,0\,0\,0\,0\,0 & 0 & 0 & 0 & 0 & 0\,0 & 0 & 1\,0\,0\,0\,0\,0\,0\,0 \\
0\,0\,0\,1\,0\,0\,0\,0\,0 & \omega+\omega_{ie}\sin\phi & 0 & 0 & 0 & 0\,0 & 0 & 0\,0\,0\,0\,0\,0\,0\,0 \\
0\,0\,0\,0\,1\,0\,0\,0\,0 & 0 & \omega+\omega_{ie}\sin\phi & 0 & \omega+\omega_{ie}\sin\phi & 0\,0 & 0 & 0\,0\,0\,0\,0\,0\,0\,0 \\
0\,0\,0\,0\,0\,1\,0\,0\,0 & 0 & 0 & \omega+\omega_{ie}\sin\phi & 0 & 0\,0 & \omega+\omega_{ie}\sin\phi & 0\,0\,0\,0\,0\,0\,0\,0 \\
0\,0\,0\,0\,0\,0\,1\,0\,0 & 0 & 0 & 0 & 0 & 0\,0 & 0 & 0\,0\,g\,0\,0\,0\,0\,0 \\
0\,0\,0\,0\,0\,0\,0\,1\,0 & 0 & -g & 0 & 0 & 0\,0 & 0 & 0\,0\,0\,g\,0\,0\,0\,0 \\
0\,0\,0\,0\,0\,0\,0\,0\,1 & 0 & 0 & -g & 0 & 0\,0 & 0 & 0\,0\,0\,0\,0\,g\,0\,0 \\
0\,0\,0\,0\,0\,0\,0\,0\,0 & 0 & 0 & 0 & 0 & 1\,0 & 0 & 0\,0\,0\,0\,0\,0\,0\,0 \\
0\,0\,0\,0\,0\,0\,0\,0\,0 & 0 & 0 & 0 & 0 & 0\,1 & 0 & 1\,0\,0\,0\,0\,0\,0\,0 \\
0\,0\,0\,0\,0\,0\,0\,0\,0 & 0 & 0 & 0 & 0 & 0\,0 & 0 & 0\,1\,0\,0\,0\,0\,0\,0 \\
0\,0\,0\,0\,0\,0\,0\,0\,0 & 0 & 0 & 0 & 0 & 0\,0 & 0 & 0\,0\,0\,0\,0\,0\,0\,0 \\
\vdots & \vdots & \vdots & \vdots & \vdots & \vdots & \vdots & \vdots \\
0\,0\,0\,0\,0\,0\,0\,0\,0 & 0 & 0 & 0 & 0 & 0\,0 & 0 & 0\,0\,0\,0\,0\,0\,0\,0
\end{pmatrix}. \tag{E.9}
$$

Hence the following linear combinations of error state space are observable.

$$
\begin{aligned}
y_1^{2,ver} &= \psi_{n\tilde{n}1} + m_{13}^g \cos\omega t + m_{12}^g \sin\omega t, \\
y_2^{2,ver} &= \psi_{n\tilde{n}2} - m_{12}^g \cos\omega t + m_{13}^g \sin\omega t, \\
y_3^{2,ver} &= \psi_{n\tilde{n}3} + m_{32}^g, \\
y_4^{2,ver} &= b_{g1} + m_{11}^g(\omega+\omega_{ie}\sin\phi), \\
y_5^{2,ver} &= b_{g2} + m_{12}^g(\omega+\omega_{ie}\sin\phi) + m_{21}^g(\omega+\omega_{ie}\sin\phi), \\
y_6^{2,ver} &= b_{g3} + m_{13}^g(\omega+\omega_{ie}\sin\phi) + m_{31}^g(\omega+\omega_{ie}\sin\phi), \\
y_7^{2,ver} &= b_{a1} + gm_{11}^a,\ y_8^{2,ver} = b_{a2} + gm_{21}^a - gm_{12}^g, \\
y_9^{2,ver} &= b_{a3} + gm_{31}^a - gm_{13}^g,\ y_{10}^{2,ver} = m_{22}^g, \\
y_{11}^{2,ver} &= m_{23}^g + m_{32}^g,\ y_{12}^{2,ver} = m_{33}^g.
\end{aligned} \tag{E.10}
$$

E.2.3 The third stage of calibration

At the third stage of calibration

$$
\begin{aligned}
&\mathbf{R}_{nb}(t)=\begin{pmatrix} -\sin\omega t & 0 & \cos\omega t \\ \cos\omega t & 0 & \sin\omega t \\ 0 & 1 & 0 \end{pmatrix}, \\
&\boldsymbol{\omega}_{ib} = \mathbf{R}_{nb}^{\mathrm{T}} \cdot \left(\boldsymbol{\omega}_{ie}^n + (0,0,\omega)^T \right), \boldsymbol{\omega}_{ie}^n = \left(0, \omega_{ie}\cos\phi, \omega_{ie}\sin\phi\right)^{\mathrm{T}}, \\
&\mathbf{f}_b = \mathbf{R}_{nb}^{\mathrm{T}} \cdot \left(0,0,g\right)^T.
\end{aligned} \tag{E.11}
$$

Reduced row echelon form of corresponding observability matrix takes the form

$$\mathbf{L}^{ver}_{3,rr}(t,\omega)=\begin{pmatrix}
1&0&0&0&0&0&0&0&0&0\\
0&1&0&0&0&0&0&0&0&0\\
0&0&1&0&0&0&0&0&0&0\\
0&0&0&1&0&\omega+\omega_{ie}\sin\phi&0&\omega+\omega_{ie}\sin\phi&0&0\\
0&0&0&0&1&0&\omega+\omega_{ie}\sin\phi&0&0&0\\
0&0&0&0&0&\omega+\omega_{ie}\sin\phi&0&\omega+\omega_{ie}\sin\phi&0&0\\
0&0&0&0&0&0&1&0&0&0\\
0&0&0&0&0&0&0&1&0&0\\
0&0&0&0&0&0&0&0&1&0\\
0&0&0&0&0&0&0&0&0&1\\
0&1&0&0&0&0&0&0&0&0\\
0&0&0&0&0&0&0&0&0&0\\
0&0&0&0&0&0&0&0&0&0\\
\vdots&\vdots&\vdots&\vdots&\vdots&\vdots&\vdots&\vdots&\vdots&\vdots\\
0&0&0&0&0&0&0&0&0&0
\end{pmatrix}\begin{matrix}
\cos\omega t&0&\sin\omega t&0&0&0&0\\
\sin\omega t&0&-\cos\omega t&0&0&0&0\\
0&0&0&-1&0&0&0\\
0&0&0&0&0&0&0\\
\omega+\omega_{ie}\sin\phi&0&0&0&0&0&0\\
0&\omega+\omega_{ie}\sin\phi&0&0&0&0&0\\
-g&0&0&0&0&0&0\\
0&0&0&0&0&g&0\\
0&0&-g&0&0&0&g\\
0&0&0&0&0&0&0\\
0&0&0&1&0&0&0\\
0&0&0&0&0&0&0\\
0&0&0&0&0&0&0\\
\vdots&\vdots&\vdots&\vdots&\vdots&\vdots&\vdots\\
0&0&0&0&0&0&0
\end{matrix}. \quad \text{(E.12)}$$

Consequently, observable linear combinations of error state space are given by

$$\begin{aligned}
&y_1^{3,ver}=\psi_{n\tilde{n}1}+m_{21}^g\cos\omega t+m_{23}^g\sin\omega t,\\
&y_2^{3,ver}=\psi_{n\tilde{n}2}-m_{23}^g\cos\omega t+m_{21}^g\sin\omega t,\\
&y_3^{3,ver}=\psi_{n\tilde{n}3}-m_{31}^g,\\
&y_4^{3,ver}=b_{g1}+m_{12}^g(\omega+\omega_{ie}\sin\phi)+m_{21}^g(\omega+\omega_{ie}\sin\phi),\\
&y_5^{3,ver}=b_{g2}+m_{22}^g(\omega+\omega_{ie}\sin\phi),\\
&y_6^{3,ver}=b_{g3}+m_{23}^g(\omega+\omega_{ie}\sin\phi)+m_{32}^g(\omega+\omega_{ie}\sin\phi),\\
&y_7^{3,ver}=b_{a1}-gm_{21}^g,\ y_8^{3,ver}=b_{a2}+gm_{22}^a,\\
&y_9^{3,ver}=b_{a3}+gm_{32}^a-gm_{23}^g,\ y_{10}^{3,ver}=m_{11}^g,\\
&y_{11}^{3,ver}=m_{13}^g+m_{31}^g,\ y_{12}^{3,ver}=m_{33}^g.
\end{aligned} \quad \text{(E.13)}$$

E.2.4 Summary of the analysis

Obviously, calibration procedure can be successful if and only if observable combinations (E.7), (E.10) and (E.13) can be solved for all the instrumental errors, which are modeled as constants and thus keep the same value throughout calibration procedure. Note, that observable combinations that include terms, dependent on orientation errors, cannot be used for calibration, because orientation errors are not constant, and their values are, in general, different at the end of each stage of calibration procedure.

Denote

$$\mathbf{y}^{i,ver}=\begin{pmatrix}y_4^{i,ver}&\dots&y_{12}^{i,ver}\end{pmatrix}^{\mathrm{T}},\ \mathbf{M}^i(\omega)=\frac{\partial\mathbf{y}^{i,ver}}{\partial(\mathbf{z}^1)^{\mathrm{T}}},\ i=1,2,3. \quad \text{(E.14)}$$

Here

$$\mathbf{z}^1=\begin{pmatrix}b_{g1}&b_{g2}&b_{g3}&b_{a1}&b_{a2}&b_{a3}&m_{11}^g&m_{12}^g&m_{13}^g&m_{21}^g&m_{22}^g&m_{23}^g&m_{31}^g&m_{32}^g&m_{33}^g&m_{11}^a&m_{21}^a&m_{22}^a&m_{31}^a&m_{32}^a&m_{33}^a\end{pmatrix}^{\mathrm{T}}. \quad \text{(E.15)}$$

Consider matrix

$$\mathbf{M}=\begin{pmatrix}(\mathbf{M}^1(\omega))^{\mathrm{T}}&(\mathbf{M}^1(-\omega))^{\mathrm{T}}&(\mathbf{M}^2(\omega))^{\mathrm{T}}&(\mathbf{M}^2(-\omega))^{\mathrm{T}}&(\mathbf{M}^3(\omega))^{\mathrm{T}}&(\mathbf{M}^3(-\omega))^{\mathrm{T}}\end{pmatrix}^{\mathrm{T}}. \quad \text{(E.16)}$$

Matrix $\mathbf{M}$ consists of 54 rows and 21 columns, but its rank is equal to 17. Thus, equation $\mathbf{M}\cdot\mathbf{z}^1=\mathbf{c}$ cannot be solved for all the instrumental errors of IMU. Moreover, rank of the matrix $\mathbf{M}$ does not depend on ω, because reduced row echelon form of $\mathbf{M}$ takes the form

$$\begin{pmatrix}
1&0&0&0&0&0&0&0&0&0&0&0&0&0&0&0&0&0&0&0&0\\
0&1&0&0&0&0&0&0&0&0&0&0&0&0&0&0&0&0&0&0&0\\
0&0&1&0&0&0&0&0&0&0&0&0&0&0&0&0&0&0&0&0&0\\
0&0&0&1&0&0&0&0&0&0&0&0&0&0&0&0&0&g&0&-g\\
0&0&0&0&1&0&0&0&0&0&0&0&0&0&0&0&0&0&g&-g\\
0&0&0&0&0&1&0&0&0&0&0&0&0&0&0&0&0&0&0&g\\
0&0&0&0&0&0&1&0&0&0&0&0&0&0&0&0&0&0&0&0\\
0&0&0&0&0&0&0&1&0&0&0&0&0&0&0&0&-1&0&0&1\\
0&0&0&0&0&0&0&0&1&0&0&0&0&0&0&0&-1&0&0&1\\
0&0&0&0&0&0&0&0&0&1&0&0&0&0&0&0&1&0&0&-1\\
0&0&0&0&0&0&0&0&0&0&1&0&0&0&0&0&0&0&0&0\\
0&0&0&0&0&0&0&0&0&0&0&1&0&0&0&0&0&-1&0&1\\
0&0&0&0&0&0&0&0&0&0&0&0&1&0&0&0&1&0&0&-1\\
0&0&0&0&0&0&0&0&0&0&0&0&0&1&0&0&0&1&0&-1\\
0&0&0&0&0&0&0&0&0&0&0&0&0&0&1&0&0&0&0&0\\
0&0&0&0&0&0&0&0&0&0&0&0&0&0&0&1&0&0&0&1\\
0&0&0&0&0&0&0&0&0&0&0&0&0&0&0&0&1&1&0&2\\
0&0&0&0&0&0&0&0&0&0&0&0&0&0&0&0&0&0&0&0\\
\vdots&&&&&&&&&&&&&&&&\vdots&\vdots&\vdots\\
0&0&0&0&0&0&0&0&0&0&0&0&0&0&0&0&0&0&0&0
\end{pmatrix}. \qquad \text{(E.17)}$$

Consequently, rotating IMU around vertical axis with various constant angular rates does not allow to determine all the instrumental errors, because dimension of unobservable space remains nonzero and equals to 4. Instrumental errors that can be determined in the procedure are gyroscope biases and scale factor errors.

E.3 Case of rotating around horizontal axis

Investigation procedure, suggested in Section 3.1.2 yields the following result.

First stage

$$\mathbf{R}_{nb}(t)=\begin{pmatrix}1&0&0\\0&\cos\omega t&-\sin\omega t\\0&\sin\omega t&\cos\omega t\end{pmatrix},$$
$$\boldsymbol{\omega}_{ib}=\mathbf{R}_{nb}^{\mathrm{T}}\cdot\left(\boldsymbol{\omega}_{ie}^{n}+(\omega,0,0)^{T}\right),$$
$$\boldsymbol{\omega}_{ie}^{n}=\left(0,\omega_{ie}\cos\phi,\omega_{ie}\sin\phi\right)^{\mathrm{T}},$$
$$\mathbf{f}_b=\mathbf{R}_{nb}^{\mathrm{T}}\cdot(0,0,g)^{T}.$$

$$y_1^{1,hor}=\psi_{n\tilde{n}1}$$
$$y_2^{1,hor}=g\psi_{n\tilde{n}2}-b_{a1}$$
$$y_3^{1,hor}=\omega_{ie}\cos\phi\cdot\psi_{n\tilde{n}3}-b_{g1}-\omega_{ie}\sin\phi/g\cdot b_{a1}-\omega m_{11}^{g}$$
$$y_4^{1,hor}=b_{g2}+\omega m_{21}^{g},\ y_5^{1,hor}=b_{g3}+\omega m_{31}^{g},$$
$$y_6^{1,hor}=b_{a2},\ y_7^{1,hor}=b_{a3},\ y_8^{1,hor}=m_{12}^{g},\ y_9^{1,hor}=m_{13}^{g},$$
$$y_{10}^{1,hor}=m_{22}^{g},\ y_{11}^{1,hor}=m_{23}^{g},\ y_{12}^{1,hor}=m_{32}^{g},\ y_{13}^{1,hor}=m_{33}^{g},$$
$$y_{14}^{1,hor}=m_{22}^{a},\ y_{15}^{1,hor}=m_{32}^{a},\ y_{16}^{1,hor}=m_{33}^{a}$$

Second stage

$$\mathbf{R}_{nb}(t)=\begin{pmatrix}0&1&0\\\cos\omega t&0&\sin\omega t\\\sin\omega t&0&-\cos\omega t\end{pmatrix},$$
$$\boldsymbol{\omega}_{ib}=\mathbf{R}_{nb}^{\mathrm{T}}\cdot\left(\boldsymbol{\omega}_{ie}^{n}+(\omega,0,0)^{T}\right),$$
$$\boldsymbol{\omega}_{ie}^{n}=\left(0,\omega_{ie}\cos\phi,\omega_{ie}\sin\phi\right)^{\mathrm{T}},$$
$$\mathbf{f}_b=\mathbf{R}_{nb}^{\mathrm{T}}\cdot(0,0,g)^{T}.$$

$$y_1^{2,hor}=\psi_{n\tilde{n}1},$$
$$y_2^{2,hor}=g\psi_{n\tilde{n}2}-b_{a2}-g\sin\omega t\cdot m_{21}^{a},$$
$$y_3^{2,hor}=\omega_{ie}\cos\phi\cdot\psi_{n\tilde{n}3}-b_{g2}-\omega_{ie}\sin\phi/g\cdot b_{a2}-$$
$$-\omega m_{22}^{g}+\omega_{ie}\cos\phi\cos\omega t\cdot m_{21}^{a},$$
$$y_4^{2,hor}=b_{g1}+\omega m_{12}^{g}-\omega m_{21}^{a},\ y_5^{2,hor}=b_{g3}+\omega m_{32}^{g},$$
$$y_6^{2,hor}=b_{a1},\ y_7^{2,hor}=b_{a3},\ y_8^{2,hor}=m_{11}^{g},\ y_9^{2,hor}=m_{13}^{g},$$
$$y_{10}^{2,hor}=m_{21}^{g}+m_{21}^{a},\ y_{11}^{2,hor}=m_{23}^{g},\ y_{12}^{2,hor}=m_{31}^{g},$$
$$y_{13}^{2,hor}=m_{33}^{g},\ y_{14}^{2,hor}=m_{11}^{a},\ y_{15}^{2,hor}=m_{31}^{a},\ y_{16}^{2,hor}=m_{33}^{a}$$

Third stage

$$\mathbf{R}_{nb}(t)=\begin{pmatrix}0&0&1\\-\sin\omega t&-\cos\omega t&0\\\cos\omega t&-\sin\omega t&0\end{pmatrix},$$
$$\boldsymbol{\omega}_{ib}=\mathbf{R}_{nb}^{\mathrm{T}}\cdot\left(\boldsymbol{\omega}_{ie}^{n}+(\omega,0,0)^{T}\right),$$
$$\boldsymbol{\omega}_{ie}^{n}=\left(0,\omega_{ie}\cos\phi,\omega_{ie}\sin\phi\right)^{\mathrm{T}},$$
$$\mathbf{f}_b=\mathbf{R}_{nb}^{\mathrm{T}}\cdot(0,0,g)^{T}.$$

$$y_1^{3,hor}=\psi_{n\tilde{n}1},$$
$$y_2^{3,hor}=g\psi_{n\tilde{n}2}-b_{a3}-g\cos\omega t\cdot m_{31}^{a}+g\sin\omega t\cdot m_{32}^{a},$$
$$y_3^{3,hor}=\omega_{ie}\cos\phi\cdot\psi_{n\tilde{n}3}-b_{g3}-\omega_{ie}\sin\phi/g\cdot b_{a3}-$$
$$-\omega m_{33}^{g}-\omega_{ie}\cos\phi\sin\omega t\cdot m_{31}^{a}-$$
$$-\omega_{ie}\cos\phi\cos\omega t\cdot m_{32}^{a},$$
$$y_4^{3,hor}=b_{g1}+\omega m_{13}^{g}-\omega m_{31}^{a},\ y_5^{3,hor}=b_{g2}+\omega m_{23}^{g}-\omega m_{32}^{a},$$
$$y_6^{3,hor}=b_{a1},\ y_7^{3,hor}=b_{a2},\ y_8^{3,hor}=m_{11}^{g},\ y_9^{3,hor}=m_{12}^{g},$$
$$y_{10}^{3,hor}=m_{21}^{g},\ y_{11}^{3,hor}=m_{22}^{g},$$
$$y_{12}^{3,hor}=m_{31}^{g}+m_{31}^{a},\ y_{13}^{3,hor}=m_{32}^{g}+m_{32}^{a},$$
$$y_{14}^{3,hor}=m_{11}^{a},\ y_{15}^{3,hor}=m_{21}^{a},\ y_{16}^{3,hor}=m_{22}^{a} \qquad \text{(E.18)}$$

In case of rotating around horizontal axis dimension of observable space equals to 16 at each stage of the calibration procedure and is greater than in case of rotating around vertical axis. Observable combinations (E.18) can be solved for all the instrumental errors. This agrees with simulation results in [108].

E.4 Numerical verification of observable combinations

Consider the second stage of calibration in case of rotating around horizontal axis. Observable combinations, obtained analytically, are given by (E.18). Denote $\mathbf{S}(t)$ a matrix of observable costates at the second stage of calibration. Then

$$\mathbf{S}(t)=\frac{\partial \mathbf{y}^{2,hor}}{\partial(\mathbf{z})^{\mathrm{T}}},\ \mathbf{y}^{2,hor}=\left(y_1^{2,hor}\quad\ldots\quad y_{16}^{2,hor}\right)^{\mathrm{T}}. \tag{E.19}$$

Explicit form of $\mathbf{S}(t)$ is as follows

$$\mathbf{S}(t)=\begin{pmatrix}
1&0&0&0&0&0&0&0&0&0&0&0&0&0&0&0\\
0&1&0&0&0&0&0&0&0&0&0&0&0&0&0&0\\
0&0&1&0&-\tan\phi/g&0&0&0&0&0&0&0&0&0&0&0\\
0&0&0&1&0&0&\omega&0&0&0&0&0&0&0&0&0\\
0&0&0&0&1&0&0&0&\omega&0&0&0&0&0&0&0\\
0&0&0&0&0&1&0&0&0&0&0&0&0&0&0&0\\
0&0&0&0&0&0&1&0&0&0&0&0&0&0&0&0\\
0&0&0&0&0&0&0&1&0&0&0&0&0&0&0&0\\
0&0&0&0&0&0&0&0&1&0&0&0&0&0&0&0\\
0&0&0&0&0&0&0&0&0&1&0&0&0&0&0&0\\
0&0&0&0&0&0&0&0&0&0&1&0&0&0&0&0\\
0&0&0&0&0&0&0&0&0&0&0&1&0&0&0&0\\
0&0&0&0&0&0&0&0&0&0&0&0&1&0&0&0\\
0&0&0&0&0&0&0&0&0&0&0&0&0&1&0&0\\
0&0&0&0&0&0&0&0&0&0&0&0&0&0&1&0\\
0&0&0&0&0&0&0&0&0&0&0&0&0&0&0&1
\end{pmatrix}. \tag{E.20}$$

Test indicator $\chi(t)$ is given on Figure 62. The following parameters were used to compute observability Gramian numerically and to evaluate matrix $\mathbf{S}(t)$

$$\phi=0.47\ [\mathrm{rad}],\ g=9.81\ [m/s^2],\ \omega=0.1\ [s^{-1}],\ \omega_{ie}=2\pi/24/3600\ [s^{-1}]. \tag{E.21}$$

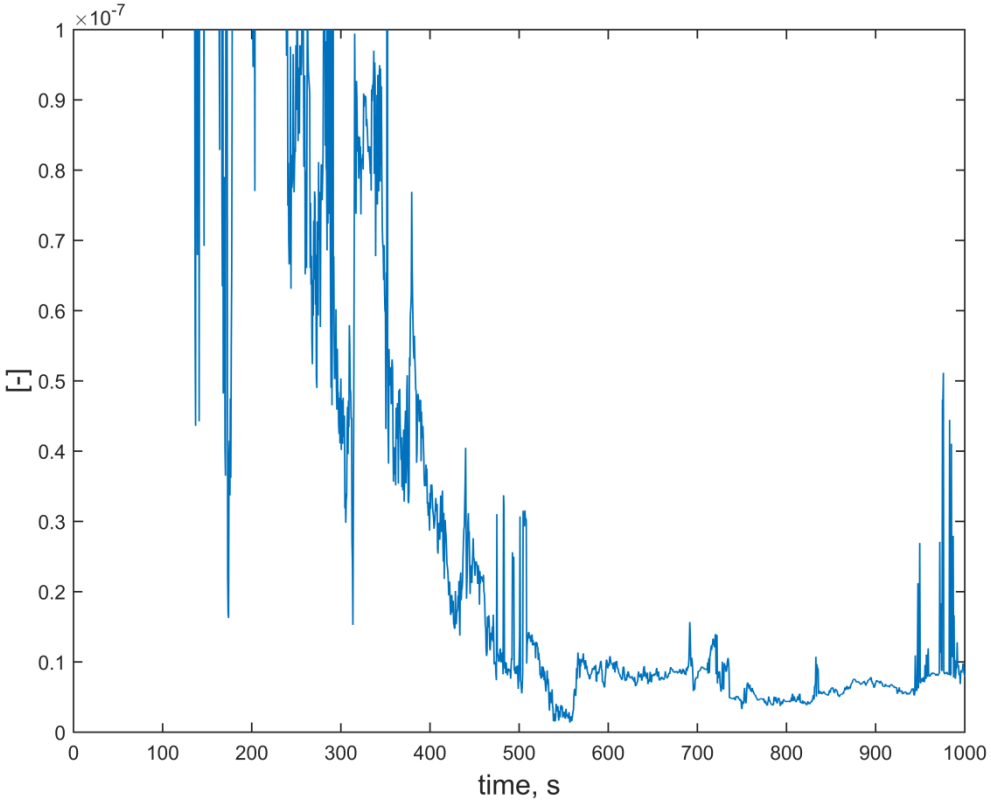

Fig. 62–Test indicators

Figure 62 shows test indicator converging to zero. After 100 seconds test indicator drop below 10^{-6} and after 400 seconds below 10^{-7}. Note, that the need to converge is due to presence of the Earth's rotation rate in the system matrix, which is a "small" effect compared to other terms in the differential equation. Presence of "small" effects causes small singular values of observability Gramian, which, in turn, are neglected when basis of Gramian's row space is determined numerically. Consequently, observable subspaces, generated by such "small" effects, need time to become distinguishable, and thus a settling period is required. Applying the same procedure with different set of parameters yields similar behavior of the test indicator. Therefore, it is concluded that observable combinations (E.18) at the second stage pass the verification, i. e. that rows of (E.20) span observable at time t subspace.

Assume now that a mistake was made during analytical derivation and a combination

$$y_4^{2,hor} = b_{g1} - \omega m_{21}^a \tag{E.22}$$

was obtained instead of

$$y_4^{2,hor} = b_{g1} + \omega m_{12}^g - \omega m_{21}^a. \tag{E.23}$$

Figure 63 shows behavior of test indicator in case of this mistake.

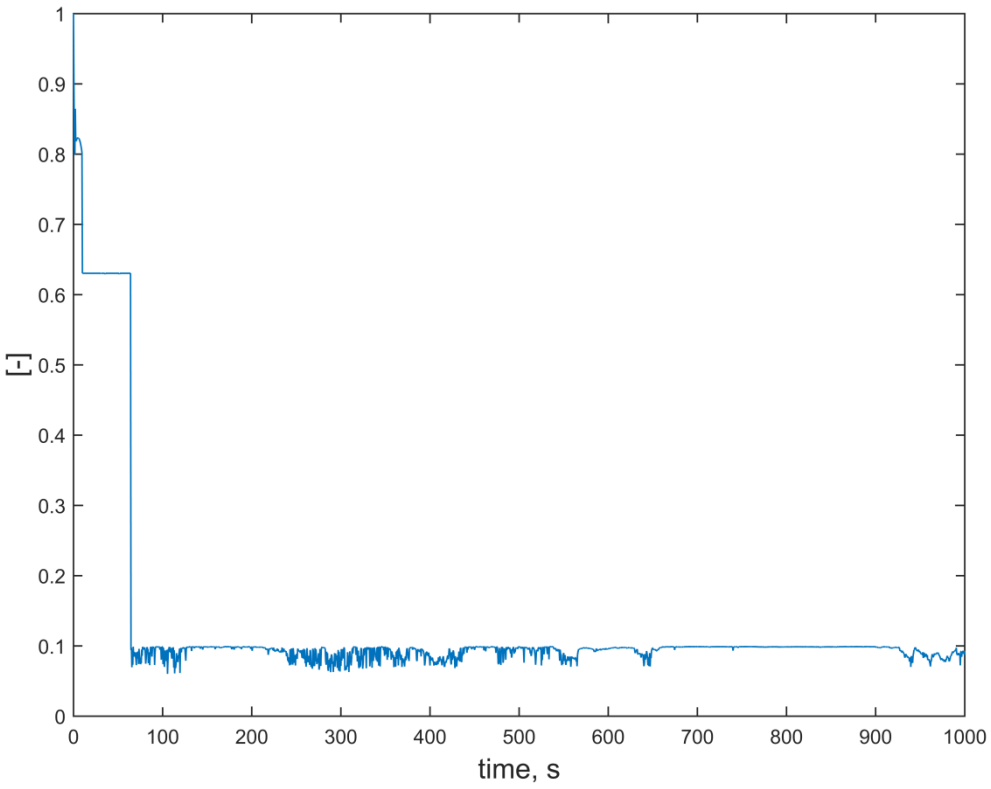

Fig. 63–Test indicators in case of mistake in combination $y_4^{2,hor}$

It is seen that test indicator settles around 0.1 and does not continue converging to zero. This fact indicates that an error in analytical analysis shall be suspected. Further consideration of matrix

$$\begin{pmatrix} \mathbf{s}_1(t)/\|\mathbf{s}_1(t)\| \\ \vdots \\ \mathbf{s}_m(t)/\|\mathbf{s}_m(t)\| \end{pmatrix} \cdot \left(\boldsymbol{\eta}_1(t),\ldots,\boldsymbol{\eta}_l(t)\right) \tag{E.24}$$

can help to find out, which observable costate appears erroneous.

Consider now that just a sign was confused in observable combination and that

$$y_2^{2,hor} = g\psi_{n\tilde{n}2} - b_{a2} + g\sin\omega t \cdot m_{21}^a \tag{E.25}$$

was obtained instead of

$$y_2^{2,hor} = g\psi_{n\tilde{n}2} - b_{a2} - g\sin\omega t \cdot m_{21}^a. \tag{E.26}$$

Behavior of the test indicator in this situation is shown on Figure 64.

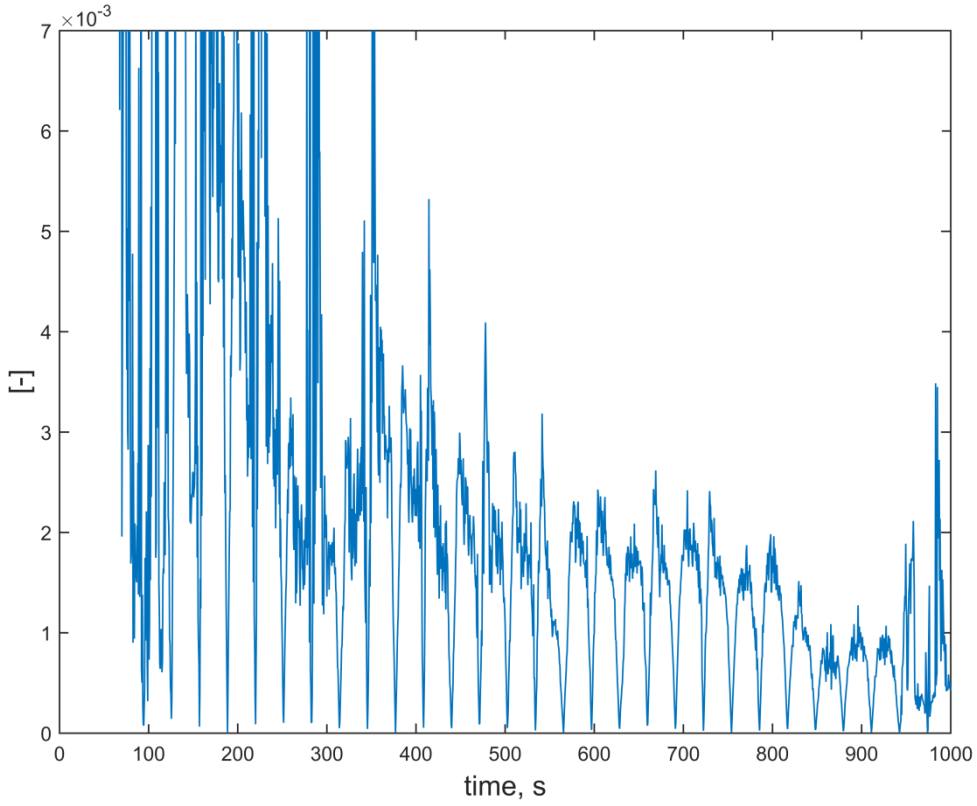

Fig. 64–Test indicators in case of mistake in combination $y_2^{2,hor}$

Test indicator is seen to remain five orders greater compared to error-free case. This, again, indicates that an error in analytical derivation should be suspected.

Another field of application of the verification algorithm suggested in Section 3.1.4 is analyzing consistency of investigations, conducted using simplified models. For example, consider that the Earth's rotation rate was neglected for the sake of simplifying analytical derivations. The procedure given in Section 3.1.2 would yield the following observable combinations for the second stage of calibration in case of rotating around horizontal axis.

$$\begin{aligned}
&y^{2,hor}_{1,\omega_{ie}=0} = \psi_{n\tilde{n}1},\ y^{2,hor}_{2,\omega_{ie}=0} = g\psi_{n\tilde{n}2} - b_{a2} - g\sin\omega t\cdot m^a_{21},\\
&y^{2,hor}_{3,\omega_{ie}=0} = b_{g1} + \omega m^g_{12} - \omega m^a_{21},\ y^{2,hor}_{4,\omega_{ie}=0} = b_{g2} + \omega m^g_{22},\\
&y^{2,hor}_{5,\omega_{ie}=0} = b_{g3} + \omega m^g_{32},\ y^{2,hor}_{6,\omega_{ie}=0} = b_{a1},\ y^{2,hor}_{7,\omega_{ie}=0} = b_{a3},\\
&y^{2,hor}_{8,\omega_{ie}=0} = m^a_{11},\ y^{2,hor}_{9,\omega_{ie}=0} = m^a_{31},\ y^{2,hor}_{10,\omega_{ie}=0} = m^a_{33}.
\end{aligned} \tag{E.27}$$

Behavior of test indicator, computed under assumption of non-rotating Earth, is shown on Figure 65.

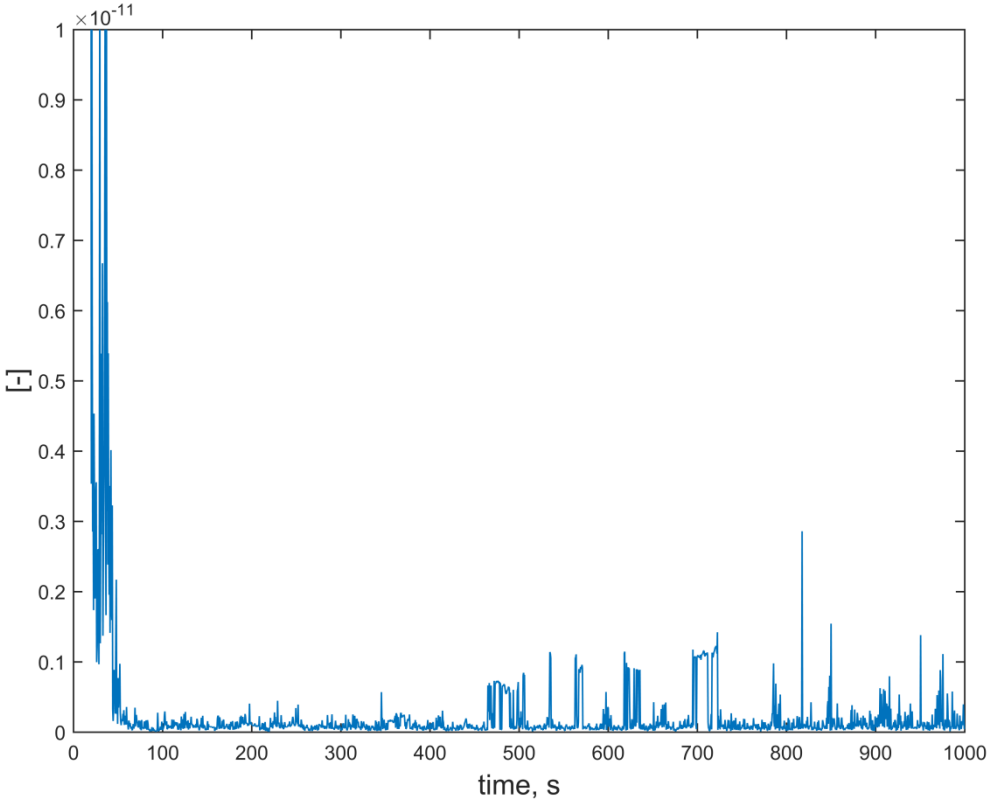

Fig. 65–Test indicators in simplified analysis

It is seen that when "small" effects are not present in dynamic system, observability Gramian appears numerically better-conditioned, and test indicator converges immediately, which proves validity of (E.27). Figure 66 shows test indicator of combinations (E.27) that was computed by the means of observability Gramian determined under assumption of rotating Earth. In other words, simplified analytical analysis is verified by the means of numerical investigation of complete model.

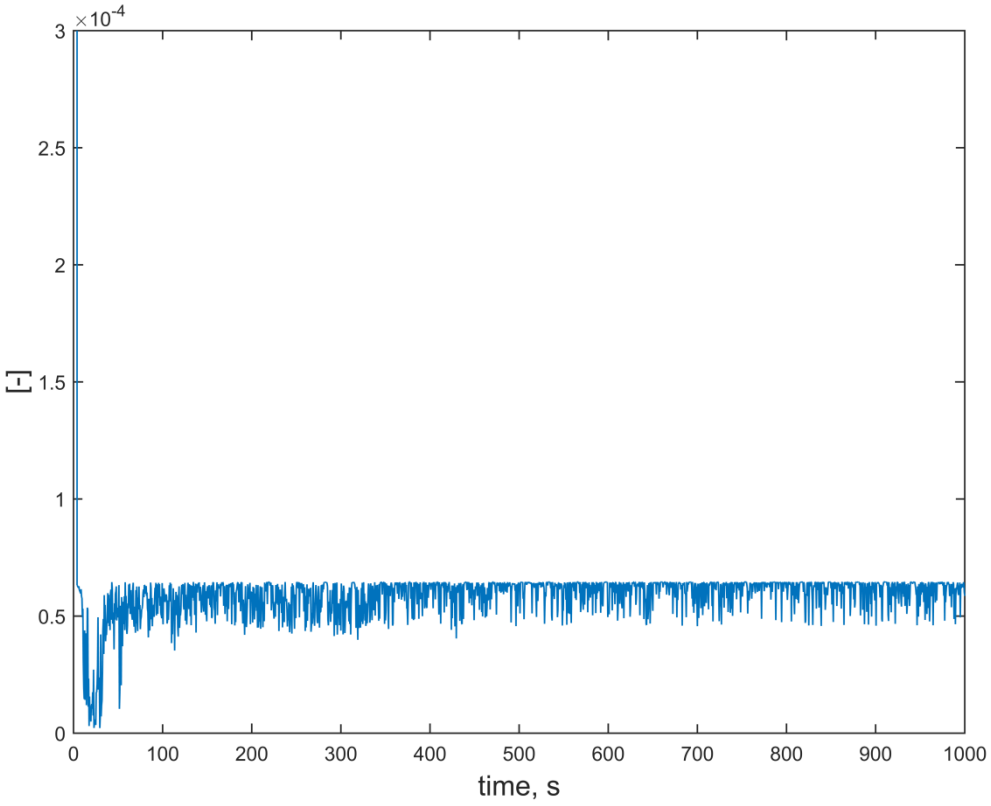

Fig. 66

Figure 66 shows test indicator stabilizing around 6×10^{-5}. This value is several orders greater than in error-free case, but at the same time is much smaller than expected in case of a mistake in analytical derivation (see Figures 63, 64). It means that neglected effect does not change observable subspace significantly and simplifying assumption is legitimate. If, in turn, the test indicator remained comparable to 1, it would indicate a need to use a more precise model for analytical analysis, because neglected effects would influence significantly geometry of observable space.

Appendix F. Justification of linearized error propagation.

All the simulations, presented in this thesis, were made under assumptions that errors were relatively small, and that error dynamics was sufficiently linear. Though, one still has a right to ask, if these assumptions are really fulfilled in the abovementioned simulations, and if linearized covariance propagation is accurate enough. In order to answer these questions and to justify the obtained results, additional investigation is performed.

Consistency of linear error propagation is suggested to be analysed by the means of comparing linearly predicted error distribution function to empherical error distribution function, obtained in Monte Carlo simulation. If the two functions appeared "close" enough, one could consider that linear error propagation provided acceptable accuracy. "Large" distance between the two functions would, in turn, indicate that nonlinear effects were considerable and should have been taken into account. Kolmogorov's statistics D_n, discussed in Section 5.2.4, can serve in this case as a good measure of distance.

Two classes of inertial sensors were considered in the investigation: industrial-grade and tactical-grade IMUs. For each of the sensor classes 1000 simulation runs of a strapdown inertial navigation algorithm were performed. Each of the simulations used different random number generator seed. The trajectory, considered in simulations, is given in the Appendix D.1.2. Parameters of the modeled inertial sensor errors are given in Appendix D.2. Results of 1000 simulations were used for computing empherical cumulative distribution functions of position, velocity, and orientation errors at different points of time. Afterwards, at those points of time the values of Kolmogorov's statistics were computed. Linearly propagated normal distributions of the navigation state errors were used as references for computation of the statistics. Figures 67 and 68 show plots of the Kolmogorov's statistics in case of tactical- and industrial-grade inertial sensors, respectively. Red horizontal lines show critical values of the Kolmogorov's statistics that correspond to false alarm probabilities of 0.01 and 0.001.

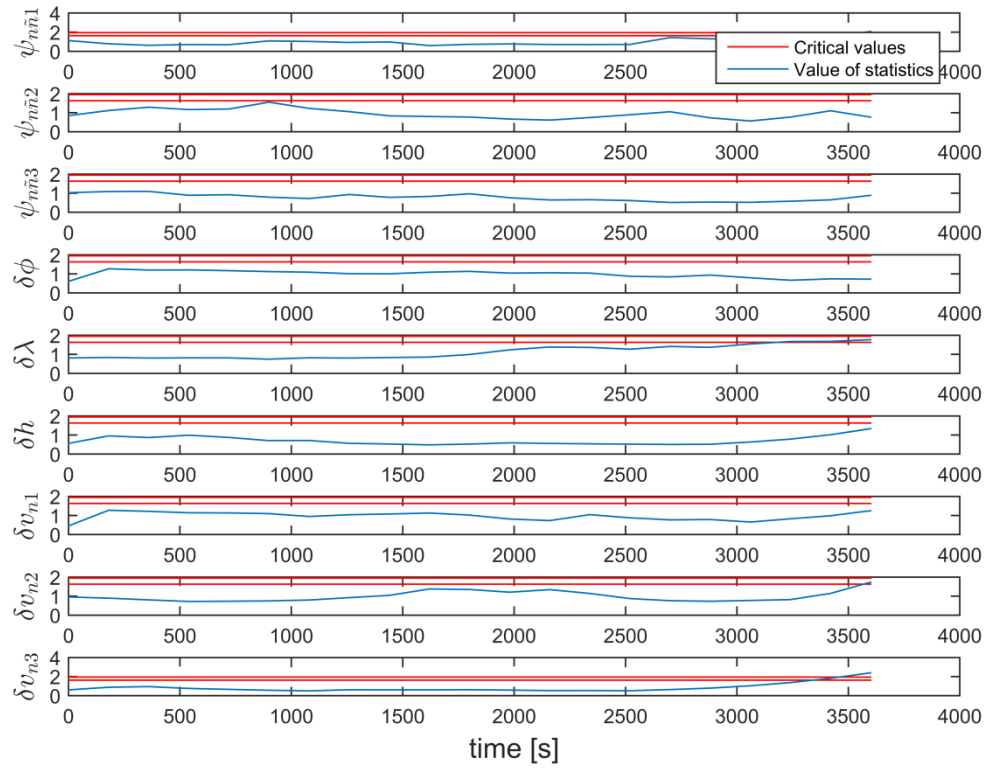

Fig. 67–Kolmogorov's statistics. Case of tactical-grade IMU.

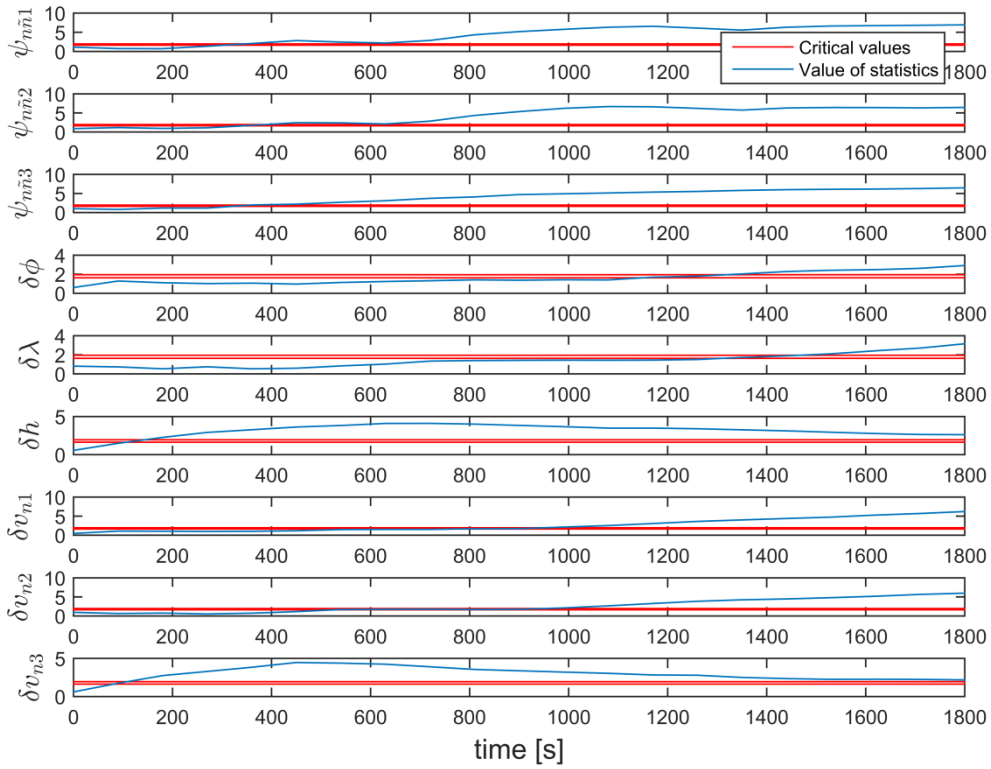

Fig. 68–Kolmogorov's statistics. Case of industrial-grade IMU.

The plots show that errors of unaided tactical grade INS behave sufficiently linear for almost an hour. In aided mode errors of the navigation solution are much smaller, than in unaided mode, and therefore usage of linearized error propagation in Chapters 3, 4, and 5 can be justified. In contrast, errors of unaided industrial-grade INS are seen to start to behave strongly nonlinear after just a short time of operation. For orientation errors critical time is about 5 minutes. In this time standard deviations of orientation errors exceed 3 degrees. Horizontal velocity errors start to behave nonlinearly after 10 minutes of operation, after their standard deviations exceed 220 m/s. Position errors, in turn, behave linearly longer, than all the other errors, and critical time for them is about 20 minutes. In 20 minutes standard deviations of latitude and longitude exceed 2 degrees. The strongest nonlinearities can be observed in the errors of the vertical channel. Although standard deviations of height and vertical speed appear comparable to the case of tactical-grade IMU, behavior of the distributions of vertical channel errors becomes strongly nonlinear. This can be explained by the fact that vertical channel is unstable and thus is sensitive to growth of attitude errors. In the simulations, presented in Chapters 3, 4, and 5 industrial-grade IMU was assumed to be aided, and standard deviations of all the navigation errors were seen not to exceed nonlinearity thresholds. Therefore, usage of linear error propagation can be justified in the case of industrial-grade IMU as well.

Appendix G. Derivation of equations for b-frame velocity vector.

Consider the second and the third equation in (2.1):

$$\begin{aligned}\dot{\mathbf{v}}_n &= \mathbf{R}_{nb}\cdot\mathbf{f}_b + \boldsymbol{\gamma}_n(\boldsymbol{\lambda}) - \left(2\mathbf{R}_{en}^{\mathrm{T}}(\boldsymbol{\lambda})\cdot\boldsymbol{\omega}_{ie} + \boldsymbol{\omega}_{en}(\boldsymbol{\lambda},\mathbf{v}_n)\right)\times\mathbf{v}_n,\\ \dot{\mathbf{R}}_{nb} &= \mathbf{R}_{nb}\boldsymbol{\Omega}_{ib} - \boldsymbol{\Omega}_{in}\mathbf{R}_{nb}.\end{aligned} \tag{G.1}$$

By definition $\mathbf{v}_b = \mathbf{R}_{nb}^{\mathrm{T}}\mathbf{v}_n$ and

$$\dot{\mathbf{v}}_b = \dot{\mathbf{R}}_{nb}^{\mathrm{T}}\mathbf{v}_n + \mathbf{R}_{nb}^{\mathrm{T}}\dot{\mathbf{v}}_n. \tag{G.2}$$

Therefore,

$$\begin{aligned}\dot{\mathbf{v}}_b &= \left(\mathbf{R}_{nb}\boldsymbol{\Omega}_{ib} - \boldsymbol{\Omega}_{in}\mathbf{R}_{nb}\right)^{\mathrm{T}}\mathbf{v}_n + \mathbf{R}_{nb}^{\mathrm{T}}\left(\mathbf{R}_{nb}\cdot\mathbf{f}_b + \boldsymbol{\gamma}_n(\boldsymbol{\lambda}) - \left(2\mathbf{R}_{en}^{\mathrm{T}}(\boldsymbol{\lambda})\cdot\boldsymbol{\omega}_{ie} + \boldsymbol{\omega}_{en}(\boldsymbol{\lambda},\mathbf{v}_n)\right)\times\mathbf{v}_n\right) =\\ &= \left(-\boldsymbol{\Omega}_{ib}\mathbf{R}_{nb}^{\mathrm{T}} + \mathbf{R}_{nb}^{\mathrm{T}}\boldsymbol{\Omega}_{in}\right)\mathbf{v}_n + \mathbf{f}_b + \mathbf{R}_{nb}^{\mathrm{T}}\boldsymbol{\gamma}_n(\boldsymbol{\lambda}) - \mathbf{R}_{nb}^{\mathrm{T}}\left(2\mathbf{R}_{en}^{\mathrm{T}}(\boldsymbol{\lambda})\cdot\boldsymbol{\omega}_{ie} + \boldsymbol{\omega}_{en}(\boldsymbol{\lambda},\mathbf{v}_n)\right)\times\mathbf{v}_n =\\ &= -\boldsymbol{\Omega}_{ib}\mathbf{v}_b + \mathbf{R}_{nb}^{\mathrm{T}}\boldsymbol{\Omega}_{in}\mathbf{R}_{nb}\mathbf{v}_b + \mathbf{f}_b + \mathbf{R}_{nb}^{\mathrm{T}}\boldsymbol{\gamma}_n(\boldsymbol{\lambda}) - \mathbf{R}_{nb}^{\mathrm{T}}\left(2\mathbf{R}_{en}^{\mathrm{T}}(\boldsymbol{\lambda})\cdot\boldsymbol{\omega}_{ie} + \boldsymbol{\omega}_{en}(\boldsymbol{\lambda},\mathbf{v}_n)\right)\times\left(\mathbf{R}_{nb}\mathbf{v}_b\right).\end{aligned} \tag{G.3}$$

By definition, $\boldsymbol{\Omega}_{in} = [\boldsymbol{\omega}_{in}\times]$, and $\boldsymbol{\omega}_{in} = \mathbf{R}_{en}^{\mathrm{T}}(\boldsymbol{\lambda})\cdot\boldsymbol{\omega}_{ie} + \boldsymbol{\omega}_{en}(\boldsymbol{\lambda},\mathbf{v}_n)$.

Thus equation (G.3) simplifies to

$$\dot{\mathbf{v}}_b = -\boldsymbol{\Omega}_{ib}\mathbf{v}_b + \mathbf{f}_b + \mathbf{R}_{nb}^{\mathrm{T}}\boldsymbol{\gamma}_n(\boldsymbol{\lambda}) - \mathbf{R}_{nb}^{\mathrm{T}}\left[\mathbf{R}_{en}^{\mathrm{T}}(\boldsymbol{\lambda})\cdot\boldsymbol{\omega}_{ie}\times\right]\mathbf{R}_{nb}\mathbf{v}_b. \tag{G.4}$$

Equation for error vector $\delta\mathbf{v}_b = \mathbf{v}_b - \tilde{\mathbf{v}}_b$ can be derived as follows.

$$\begin{aligned}\delta\dot{\mathbf{v}}_b &= \dot{\mathbf{v}}_b - \dot{\tilde{\mathbf{v}}}_b =\\ &= -\boldsymbol{\Omega}_{ib}\mathbf{v}_b + \mathbf{f}_b + \mathbf{R}_{nb}^{\mathrm{T}}\boldsymbol{\gamma}_n(\boldsymbol{\lambda}) - \mathbf{R}_{nb}^{\mathrm{T}}\left[\mathbf{R}_{en}^{\mathrm{T}}(\boldsymbol{\lambda})\cdot\boldsymbol{\omega}_{ie}\times\right]\mathbf{R}_{nb}\mathbf{v}_b -\\ &\quad -\left(-\tilde{\boldsymbol{\Omega}}_{ib}\tilde{\mathbf{v}}_b + \tilde{\mathbf{f}}_b + \mathbf{R}_{\tilde{n}b}^{\mathrm{T}}\boldsymbol{\gamma}_n(\tilde{\boldsymbol{\lambda}}) - \mathbf{R}_{\tilde{n}b}^{\mathrm{T}}\left[\mathbf{R}_{en}^{\mathrm{T}}(\tilde{\boldsymbol{\lambda}})\cdot\boldsymbol{\omega}_{ie}\times\right]\mathbf{R}_{\tilde{n}b}\tilde{\mathbf{v}}_b\right).\end{aligned} \tag{G.5}$$

$$\begin{aligned}-\boldsymbol{\Omega}_{ib}\mathbf{v}_b + \tilde{\boldsymbol{\Omega}}_{ib}\tilde{\mathbf{v}}_b &= -\boldsymbol{\Omega}_{ib}\mathbf{v}_b + \left(\boldsymbol{\Omega}_{ib} - \delta\boldsymbol{\Omega}_{ib}\right)\left(\mathbf{v}_b - \delta\mathbf{v}_b\right) =\\ &= -\boldsymbol{\Omega}_{ib}\delta\mathbf{v}_b - \delta\boldsymbol{\Omega}_{ib}\mathbf{v}_b + h.o.t = -\boldsymbol{\Omega}_{ib}\delta\mathbf{v}_b + \left[\mathbf{v}_b\times\right]\delta\boldsymbol{\omega}_{ib} + h.o.t\ ,\end{aligned}$$

$$\mathbf{f}_b - \tilde{\mathbf{f}}_b = \delta\mathbf{f}_b, \tag{G.6}$$

$$\begin{aligned}\mathbf{R}_{nb}^{\mathrm{T}}\boldsymbol{\gamma}_n(\boldsymbol{\lambda}) - \mathbf{R}_{\tilde{n}b}^{\mathrm{T}}\boldsymbol{\gamma}_n(\tilde{\boldsymbol{\lambda}}) &= \mathbf{R}_{nb}^{\mathrm{T}}\boldsymbol{\gamma}_n(\boldsymbol{\lambda}) - \mathbf{R}_{nb}^{\mathrm{T}}\mathbf{R}_{n\tilde{n}}\boldsymbol{\gamma}_n(\boldsymbol{\lambda} - \delta\boldsymbol{\lambda}) =\\ &= \mathbf{R}_{nb}^{\mathrm{T}}\boldsymbol{\gamma}_n(\boldsymbol{\lambda}) - \mathbf{R}_{nb}^{\mathrm{T}}\left(\mathbf{I} + \left[\psi_{n\tilde{n}}\times\right]\right)\left(\boldsymbol{\gamma}_n(\boldsymbol{\lambda}) - \left.\frac{\partial\boldsymbol{\gamma}_n(\tilde{\boldsymbol{\lambda}})}{\partial\tilde{\boldsymbol{\lambda}}^{\mathrm{T}}}\right|_{\boldsymbol{\lambda}}\cdot\delta\boldsymbol{\lambda}\right) + h.o.t =\end{aligned}$$

$$= -\mathbf{R}_{nb}^{\mathrm{T}}\left[\psi_{n\tilde{n}}\times\right]\boldsymbol{\gamma}_n(\boldsymbol{\lambda}) + \mathbf{R}_{nb}^{\mathrm{T}}\left.\frac{\partial\boldsymbol{\gamma}_n(\tilde{\boldsymbol{\lambda}})}{\partial\tilde{\boldsymbol{\lambda}}^{\mathrm{T}}}\right|_{\boldsymbol{\lambda}}\cdot\delta\boldsymbol{\lambda} + h.o.t = \mathbf{R}_{nb}^{\mathrm{T}}\left[\boldsymbol{\gamma}_n(\boldsymbol{\lambda})\times\right]\cdot\psi_{n\tilde{n}} + \mathbf{R}_{nb}^{\mathrm{T}}\left.\frac{\partial\boldsymbol{\gamma}_n(\tilde{\boldsymbol{\lambda}})}{\partial\tilde{\boldsymbol{\lambda}}^{\mathrm{T}}}\right|_{\boldsymbol{\lambda}}\cdot\delta\boldsymbol{\lambda} + h.o.t\ ,$$

$$\begin{aligned}
&-\mathbf{R}_{nb}^{\mathrm{T}}\left[\mathbf{R}_{en}^{\mathrm{T}}(\boldsymbol{\lambda})\cdot\boldsymbol{\omega}_{ie}\times\right]\mathbf{R}_{nb}\mathbf{v}_b + \mathbf{R}_{\tilde{n}b}^{\mathrm{T}}\left[\mathbf{R}_{en}^{\mathrm{T}}(\tilde{\boldsymbol{\lambda}})\cdot\boldsymbol{\omega}_{ie}\times\right]\mathbf{R}_{\tilde{n}b}\tilde{\mathbf{v}}_b = \\
&= -\mathbf{R}_{nb}^{\mathrm{T}}\left[\mathbf{R}_{en}^{\mathrm{T}}(\boldsymbol{\lambda})\cdot\boldsymbol{\omega}_{ie}\times\right]\mathbf{R}_{nb}\mathbf{v}_b + \mathbf{R}_{nb}^{\mathrm{T}}\mathbf{R}_{n\tilde{n}}\left[\mathbf{R}_{en}^{\mathrm{T}}(\boldsymbol{\lambda}-\delta\boldsymbol{\lambda})\cdot\boldsymbol{\omega}_{ie}\times\right]\mathbf{R}_{n\tilde{n}}^{\mathrm{T}}\mathbf{R}_{nb}\left(\mathbf{v}_b - \delta\mathbf{v}_b\right) = \\
&= -\mathbf{R}_{nb}^{\mathrm{T}}\left[\mathbf{R}_{en}^{\mathrm{T}}(\boldsymbol{\lambda})\cdot\boldsymbol{\omega}_{ie}\times\right]\mathbf{R}_{nb}\mathbf{v}_b + \mathbf{R}_{nb}^{\mathrm{T}}\left(\mathbf{I}+\left[\psi_{n\tilde{n}}\times\right]\right)\left[\mathbf{R}_{en}^{\mathrm{T}}(\boldsymbol{\lambda}-\delta\boldsymbol{\lambda})\cdot\boldsymbol{\omega}_{ie}\times\right]\left(\mathbf{I}-\left[\psi_{n\tilde{n}}\times\right]\right)\mathbf{R}_{nb}\left(\mathbf{v}_b - \delta\mathbf{v}_b\right) = \\
&= -\mathbf{R}_{nb}^{\mathrm{T}}\left[\mathbf{R}_{en}^{\mathrm{T}}(\boldsymbol{\lambda})\cdot\boldsymbol{\omega}_{ie}\times\right]\mathbf{R}_{nb}\mathbf{v}_b + \\
&\quad + \mathbf{R}_{nb}^{\mathrm{T}}\left(\mathbf{I}+\left[\psi_{n\tilde{n}}\times\right]\right)\left[\left(\mathbf{R}_{en}^{\mathrm{T}}(\boldsymbol{\lambda})\cdot\boldsymbol{\omega}_{ie} - \left.\frac{\partial\mathbf{R}_{en}^{\mathrm{T}}(\tilde{\boldsymbol{\lambda}})\cdot\boldsymbol{\omega}_{ie}}{\partial\tilde{\boldsymbol{\lambda}}^{\mathrm{T}}}\right|_{\boldsymbol{\lambda}}\cdot\delta\boldsymbol{\lambda}\right)\times\right]\left(\mathbf{R}_{nb}\mathbf{v}_b - \left[\psi_{n\tilde{n}}\times\right]\mathbf{R}_{nb}\mathbf{v}_b - \mathbf{R}_{nb}\delta\mathbf{v}_b\right) + h.o.t = \\
&= -\mathbf{R}_{nb}^{\mathrm{T}}\left[\mathbf{R}_{en}^{\mathrm{T}}(\boldsymbol{\lambda})\cdot\boldsymbol{\omega}_{ie}\times\right]\mathbf{R}_{nb}\mathbf{v}_b + \\
&\quad + \mathbf{R}_{nb}^{\mathrm{T}}\left(\mathbf{I}+\left[\psi_{n\tilde{n}}\times\right]\right)\left(\left[\mathbf{R}_{en}^{\mathrm{T}}(\boldsymbol{\lambda})\cdot\boldsymbol{\omega}_{ie}\times\right]\mathbf{R}_{nb}\mathbf{v}_b - \left[\left.\frac{\partial\mathbf{R}_{en}^{\mathrm{T}}(\tilde{\boldsymbol{\lambda}})\cdot\boldsymbol{\omega}_{ie}}{\partial\tilde{\boldsymbol{\lambda}}^{\mathrm{T}}}\right|_{\boldsymbol{\lambda}}\cdot\delta\boldsymbol{\lambda}\times\right]\mathbf{R}_{nb}\mathbf{v}_b - \right. \\
&\quad \left. - \left[\mathbf{R}_{en}^{\mathrm{T}}(\boldsymbol{\lambda})\cdot\boldsymbol{\omega}_{ie}\times\right]\left[\psi_{n\tilde{n}}\times\right]\mathbf{R}_{nb}\mathbf{v}_b - \left[\mathbf{R}_{en}^{\mathrm{T}}(\boldsymbol{\lambda})\cdot\boldsymbol{\omega}_{ie}\times\right]\mathbf{R}_{nb}\delta\mathbf{v}_b\right) + h.o.t = \\
&= \mathbf{R}_{nb}^{\mathrm{T}}\left[\psi_{n\tilde{n}}\times\right]\left[\mathbf{R}_{en}^{\mathrm{T}}(\boldsymbol{\lambda})\cdot\boldsymbol{\omega}_{ie}\times\right]\mathbf{R}_{nb}\mathbf{v}_b - \mathbf{R}_{nb}^{\mathrm{T}}\left[\left.\frac{\partial\mathbf{R}_{en}^{\mathrm{T}}(\tilde{\boldsymbol{\lambda}})\cdot\boldsymbol{\omega}_{ie}}{\partial\tilde{\boldsymbol{\lambda}}^{\mathrm{T}}}\right|_{\boldsymbol{\lambda}}\cdot\delta\boldsymbol{\lambda}\times\right]\mathbf{R}_{nb}\mathbf{v}_b - \\
&\quad - \mathbf{R}_{nb}^{\mathrm{T}}\left[\mathbf{R}_{en}^{\mathrm{T}}(\boldsymbol{\lambda})\cdot\boldsymbol{\omega}_{ie}\times\right]\left[\psi_{n\tilde{n}}\times\right]\mathbf{R}_{nb}\mathbf{v}_b - \mathbf{R}_{nb}^{\mathrm{T}}\left[\mathbf{R}_{en}^{\mathrm{T}}(\boldsymbol{\lambda})\cdot\boldsymbol{\omega}_{ie}\times\right]\mathbf{R}_{nb}\delta\mathbf{v}_b + h.o.t = \\
&= -\mathbf{R}_{nb}^{\mathrm{T}}\left[\left(\mathbf{R}_{en}^{\mathrm{T}}(\boldsymbol{\lambda})\cdot\boldsymbol{\omega}_{ie}\times\mathbf{R}_{nb}\mathbf{v}_b\right)\times\right]\cdot\psi_{n\tilde{n}} + \mathbf{R}_{nb}^{\mathrm{T}}\left[\mathbf{R}_{nb}\mathbf{v}_b\times\right]\cdot\left.\frac{\partial\mathbf{R}_{en}^{\mathrm{T}}(\tilde{\boldsymbol{\lambda}})\cdot\boldsymbol{\omega}_{ie}}{\partial\tilde{\boldsymbol{\lambda}}^{\mathrm{T}}}\right|_{\boldsymbol{\lambda}}\cdot\delta\boldsymbol{\lambda} + \\
&\quad + \mathbf{R}_{nb}^{\mathrm{T}}\left[\mathbf{R}_{en}^{\mathrm{T}}(\boldsymbol{\lambda})\cdot\boldsymbol{\omega}_{ie}\times\right]\left[\mathbf{R}_{nb}\mathbf{v}_b\times\right]\cdot\psi_{n\tilde{n}} - \mathbf{R}_{nb}^{\mathrm{T}}\left[\mathbf{R}_{en}^{\mathrm{T}}(\boldsymbol{\lambda})\cdot\boldsymbol{\omega}_{ie}\times\right]\mathbf{R}_{nb}\delta\mathbf{v}_b + h.o.t = \\
&= \mathbf{R}_{nb}^{\mathrm{T}}\left[\mathbf{R}_{nb}\mathbf{v}_b\times\right]\cdot\left.\frac{\partial\mathbf{R}_{en}^{\mathrm{T}}(\tilde{\boldsymbol{\lambda}})\cdot\boldsymbol{\omega}_{ie}}{\partial\tilde{\boldsymbol{\lambda}}^{\mathrm{T}}}\right|_{\boldsymbol{\lambda}}\cdot\delta\boldsymbol{\lambda} - \mathbf{R}_{nb}^{\mathrm{T}}\left[\mathbf{R}_{en}^{\mathrm{T}}(\boldsymbol{\lambda})\cdot\boldsymbol{\omega}_{ie}\times\right]\mathbf{R}_{nb}\delta\mathbf{v}_b + \\
&\quad + \mathbf{R}_{nb}^{\mathrm{T}}\left(-\left[\left(\mathbf{R}_{en}^{\mathrm{T}}(\boldsymbol{\lambda})\cdot\boldsymbol{\omega}_{ie}\times\mathbf{R}_{nb}\mathbf{v}_b\right)\times\right] + \left[\mathbf{R}_{en}^{\mathrm{T}}(\boldsymbol{\lambda})\cdot\boldsymbol{\omega}_{ie}\times\right]\left[\mathbf{R}_{nb}\mathbf{v}_b\times\right]\right)\cdot\psi_{n\tilde{n}} + h.o.t\ .
\end{aligned} \tag{G.7}$$

Combining (G.5), (G.6), (G.7) and neglecting higher order terms yields

$$\begin{aligned}
\delta\dot{\mathbf{v}}_b = &\mathbf{R}_{nb}^{\mathrm{T}}\left(\left.\frac{\partial\boldsymbol{\gamma}_n(\tilde{\boldsymbol{\lambda}})}{\partial\tilde{\boldsymbol{\lambda}}^{\mathrm{T}}}\right|_{\boldsymbol{\lambda}} + \left[\mathbf{R}_{nb}\mathbf{v}_b\times\right]\cdot\left.\frac{\partial\mathbf{R}_{en}^{\mathrm{T}}(\tilde{\boldsymbol{\lambda}})\cdot\boldsymbol{\omega}_{ie}}{\partial\tilde{\boldsymbol{\lambda}}^{\mathrm{T}}}\right|_{\boldsymbol{\lambda}}\right)\cdot\delta\boldsymbol{\lambda} + \\
&+\left(-\boldsymbol{\Omega}_{ib} - \mathbf{R}_{nb}^{\mathrm{T}}\left[\mathbf{R}_{en}^{\mathrm{T}}(\boldsymbol{\lambda})\cdot\boldsymbol{\omega}_{ie}\times\right]\mathbf{R}_{nb}\right)\cdot\delta\mathbf{v}_b + \\
&+\mathbf{R}_{nb}^{\mathrm{T}}\left(\left[\boldsymbol{\gamma}_n(\boldsymbol{\lambda})\times\right] - \left[\left(\mathbf{R}_{en}^{\mathrm{T}}(\boldsymbol{\lambda})\cdot\boldsymbol{\omega}_{ie}\times\mathbf{R}_{nb}\mathbf{v}_b\right)\times\right] + \left[\mathbf{R}_{en}^{\mathrm{T}}(\boldsymbol{\lambda})\cdot\boldsymbol{\omega}_{ie}\times\right]\left[\mathbf{R}_{nb}\mathbf{v}_b\times\right]\right)\cdot\psi_{n\tilde{n}} + \\
&+\delta\mathbf{f}_b + \left[\mathbf{v}_b\times\right]\delta\boldsymbol{\omega}_{ib}.
\end{aligned} \tag{G.8}$$

Note, that to a first approximation

$$
\begin{aligned}
\delta\dot{\mathbf{v}}_b = {} & \mathbf{R}_{\tilde{n}b}^{\mathrm{T}}\left(\left.\frac{\partial\boldsymbol{\gamma}_n(\boldsymbol{\lambda})}{\partial\boldsymbol{\lambda}^{\mathrm{T}}}\right|_{\tilde{\boldsymbol{\lambda}}} + \left[\mathbf{R}_{\tilde{n}b}\tilde{\mathbf{v}}_b\times\right]\cdot\left.\frac{\partial\mathbf{R}_{en}^{\mathrm{T}}(\boldsymbol{\lambda})\cdot\boldsymbol{\omega}_{ie}}{\partial\boldsymbol{\lambda}^{\mathrm{T}}}\right|_{\tilde{\boldsymbol{\lambda}}}\right)\cdot\delta\boldsymbol{\lambda} + \\
& + \left(-\tilde{\boldsymbol{\Omega}}_{ib} - \mathbf{R}_{\tilde{n}b}^{\mathrm{T}}\left[\mathbf{R}_{en}^{\mathrm{T}}(\tilde{\boldsymbol{\lambda}})\cdot\boldsymbol{\omega}_{ie}\times\right]\mathbf{R}_{\tilde{n}b}\right)\cdot\delta\mathbf{v}_b + \\
& + \mathbf{R}_{\tilde{n}b}^{\mathrm{T}}\left(\left[\boldsymbol{\gamma}_n(\tilde{\boldsymbol{\lambda}})\times\right] - \left[\left(\mathbf{R}_{en}^{\mathrm{T}}(\tilde{\boldsymbol{\lambda}})\cdot\boldsymbol{\omega}_{ie}\times\mathbf{R}_{\tilde{n}b}\tilde{\mathbf{v}}_b\right)\times\right] + \left[\mathbf{R}_{en}^{\mathrm{T}}(\tilde{\boldsymbol{\lambda}})\cdot\boldsymbol{\omega}_{ie}\times\right]\left[\mathbf{R}_{\tilde{n}b}\tilde{\mathbf{v}}_b\times\right]\right)\cdot\boldsymbol{\psi}_{n\tilde{n}} + \\
& + \delta\mathbf{f}_b + \left[\tilde{\mathbf{v}}_b\times\right]\delta\boldsymbol{\omega}_{ib}.
\end{aligned}
\tag{G.9}
$$

Therefore, the system of b-frame navigation equations takes the form

$$
\begin{aligned}
& \dot{\boldsymbol{\lambda}} = \mathbf{D}^{-1}(\boldsymbol{\lambda})\cdot\mathbf{R}_{nb}\mathbf{v}_b, \\
& \dot{\mathbf{v}}_b = -\boldsymbol{\Omega}_{ib}\mathbf{v}_b + \mathbf{f}_b + \mathbf{R}_{nb}^{\mathrm{T}}\mathbf{v}_n(\boldsymbol{\lambda}) - \mathbf{R}_{nb}^{\mathrm{T}}\left[\mathbf{R}_{en}^{\mathrm{T}}(\boldsymbol{\lambda})\cdot\boldsymbol{\omega}_{ie}\times\right]\mathbf{R}_{nb}\mathbf{v}_b, \\
& \dot{\mathbf{R}}_{nb} = \mathbf{R}_{nb}\boldsymbol{\Omega}_{ib} - \boldsymbol{\Omega}_{in}\mathbf{R}_{nb}, \\
& \mathbf{D}(\boldsymbol{\lambda}) = diag\left(M(\phi)+h,\left(N(\phi)+h\right)\cdot\cos\phi,-1\right).
\end{aligned}
\tag{G.10}
$$

Corresponding error propagation equations are given by

$$
\begin{aligned}
\delta\dot{\boldsymbol{\lambda}} = {} & \left.\frac{\partial\left(\mathbf{D}^{-1}(\boldsymbol{\lambda})\cdot\mathbf{v}_n\right)}{\partial\boldsymbol{\lambda}^{\mathrm{T}}}\right|_{\tilde{\boldsymbol{\lambda}},\mathbf{R}_{\tilde{n}b}\tilde{\mathbf{v}}_b}\cdot\delta\boldsymbol{\lambda} + \mathbf{D}^{-1}\left(\tilde{\boldsymbol{\lambda}}\right)\cdot\mathbf{R}_{\tilde{n}b}\delta\mathbf{v}_b - \mathbf{D}^{-1}\left(\tilde{\boldsymbol{\lambda}}\right)\left[\mathbf{R}_{\tilde{n}b}\tilde{\mathbf{v}}_b\times\right]\cdot\boldsymbol{\psi}_{n\tilde{n}}, \\
\delta\dot{\mathbf{v}}_b = {} & \mathbf{R}_{\tilde{n}b}^{\mathrm{T}}\left(\left.\frac{\partial\boldsymbol{\gamma}_n(\boldsymbol{\lambda})}{\partial\boldsymbol{\lambda}^{\mathrm{T}}}\right|_{\tilde{\boldsymbol{\lambda}}} + \left[\mathbf{R}_{\tilde{n}b}\tilde{\mathbf{v}}_b\times\right]\cdot\left.\frac{\partial\mathbf{R}_{en}^{\mathrm{T}}(\boldsymbol{\lambda})\cdot\boldsymbol{\omega}_{ie}}{\partial\boldsymbol{\lambda}^{\mathrm{T}}}\right|_{\tilde{\boldsymbol{\lambda}}}\right)\cdot\delta\boldsymbol{\lambda} + \\
& + \left(-\tilde{\boldsymbol{\Omega}}_{ib} - \mathbf{R}_{\tilde{n}b}^{\mathrm{T}}\left[\mathbf{R}_{en}^{\mathrm{T}}(\tilde{\boldsymbol{\lambda}})\cdot\boldsymbol{\omega}_{ie}\times\right]\mathbf{R}_{\tilde{n}b}\right)\cdot\delta\mathbf{v}_b + \\
& + \mathbf{R}_{\tilde{n}b}^{\mathrm{T}}\left(\left[\boldsymbol{\gamma}_n(\tilde{\boldsymbol{\lambda}})\times\right] - \left[\left(\mathbf{R}_{en}^{\mathrm{T}}(\tilde{\boldsymbol{\lambda}})\cdot\boldsymbol{\omega}_{ie}\times\mathbf{R}_{\tilde{n}b}\tilde{\mathbf{v}}_b\right)\times\right] + \left[\mathbf{R}_{en}^{\mathrm{T}}(\tilde{\boldsymbol{\lambda}})\cdot\boldsymbol{\omega}_{ie}\times\right]\left[\mathbf{R}_{\tilde{n}b}\tilde{\mathbf{v}}_b\times\right]\right)\cdot\boldsymbol{\psi}_{n\tilde{n}} + \\
& + \delta\mathbf{f}_b + \left[\tilde{\mathbf{v}}_b\times\right]\delta\boldsymbol{\omega}_{ib}, \\
\dot{\boldsymbol{\psi}}_{n\tilde{n}} = {} & -\left.\frac{\partial\boldsymbol{\omega}_{in}\left(\boldsymbol{\lambda},\mathbf{v}_n\right)}{\partial\boldsymbol{\lambda}^{\mathrm{T}}}\right|_{\tilde{\boldsymbol{\lambda}},\mathbf{R}_{\tilde{n}b}\tilde{\mathbf{v}}_b}\cdot\delta\boldsymbol{\lambda} - \left.\frac{\partial\boldsymbol{\omega}_{in}\left(\boldsymbol{\lambda},\mathbf{v}_n\right)}{\partial\mathbf{v}_n{}^{\mathrm{T}}}\right|_{\tilde{\boldsymbol{\lambda}},\mathbf{R}_{\tilde{n}b}\tilde{\mathbf{v}}_b}\cdot\mathbf{R}_{\tilde{n}b}\delta\mathbf{v}_b + \\
& + \left(\left.\frac{\partial\boldsymbol{\omega}_{in}\left(\boldsymbol{\lambda},\mathbf{v}_n\right)}{\partial\mathbf{v}_n{}^{\mathrm{T}}}\right|_{\tilde{\boldsymbol{\lambda}},\mathbf{R}_{\tilde{n}b}\tilde{\mathbf{v}}_b}\cdot\left[\mathbf{R}_{\tilde{n}b}\tilde{\mathbf{v}}_b\times\right] - \boldsymbol{\Omega}_{in}\left(\tilde{\boldsymbol{\lambda}},\tilde{\mathbf{v}}_n\right)\right)\cdot\boldsymbol{\psi}_{n\tilde{n}} + \mathbf{R}_{\tilde{n}b}\cdot\delta\boldsymbol{\omega}_{ib}.
\end{aligned}
\tag{G.11}
$$

Then air data measurement equations will take the following form.

For barometric altitude measurement:

$$
\begin{aligned}
& y_{baro,b} = h_{baro}, \\
& \Delta y_{baro,b} = \tilde{y}_{baro} - \tilde{h} \approx \delta h - \delta h_{atm} - b_{baro} - \nu_{baro}.
\end{aligned}
\tag{G.12}
$$

For TAS measurement:

$$
\begin{aligned}
&y_{TAS,b} = \left\| \mathbf{v}_b - \mathbf{R}_{nb}^{\mathsf{T}} \mathbf{v}_n^W \right\|, \\
&\Delta y_{TAS,b} = \tilde{y}_{TAS} - \left\| \tilde{\mathbf{v}}_b - \mathbf{R}_{\tilde{n}b}^{\mathsf{T}} \tilde{\mathbf{v}}_n^W \right\| \approx \frac{1}{\left\| \tilde{\mathbf{v}}_n - \tilde{\mathbf{v}}_n^W \right\|} \left(\tilde{\mathbf{v}}_n - \tilde{\mathbf{v}}_n^W \right)^{\mathsf{T}} \cdot \left(\delta \mathbf{v}_n - \delta \mathbf{v}_n^W \right) - \nu_{TAS}, \\
&y_{TAS2,b} = \left\| \mathbf{v}_b - \mathbf{R}_{nb}^{\mathsf{T}} \mathbf{v}_n^W \right\|^2, \\
&\Delta y_{TAS2,b} = \tilde{y}_{TAS2} - \left\| \tilde{\mathbf{v}}_b - \mathbf{R}_{\tilde{n}b}^{\mathsf{T}} \tilde{\mathbf{v}}_n^W \right\|^2 \approx 2 \left(\tilde{\mathbf{v}}_b - \mathbf{R}_{\tilde{n}b}^{\mathsf{T}} \tilde{\mathbf{v}}_n^W \right)^{\mathsf{T}} \cdot \left(\delta \mathbf{v}_b - \mathbf{R}_{\tilde{n}b}^{\mathsf{T}} \left(\delta \mathbf{v}_n^W + \left[\tilde{\mathbf{v}}_n^W \times \right] \cdot \psi_{n\tilde{n}} \right) \right) - \nu_{TAS2}.
\end{aligned}
\tag{G.13}
$$

For AOA measurement:

$$
\begin{aligned}
&y_{AOA,b} = \arctan \frac{w - w^W}{u - u^W}, \\
&\Delta y_{AOA,b} = \tilde{y}_{AOA} - \arctan \frac{\tilde{w} - \tilde{w}^W}{\tilde{u} - \tilde{u}^W} \approx \\
&\approx \begin{pmatrix} -\dfrac{\tilde{w} - \tilde{w}^W}{\left(\tilde{u} - \tilde{u}^W \right)^2} & 0 & \dfrac{1}{\tilde{u} - \tilde{u}^W} & \dfrac{\tilde{w} - \tilde{w}^W}{\left(\tilde{u} - \tilde{u}^W \right)^2} & 0 & -\dfrac{1}{\tilde{u} - \tilde{u}^W} \end{pmatrix} \cdot \begin{pmatrix} \delta \mathbf{v}_b \\ \mathbf{R}_{\tilde{n}b}^{\mathsf{T}} \left(\delta \mathbf{v}_n^{\mathsf{w}} + \left[\tilde{\mathbf{v}}_n^{\mathsf{w}} \times \right] \cdot \psi_{n\tilde{n}} \right) \end{pmatrix} - \nu_{AOA}.
\end{aligned}
\tag{G.14}
$$

For AOS measurement:

$$
\begin{aligned}
&y_{AOS,b} = \arctan \frac{v - v^W}{u - u^W}, \\
&\Delta y_{AOS,b} = \tilde{y}_{AOS} - \arctan \frac{\tilde{v} - \tilde{v}^W}{\tilde{u} - \tilde{u}^W} \approx \\
&\approx \begin{pmatrix} -\dfrac{\tilde{v} - \tilde{v}^W}{\left(\tilde{u} - \tilde{u}^W \right)^2} & \dfrac{1}{\tilde{u} - \tilde{u}^W} & 0 & \dfrac{\tilde{v} - \tilde{v}^W}{\left(\tilde{u} - \tilde{u}^W \right)^2} & -\dfrac{1}{\tilde{u} - \tilde{u}^W} & 0 \end{pmatrix} \cdot \begin{pmatrix} \delta \mathbf{v}_b \\ \mathbf{R}_{\tilde{n}b}^{\mathsf{T}} \left(\delta \mathbf{v}_n^{\mathsf{w}} + \left[\tilde{\mathbf{v}}_n^{\mathsf{w}} \times \right] \cdot \psi_{n\tilde{n}} \right) \end{pmatrix} - \nu_{AOS}.
\end{aligned}
\tag{G.15}
$$

For b-frame velocity w.r.t. wind measurement:

$$
\begin{aligned}
&\mathbf{y}_{\mathbf{vb},rel} = \mathbf{v}_b - \mathbf{v}_b^W = \mathbf{v}_b - \mathbf{R}_{nb}^{\mathsf{T}} \mathbf{v}_n^W, \\
&\Delta \mathbf{y}_{\mathbf{vb},rel} = \tilde{\mathbf{y}}_{\mathbf{vb},rel} - \left(\tilde{\mathbf{v}}_b - \mathbf{R}_{\tilde{n}b}^{\mathsf{T}} \tilde{\mathbf{v}}_n^W \right) = \\
&\quad = \mathbf{y}_{\mathbf{vb},rel} - \mathbf{v}_{\mathbf{vb},rel} - \left(\tilde{\mathbf{v}}_b - \mathbf{R}_{\tilde{n}b}^{\mathsf{T}} \tilde{\mathbf{v}}_n^W \right) \approx \\
&\quad \approx \delta \mathbf{v}_b - \mathbf{R}_{\tilde{n}b}^{\mathsf{T}} \delta \mathbf{v}_n^W - \mathbf{R}_{\tilde{n}b}^{\mathsf{T}} \left[\tilde{\mathbf{v}}_n^W \times \right] \cdot \psi_{n\tilde{n}} - \mathbf{v}_{\mathbf{vb},rel}.
\end{aligned}
\tag{G.16}
$$

Appendix H. Comparison of b- and n-frame mechanizations.

B- and n-frame mechanizations can alternatively be used for prediction of covariance of the navigation solution provided by even industrial-grade unaided INS. Both mechanizations appear robust to error growth in a sense that propagating along the true trajectory and along the computed one yields the same result. This is illustrated by Figures 69–72, which show standard deviations of position, velocity, and orientation errors, respectively, propagated along aerobatic flight trajectory (see Appendix D.1.3) for industrial-grade INS. Solid lines on the plots correspond to standard deviations, computed along the *true* trajectory, while dashed lines denote standard deviations, propagated along *computed* navigation solution. The figures demonstrate that independently of mechanization covariance propagation appears almost insensitive to an error of the navigation state and therefore can be said to be "robust" to "perturbations" of the system matrix, caused by linearizing at the computed point, rather than in the true one. Note that abrupt variations of $\sigma_{\delta v_{b2}}$ and $\sigma_{\delta v_{b3}}$ are due to exchange between uncertainties along lateral and longitudal axes during aerobatic maneuvers like, for example, inside loop and roll. This is illustrated by a plot of root sum squared (RSS) of velocity vector standard deviations (see Figure 71). Both n- and b-frame Kalman filters were initialized with the same initial value of covariance matrix, discussed in Appendix D.7.1, i. e. $\mathbf{P}_n(0) = \mathbf{P}_b(0) = \mathbf{P}_0$.

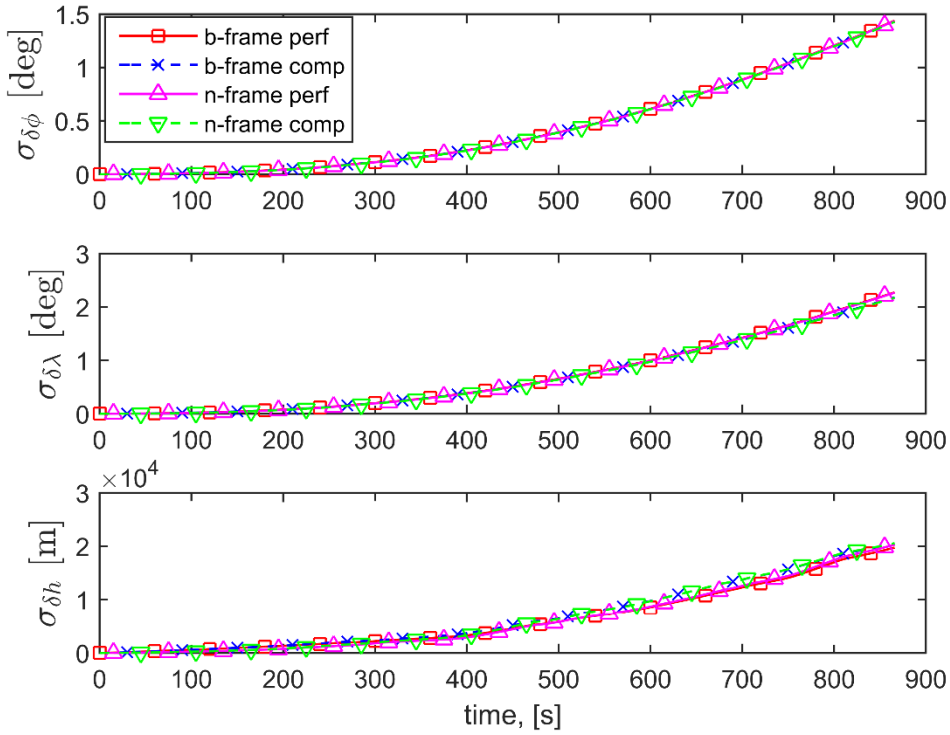

Fig. 69–Standard deviations of latitude, longitude, and height errors. Industrial-grade INS. Aerobatic trajectory. Purely inertial mode.

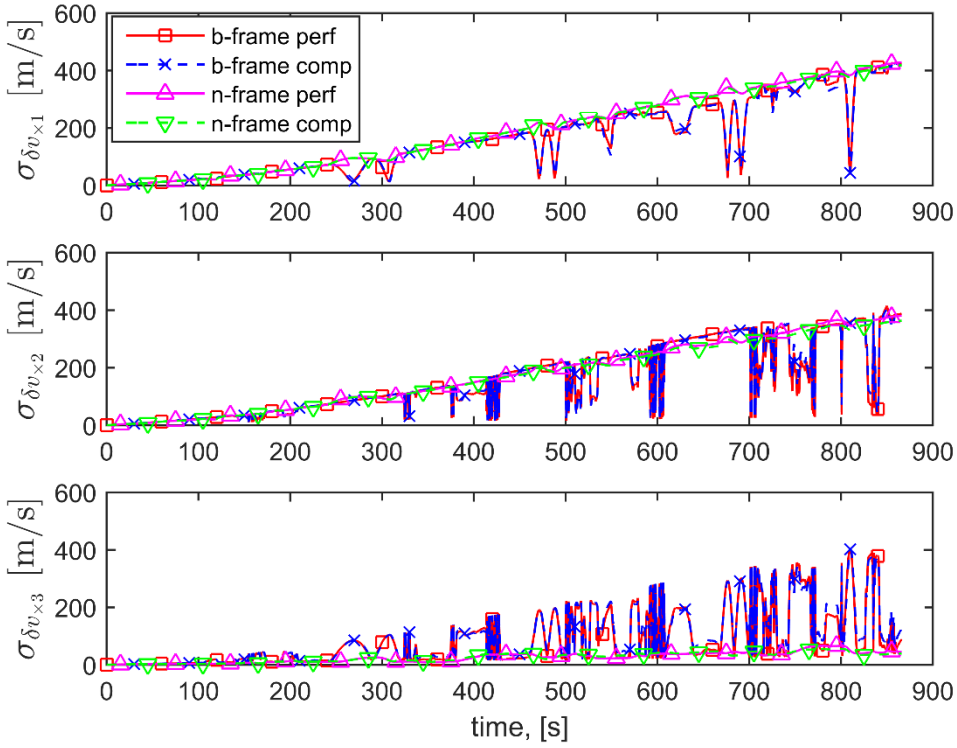

Fig. 70–Standard deviations of velocity errors in b- and n-frames, respectively. Industrial-grade INS. Aerobatic trajectory. Purely inertial mode.

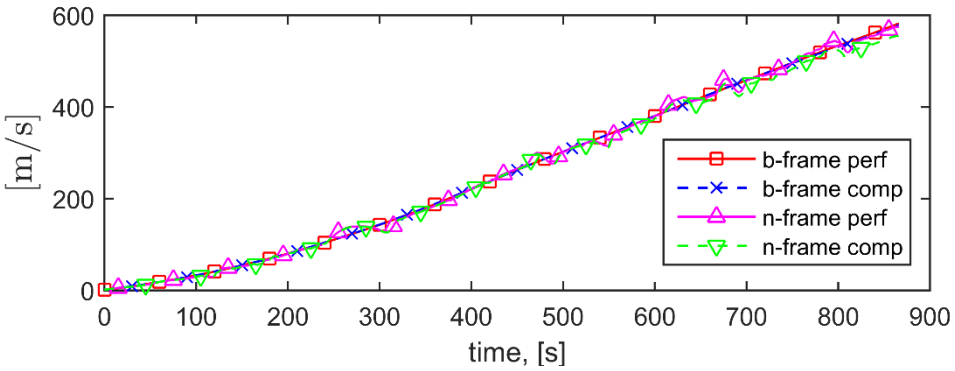

Fig. 71–RSS of velocity vector standard deviations. Industrial-grade INS. Aerobatic trajectory. Purely inertial mode.

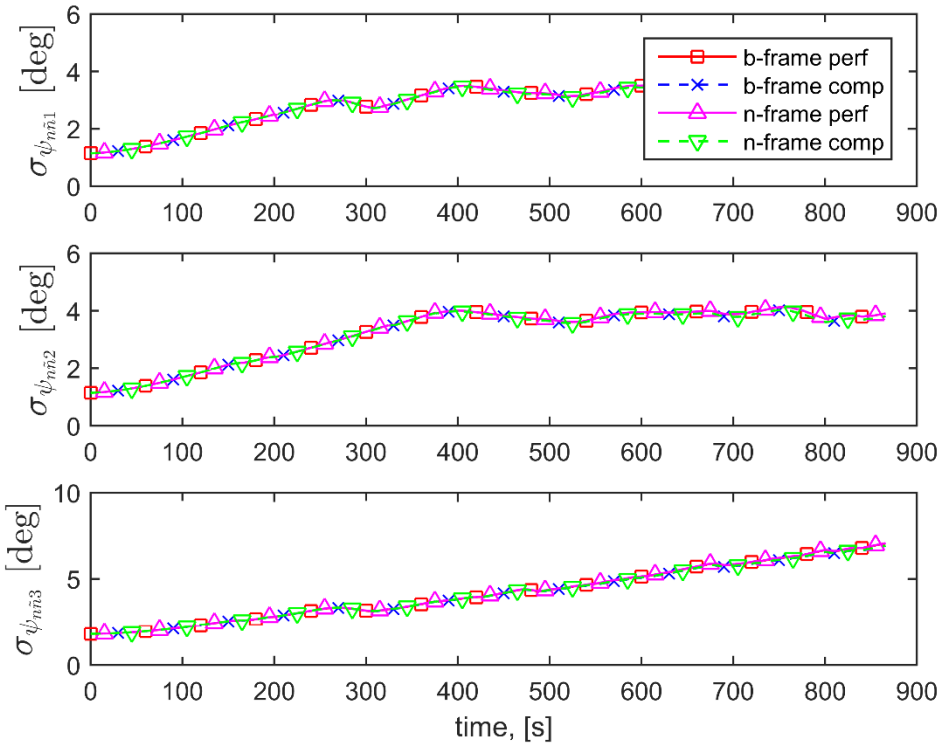

Fig. 72–Standard deviations of orientation errors. Industrial-grade INS. Aerobatic trajectory. Purely inertial mode.

However, in aided case b- and n-frame mechanizations can hardly be considered equivalent. For example, if INS is aided by information on TAS, AOA, and AOS, the filter, mechanized in b-frame, appears much more robust. This phenomenon is illustrated by Figures 73–79, which show standard deviations of position, velocity, and orientation errors of air data aided industrial-grade INS. Again, aerobatic flight trajectory was considered in the simulation. Poor behavior of the filter mechanized in n-frame is completely due to large errors of some of the navigation parameters, because such an effect cannot be observed in case of tactical-grade INS (see Figures 80–85). Moreover, in aided case behavior of latitude and longitude variances is seen to differ considerably. Comparing Figures 73 and 80, i. e. position standard deviations for aided industrial- and tactical-grade systems, clearly shows that

a change in behavior is not caused by an error of navigation state. In fact the effect appears to be caused by filter initialization. As was explained above, b- and n-frame filters were initialized with the same value of diagonal covariance matrix, and therefore linear relation

$$\delta\mathbf{v}_b = \mathbf{R}_{nb}^{\mathsf{T}}\left(\delta\mathbf{v}_n + \left[\mathbf{v}_n\times\right]\psi_{n\tilde{n}}\right) \tag{H.1}$$

between errors $\delta\mathbf{v}_b$ and $\delta\mathbf{v}_n$ appeared to be violated. Instead of initializing filters independently, one could consider assuming some initial value $\mathbf{P}_n(0)$ of covariance matrix for n-frame filter and computing initial covariance for b-frame filter as

$$\mathbf{P}_b(0) = \mathbf{T}\mathbf{P}_n(0)\mathbf{T}^{\mathsf{T}} \tag{H.2}$$

where

$$\mathbf{T} = \begin{pmatrix} \mathbf{I}_{3\times3} & \mathbf{0}_{3\times3} & \mathbf{0}_{3\times3} & \mathbf{0}_{3\times9} \\ \mathbf{0}_{3\times3} & \mathbf{R}_{nb}^{\mathsf{T}}(0) & \mathbf{R}_{nb}^{\mathsf{T}}(0)\left[\mathbf{v}_n(0)\times\right] & \mathbf{0}_{3\times9} \\ \mathbf{0}_{3\times3} & \mathbf{0}_{3\times3} & \mathbf{I}_{3\times3} & \mathbf{0}_{3\times9} \\ \mathbf{0}_{9\times3} & \mathbf{0}_{9\times3} & \mathbf{0}_{9\times3} & \mathbf{I}_{9\times9} \end{pmatrix}. \tag{H.3}$$

This would preserve the linear relation (H.1) and would make position variance propagation equivalent (see Figure 74). Though if navigation system aligns stationary on ground, initialization of b-frame filter according to (H.2) hardly makes sense because initial errors of orientation do not in fact contribute to initial uncertainty of velocity vector.

Note that RSS of velocity vector standard deviations for n-frame filter does not drift monotonically and can experience both growth and decrease. This happens because observability of velocity errors depends strongly on maneuvering. Measurement equation for velocity w.r.t. wind takes the form

$$\Delta\mathbf{y}_{\mathbf{vb},rel} = \left(\delta\mathbf{v}_n - \delta\mathbf{v}_n^W\right) + \left[\left(\tilde{\mathbf{v}}_n - \tilde{\mathbf{v}}_n^W\right)\times\right]\psi_{n\tilde{n}} - \mathbf{R}_{\tilde{n}b}\mathbf{v}_{\mathbf{vb}} \tag{H.4}$$

and thus the higher horizontal velocity is, the more weight in the measurement equation heading error gets. Consequently, velocity vector will be corrected most accurately if coupling of velocity and heading errors is eliminated. This happens, for example, when an airplane performs an inside loop. The aerobatic trajectory that was used in the simulation features this maneuver several times, and, accordingly, the RSS is seen to achieve local minimums shortly before the times 500 and 700 seconds, as well as shortly after 800 seconds. Despite heading error is unobservable, its variance is seen to grow much slower than in unaided mode (see Figures 72, 79). Such a behavior is reasonable, because aiding by ADS during aerobatic flight makes, among other sensor errors, the error of down gyroscope observable, and consequently considerable part of heading drift gets compensated by navigation filter. Though, initial error of heading cannot be observed and corrected.

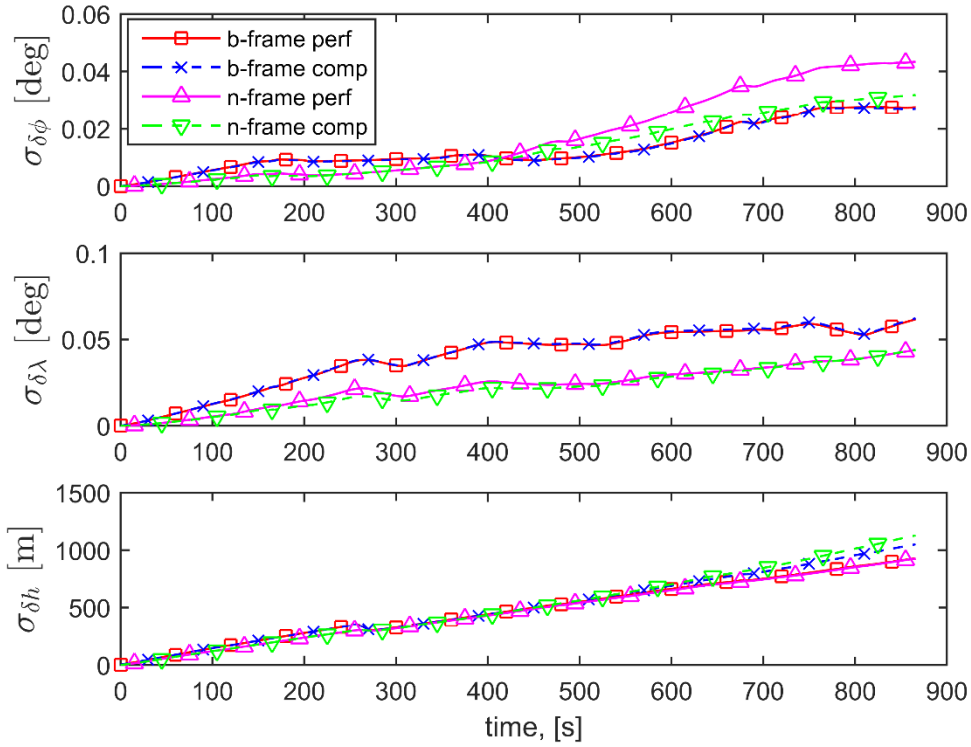

Fig. 73–Standard deviations of latitude, longitude, and height errors. Industrial-grade INS. Aerobatic trajectory. Aiding by TAS, AOA, and AOS.

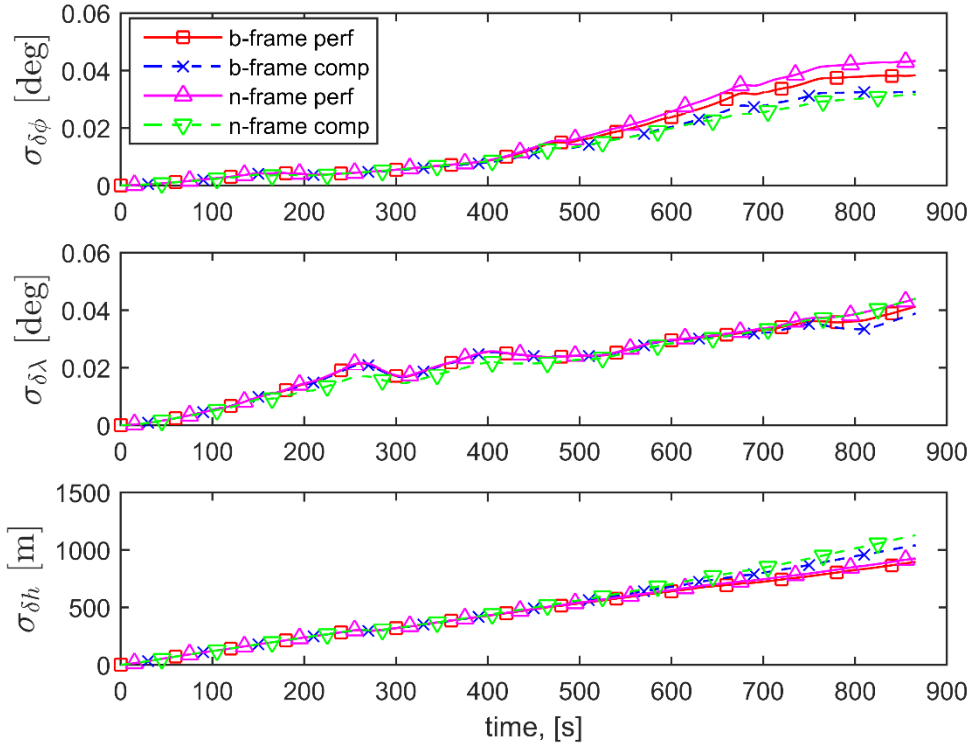

Fig. 74–Standard deviations of latitude, longitude, and height errors. Industrial-grade INS. Aerobatic trajectory. Aiding by TAS, AOA, and AOS. Filter initialization according to relation (H.2).

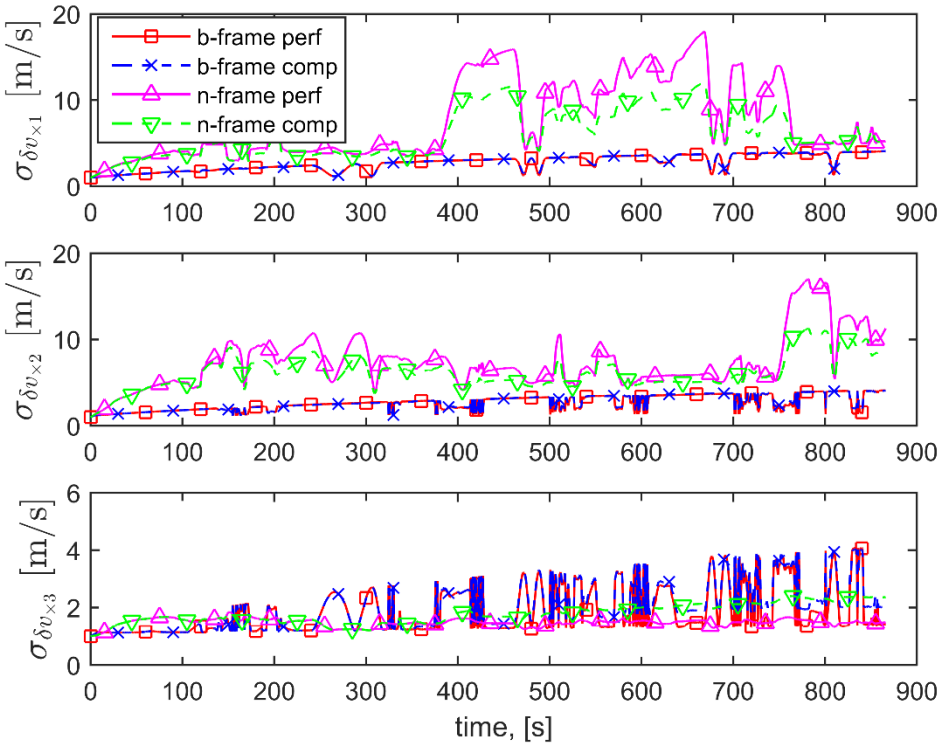

Fig. 75–Standard deviations of velocity errors in b- and n-frames, respectively. Industrial-grade INS. Aerobatic trajectory. Aiding by TAS, AOA, and AOS.

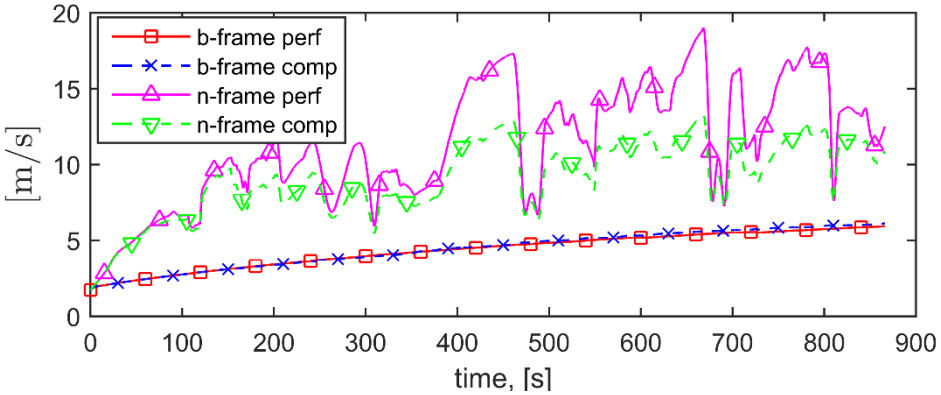

Fig. 76–RSS of velocity vector standard deviations. Industrial-grade INS. Aerobatic trajectory. Aiding by TAS, AOA, and AOS.

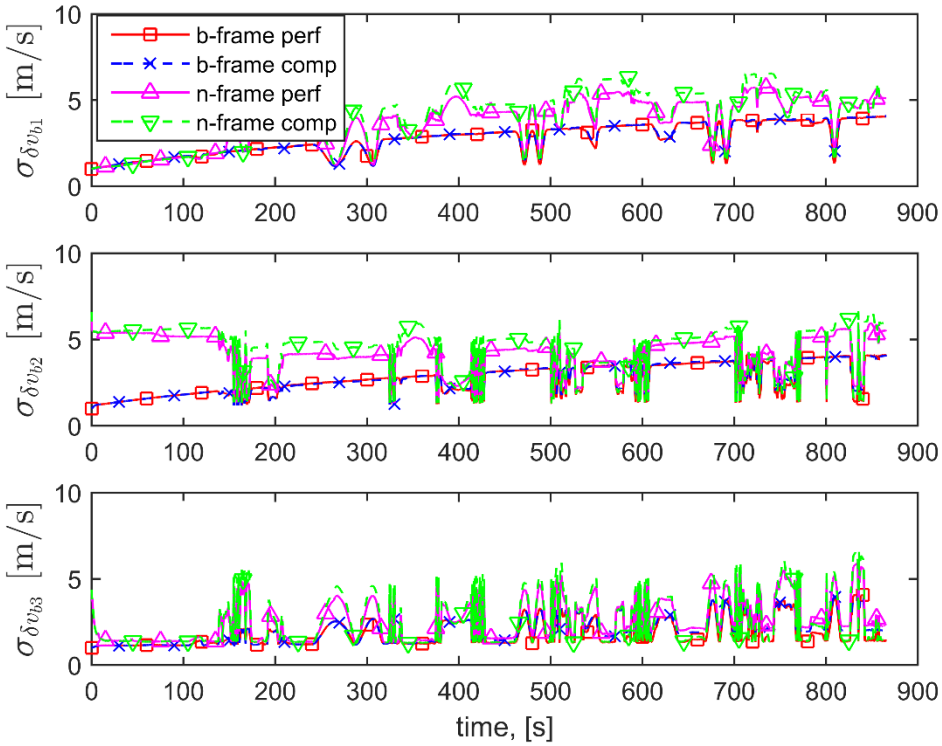

Fig. 77–Standard deviations of errors of b-frame velocity vector. Industrial-grade INS. Aerobatic trajectory. Aiding by TAS, AOA, and AOS.

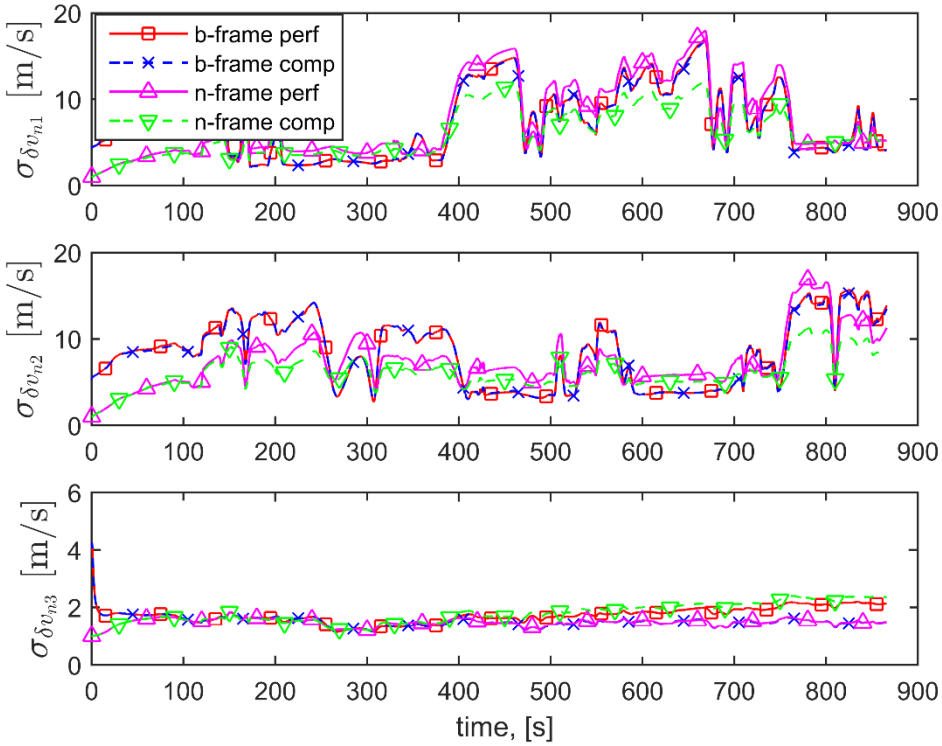

Fig. 78–Standard deviations of errors of n-frame velocity vector. Industrial-grade INS. Aerobatic trajectory. Aiding by TAS, AOA, and AOS.

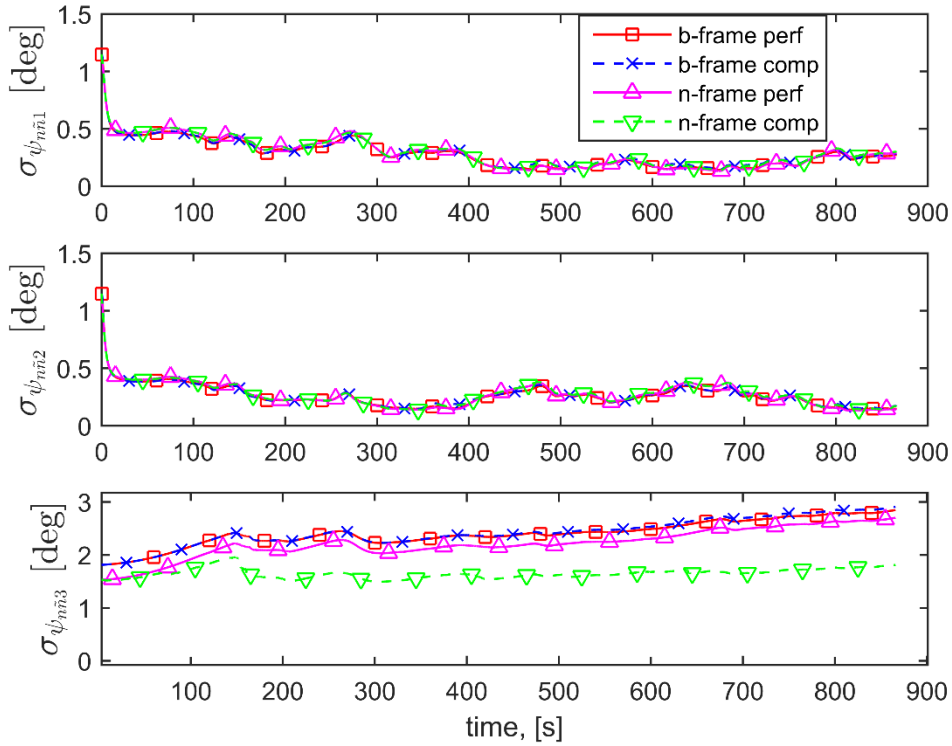

Fig. 79–Standard deviations of orientation errors. Industrial-grade INS. Aerobatic trajectory. Aiding by TAS, AOA, and AOS.

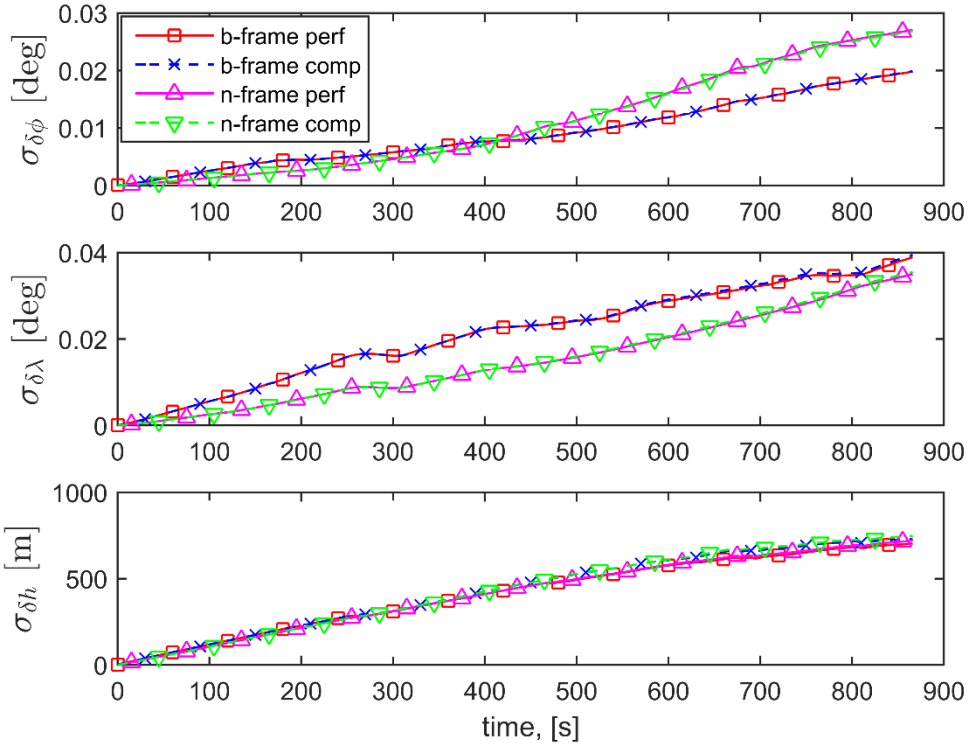

Fig. 80–Standard deviations of latitude, longitude, and height errors. Tactical-grade INS. Aerobatic trajectory. Aiding by TAS, AOA, and AOS.

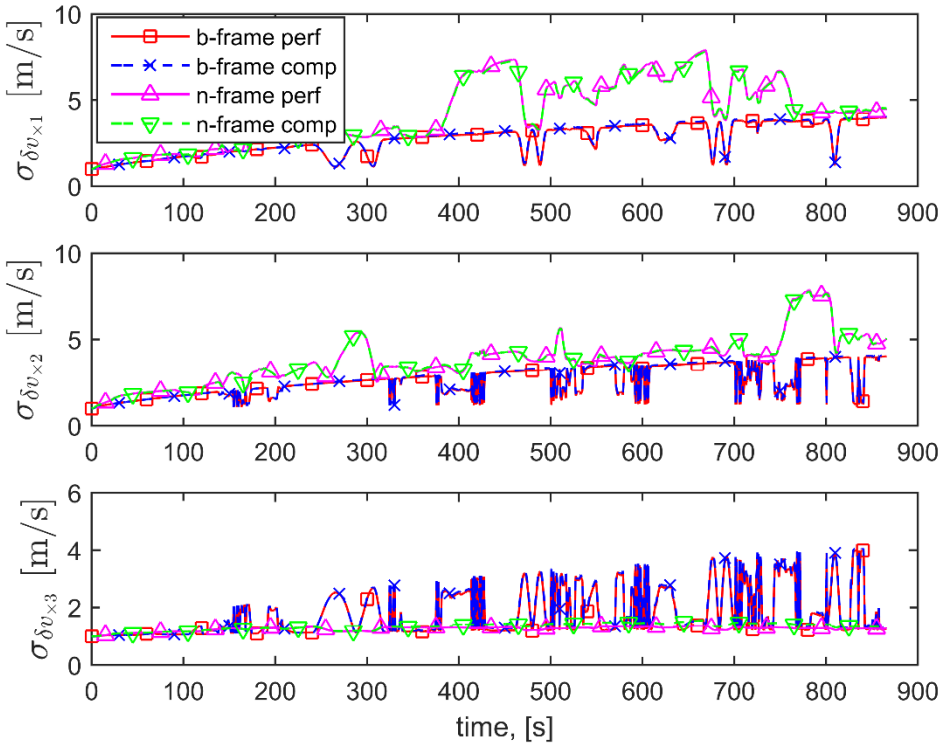

Fig. 81–Standard deviations of velocity errors in b- and n-frames, respectively. Tactical-grade INS. Aerobatic trajectory. Aiding by TAS, AOA, and AOS.

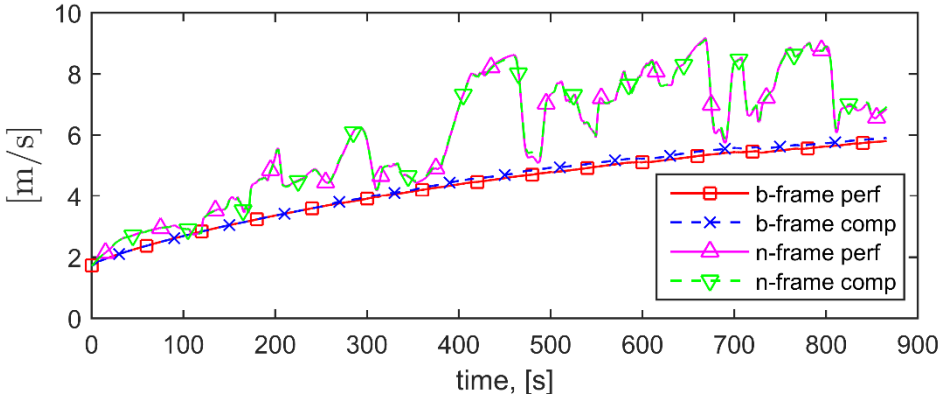

Fig. 82–RSS of velocity vector standard deviations. Tactical-grade INS. Aerobatic trajectory. Aiding by TAS, AOA, and AOS.

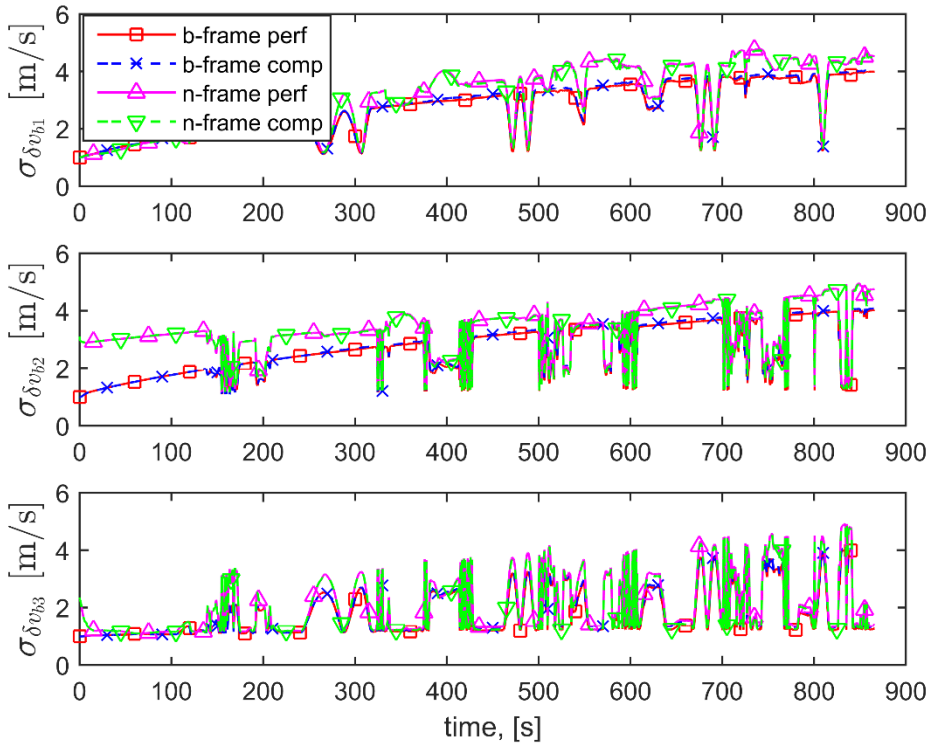

Fig. 83–Standard deviations of errors of b-frame velocity vector. Tactical-grade INS. Aerobatic trajectory. Aiding by TAS, AOA, and AOS.

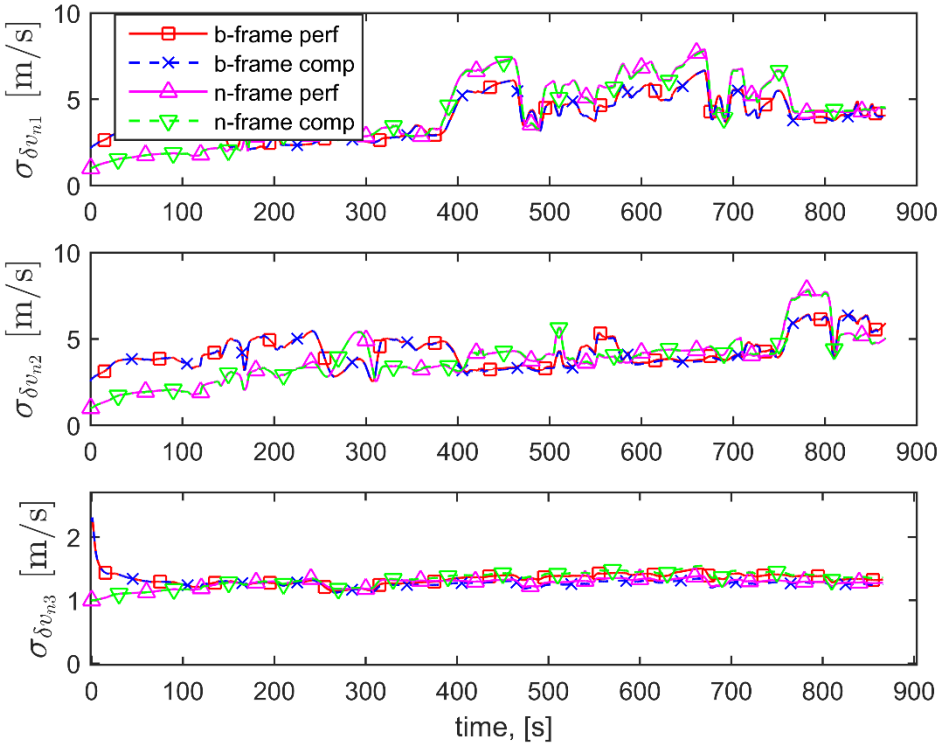

Fig. 84–Standard deviations of errors of n-frame velocity vector. Tactical-grade INS. Aerobatic trajectory. Aiding by TAS, AOA, and AOS.

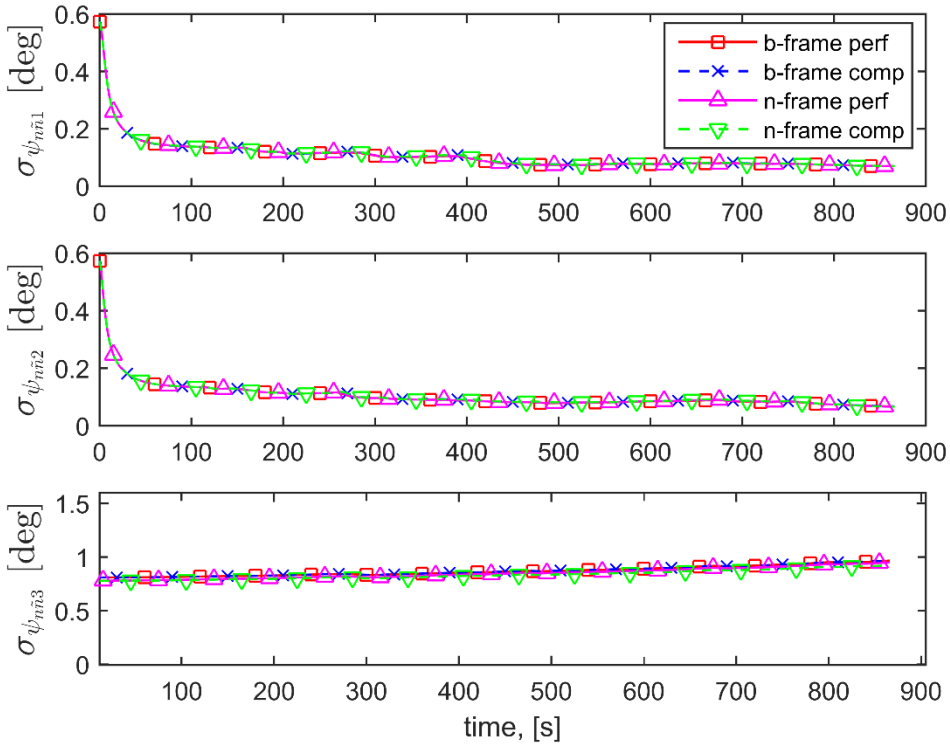

Fig. 85–Standard deviations of orientation errors. Tactical-grade INS. Aerobatic trajectory. Aiding by TAS, AOA, and AOS.

Though, advantages of b-frame mechanization in case of aiding by air data do not mean that n-frame mechanization is in general worse. For example, simulating INS, aided by altitude information, shows opposite situation. In this case n-frame mechanization appears more robust to an error of navigation solution (see Figures 86–89). Again, difference in performance of mechanizations can hardly be noticed if higher-grade inertial sensors are considered (see Figures 90–93). Moreover, on the Figure 88 uncertainty of b-frame velocity is seen to grow much faster than uncertainty of n-frame velocity in the beginning of the flight. This happens because during initial steady climb gyroscope errors are not observable, and their large uncertainties are amplified considerably by vehicle's speed vector in the equation (G.9). After the vehicle starts flying aerobatic figures, gyroscope errors get estimated and velocity uncertainty is partly compensated and stabilized. In n-frame filter mechanization, in turn, gyroscope errors do not contribute directly to velocity error growth and are not amplified (see equation (2.9)), which is why n-frame filter shows much better performance at the initial stage.

The presented simulation results demonstrate that for integrated navigation systems featuring low-cost inertial sensors right choice of filter mechanization is of high importance and can provide certain benefits. Moreover, mechanization shall be chosen dependent on the type of aiding being used. In fact, such a dependency of filter robustness on the type of aiding information encourages to suspect that the phenomenon is somehow related to observability, and thus below the author will try to offer a reasonable explanation of it.

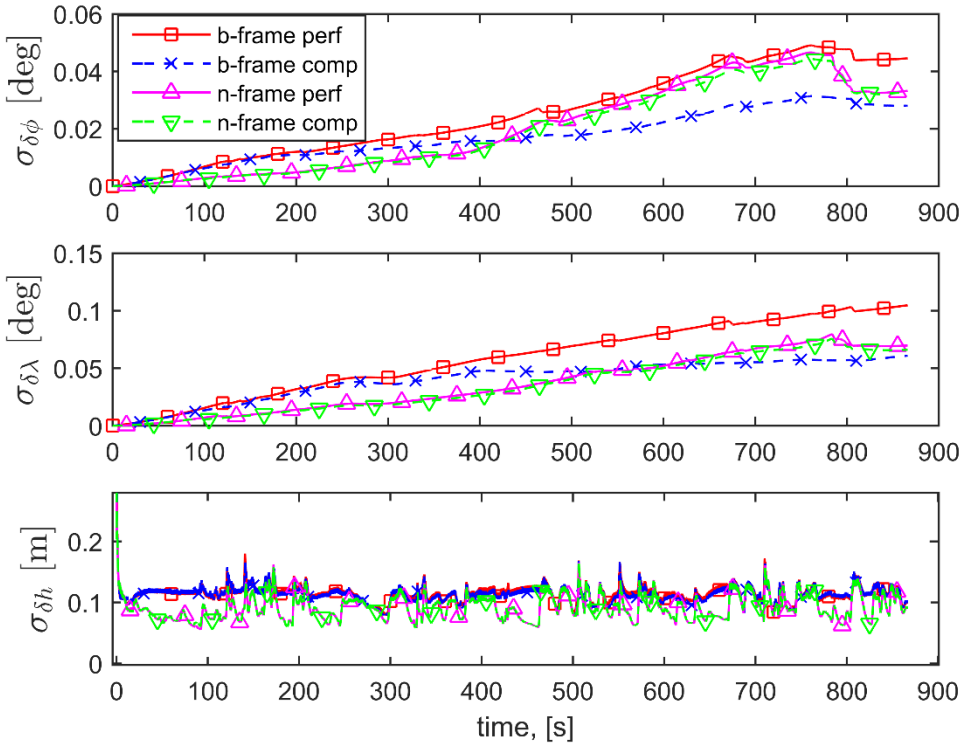

Fig. 86–Standard deviations of latitude, longitude, and height errors. Industrial-grade INS. Aerobatic trajectory. Aiding by barometric altitude.

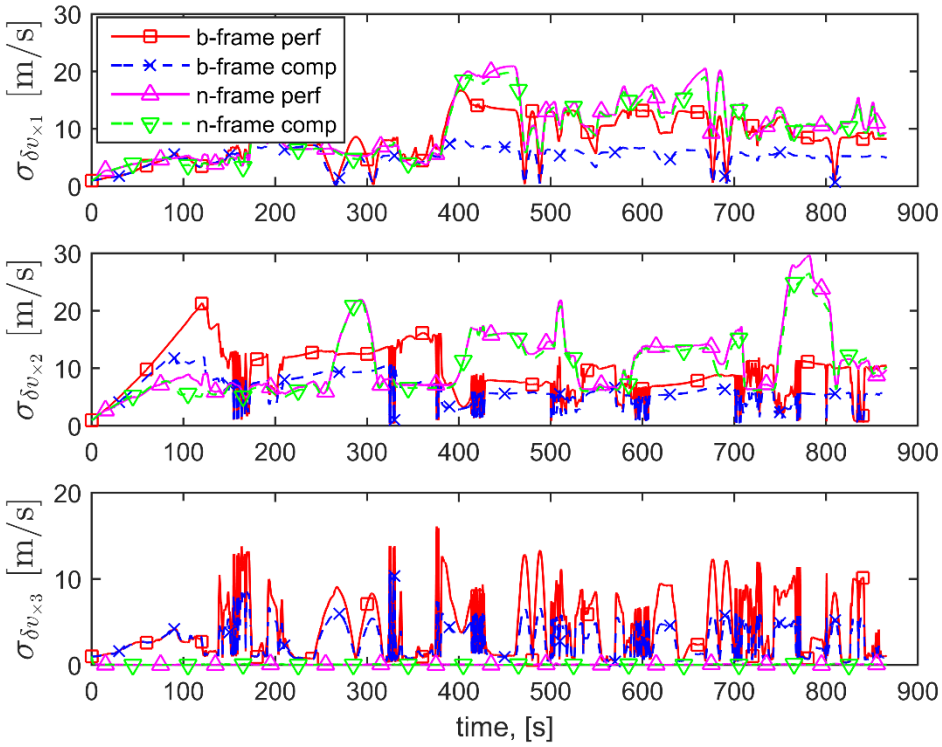

Fig. 87–Standard deviations of velocity errors in b- and n-frames, respectively. Industrial-grade INS. Aerobatic trajectory. Aiding by barometric altitude.

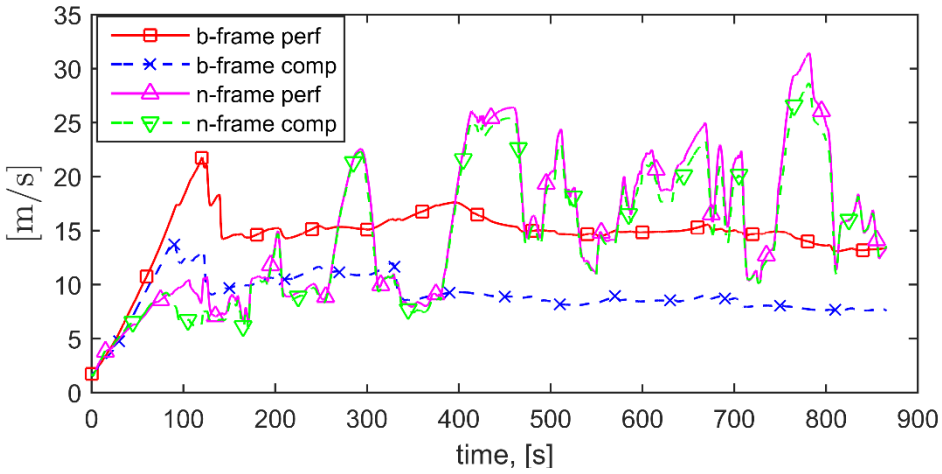

Fig. 88–RSS of velocity vector standard deviations. Industrial-grade INS. Aerobatic trajectory. Aiding by barometric altitude.

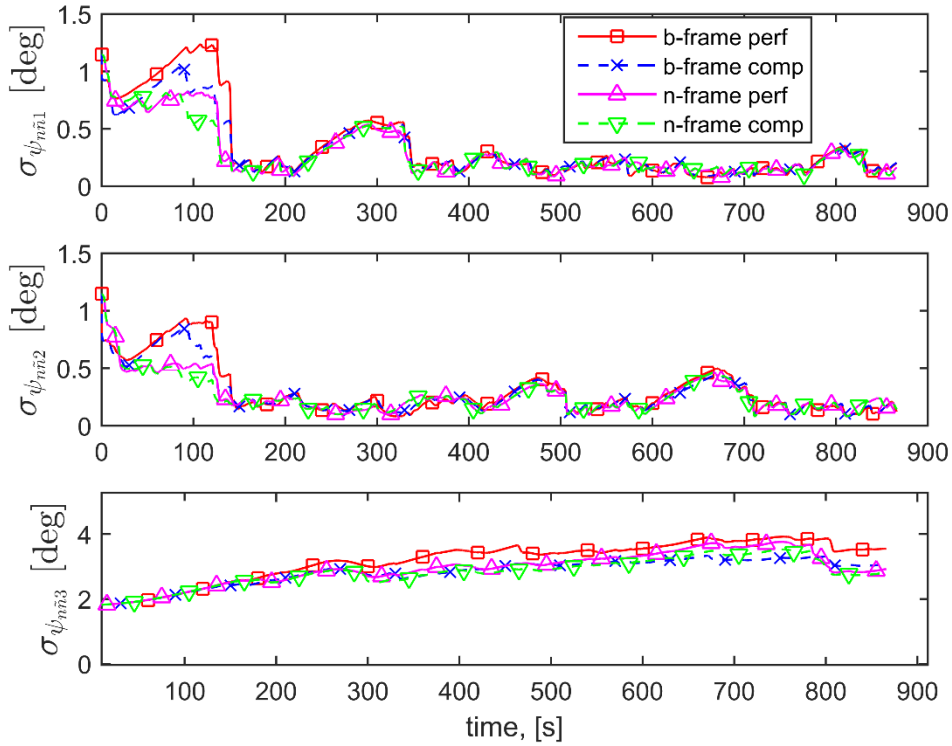

Fig. 89–Standard deviations of orientation errors. Industrial-grade INS. Aerobatic trajectory. Aiding by barometric altitude.

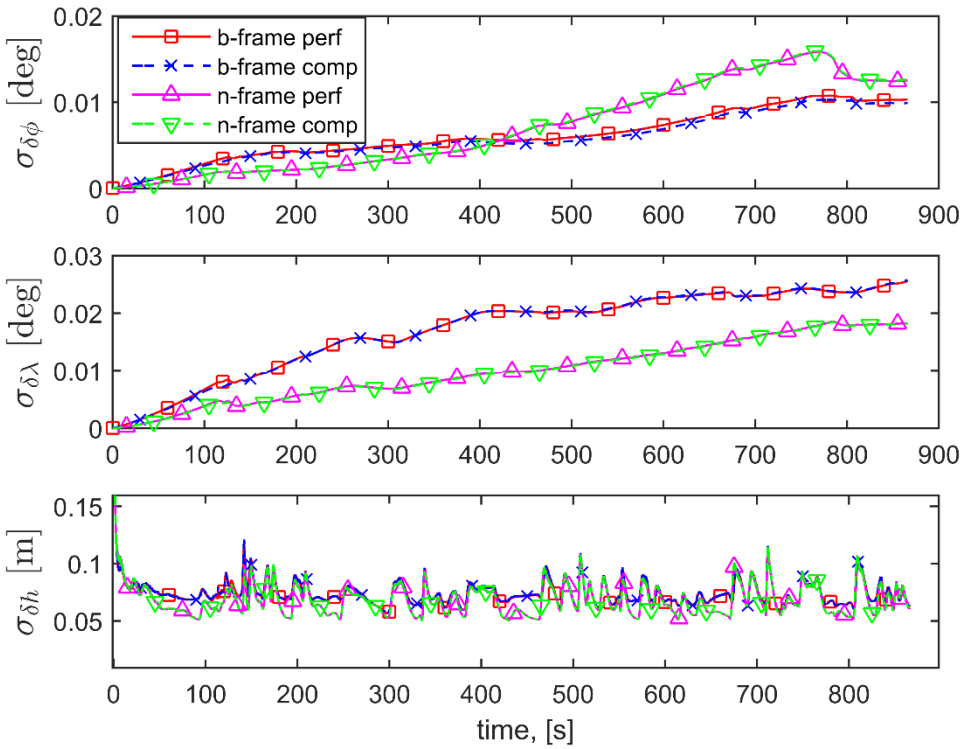

Fig. 90–Standard deviations of latitude, longitude, and height errors. Tactical-grade INS. Aerobatic trajectory. Aiding by barometric altitude.

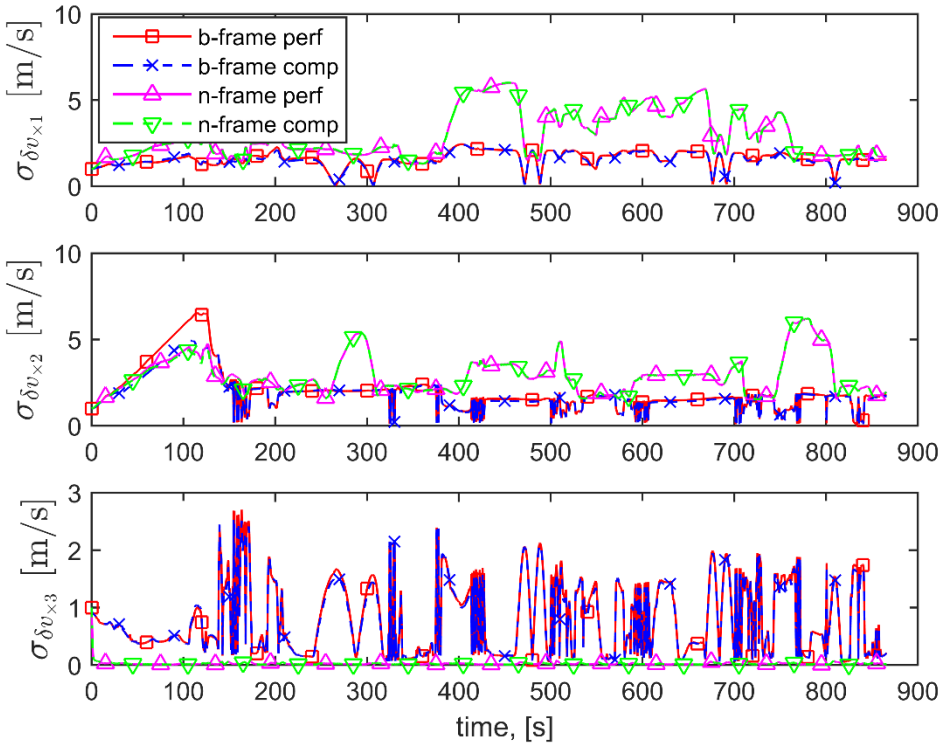

Fig. 91–Standard deviations of velocity errors in b- and n-frames, respectively. Tactical-grade INS. Aerobatic trajectory. Aiding by barometric altitude.

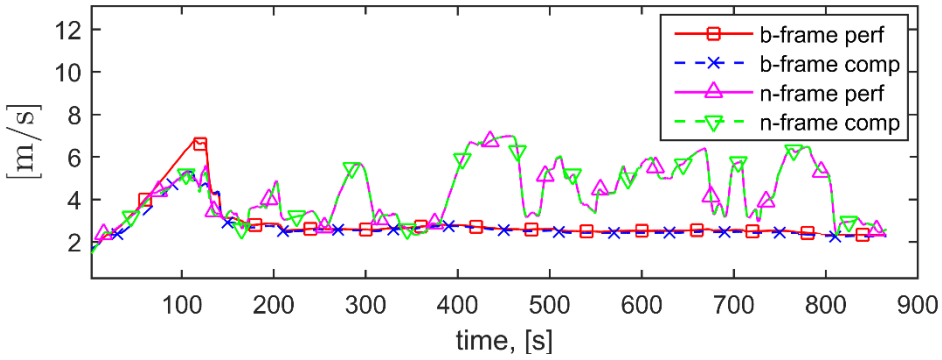

Fig. 92–RSS of velocity vector standard deviations. Tactical-grade INS. Aerobatic trajectory. Aiding by barometric altitude.

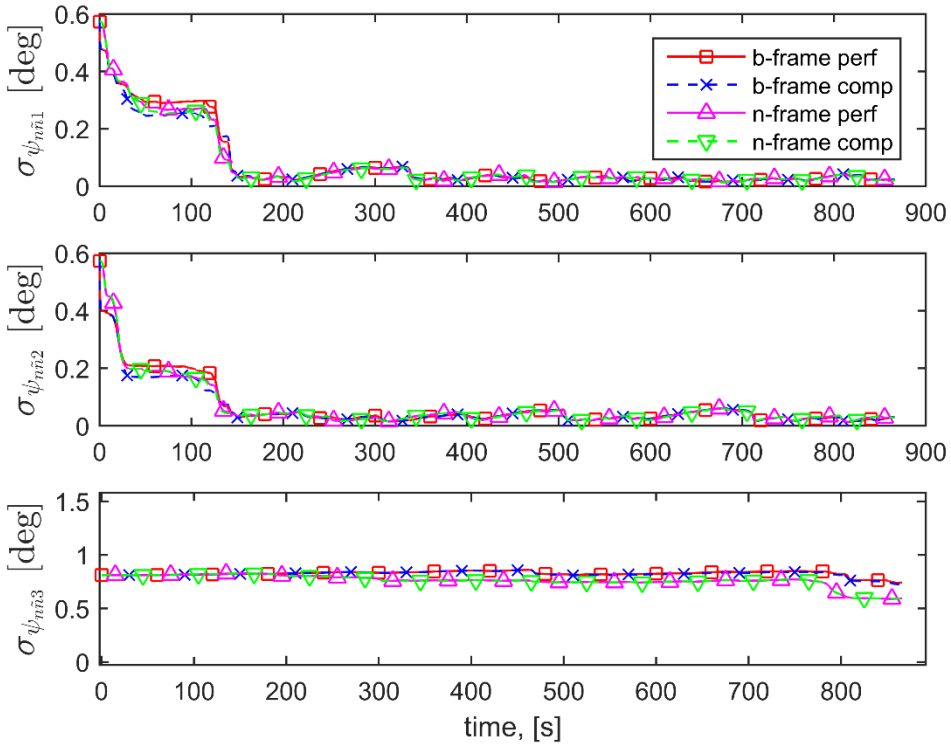

Fig. 93–Standard deviations of orientation errors. Tactical-grade INS. Aerobatic trajectory. Aiding by barometric altitude.

At first let us explain why b-frame mechanization is more efficient for INS aided by measurements of TAS, AOA, and AOS. Consider velocity w.r.t. measurement equations for n- and b-frame mechanizations, respectively:

$$\begin{aligned}\Delta\mathbf{y}^{n}_{\mathbf{vb},rel} &= \left(\delta\mathbf{v}_n - \delta\mathbf{v}^{W}_{n}\right) + \left[\left(\tilde{\mathbf{v}}_n - \tilde{\mathbf{v}}^{W}_{n}\right)\times\right]\psi_{n\tilde{n}} - \mathbf{R}_{\tilde{n}b}\mathbf{v}_{\mathbf{vb}},\\ \Delta\mathbf{y}^{b}_{\mathbf{vb},rel} &= \delta\mathbf{v}_b - \mathbf{R}^{\mathsf{T}}_{\tilde{n}b}\delta\mathbf{v}^{W}_{n} - \mathbf{R}^{\mathsf{T}}_{\tilde{n}b}\left[\tilde{\mathbf{v}}^{W}_{n}\times\right]\psi_{n\tilde{n}} - \mathbf{v}_{\mathbf{vb},rel}.\end{aligned} \tag{H.5}$$

Obviously, if filter is mechanized in n-frame and vehicle moves fast, orientation error will get large weight in the measurement equation, and thus corresponding filter gains will increase considerably. As was shown in Section 3.2.11, heading error is unobservable in air data aided systems, and thus it can quickly become large, especially if IMU is low-cost. Large error of heading, in turn, causes large error of n-frame velocity vector and, consequently, makes the measurement equation more and more inconsistent with time. At some point induced errors in computed Kalman filer gains for unobservable states become critical, and some parts of covariance matrix loose statistical consistency. When filter is mechanized in b-frame, however, KF updates appear much less vulnerable to growth of heading error, because in the measurement equation $\delta\mathbf{v}_b$ is coupled with $\psi_{n\tilde{n}}$ solely due to nonzero speed of wind. Wind speed, in turn, usually takes a value between ±15 m/s, and thus appears to be 5 to 20 times less than a speed of an airplane. Therefore eliminating aircraft's velocity vector from the measurement equation relaxes considerably influence of heading inaccuracy on other navigation states. Moreover, one could consider approximating wind speed with zero throughout operation, i. e. assume $\tilde{\mathbf{v}}^{W}_{n} \approx \mathbf{0}$,

and therefore coupling of orientation and velocity errors in the measurement equation would be completely eliminated in the filter mechanized in b-frame.

In order to illustrate the discussed effects, plots of KF gains for orientation are presented on the Figures 94–96. It is seen that b- and n-frame mechanizations provide equal gains for observable errors of orientation, i. e. for $\psi_{n\tilde{n}1}$ and $\psi_{n\tilde{n}2}$, while at least one of the gains for $\psi_{n\tilde{n}3}$, namely the gain that corresponds to TAS measurement, has different value.

The reasons, why n-frame mechanization is more robust in case of aiding INS by altitude information, are, in fact, similar to reasons, why b-frame mechanization has advantages for air data aided systems. As was shown in the Section 3.2.3, external information on altitude allowed to observe

$$\delta v_{n3},\ \psi_{n\tilde{n}1},\ \psi_{n\tilde{n}2}, \tag{H.6}$$

as long as vehicle maneuvered sufficiently. Errors of heading and horizontal components of n-frame speed vector, though, remained unobservable. Therefore, a filter, mechanized in b-frame, tries to distribute its "good knowledge" of δv_{n3} between components of $\delta \mathbf{v}_b$ using relation

$$\delta \mathbf{v}_b = \mathbf{R}_{\tilde{n}b}^{\mathrm{T}}(\delta \mathbf{v}_n + [\tilde{\mathbf{v}}_n \times] \cdot \psi_{n\tilde{n}}). \tag{H.7}$$

Obviously, the less accurate the $\mathbf{R}_{\tilde{n}b}$ and $\tilde{\mathbf{v}}_n$ become, the more inaccurately covariance of $\delta \mathbf{v}_b$ is corrected, which, again, causes inconsistencies in some parts of the covariance matrix.

In summary, several important conclusions can be made.

Firstly,

aided navigation systems featuring low-cost inertial sensors can benefit considerably from a suitable choice of filter mechanization.

Secondly,

filter mechanization shall be chosen dependent on type of information being used for aiding and thus is observability-specific.

Thirdly,

if possible, filter mechanization shall be chosen in such a way as to avoid dependencies of measurement matrix on navigation parameters that cannot be estimated accurately enough.

And fourth,

the simpler observable combinations are expressed in terms of the chosen error state vector, the more robust navigation (Kalman) filter becomes.

Taking these conclusions into consideration, b-frame mechanization of navigation filter shall be recommended for AHRS design, proposed in the Sections 4.3 and 5.5 (IMU+altimeter+magnetometer), while for the design, proposed in the Section 4.2 (IMU+altimeter+magnetometer), n-frame mechanization appears already optimal. Though, if due to ADS failures only altitude measurement remains available, AHRS mechanized in b-frame will be more vulnerable than the one mechanized in n-frame. Therefore choice of mechanization may still present a tradeoff between performances in normal and failure modes.

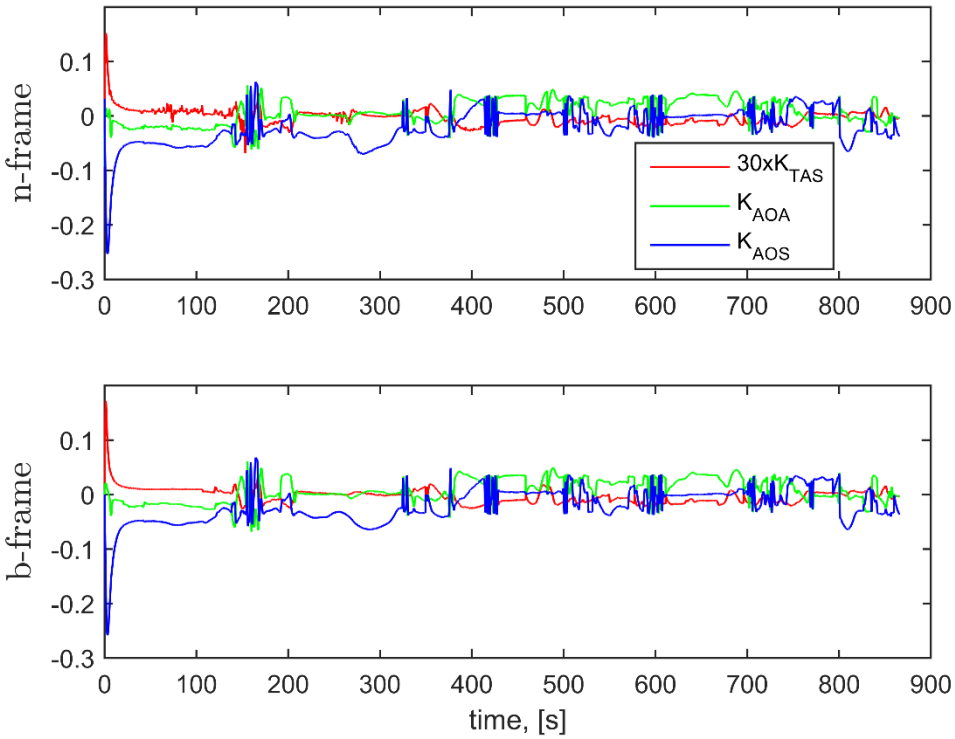

Fig. 94–$\psi_{n\tilde{n}1}$ gains.

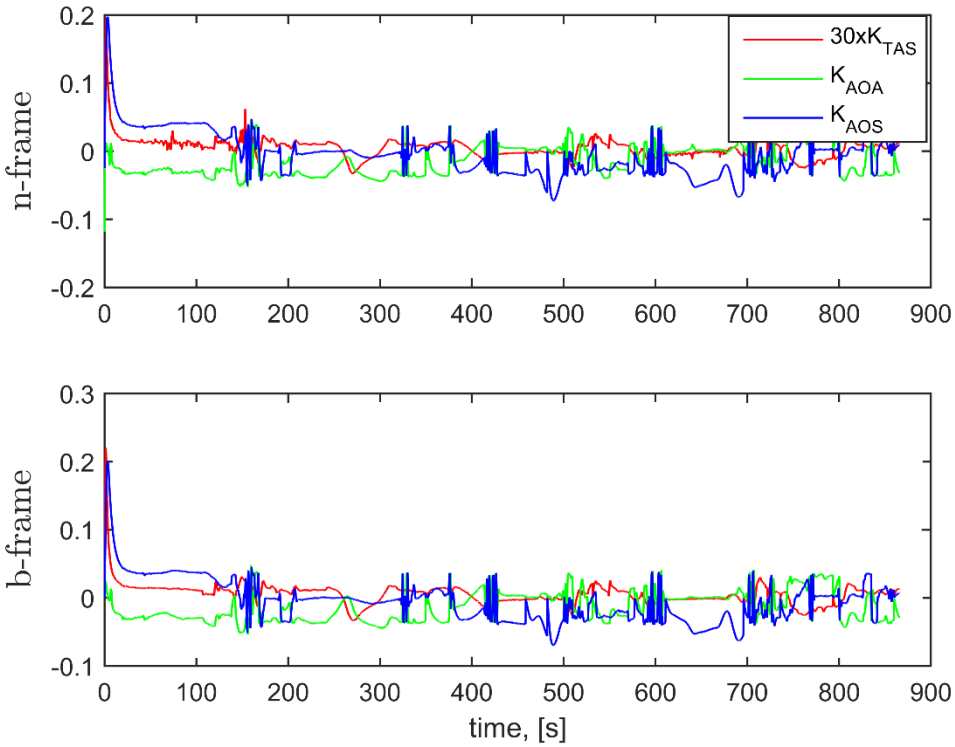

Fig. 95–$\psi_{n\tilde{n}2}$ gains.

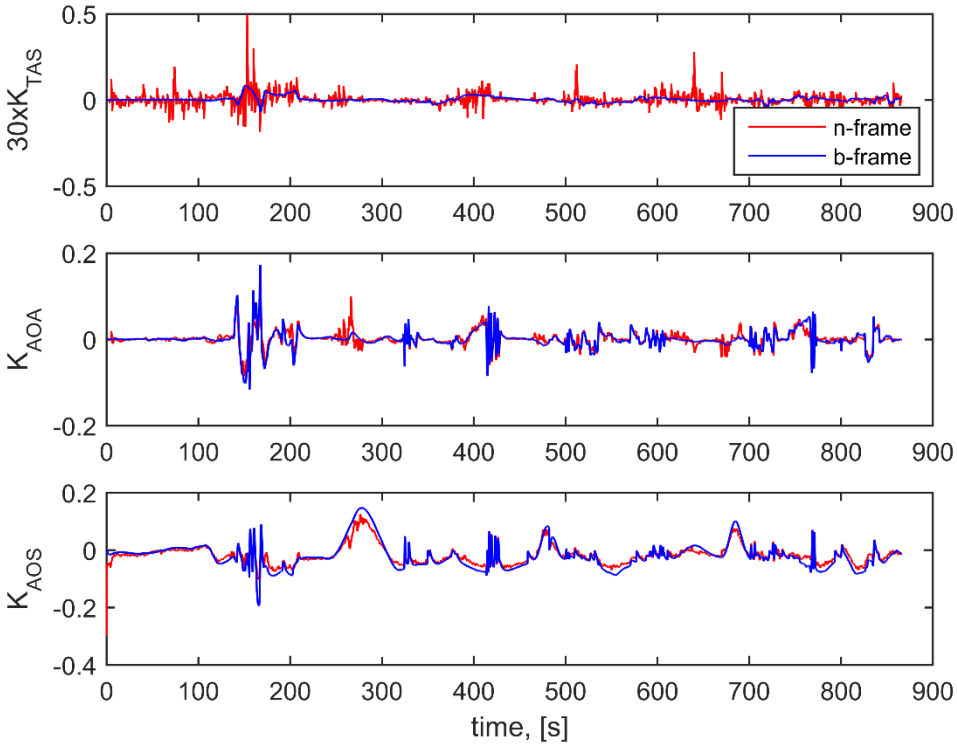

Fig. 96–$\psi_{n\tilde{n}3}$ gains.

Appendix I. Optimal sensor geometries.

I.1 Three sensors

1	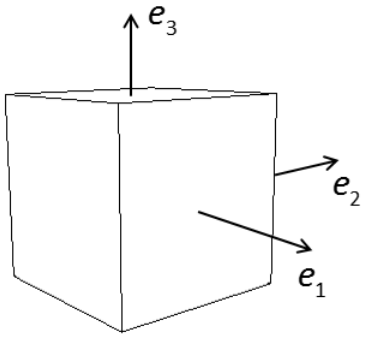	$\mathbf{H}=\begin{pmatrix}1 & 0 & 0\\ 0 & 1 & 0\\ 0 & 0 & 1\end{pmatrix}$

I.2 Four sensors

1	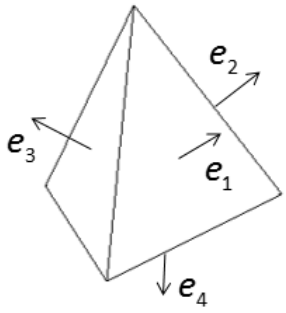	$\mathbf{H}=\begin{pmatrix}\frac{2\sqrt{2}}{3} & 0 & \frac{1}{3}\\ -\frac{\sqrt{2}}{3} & \frac{\sqrt{6}}{3} & \frac{1}{3}\\ -\frac{\sqrt{2}}{3} & -\frac{\sqrt{6}}{3} & \frac{1}{3}\\ 0 & 0 & 1\end{pmatrix}$
2	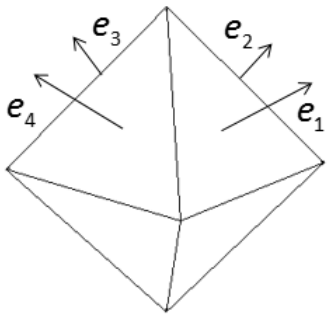	$\mathbf{H}=\frac{1}{\sqrt{3}}\begin{pmatrix}-1 & -1 & 1\\ 1 & -1 & 1\\ 1 & 1 & 1\\ -1 & 1 & 1\end{pmatrix}$

I.3 Five sensors

1	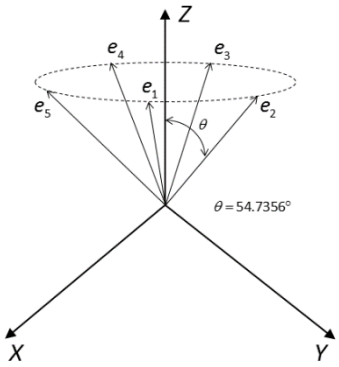	$\mathbf{H} = \begin{pmatrix} 1/\sqrt{3} & 1/\sqrt{3} & 1/\sqrt{3} \\ -0.3707 & 0.7275 & 1/\sqrt{3} \\ -0.8064 & -0.1277 & 1/\sqrt{3} \\ -0.1277 & -0.8064 & 1/\sqrt{3} \\ 0.7275 & -0.3707 & 1/\sqrt{3} \end{pmatrix}$
2	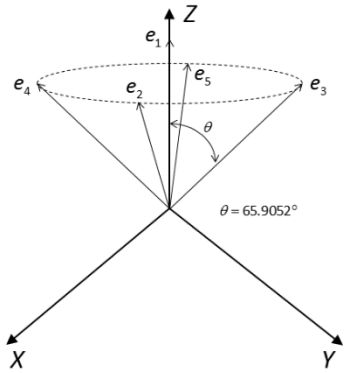	$\mathbf{H} = \begin{pmatrix} 0 & 0 & 1 \\ \sqrt{\frac{5}{12}} & \sqrt{\frac{5}{12}} & \frac{1}{\sqrt{6}} \\ -\sqrt{\frac{5}{12}} & \sqrt{\frac{5}{12}} & \frac{1}{\sqrt{6}} \\ -\sqrt{\frac{5}{12}} & -\sqrt{\frac{5}{12}} & \frac{1}{\sqrt{6}} \\ \sqrt{\frac{5}{12}} & -\sqrt{\frac{5}{12}} & \frac{1}{\sqrt{6}} \end{pmatrix}$
3	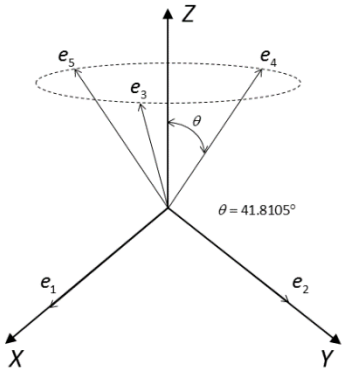	$\mathbf{H} = \begin{pmatrix} 1 & 0 & 0 \\ 0 & 1 & 0 \\ 0.4714 & 0.4714 & 0.7454 \\ -0.6440 & 0.1725 & 0.7454 \\ 0.1725 & -0.6440 & 0.7454 \end{pmatrix}$

I.4 Six sensors

1	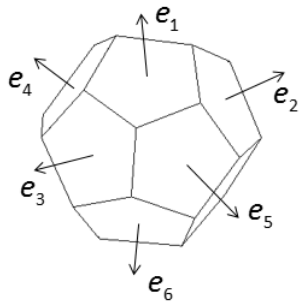	$\mathbf{H}=\begin{pmatrix} 0.5257 & 0 & 0.8507 \\ -0.5257 & 0 & 0.8507 \\ 0.8507 & 0.5257 & 0 \\ 0.8507 & -0.5257 & 0 \\ 0 & 0.8507 & 0.5257 \\ 0 & 0.8507 & -0.5257 \end{pmatrix}$
2	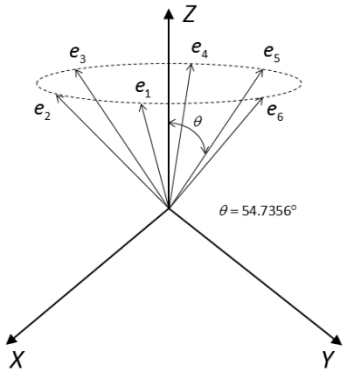	$\mathbf{H}=\begin{pmatrix} 0.8165 & 0 & 0.5744 \\ 0.4082 & 0.7071 & 0.5744 \\ -0.4082 & 0.7071 & 0.5744 \\ -0.8165 & 0 & 0.5744 \\ -0.4082 & -0.7071 & 0.5744 \\ 0.4082 & -0.7071 & 0.5744 \end{pmatrix}$
3	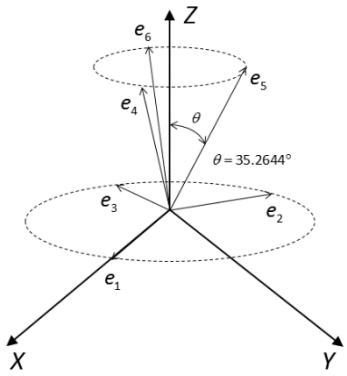	$\mathbf{H}=\begin{pmatrix} 1 & 0 & 0 \\ -0.5 & 0.8660 & 0 \\ -0.5 & -0.8660 & 0 \\ 0.5774 & 0 & 0.8165 \\ -0.2884 & 0.5 & 0.8165 \\ -0.2884 & -0.5 & 0.8165 \end{pmatrix}$

I.5 Seven sensors

1	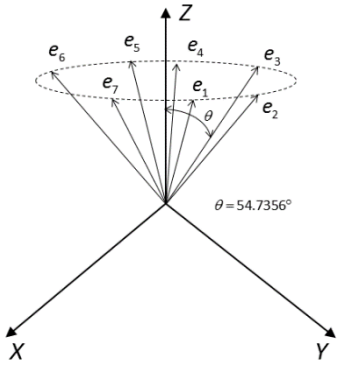	$\mathbf{H} = \begin{pmatrix} 0.8165 & 0 & 0.5774 \\ 0.5091 & 0.6384 & 0.5774 \\ -0.1817 & 0.7960 & 0.5774 \\ -0.7356 & 0.3543 & 0.5774 \\ -0.7356 & -0.3543 & 0.5774 \\ -0.1817 & -0.7960 & 0.5774 \\ 0.5091 & -0.6384 & 0.5774 \end{pmatrix}$
2	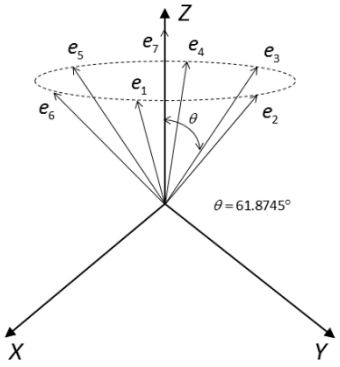	$\mathbf{H} = \begin{pmatrix} 0.8819 & 0 & 0.4714 \\ 0.4410 & 0.7638 & 0.4714 \\ -0.4410 & 0.7638 & 0.4714 \\ -0.8819 & 0 & 0.4714 \\ -0.4410 & -0.7638 & 0.4714 \\ 0.4410 & -0.7638 & 0.4714 \\ 0 & 0 & 1 \end{pmatrix}$
3	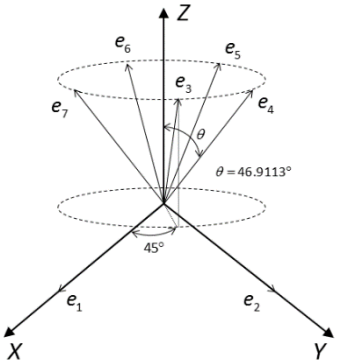	$\mathbf{H} = \begin{pmatrix} 1 & 0 & 0 \\ 0 & 1 & 0 \\ 0.5164 & 0.5164 & 0.6831 \\ -0.3315 & 0.6507 & 0.6831 \\ -0.7213 & -0.1142 & 0.6831 \\ -0.1142 & -0.7213 & 0.6831 \\ 0.6507 & -0.3315 & 0.6831 \end{pmatrix}$

4	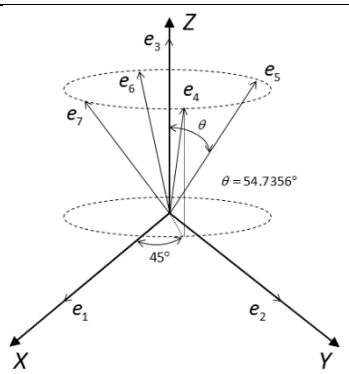	$\mathbf{H} = \begin{pmatrix} 1 & 0 & 0 \\ 0 & 1 & 0 \\ 0 & 0 & 1 \\ 0.5774 & 0.5774 & 0.5774 \\ -0.5774 & 0.5774 & 0.5774 \\ -0.5774 & -0.5774 & 0.5774 \\ 0.5774 & -0.5774 & 0.5774 \end{pmatrix}$

I.6 Ten sensors

1	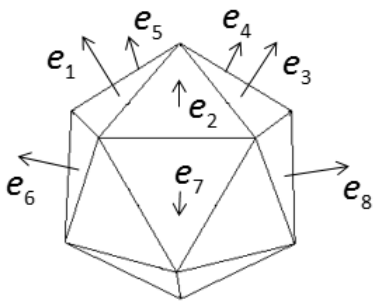	$\mathbf{H} = \begin{pmatrix} 0.7071 & 0 & 0.7071 \\ 0.2185 & 0.6725 & 0.7071 \\ -0.5721 & 0.4156 & 0.7071 \\ -0.5721 & -0.4156 & 0.7071 \\ 0.2185 & -0.6725 & 0.7071 \\ 0.9280 & 0 & 0.3727 \\ 0.2868 & 0.8525 & 0.3727 \\ -0.7507 & 0.5454 & 0.3727 \\ -0.7507 & -0.5454 & 0.3727 \\ 0.2868 & -0.8825 & 0.3727 \end{pmatrix}$
2	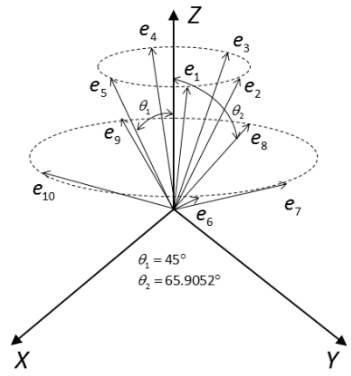	$\mathbf{H} = \begin{pmatrix} 0.7071 & 0 & 0.7071 \\ 0.2185 & 0.6725 & 0.7071 \\ -0.5721 & 0.4156 & 0.7071 \\ -0.5721 & -0.4156 & 0.7071 \\ 0.2185 & -0.6725 & 0.7071 \\ 0.9129 & 0 & 0.4082 \\ 0.2821 & 0.8682 & 0.4082 \\ -0.7385 & 0.5356 & 0.4082 \\ -0.7385 & -0.5366 & 0.4082 \\ 0.2821 & -0.8682 & 0.4082 \end{pmatrix}$

3	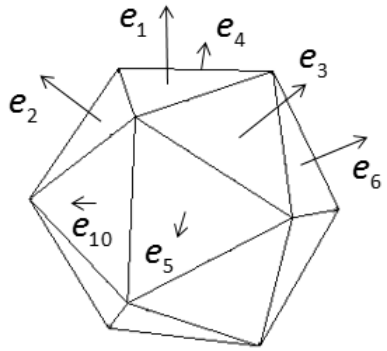	$\mathbf{H}=\begin{pmatrix} 0 & 0 & 1 \\ 0.667 & 0 & 0.7454 \\ -1/3 & 0.5774 & 0.7454 \\ -1/3 & -0.5774 & 0.7454 \\ 0.7454 & 0.5773 & 1/3 \\ 0.1273 & 0.9342 & 1/3 \\ -0.8727 & 0.3568 & 1/3 \\ -0.8727 & -0.3568 & 1/3 \\ 0.1273 & -0.9342 & 1/3 \\ 0.7454 & -0.5773 & 1/3 \end{pmatrix}$
4	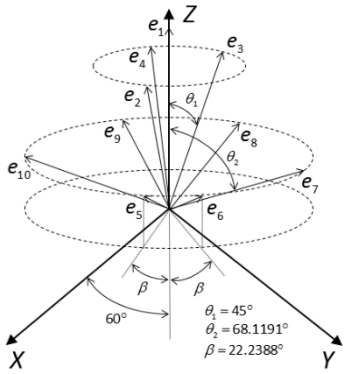	$\mathbf{H}=\begin{pmatrix} 0 & 0 & 1 \\ 0.7071 & 0 & 0.7071 \\ -0.3536 & 0.6124 & 0.7071 \\ -0.3536 & -0.6124 & 0.7071 \\ 0.7336 & 0.5683 & 0.3727 \\ 0.1253 & 0.9195 & 0.3727 \\ -0.8589 & 0.3512 & 0.3727 \\ -0.8589 & -0.3512 & 0.3727 \\ 0.1253 & -0.9195 & 0.3727 \\ 0.7336 & -0.5683 & 0.3727 \end{pmatrix}$

Bibliography

[1] Groves, P.D., *Principles of GNSS, Inertial, and Multisensor Integrated Navigation Systems*, 2 ed, Artech House, Boston, 2013.

[2] Farrell, J.A., *Aided Navigation, GPS with High Rate Sensors*, McGraw-Hill, USA, 2008.

[3] Cavallo, A., Cirillo, A., Cirillo, P., De Maria, G., Falco, P., Natale, C., Pirozzi, S., "Experimental Comparison of Sensor Fusion Algorithms for Attitude Estimation," *19th World Congress of The International Federation of Automatic Control*, 2014.

[4] Greene, M., Trent, V., "Software Algorithms in Air Data Attitude Heading Reference Systems," *Aircraft Engineering and Aerospace Technology*, Vol. 75, No. 5, 2003, pp. 470-476.

[5] Lundberg, M., Nordlund, P.-J., and Stahl-Gunnarsson, K., *Synthetic Attitude and Heading Reference for Saab Gripen*, in *39th IEEE Conference on Decision and Control*, 2000, Sydney: IEEE.

[6] Cho, A., Kim, J., Lee, S., and Kee, C., "Wind Estimation and Airspeed Calibration using a UAV with Single-Antenna GPS Receiver and Pitot Tube," *IEEE Transactions on Aerospace and Electronic Systems*, Vol. 47, No. 1, 2011, pp. 109-117.

[7] Langelaan, J.W., Alley, N., and Niedhoefer, J., "Wind Field Estimation for Small Unmanned Aerial Vehicles," *AIAA Guidance, Navigation, and Control Conference*, Toronto, Canada, 2010.

[8] Rhudy, M.B. and Chao, H., "UAV Attitude, Heading, and Wind Estimation Using GPS/INS and an Air Data System," *AIAA Guidance, Navigation, and Control (GNC) Conference*, Boston, MA, 2013.

[9] Savage, P.G. and Hartman, G.L., "Optimum Aiding of Inertial Navigation Systems," *AIAA Guidance and Control Conference*, Stanford, CA, 1972.

[10] Titterton, D.H., Weston, J. L. , *Strapdown Inertial Navigation Technology*, Lavenham Press Ltd., UK, 1997.

[11] Britting, K.R., *Inertial Navigation Systems Analysis*, John Wiley & Sons, New York, 1971.

[12] Chatfield, A.B., *Fundamentals of High Accuracy Inertial Navigation*, AIAA, 1997.

[13] Golovan, A.A. and Parusnikov, N.A., *Fundamentals of Navigation Systems (in Russian)*, MAKS Press, Moscow, 2011.

[14] Savage, P.G., *Strapdown Analytics*, Vol. 1, Strapdown Associates, Inc., Mapl Plain, Minnessota, 1997.

[15] Dachs, A., "Rechenzeitoptimierung, Robustifizierung und Tuning eines Kalmanfilters zur Datenfusion für Navigationsanwendungen," PhD Thesis, Fakultät für Luft- und Raumfahrttechnik, Universität der Bundeswehr München, Neubiberg, 2010.

[16] Kwakernaak, H. and Sivan, R., *Linear Optimal Control Systems*, Wiley-Interscience, USA, 1972.

[17] Jazwinski, A.H., *Stochastic Processes and Filtering Theory*, Dover Publications, Inc., Mineola, New York, 2007.

[18] Kalman, R.E., "Canonical Structure of Linear Dynamic Systems," *Proc. Natl Acad Sci U S A*, Vol. 48, No. 4, 1962, pp. 596-600.

[19] Kalman, R.E., "Lectures on Controllability and Observability," C.I.M.E., Bologna, 1968.

[20] Kalman, R.E., Falb, P.L., and Arbib, M.A., *Topics in Mathematical System Theory*, McGraw-Hill, New York, 1969.

[21] Minkler, G. and Minkler, J., *Theory and Application of Kalman Filtering*, Magellan Book Company, USA, 1993.

[22] Jikuya, I. and Hodaka, I., "Kalman Canonical Decomposition of Linear Time-Varying Systems," *SIAM J. Control and Optimization*, Vol. 52, No. 1, 2014, pp. 271-310.
[23] Krasovsky, N.N., *Theory of Control of Motion (in Russian)*, Nauka, Moscow, 1968.
[24] Alexandrov, V.V., Boltianski, V.G., Lemak, S.S., Parusnikov, N.A., and Tikhomirov, V.M., *Optimal Control of Motion (in Russian)*, FIZMATLIT, Moscow, 2005.
[25] Kalenova, V.I. and Morozov, V.M., *Linear Time-Varying Systems and Their Application to Problems in Mechanics (in Russian)*, FIZMATLIT, Moscow, 2010.
[26] Chang, A., "An Algebraic Characterization of Controllability," *IEEE Transactions on Automatic Control*, Vol. 10, No. 1, 1965, pp. 112-113.
[27] *State-of-the-Art Air Data Products Solution Guide*, SpaceAge Control Inc., 2015.
[28] Gracey, W., "Measurement of Static Pressure on Aircraft," NACA, Report 1364, 1957.
[29] Gracey, W., "Summary of Methods of Measuring Angle of Attack on Aircraft," NACA, Technical note 4351, 1958.
[30] Thompson, F.L., "The Measurement of Air Speed of Airplanes," NACA, Technical note 616, 1937.
[31] Ausman, S., "Baro-Inertial Loop for the USAF Standard RLG INU," *NAVIGATION, Journal of The Institute of Navigation*, Vol. 38, No. 2, Summer 1991, pp. 205-220.
[32] Chueh, V., Te-Chang, Li, Grethel, R., "INS/Baro vertical channel performance using improved pressure altitude as a reference," *Position, Location and Navigation Symposium*, IEEE/ION, 2008.
[33] Windnall, W., Sinha, P., "Optimizing the Gains of the Baro-Inertial Vertical Channel," *J. Guidance and Control*, Vol. 3, No. 2, 1980, pp. 172-178.
[34] Clancy, L.J., *Aerodynamics*, Pitman Publishing, London, 1975.
[35] Berman, Z. and Powell, D., "The Role of Dead Reckoning and Inertial Sensors in Future General Aviation Navigation," *Position Location and Navigation Symposium*, IEEE, 1998.
[36] Hinze, W.J., Frese, R. R., Saad, A. H., *Gravity and Magnetic Explorations: Principles, Practices, and Applications*, Cambridge University Press, New York, 2013.
[37] Chulliat, A., Macmillan P., Alken, P., Beggan, C., Nair, M., Hamilton, B., Woods, A., Ridley, V., Maus, S., Thompson, A., "The US/UK World Magnetic Model for 2015-2020: Technical Report," National Geophhysical Data Center, NOAA, 2015.
[38] Thébault, E., et al, "International Geomagnetic Reference Field: the 12th generation," *Earth, Planets and Space*, Vol. 67, No. 79, 2015.
[39] Heiskanen, W., Moritz, H., *Physical Geodesy*, W. H. Freeman and Company, San Francisco, 1967.
[40] http://www.ngdc.noaa.gov/geomag/. Retrieved on 19th of January 2016.
[41] Kayton, M. and Fried, W.R., *Avionics Navigation Systems*, Second ed, John Wiley & Sons, Inc., New York, 1997.
[42] ICAO, *Performance-based Navigation (PNB) Manual*, 2013.
[43] EASA, *CS-25 Certification Specifications for Large Airplanes*, 2010.
[44] White, E. and Rios, J.A., "FAA Certification of a MEMS Attitude and Heading Reference System," *Proceedings of the 2002 National Technical Meeting of The Institute of Navigation*, San Diego, CA, 2002.
[45] Nonami, K., Kendoul F., Suzuki, S., Wang, W., and Nakazawa, D., *Autonomous Flying Robots: Unmanned Aerial Vehicles and Micro Aerial Vehicles*, Springer Japan, 2010.
[46] Bryson, M. and Sukkarieh, S., "Building a Robust Implementation of Bearing-only Inertial SLAM for a UAV," *Journal of Field Robotics*, Vol. 24, No. 1-2, 2007, pp. 113-143.
[47] Conroy, J., Gremillion, G., Ranganathan, B., and Humbert, J.S., "Implementation of Wide-Field Integration of Optic Flow for Autonomous Quadrotor Navigation," *Autonomous Robots*, Vol. 27, No. 3, 2009, pp. 189–198.
[48] Achtelik, M., Bachrach, A., and He, R., *Stereo Vision and Laser Odometry for Autonomous Helicopters in GPS-denied Indoor Environments*, in *Unmanned Systems Technology XI*, 2009, SPIE: Society of Photo-Optical Instrumentation Engineers.
[49] Tarhan, M. and Altug, E., "EKF Based Attitude Estimation and Stabilization of a Quadrotor UAV Using Vanishing Points in Catadioptric Images," *Journal of Intelligent and Robotic Systems*, Vol. 62, No. 3-4, pp. 587-607.
[50] Siciliano, B. and Khatib, O., *Springer Handbook of Robotics*, Springer-Verlag Berlin Heidelberg, 2008.

[51] Seel, T., Raisch, J., and Schauer, T., "IMU-Based Joint Angle Measurement for Gait Analysis," *Sensors*, Vol. 14, No. 4, 2014, pp. 6891-6909.
[52] Van Nimmen, K., Van den Broeck, P., Lombaert, G., and De Roeck, G., "*Simultaneous Registration of Walking Behavior and Structural Response*", in *Research and Applications in Structural Engineering, Mechanics and Computation*, Zingoni, A., Editor. 2013, CRC Press. p. 47-48.
[53] Eckardt, F., Münz, A., and Witte, K., "Application of a Full Body Inertial Measurement System in Dressage Riding," *Journal of Equine Veterinary Science*, Vol. 34, No. 11-12, 2014, pp. 1294–1299.
[54] Merhav, S., *Aerospace Sensor Systems and Applications*, Springer-Verlag New York, 1996.
[55] Parkinson, B.W. and Spilker, J.J.J., *Global Positioning System: Theory and Applications*, Progress in Astronautics and Aeronautics, Vol. 2, AIAA, 1996.
[56] Cox, D.B., "Integration of GPS with Inertial Navigation Systems (Miscellaneous Topics)," *NAVIGATION, Journal of The Institute of Navigation*, Vol. 25, No. 2, 1978, pp. 236 - 245.
[57] Sabatini, A., "Quaternion-based Extended Kalman filter for Determining Orientation by Inertial and Magnetic Sensing," *IEEE Transactions on Biomedical Engineering*, 2006.
[58] Madgwick, S., Harrison, A., Vaidyanathan, R., "Estimation of IMU and MARG Orientation Using a Gradient Descent Algorithm," *IEEE International Conference on Rehabilitation Robotics*, 2011.
[59] Mahony, R., Hamel, T., and Pflimlin, J.M., "Nonlinear Complementary Filters on the Special Orthogonal Group," *IEEE Transactions on Automatic Control*, 2011.
[60] *iNAV-RQH-1003. Inertial Navigation System for Advanced Applications*, iMAR Navigation GmbH, 2011.
[61] "Mimimum Operational Performance Standards (MOPS) for Strapdown Attitude and Heading Reference Systems (AHRS)," RTCA Inc., 2012.
[62] Jia, H., "Data Fusion Methodologies For Multisensor Aircraft Navigation Systems," PhD Thesis, College of Aeronautics, Cranfield University, 2004.
[63] Vanderwerf, K. and Wefald, K., "Fault tolerant inertial navigation system," *Digital Avionics Systems Conference*, AIAA, San Jose, CA, U.S.A.
[64] Daly, K.C., Gai, E., and Harrison, J.V., "Generalized Likelihood Test for FDI in Redundant Sensor Configurations," *Journal of Guidance Control and Dynamics*, Vol. 2, No. 1, 1979, pp. 9-17.
[65] Luenberger, D.G., *Optimization by Vector Space Methods*, John Wiley & Sons, Inc. , New York, 1969.
[66] Sturza, M.A., "Navigation System Integrity Monitoring Using Redundant Measurements," *NAVIGATION, Journal of The Institute of Navigation*, Vol. 35, No. 4, 1989, pp. 69-87.
[67] Guerrier, S., Waegli, A., Skaloud, J., and Victoria-Feser, M.-P., "Fault Detection and Isolation in Multiple MEMS-IMUs Configurations," *IEEE Transactions on Aerospace and Electronic Systems*, Vol. 48, No. 3, 2012, pp. 2015-2031.
[68] Dodge, Y., *The Concise Encyclopedia of Statistics* Springer, New York, 2010.
[69] Pejsa, A.J., "Optimum Skewed Redundant Inertial Navigators," *AIAA Journal*, Vol. 12, No. 7, 1974, pp. 899-902.
[70] Sukkarieh, S., Gibbens, P., Grocholsky, B., Willis, K., and Durrant-Whyte, H.F., "A Low-Cost Redundant Inertial Measurement Unit for Unmanned Air Vehicle," *The International Journal of Robotics Research*, Vol. 19, No. 11, 2000, pp. 1089-1103.
[71] Jafari, M. and Roshanian, J., "Inertial Navigation Accuracy Increasing Using Redundant Sensors," *Journal of Science and Engineering*, Vol. 1, No. 1, 2013, pp. 55-66.
[72] Shim, D.-S. and Yang, C.-K., "Optimal Configuration of Redundant Inertial Sensors for Navigation and FDI Performance," *Sensors*, Vol. 10, No. 7, 2010, pp. 6497-6512.
[73] Harrison, J.V. and Gai, E., "Evaluating Sensor Orientations for Navigation Performance and Failure Detection," *IEEE Transactions on Aerospace and Electronic Systems*, Vol. 13, No. 6, 1977.
[74] Gai, E., Harrison, J.V., and Daly, K.C., "FDI Performance of Two Redundant Sensor Configurations," *IEEE Transactions on Aerospace and Electronic Systems*, Vol. 15, No. 3, 1979, pp. 405-413.
[75] Stuart, A., Ord, K., and Arnold, S., *Kendall's Advanced Theory of Statistics, Volume 2A: Classical Inference and the Linear Model*, 6th ed, Arnold, London, 1999.

[76] Owen, D.B., *Handbook of Statistical Tables*, Addison-Wesley Publishing Company, Inc., Reading, Massachusetts, 1962.
[77] *µIMU-I: Micro Inertial Measurement Unit*, Northrop Grumman LITEF, 2013.
[78] *ADIS16362 Datasheet*, Analog Devices, 2012.
[79] Willsky, A.S., "A Survey of Design Methods for Failure Detection in Dynamic Systems," *Automatica*, Vol. 12, No., 1976, pp. 601-611.
[80] Gertler, J., "Analytical Redundancy Methods in Fault Detection and Isolation," *Fault Detection, Supervision and Safety for Tech. Process*, IFAC, 1992.
[81] Isermann, R., "Supervision, Fault-Detection and Fault-Diagnosis Methods - An Introduction," *Control Engineering Practice*, Vol. 5, No. 5, 1997, pp. 639-652.
[82] Baseville, M. and Nikiforov, I.V., *Detection of Abrupt Changes: Theory and Application*, Prentice-Hall, Inc., 1993.
[83] Zhang, W., *Fault Detection*, InTech, 2010.
[84] Mironovski, L.A., *Functional Diagnosis of Dynamic Systems (in Russian)*, MSU-GRIF, St. Petersburg, 1998.
[85] Chen, J., "Robust Residual Generation for Model-Based Diagnosis of Dynamic Systems," PhD Thesis, Department of Electronics, University of York, 1995.
[86] Beard, R.V., "Failure Accomondation in Linear Systems Through Self-Reorganization," PhD Thesis, Department of Aeronautics and Astronautics, Massachusetts Institute of Technology, 1971.
[87] Jones, H.L., "Failure Detection in Linear Systems," PhD Thesis, Department of Aeronautics and Austronautics, Massachusetts Institute of Technology, 1973.
[88] Willsky, A.S. and Jones, H.L., "A Generalized Likelihood Ratio Approach to the Detection and Estimation of Jumps in Linear Systems," *IEEE Transactions on Automatic Control*, Vol. 21, No., 1976, pp. 108-112.
[89] Mironovski, L.A., "Functional Diagnosis of Linear Dynamic Systems," *Automation and Remote Control*, Vol. 40, No. 8, 1979, pp. 120-128.
[90] Chow, E.Y. and Willsky, A.S., "Analytical Redundancy and the Design of Robust Failure Detection Systems," *IEEE Transactions on Automatic Control*, Vol. AC-29, No. 7, 1984, pp. 603-614.
[91] Mehra, R.K. and Peschon, J., "An Innovations Approach to Fault Detection and Diagnosis in dynamic Systems," *Automatica*, Vol. 7, No., 1971, pp. 637-640.
[92] McMillan, C.J., Bird, J.S., and Arden, D.A.G., "Techniques for Soft-Failure Detection in a Multisensor Integrated System," *NAVIGATION, Journal of The Institute of Navigation*, Vol. 40, No. 3, 1993, pp. 227-248.
[93] Young, R.S.Y. and McGraw, G.A., "Fault Detection and Exclusion Using Normalized Solution Separation and Residual Monitoring Methods," *NAVIGATION, Journal of The Institute of Navigation*, Vol. 50, No. 3, 2003, pp. 151-169.
[94] Clark, B.J. and Bevly, D.M., *FDE Implementations for a Low-Cost GPS/INS Module*, in *22nd International Meeting of the Satellite Division of The Institute of Navigation*, 2009, Savannah, GA.
[95] Anderson, T.W. and Darling, D.A., "A Test of Goodness of Fit," *Journal of the American Statistical Association*, Vol. 49, No. 268, 1954, pp. 765-769.
[96] Braun, B., "High Performance Kalman Filter Tuning for Integrated Navigation Systems," PhD Thesis, Fakultät für Maschienenwesen, Technische Universität München, 2016.
[97] Boyd, S. and Vandenberghe, L., *Convex optimization*, Cambrige University Press, 2004.
[98] Matasov, A.I., *Estimators for Uncertain Dynamic Systems*, Springer Netherlands, 1998.
[99] Akimov, P.A., Derevyankin, A.V., and Matasov, A.I., *Guaranteed Approach to l_1-norm Approximation in the Problems of SDINS Parameter Estimation under Bench Testing*, Moscow University Press, Moscow, 2012.
[100] Ventcel, E.S., *Operations Research (in Russian)*, Soviet Radio, Moscow, 1972.
[101] Rausand, M. and Hoyland, A., *System Reliability Theory: Models, Statistical Methods, and Applications*, 2nd ed, John Wiley & Sons, Inc., New Jersey, 2004.
[102] Zorich, V.A., *Mathematical Analysis*, Vol. 1, Springer, Berlin, 2004.
[103] Gantmacher, F.R., *The Theory of Matrices*, Chelsea Publishing Company, New York, 1959.
[104] Kailath, T., *Linear Systems*, Prentice-Hall, Englewood Cliffs, N. J. , 1980.

[105] Rugh, W.J., *Linear System Theory*, 2nd ed, Prentice-Hall, Upper Saddle River, New Jersey, 1996.
[106] Sontag, E.D., *Mathematical Control Theory*, Springer-Verlag, New York, 1998.
[107] Ham, F., Brown, R., "Observability, Eigenvalues and Kalman Filtering," *IEEE Transactions on Aerospace and Electronic Systems*, Vol. 19, No. 2, 1983, pp. 269-273.
[108] Sazonov, I.U., "Calibration of a Strapdown Inertial Navigation System on a Low-grade Turntable (in Russian)," PhD Thesis, Faculty of Mechanics and Mathematics, Moscow State University, Moscow, 2012.
[109] Rhee, I., Abdel-Hafez, M.F., and Speyer, J.L., "Observability of an Integrated GPS/INS During Maneuvers," *IEEE Transactions on Aerospace and Electronic Systems*, Vol. 40, No. 2, 2004, pp. 526-535.
[110] Rothman, Y., Klein, I., Filin, S., "Analytical Observability Analysis of INS with Vehicle Constraints," *NAVIGATION, Journal of The Institute of Navigation*, Vol. 62, No. 3, 2014, pp. 227-236.
[111] Wang, L., Niu, X., Zhang, Q., Zhang, H., and Jiang, W., *High-Precision Image Aided Inertial Navigation with Known Features: Observability Analysis and Performance Evaluaton*, in *Proceedings of the 27th International Technical Meeting of the ION Satellite Division, ION GNSS+*, 2014, Tampa, Florida.
[112] Yonezawa, K., "Reduced-Order Kalman Filtering with Incomplete Observability," *Journal of Guidance, Control, and Dynamics*, Vol. 3, No. 3, 1980, pp. 280-282.
[113] Görcke, L., Holzapfel, F., Dambeck, J., "Aerodynamic Flight Simulation in Inertial Quality," *Proceedings of the ION International Technical Meeting, January 2013, San Diego, CA*.
[114] Crocoll, P., Görcke, L., Trommer, G., Holzapfel, F., "Unified Model Technique for Inertial Navigation Aided by Vehicle Dynamics Model," *NAVIGATION, Journal of The Institute of Navigation*, Vol. 60, No. 3, 2013, pp. 179-193.
[115] IEEE, *Standard Specification Format Guide and Test Procedure for Single-Axis Interferometric Fiber Optic Gyros*, 2008.
[116] *U.S. Military Specification MIL-F-8785C*, November 1980.
[117] *Smart Digital Magnetometer HMR2300*, Honeywell, 2012.
[118] Kozlov, A., Sazonov, I., Vavilova, N., and Parusnikov, N., "Calibration af an Inertial Measurement Unit on a Low-grade Turntable with Consideration of Spatial Offsets of Accelerometer Proof Masses," *20th Saint Petersburg International Conference on Integrated Navigation Systems*, Concern CSRI Elektropribor, Saint Petersburg, 2013.
[119] Kozlov, A., Tarygin, I., and Golovan, A., "Calibration of Inertial Measurement Units on a Low-Grade Turntable with Simultaneous Estimation of Temperature Coefficients," *21st Saint Petersburg International Conference on Integrated Navigation Systems*, Concern CSRI Elektropribor, Saint Petersburg, 2014.